Fabrication of Micro-Engineered Scaffolds for Biomedical Application

Fabrikation von Scaffolds mit optimierter Mikroarchitektur für biomedizinische Anwendungen

Doctoral thesis for a doctoral degree

at the Graduate School of Life Sciences,

Julius-Maximilians-Universität Würzburg,

Section Biomedicine

submitted by

Almoatazbellah Youssef

from

Cairo

Würzburg, 2020

Submitted on: ……

Office stamp

Members of the Thesis Committee

Chairperson: Prof. Dr. Carmen Villmann

Primary Supervisor: Prof. Dr. Paul Dalton

Supervisor (Second): Prof. Dr. Jürgen Groll

Supervisor (Third): Prof. Dr. Franz Jakob

Supervisor (Fourth): Prof. Dr. Torsten Blunk

Date of Public Defense: ……

Date of Receipt of Certificates: ……

This work was conducted from July 2015 until May 2019 at the Department of Functional Materials in Medicine and Dentistry, University Hospital Würzburg, Würzburg, Germany, under the supervision of Prof. Dr. Paul D. Dalton.

“There is nothing like looking, if you want to find something. You certainly usually find something, if you look, but it is not always quite the something you were after.”

- J. R. R. Tolkien, *The Hobbit, or There and Back Again*

Affidavit

I hereby confirm that my thesis entitled “Fabrication of micro-engineered scaffolds for biomedical application” is the result of my own work. I did not receive any help or support from commercial consultants. All sources and/or materials applied are listed and specified in the thesis.

Furthermore, I confirm that this thesis has not yet been submitted as part of another examination process neither in identical nor in similar form.

Place. Date Signature

Eidesstattliche Erklärung

Hiermit erkläre ich an Eides statt, die Dissertation „Fabrikation von Scaffolds mit optimierter Mikroarchitektur für biomedizinische Anwendungen“ eigenständig, d. h. insbesondere selbständig und ohne Hilfe eines kommerziellen Promotionsberaters, angefertigt und keine anderen als die von mir angegebenen Quellen und Hilfsmittel verwendet zu haben.

Ich erkläre außerdem, dass die Dissertation weder in gleicher noch in ähnlicher Form bereits in einem anderen Prüfungsverfahren vorgelegen hat.

Ort, Datum Unterschrift

List of publications

The following publications resulted from work done during the timeframe of this thesis.

As first author

Youssef, A., Hollister, S. J., Dalton, P. D. (2017) "Additive manufacturing of polymer melts for implantable medical devices and scaffolds." Biofabrication 9(1): 012002. DOI: 10.1088/1758-5090/aa5766.

Youssef, A., Hrynevich, A., Fladeland, L., Balles, A. Groll, J., Dalton, P. D., Zabler, S. (2018) "The Impact of Melt Electrowritten Scaffold Design on Porosity Determined by X-ray Micro-tomography." Tissue Eng Part C Methods 25(6): 367-379. DOI: 10.1089/ten.TEC.2018.0373.

As co-author

Hochleitner, G., **Youssef, A.**, Hrynevich, A., Haigh, J. N., Jungst, T., Groll, J., Dalton, P. D. (2016) "Fiber pulsing during melt electrospinning writing." BioNanoMaterials 17(3-4): 159–171. DOI: 10.1515/bnm-2015-0022.

Hrynevich, A., Şen Elçi, B., Haigh, J. N., McMaster, R., **Youssef, A.**, Blum, C., Blunk, T., Hochleitner, G., Groll, J., Dalton, P. D. (2018) "Dimension-based design of melt electrowritten scaffolds." Small 14(22): e1800232. DOI: 10.1002/smll.201800232.

Fuchs, A., **Youssef, A.**, Seher, A., Hartmann, S., Brands, R. C., Müller-Richter, U. D. A., Kübler, A., Linz, C. (2019) "A new multilayered membrane for tissue engineering of oral hard- and soft tissue by means of melt electrospinning writing and film casting – an in vitro study." J Craniomaxillofac Surg 47(4): 695-703. DOI: 10.1016/j.jcms.2019.01.043.

Fuchs, A., **Youssef, A.**, Seher, A., Dalton, P. D., Hartmann, S., Müller-Richter, U. D. A., Linz, C. (2019) "Medical-grade polycaprolactone scaffolds made by melt electrospinning writing for oral bone regeneration–a pilot study in vitro." BMC Oral Health 19 (1), 28. DOI: 10.1186/s12903-019-0717-5.

Submitted

Ran An, Pamela L. Strissel, Majida Al-Abboodi, Jan W. Robering, Reakasame Supachai, Markus Eckstein, Ajay Peddi, Theresa Hauck, Tobias Bäuerle, Aldo R. Boccaccini, **Almoatazbellah Youssef**, Paul D. Dalton, Jiaming Sun, Reiner Strick, Raymund E. Horch, Anja M. Boos, Annika Kengelbach-Weigand "An innovative arteriovenous (AV) loop breast cancer model tailored for cancer research." Submitted to Nature Communications.

In preparation

Youssef, A., Tandon, B., Ziani, N. T., Groll, J., Jungst, T., Dalton, P. D. "The estimation of mass flow rate of melt electrowritten polycaprolactone scaffolds."

Youssef, A., Ewald, A., Hrynevich, A., Jungst, T., Groll, J., Dalton, P. D. "The foreign body reaction to micro-scale melt electrowritten flat polycaprolactone scaffolds."

Table of contents

Abstract

Thermoplastic polymers have a history of decades of safe and effective use in the clinic as implantable medical devices. In recent years additive manufacturing (AM) saw increased clinical interest for the fabrication of customizable and implantable medical devices and training models using the patients' own radiological data. However, approval from the various regulatory bodies remains a significant hurdle. A possible solution is to fabricate the AM scaffolds using materials and techniques with a clinical safety record, e.g. melt processing of polymers. Melt Electrowriting (MEW) is a novel, high resolution AM technique which uses thermoplastic polymers. MEW produces scaffolds with microscale fibers and precise fiber placement, allowing the control of the scaffold microarchitecture. Additionally, MEW can process medical-grade thermoplastic polymers, without the use of solvents paving the way for the production of medical devices for clinical applications. This pathway is investigated in this thesis, where the layout is designed to resemble the journey of a medical device produced via MEW from conception to early *in vivo* experiments. To do so, first, a brief history of the development of medical implants and the regenerative capability of the human body is given in Chapter 1. In Chapter 2, a review of the use of thermoplastic polymers in medicine, with a focus on poly(ε-caprolactone) (PCL), is illustrated, as this is the polymer used in the rest of the thesis. This review is followed by a comparison of the state of the art, regarding *in vivo* and clinical experiments, of three polymer melt AM technologies: melt-extrusion, selective laser sintering and MEW. The first two techniques already saw successful translation to the bedside, producing patient-specific, regulatory-approved AM implants. To follow in the footsteps of these two technologies, the MEW device parameters need to be optimized. The MEW process parameters and their interplay are further discussed in Chapter 3 focusing on the importance of a steady mass flow rate of the polymer during printing. MEW reaches a balance between polymer flow, the stabilizing electric field and moving collector to produce reproducible, high-resolution scaffolds. An imbalance creates phenomena like

fiber pulsing or arcing which result in defective scaffolds and potential printer damage. Chapter 4 shows the use of X-ray microtomography (µCT) as a non-destructive method to characterize the pore-related features: total porosity and the pore size distribution. MEW scaffolds are three-dimensional (3D) constructs but have long been treated in the literature as two-dimensional (2D) ones and characterized mainly by microscopy, including stereo- and scanning electron microscopy, where pore size was simply reported as the distance between the fibers in a single layer. These methods, together with the trend of producing scaffolds with symmetrical pores in the 0/90° and 0/60/120° laydown patterns, disregarded the lateral connections between pores and the potential of MEW to be used for more complex 3D structures, mimicking the extracellular matrix. Here we characterized scaffolds in the aforementioned symmetrical laydown patterns, along with the more complex 0/45/90/135° and 0/30/60/90/120/150° ones. A 2D pore size estimation was done first using stereomicroscopy, followed by and compared to µCT scanning. The scaffolds with symmetrical laydown patterns resulted in the predominance of one pore size, while those with more complex patterns had a broader distribution, which could be better shown by µCT scans. Moreover, in the symmetrical scaffolds, the size of 3D pores was not able to reach the value of the fiber spacing due to a flattening effect of the scaffold, where the thickness of the scaffold was less than the fiber spacing, further restricting the pore size distribution in such scaffolds. This method could be used for quality assurance of fabricated scaffolds prior to use in *in vitro* or *in vivo* experiments and would be important for a clinical translation. Chapter 5 illustrates a proof of principle subcutaneous implantation *in vivo experiment.* MEW scaffolds were already featured in small animal *in vivo* experiments, but to date, no analysis of the foreign body reaction (FBR) to such implants was performed. FBR is an immune reaction to implanted foreign materials, including medical devices, aimed at protecting the host from potential adverse effects and can interfere with the function of some medical implants. Medical-grade PCL was used to melt electrowrite scaffolds with 50 and 60 µm fiber spacing for the 0/90° and 0/60/120° laydown patterns, respectively. These implants were implanted subcutaneously in immunocompetent, outbred mice, with appropriate controls, and explanted after 2, 4, 7 and 14 days. A thorough characterization of the

scaffolds before implantation was done, followed by a full histopathological analysis of the FBR to the implants after excision. The scaffolds, irrespective of their pore geometry, induced an extensive FBR in the form of accumulation of foreign body giant cells around the fiber walls, in a manner that almost occluded available pore spaces with little to no neovascularization. This reaction was not induced by the material itself, as the same reaction failed to develop in the PCL solid film controls. A discussion of the results was given with special regard to the literature available on flat surgical meshes, as well as other hydrogel-based porous scaffolds with similar pore sizes. Finally, a general summary of the thesis in Chapter 6 recapitulates the most important points with a focus on future directions for MEW.

Zusammenfassung

Thermoplastische Polymere werden seit Jahrzehnten erfolgreich in der Klinik eingesetzt und für die Herstellung von Medizinprodukten verwendet. Vorangetrieben durch das zunehmende klinische Interesse an additiven Fertigungsverfahren, z.B. zur Herstellung patientenspezifischer Trainingsmodelle und implantierbarer Medizinprodukte, rücken thermoplastische Materialien noch mehr in den Fokus der klinischen Forschung. Allerdings stellt die Marktzulassung durch die verschiedenen Gesundheitsbehörden eine große Hürde dar. Eine mögliche Lösung ist die Gerüstfabrikation mit Materialien und Verfahren, die bereits etablierte Sicherheitsstandards durchlaufen haben, z. B. die Schmelzverarbeitung der Polymere. Ein neuartiges und hochauflösendes additives Fertigungsverfahren, welches die Verarbeitung von Thermoplasten ermöglicht, ist Melt Electrowriting (MEW). Mittels MEW lassen sich Gerüste, die aus Fasern mit Durchmessern im Mikrometerbereich zusammengesetzt sind, herstellen. Neben der hohen Kontrolle über den Faserdurchmesser ermöglicht MEW auch eine genaue Ablage der Fasern und erlaubt dadurch, die Mikroarchitektur der Konstrukte vorzugeben. Zudem kann das Verfahren medizinisch zugelassene thermoplastische Polymere ohne die Verwendung von Lösungsmitteln verarbeiten und ist somit für die Herstellung medizinischer Produkte sehr relevant.

Diese Relevanz sollte im Rahmen der vorliegenden Dissertation evaluiert werden, indem der Weg, den ein Medizinprodukt von der Konzeption bis hin zu *in vivo* Vorversuchen durchlaufen muss, anhand von Konstrukten, die mittels MEW hergestellt wurden, nachgeahmt wurde. Um eine Basis für das Verständnis dieses Prozesses zu schaffen, wird in Kapitel 1 erst die Geschichte der Entwicklung medizinischer Implantate zusammengefasst sowie ein Einblick in die regenerativen Fähigkeiten des menschlichen Körpers gegeben. Das zweite Kapitel befasst sich mit der Anwendung von thermoplastischen Polymeren im Bereich implantierbarer Medizinprodukte, wobei der Hauptfokus auf Poly(ε-caprolactone) (PCL) liegt, da dies der in der vorliegenden Arbeit verwendete Thermoplast

ist. Es folgt ein Vergleich von *in vivo* sowie klinischen Versuchen dreier für die Biomedizin relevanten additiven Fertigungsverfahren, mit denen sich thermoplastische Polymere verarbeiten lassen: Die Mikro-Schmelzextrusion, das selektive Lasersintern und das MEW. Die ersten zwei Verfahren sind bereits erfolgreich in klinischen Anwendungen etabliert und ermöglichen die routinemäßige Herstellung von additiv gefertigten, patientenspezifischen, auf dem Markt zugelassenen Implantaten. Damit MEW in diese Fußstapfen treten kann, müssen die Prozessparameter und deren Zusammenspiel genau analysiert werden. Dieser Thematik widmet sich Kapitel 3, wobei die Untersuchung des Massendurchsatzes des Polymers während des Druckens diskutiert wird. Um den MEW-Prozess kontrollieren zu können, muss eine Balance zwischen Polymerdurchsatz, dem stabilisierenden elektrischen Feld und dem beweglichen Kollektor erreicht werden. Dies ist Grundlage für die reproduzierbare Herstellung hochaufgelöster Konstrukte. Ein Ungleichgewicht der Prozessparameter verursacht Phänomene wie Fiber Pulsing oder sogar elektrischen Durchschlag, welche zu defekten Konstrukten oder sogar zur Schädigung des Druckers führen können. Kapitel 4 zeigt die Anwendung der Röntgenmikrocomputertomographie (µCT) als eine zerstörungsfreie Charakterisierungsmethode für MEW-Konstrukte, die die Quantifizierung charakteristischer Eigenschaften wie der Porosität und der Porengrößenverteilung ermöglicht. MEW-Konstrukte wurden in der Literatur lange als zweidimensional behandelt und hauptsächlich durch mikroskopische Verfahren wie die Stereo- und Rasterelektronmikroskopie charakterisiert. Die zweidimensionale Porengröße wurde hauptsächlich durch die Bestimmung des Faserabstands definiert und daraus errechnet, mit einer Tendenz der Herstellung der Konstrukte mit symmetrischen Poren in 0/90° und 0/60/120° Ablagemustern. Da es sich bei den Konstrukten jedoch um dreidimensionale (3D) Fasergerüste handelt, wurden die seitlichen Verbindungen zwischen den Poren und das Potential der Anwendung des MEW für die Herstellung von komplexeren 3D-Strukturen, wie bei der extrazellulären Matrix mit interkonnektierenden Poren, vernachlässigt. Aus diesem Grund wurden in der vorliegenden Arbeit µCT-Scans verwendet, um die Porosität der Konstrukte besser wiedergeben zu können. Hierzu wurden verschiedene Ablagemuster mit symmetrischen Poren in 0/90° und 0/60/120°

Mustern und komplexere Porenstrukturen durch Ablagen von 0/45/90/135° und 0/30/60/90/120/150° Geometrien hergestellt. Diese Konstrukte wurden dann mittels mikroskopischer und tomographischer Aufnahmen charakterisiert und die Ergebnisse miteinander verglichen. Es zeigte sich, dass symmetrische Ablagemuster zu Konstrukten mit der Prädominanz einer Porengröße geführt haben. Bei den komplexeren Strukturen ergab sich jedoch ein klarer Unterschied, weil die interkonnektierenden Poren nur mit Hilfe von µCT-Scans erfasst werden konnten. Dies zeigte sich durch eine breitere Porenverteilung bei der Auswertung der rekonstruierten Scans. Die Porengrößen in den Konstrukten mit den symmetrischen Mustern konnten aufgrund einer Verflachungswirkung nicht die des Faserabstands erreichen. Die Dicke der Konstrukte war geringer als der Faserabstand mit einer weiteren einschränkenden Wirkung auf die Porenverteilung in den symmetrischen Konstrukten. µCT kann deshalb für die Qualitätssicherung von medizinischen Produkten, die mittels MEW hergestellt wurden, eingesetzt werden. Da die Methode zerstörungsfrei ist, könnte sie auch vor *in vitro* oder *in vivo* Versuchen verwendet werden. Kapitel 5 präsentiert eine Machbarkeitsstudie eines subkutanen *in vivo* Implantationsversuchs. Aus der Literatur ist zwar bekannt, dass MEW-Konstrukte bereits *in vivo* in Kleintierversuchen verwendet wurden, eine Analyse der Fremdkörperreaktion (FKR) zu solchen Implantaten wurde bisher jedoch noch nicht durchgeführt. FKR ist eine Immunreaktion gegen fremde, implantierte Materialien, einschließlich medizinischer Geräte, um den Wirt vor potenziellen Nebenwirkungen zu schützen. Allerdings könnte sie die Funktion verschiedener medizinischer Implantate beeinträchtigen Um dieser Fragestellung nachzugehen, wurde im Rahmen der vorliegenden Dissertation PCL mittels MEW zu Konstrukten mit 50 und 60 µm Fiberabstand in 0/90° bzw. 0/60/120° Ablagemuster verarbeitet. Diese Konstrukte wurden subkutan in immunkompetente, fremdgezüchtete Mäuse mit entsprechenden Kontrollen implantiert und nach 2, 4, 7 und 14 Tagen explantiert. Vor der Implantation wurde die Konstrukte ausführlich charakterisiert, gefolgt von einer vollen histopathologischen Analyse des FKR. Unabhängig von der Porengeometrie haben die Konstrukte eine deutliche Immunreaktion im Sinne einer Ansammlung von Fremdkörperriesenzellen um die Fasern der Konstrukte hervorgerufen. Hierbei wurden die Poren fast

komplett verschlossen, ohne dass es zu einer Neovaskularisation kam. Es konnte nachgewiesen werden, dass die deutliche Immunantwort nicht durch das Material hervorgerufen wurde, da sie bei der Implantation von dichtem PCL-Film nicht beobachtet wurde. Eine Diskussion der Ergebnisse erfolgte unter Berücksichtigung aktueller Literatur zu klinischen Versuchen von flachen chirurgischen Netzen sowie porösen Hydrogel-basierten Implantaten mit vergleichbarer Porengröße. Abschließend wird die Arbeit in Kapitel 6 zusammengefasst und die wichtigsten Punkte rekapituliert. Der Fokus des Kapitels liegt hierbei auf dem zukünftigen Potential des MEW als Fabrikationsmethode für medizinische Produkte.

Chapter 1

1.1 Tissue injury and regeneration potential

Tissue regeneration is an inherent biological function that exists in all plant and animal lifeforms. Different than growth and proliferation, it is an essential means to replace cells and tissues lost due to injury, disease and aging (Goldman 2014). The complexity of the organism in the animal kingdom is inversely proportional with its healing capabilities (Suzuki *et al.* 2006) and, in general, there are two main modalities for regeneration, namely, epimorphosis and morphallaxis. Epimorphosis is how a mass of undifferentiated cells forms at the trauma site from which a new tissue or limb will be regenerated, through the proliferation of present progenitor cells or dedifferentiation of mature, differentiated cells. Morphallaxis, which is mainly observed in invertebrates, on the other hand, is achieved by rearrangement and remodeling of the remaining damaged tissue at the trauma site, in an attempt to restore the tissue integrity, with limited cellular proliferation (Agata *et al.* 2007, Birnbaum and Sanchez Alvarado 2008). The overall regenerative potential is, however, limited in higher vertebrates and mammals (Iismaa *et al.* 2018). While limited in comparison to lower vertebrates, such as newts and axolotls, the human body still possesses a remarkable ability to regenerate itself (Brockes and Kumar 2008). **Figure 1.1** shows a schematic of regeneration of different tissues across different tissue types in humans, mice, and salamanders during different developmental stages of life.

In adults there are tissues that exemplify excellent regenerative capability. For example, in blood, a specialized form of connective tissue, erythrocytes have a life span of 100-120 days and are produced at an approximate rate of $2x10^6$ cells per second from the bone marrow to replace retired cells (Higgins 2015). Partial hepatectomy patients with healthy livers will regenerate the pre-resection hepatic volume from the remaining lobes within 1-2 months, with the regenerating cells originating from the endogenous hepatic cell population of hepatocytes, biliary epithelial cells, vascular endothelial cells and Kupffer cells – without relying on differentiation of stem cells (Yamanaka *et al.* 1993, Michalopoulos and DeFrances 1997). This process is a variant of epimorphosis, as it occurs

without the recruitment of undifferentiated or dedifferentiated cells, but rather through the endogenous, already differentiated hepatic cells (Iismaa *et al.* 2018).

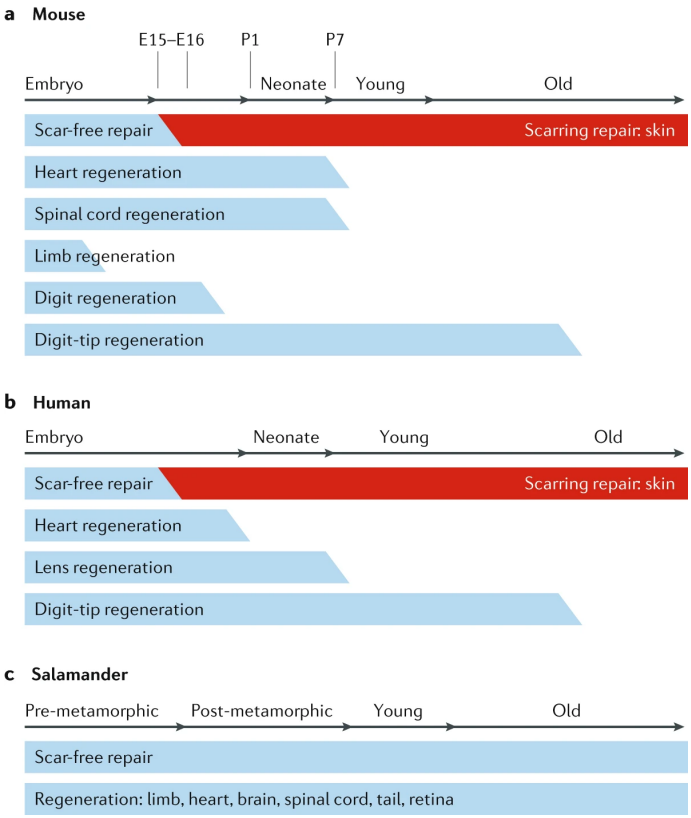

Figure 1.1. Graphical representation of regenerative potentials of different tissue types across mouse (A), human (B), and salamander (C). E15 and E16: embryonic week 15 and 16, respectively; P1 and P7: postnatal day 1 and 7, respectively. Reproduced from (Xia *et al.* 2018), with permission from Springer Nature.

In addition to the liver, bone tissue can also regenerate without scar tissue formation in adults (Schmidt-Bleek *et al.* 2014). Bone fractures can completely heal without scar tissue formation, provided certain conditions are met. Through fixation of the fracture, the gap between both ends is eliminated and primary fracture healing can proceed. When a gap still exists, but is less than the so-called critical defect, healing through callus formation will take place. Bone healing results in a functional tissue (here, bone), but without the fibrosis that is seen in tissue healing elsewhere in the body, through the calcification of the callus and then remodeling of the newly formed bone to the form of the original one. Bone regeneration is also a life-long process as the skeleton is constantly being remodeled and rebuilt through the action of osteoclasts and osteoblasts, respectively (Sims and Martin 2014).

The regenerative capabilities of the skin, due to its accessible anatomical location allowing easy observation, were subjected to intense study over the past two decades (Canedo-Dorantes and Canedo-Ayala 2019). Skin heals postnatally through the formation of scar tissue, which is a disorganized laydown of extracellular matrix (ECM) made by fibroblasts under the influence of several cytokines and signaling cascades in the injury site (Takeo *et al.* 2015). Healing of skin wounds in utero happens without any scar tissue (Lorenz *et al.* 1992). In adults, when the wound gap is not large and in the presence of a clean wound without chronic debilitating diseases (e.g. diabetes mellitus or vascular insufficiency), skin healing happens by primary intention, which usually happens in minor wounds and clean surgical wounds. Secondary intention happens when the conditions are unsuitable, whether through an infected wound or a chronic disease, leading to delayed wound closure and excessive scarring (Canedo-Dorantes and Canedo-Ayala 2019).

While remarkable, the regenerative capability of the human body is limited compared to what an invertebrate can achieve. For example, *Schmidtea mediterranea*, a freshwater flatworm can regenerate a whole worm from a fragment of $1/279^{th}$ the size of the original one, while healing the injury in the parent organism (Sanchez Alvarado *et al.* 2002).

When the physiological limits of normal healing in humans are stretched, the failure to return to the baseline status before the injury and/or disease will proceed to form a pathology on its own. Thus, bone fractures can result in mal- or non-union (Schemitsch 2017, Henderson *et al.* 2019). Worn-out cartilage in osteoarthritis will lead to a huge limitation of movement and affection of the lifestyle of patients, leading up to a total joint replacement (Hunter and Bierma-Zeinstra 2019). Vascular accidents in or trauma to the central nervous system can lead to lifelong neurological deficits, while peripheral nerve injuries will affect motor, sensory or both functions (Tian *et al.* 2015). Diabetes mellitus can lead to a lifelong dependence on exogenous insulin. Chronic renal illness will develop a dependence on dialysis for survival.

1.2 The development and need for implants

What humans lack in regeneration capabilities is compensated by one of their strongest abilities: invention. The limited regenerative capacity of the human body meant that large wounds needed to be sutured, complex fractures required fixation, or missing limbs to be artificially replaced. Ancient humans understood these challenges, and this led to the rise and development of protheses and implants. Implants can be defined as a device or tissue that can be placed inside or on the surface of the body, while delivering medication, supporting organs and/or tissues and monitoring body function. It can be permanent or removable. On the other hand, a prosthesis is defined as an implant which aims to replace a missing body part, whether internally or externally (FDA 2019a). In case of protheses, these provided a functional replacement, as well as an aesthetic one. While in the case of implants, these relied on the natural ability of the body to regenerate, and functioned by reinforcing, accelerating or supporting this ability. In short, all these efforts were to treat traumatic or degenerative diseases, against which, the human body had little or no regenerative countermeasures.

The history of ancient medicine tells of prosthetics and implants that were used due to injury or disease (Migonney 2014). One of the first recorded instances of using a prosthetic is the Cairo Toe (1550-700 BC) which is a big toe wearable prosthetic made of wood and leather that was found attached to a mummy of an elder female, who was thought to have had an amputation of her right big toe resulting from diabetes (Hildebrand 2013). The earliest description of sutures were mentioned in the Smith Papyrus from Ancient Egypt (circa 1600 BC) made from hair, plant fibers and tendons, while in ancient India, giant Bengali ants were used to close wounds by allowing their jaws to close around the skin wound and then, their thoracic and abdominal segments are removed (Klimczak *et al.* 2011). Sutures for wound closure were made of linen and other materials, while metal and sea shells were used to make artificial teeth (Ratner 2013). Cranioplasty was performed since at least 2000 BC in Peru to cover trepanation defects made for ritualistic or medical reasons. These pre-Incan and pre-

Columbian civilizations used gold plates, with fossils showing calvarial bone healing around the implant, which happened in the lifetime of the patient (Abhay and Haines 1997).

One can safely say that the evolution of implants throughout the centuries is in the most part related to the evolution of materials used to produce them. The search for materials that can be safely used in the human body, led to the development of biomaterials which are simply defined as materials aimed to be used in contact with living tissues or living organisms (Vert *et al.* 2012). While the 20th century witnessed remarkable and rapid scientific and medical breakthroughs, it also had two destructive and brutal world wars. The experience and accumulation of knowledge due to these unfortunate events, pushed the development of implants, especially in the field of orthopedics, from production and material selection to the refinement of the surgical technique needed for implantation and later for case follow up (Flanigan *et al.* 2014, Dougherty *et al.* 2004, Scotland 2014). The technique of intramedullary nailing was popularized in the 1930s by Gerhard Küntscher. In the 1950s, the Soviet surgeon, Gavriil Ilizarov, popularized the method that carried his name for the external fixation and management of complex fractures, often with soft tissue injuries. This was followed by the widespread use of plate and screw osteosynthesis, heralded by the Arbeitsgemeinschaft für Osteosynthesefragen (The AO Foundation) in 1958 and later the limited contact dynamic compression plates in the 1980s (Broos and Sermon 2004, Uhthoff *et al.* 2006). Polymethyl methacrylate (PMMA) was first used as an implant after small fragments were found to cause no adverse reaction in the bodies and eyes of World War II fighter pilots who had PMMA shrapnel embedded in their bodies during aerial combat (Ratner 2013). PMMA saw extensive use as a bone cement in joint replacement surgeries (Webb and Spencer 2007, Arora *et al.* 2013). Since osteoarthritis is a major cause of morbidity, with an estimated one million joint replacement surgeries per year in the United States (Maradit Kremers *et al.* 2015), the use of artificial knee and hip joints was a necessity to bypass the poor regeneration of articular hyaline cartilage. The issue with such surgeries is that the high rate of revision surgeries that are needed on account of the decreased durability of the artificial joint, as well as the development of complications such as loosening and infection (Aicale and Maffulli 2019).

1.3 The age of tissue engineering

With increased scientific and research output and with an ever-increasing number of patients in need of functional replacements to pathological tissue, the era of tissue engineering was ushered in in the early 1990s (Langer *et al.* 1990), with bold promises of treating a wide range of diseases and producing human spare parts that would cut down on the wait for organ donors and decrease patient mortality and morbidity due to transplant rejection (Langer and Vacanti 1993). Despite decades of research and billions of dollars in funding, many of these promises are still unfulfilled (Ronfard *et al.* 2017).

One reason for this discontinuity between the enormous amount of research activity in the tissue engineering and regenerative medicine field and the paucity of products available for patients is the need of such new products to be approved by regulatory bodies throughout the world (Hollister 2009a). To protect the public against ineffective, untested, falsely labelled or other dangerous implants and medical devices, the regulatory bodies in several countries have set up a rigid set of rules and laws that govern what can be sold in the market to be used by physicians on patients. Despite this, tissue engineered products have still led to unintended complications (Charo and Sipp 2018). Throughout this thesis, the United States Food and Drug Administration (FDA) will be used as an example, however the underlying principles between the various national regulatory bodies are similar globally.

The roots of the FDA regulations are based on the 1938 Federal Food, Drug and Cosmetic Act which was passed as a result of the fallout of the 1937 Elixir Sulfanilamide preparation that contained diethylene glycol as a solvent and caused at least 100 reported deaths because of its use (FDA 2019b, FDA 2018a). While drug testing is not the focus of this thesis, the regulations for medical devices stemmed from drug regulations, albeit with accelerated pathways to facilitate and shorten the approval process for products similar to already marketed products, or to those which have proven

efficacy and will be used in a humanitarian situation. These topics will be further discussed in detail in the following chapter.

The structure of this thesis is based on the journey that a new medical device will take to pass the regulatory hurdles and cross the long path from conception on the bench to being implanted and/or used in or on a patient. The aim of the thesis is the investigation of melt electrowritten scaffolds for a potential biomedical application. Melt electrowriting (MEW) is an additive manufacturing (AM) technique using polymer melts. The state of the art will be discussed in Chapter 2 with a comparison of similar AM, polymer-based techniques and an overview of the FDA regulatory pathway for medical device. Chapter 3 will focus on the method of MEW and the fabrication parameters needed to produce the scaffolds. Chapter 4 will discuss the process validation, where the intended design is compared to the scaffold outcome using a high-fidelity, non-destructive testing method. Chapter 5 focuses on a proof of principle *in vivo* experiment to investigate an important biological response to MEW scaffolds implanted subcutaneously: the foreign body reaction. Finally, Chapter 6 provides a general summary and a conclusion to the thesis.

Chapter 2

This chapter was previously published as:

Youssef, A., Hollister, S. J., Dalton, P. D. (2017). "Additive manufacturing of polymer melts for implantable medical devices and scaffolds." Biofabrication 9(1): 012002. DOI: 10.1088/1758-5090/aa5766

Abstract: “Melt processing is routinely used to fabricate medical polymeric devices/implants for clinical reconstruction and can be incorporated into quality systems procedures for medical device manufacture. As additive manufacturing (AM) becomes increasingly used for biomaterials and biofabrication, the translation of new, customizable, medical devices to the clinic becomes paramount. Melt processing is therefore a distinguishable group within AM that provides an avenue to manufacture scaffolds/implants with a clinical endpoint. Three key melt processing AM technologies are highlighted in this review: melt micro-extrusion, selective laser sintering and melt electrospinning writing. The *in vivo* (including clinical) outcomes of medical devices and scaffolds made with these processes are reviewed. Together, they encompass the melt AM of scaffold architectures with feature sizes and resolutions ranging from 800 nm up to 700 µm.”

The text of this chapter was edited and thoroughly updated to reflect the state of the art in 2020 (year of thesis submission) compared to 2017 (year of review publication), while the abstract above is quoted from the original publication, with permission from IOP Publishing. Since submission, the publication has been cited 83 times (Google Scholar; accessed 12.12.2020).

2.1 Introduction

Medical devices had, in 2018, a global market size of approximately 423.8 billion US dollars, increasing from approximately 350 billion US dollars in 2012 and is expected to grow to 521.64 billion US dollars in 2022 (Holtzman and WTP Advisors 2012, Research and Markets 2019). These devices are routinely used in everyday clinical situations and range in complexity from a tongue depressor to a cochlear implant. Medical devices can be defined as an instrument, machine, implant or apparatus intended for the diagnosis, treatment, prevention and/or monitoring a disease and/or injury, or to replace, investigate or modify an anatomical structure or a physiological process in the human body. The device must perform these tasks without pharmacological, immunological or metabolic means. The definition includes devices intended for *in vitro*, *in vivo* and *in silico* use (Study Group 1 of the Global Harmonization Task Force WHO 2012). Additive manufacturing (AM) changed long established rules in the supply chain of medical devices by adding the possibility of making the medical device inside a healthcare facility via “bedside manufacturing”.

Medical devices should achieve their intended function without pharmacological, immunological or metabolic means, but they still need to be approved by regulatory bodies worldwide. In the United States, the governmental agency tasked with this is the Food and Drug Agency (FDA) and it ensures compliance to local laws and guidelines before medical devices are available to the patients.

In this chapter, the development of medical devices through polymer melts will be described along with the state of the art of three different polymer melt-based AM techniques and the results of clinical and *in vivo* animal studies performed with scaffolds from such techniques. These techniques are micro-extrusion, selective laser sintering (SLS) and melt electrowriting (MEW). The regulatory framework of the FDA regarding the approval of medical devices will also be mentioned.

2.1.1 The use of polymers in medicine

Thermoplastic polymers have been used in medicine for the production of medical devices for decades (Ratner *et al.* 2013). Perhaps the first such use and the beginning of a whole new of era of synthetic medical polymers was the introduction of nylon sutures in the 1930s by Ethicon (then, G. F. Mersons Limited) (Ethilon™) to replace silk sutures. Polypropylene (PP) was later used in the 1950s as a non-resorbable suture material (Prolene™) and is still in active use (**Figure 2.1A**). Polyvinyl alcohol (PVA) was used as a resorbable suture and was also developed in the 1930s (Pillai and Sharma 2010). Several resorbable sutures followed, for example, polyglycolic acid (PGA) (Dexon™) (Frazza and Schmitt 1971) and polyglactin 910 (or polyglycolide-L-lactide (Vicryl™) (Conn *et al.* 1974). PGA was found to be superior to chromic catgut in terms of wound closure strength (Barham *et al.* 1978). These novel materials managed to replace catgut by being easier to produce and sterilize with less risk of disease transmission as in the case with the theoretical possibility of variant Creutzfeldt-Jakob disease (vCJD) transmission with catgut suture material (Klimczak *et al.* 2011). It is worth mentioning, though, that there have been no reported cases of vCJD as a result of using catgut (Collee *et al.* 2006), but it remains a possibility, nonetheless. Moreover, a study of the Cochrane Database of Systemic Reviews concluded that using synthetic sutures might decrease short-term pain compared to catgut (Kettle *et al.* 2010).

Similarly, surgical meshes saw a similar transition towards thermoplastic polymers away from metal meshes. Hernia is a common complication of abdominal and pelvic surgery (Deerenberg *et al.* 2015). It was formerly treated with silver or steel meshes, to induce inflammation and fibrosis. In the 1950s, polyethylene (PE) meshes were introduced, followed by PP ones, made from melt-spun polymer fibers (**Figure 2.1B**). They provided superior results in hernia repair surgeries by being light-weight and simple to work with (Bringman *et al.* 2010). In recent years, melt-processed polyvinylidene fluoride (PVDF) was introduced as a surgical mesh (Klinge *et al.* 2002, Baylon *et al.* 2017). Several authors reviewed the biology of polymer hernia meshes and their use in modern surgery (Luijendijk

et al. 2000, Bilsel and Abci 2012, Cortes *et al.* 2008b, Cortes *et al.* 2008a, Barbolt 2006). Surgical meshes saw in recent years renewed interest, on account of product recalls, re-classification or approval revocation due to patient complaints and will be discussed later.

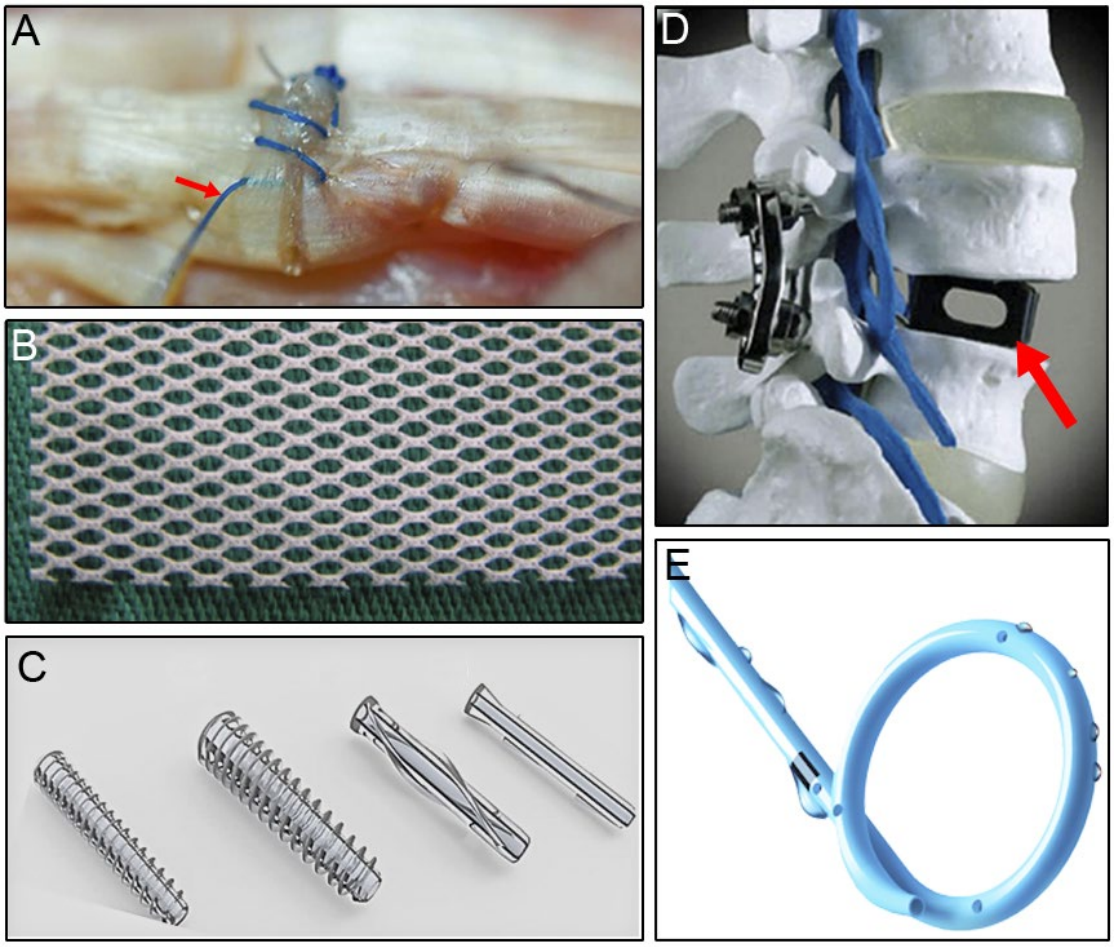

Figure 2.1. Current examples of medical devices made through melt processing of polymers. (A) Ethicon Prolene™ polypropylene (PP) suture, reproduced from (Pike and Gelberman 2010) with permission from Elsevier. (B) Ethicon Prolene™ PP hernia mesh, reprouced from (Zyczkowski *et al.* 2014) under the CC BY 3.0 License. (C) Acumed Biotrak™ polylactic acid (PLA) orthopedic and dental screws, reproduced from (Narayanan *et al.* 2016) with permission from Elsevier. (D) Invibio carbon fiber reinforced poly(ether-ether-ketone) Brantigan spine fusion cage (PEEK-OPTIMA™) (red arrow), reproduced from (Kurtz and Devine 2007) with permission from Elsevier. (E) Coloplast Vortek® polyurethane double loop ureteral stent, reproduced from (Youssef *et al.* 2017) with permission from IOP Publishing.

Screws and fixation pins for orthopedic surgery have also been manufactured using melt-processed polymers. PLA was first used as an orthopedic implant in 1971 and today all the major orthopedic medical devices manufacturers produce resorbable implants (**Figure 2.1C**), which saw an expanded use in several fields of orthopedics and trauma surgery (Ambrose and Clanton 2004,

Middleton and Tipton 2000, Kontakis *et al.* 2007, Park *et al.* 2007, Agrawal *et al.* 1995). PGA or PLA interference screws can be used for the reconstruction surgeries of the anterior cruciate ligament. These polymeric screws have the advantage of being resorbable as well as radiolucent, while being fabricated via melt processing (here: injection molding) of thermoplastic polymers (Barber and Dockery 2006, Ntagiopoulos *et al.* 2015, Liu *et al.* 2016, Narayanan *et al.* 2016).

Poly(ether-ether-ketone) (PEEK) was used as a melt-processed orthopedic implant since the 1980s, and later as a spinal cage for spinal fusion since the 1990s (**Figure 2.1D**) (Kurtz and Devine 2007). With one million joint replacement surgeries in the US per year, knee and hip replacements saw a transition as a routine surgery with an excellent prognosis (Maradit Kremers *et al.* 2015). There are several configurations for the structure of the artificial joints, but the most commonly used one is the metal-on-plastic variant, namely ultra-high molecular weight polyethylene (UHMWPE) as an joint insert (Brach Del Prever *et al.* 2009). The UHMWPE joint insert (tibial or acetabular components or bearings, for knee or hip arthroplasties, respectively) can be processed by melt compression molding or by milling of extruded polymer rods (Kurtz *et al.* 1999). Moreover, re-melting UHMWPE can be a method to decrease the amount of free radicals that are a residual by-product of crosslinking by irradiation, a method to increase wear resistance by up to 80% (Muratoglu *et al.* 2002).

Other examples of thermoplastic polymers in medical devices include polyethylene terephthalate (PET, Dacron™), used in vascular grafts as an alternative to using an auto- or allograft vein in vascular bypass surgeries (Roll *et al.* 2008, Abruzzo *et al.* 2014, Kannan *et al.* 2005, Ravi and Chaikof 2010). PET is also melt-processed when it is made into sutures (He and Benson 2014). Polyurethane (PU) ureteral stents can also be made by thermoplastic extrusion (**Figure 2.1E**) (Vogt *et al.* 2015, Gellman 2011).

In summary, several thermoplastic polymers have seen extended and decades-long clinical use with safe and effective results, this includes but is not limited to: poly(ε-caprolactone) (PCL), PGA, polylactic acid (PLA), PP, polydioxanone (PDO, PDS™), PU and PEEK and there are several reviews that

discuss material properties and biological response of such polymers (Woodruff and Hutmacher 2010, Ramot *et al.* 2016, Evans *et al.* 2015, McKeen 2014, Teo *et al.* 2016, Ulery *et al.* 2011, Benicewicz and Hopper 1990, Benicewicz and Hopper 1991, Buffington *et al.* 2014).

2.1.2 Poly(ε-caprolactone) (PCL)

PCL receives special attention since it is the polymer of choice for most of the AM approaches that are discussed later in this chapter. PCL has a history of medical use in suture materials as a copolymer with PGA (Monocryl™) (Bezwada *et al.* 1995) and as a subcutaneous contraceptive implant carrying levonorgestrel (Capronor™) (Darney *et al.* 1989). Recently, PCL saw increased use as a dermal filling material in aesthetic surgery (Christen and Vercesi 2020). PCL is known to be resorbable both *in vivo* and *in vitro* by hydrolysis (Piskin *et al.* 2007), an autocatalytic process through which, cleaving of the ester linkages accelerate further degradation. Pitt *et al*. (Pitt, Chasalow*, et al.* 1981, Pitt, Gratzl*, et al.* 1981) observed that PCL films and capsules produced by melt extrusion or molding and implanted in rabbits had the same degradation rate as samples submerged in water at 40 °C which is the body temperature of rabbits. The degradation was described in two stages: initially bulk degradation with a molecular weight decrease, with no mass loss or deformation could be seen. This is followed by chain scission when the molecular weight becomes less than 5000. Oligomeric particles will begin diffusing from the bulk of the scaffold leading to fragmentation and release of the monomer (Cooke and Whittington 2016). Sun *et al.* (Sun *et al.* 2006) conducted a long term degradation study *in vivo* in rats using radio-labeled PCL and after 2 years of *in vivo* implantation, PCL maintained its form while the molecular weight decreased. Ultimately, the radio-labeled PCL was excreted from the body, albeit through an unknown mechanism, in feces and urine without accumulation in the body (Pitt and Schindler 1981, Pitt, Gratzl*, et al.* 1981). Woodward *et al*. described the *in vivo* response to the implantation of both a PCL cylinder as well as low molecular weight PCL powder particles (which mimicked the second phase of PCL degradation). He reported intracellular PCL particles, visible using transmission electron microscopy, inside macrophages and fibroblasts. The reaction starts with

encapsulation by an avascular connective tissue capsule, which contained foreign body giant cells (FBGCs) and measured less than 100 µm in thickness within two weeks post-implantation, after a quick acute inflammatory phase. When the second phase of degradation started, or in the case of the low molecular weight powder particles from the beginning, there is a second foreign body response containing macrophages and FBGCs but few neutrophils. Complete resorption after this phase was within three months, with particles of up to 10 µm in size completely absorbed within 60 to 120 days. (Woodward *et al.* 1985). The foreign body reaction to implanted PCL scaffolds is the focus of Chapter 5 of this thesis and will be discussed in detail.

2.2 AM use in today's clinic

The main principal of AM is the layer-by-layer manufacturing of objects from a digital file. This digital information naturally combines with two important imaging techniques used today in the clinic, e.g. magnetic resonance imaging (MRI) and computed tomography (CT). These imaging techniques provide a direct path to involve AM in clinical situations by providing high-quality, digital, sliceable data, which can be used to design patient-specific medical devices and/or models. Imaging data are mostly generated in an industry-standard, Digital Imaging and Communications in Medicine (DICOM) file, which can be exported into different software packages to generate three-dimensional (3D), editable, computer-aided design (CAD) files, and these in turn can be exported to the AM-specific Standard Tessellation Format (STL) file. Based on this STL file, a computer-controlled AM device has sufficient information to process and build the object, layer-by-layer (Huotilainen *et al.* 2014).

In the current clinical setting, AM is predominantly used to produce physical medical models out of thermoplastic polymers (Salmi *et al.* 2013) that can be used in preoperative planning of complex surgeries or in hard to reach operating fields as well as for medical education of students and junior doctors (Hurson *et al.* 2007, Mori *et al.* 2008, Wanibuchi *et al.* 2010, Berry *et al.* 2002, Wanibuchi *et al.* 2016). Such physical models can be used for research and development of new treatment modalities, for example aerosol dispersion in an airway model (Clinkenbeard *et al.* 2002). Physical

models can also be used for the production and assessment of prostheses (Wu *et al.* 2009, Feng *et al.* 2010, Mueller *et al.* 2011, Creylman *et al.* 2013, Jin *et al.* 2016, Moulic *et al.* 2019) and for the production of implantable parts by functioning as an intermediate mold for another, more traditional fabrication method (Gronet *et al.* 2003, Hott *et al.* 2004, Kasper *et al.* 2019). The customizable nature of AM can be used in personalized medicine for the production of on-demand parts for better fitting of permanent prostheses (Long *et al.* 2012). With a complicated anatomy, the head and neck region represented a prime candidate for such interplay between AM and patient care. Indeed, most of the literature sources mentioned above were in that anatomical region (Bartnikowski *et al.* 2020, Kasper *et al.* 2019, Pfaff and Steinbacher 2016, Wanibuchi *et al.* 2016, Muto *et al.* 2017). With respect to implantable polymeric AM scaffolds, which were used in clinical studies, several studies were conducted, and these will be mentioned in the respective sections below.

Following in the footsteps of metal AM implants, which are already in broader use clinically, polymer melt-based AM could have a rapid translation to the clinic. AM metal implants (Sing *et al.* 2016) use many of the imaging modalities and software programs that are also applicable to their polymer melt-based counterparts. This point is particularly relevant to SLS, since both metals and polymers are processed in a solvent-free approach inside the same device (Mazzoli 2013).

Implantable AM metal medical devices can be made via SLS, selective laser melting (SLM), electron beam melting (EBM) and direct metal laser sintering (DMLS) (Sing *et al.* 2016, Mangano *et al.* 2014, Mazzoli 2013). In one example, patient-specific mandibular reconstruction metal plates were designed using the patient's own CT scans and manufactured using DMLS. This approach used CAD and computer-aided manufacturing (CAM) to fabricate custom-contoured plates for better fitting and more facial symmetry (Tarsitano *et al.* 2016). Fernandes *et al*. reported the use of a customized titanium implant made using SLS for a patient with a rare malignant tumor of the nerve sheath of the trigeminal nerve. Surgical removal of the tumor created a massive mid-facial defect that was not possible to treat using available zygomatic implants (Fernandes *et al.* 2016). Probst *et al*. compared

the outcome of six patients in a retrospective study where patients either had intraoperatively bent commercial mandibular reconstruction plates or implants which were made by CAD/CAM either by milling or by SLS. The outcome of CAD/CAM designs was encouraging and allowed for easier application (Probst *et al.* 2016). And finally, Gianni *et al.* fabricated a patient-specific talonavicular prosthesis for a complicated talonavicular fracture in a professional rock climber with the restoration of the ankle range of movement, instead of undergoing an ankle arthrodesis (Giannini *et al.* 2016).

The transition to polymer-based melt AM already follows the established and accepted clinical track record of AM metal implants, and in the case of SLS, using the exact same AM technique, with different materials. However, polymers would be more suitable and applicable in soft tissue implantation, or when a resorbable implant is needed, rather than a metallic one.

2.3 FDA regulations for medical devices

The purpose of this thesis is the investigation of polymeric scaffolds produced through MEW for biomedical application. The scaffolds, made from medical grade PCL, were not loaded with drugs or seeded with cells. Therefore, in the next section, the main focus will be to illustrate the more traditional regulatory pathways for the approval of a thermoplastic medical device, regardless if the method of fabrication was additive or traditional, i.e. less emphasis on combination medical devices with drugs and biologics.

As previously discussed in Chapter 1, the presence of rules and regulations regarding the introduction of a new drug or medical device to the market aim at ensuring the safety and efficacy of such products before they are available for use by the public. The lessons learned from the Elixir Sulfanilamide preparation and thalidomide-induced congenital defects indicated that products must be thoroughly tested and declared as safe, to the best of the current knowledge, before they are sold (FDA 2018a). Some medical devices are invasive in the way they are implemented or implanted in the human body, warranting a careful examination of the safety and efficacy of the device. Established

definitions of a medical device by the WHO, FDA and other regulatory bodies indicate that it does not function through pharmacological means. This is an important practical and regulatory factor distinguishing medical devices from drugs or biologics. However, the rise of tissue engineering (TE) and regenerative medicine introduced combinations of medical devices which release drugs and/or biologics or are coated with such compounds. This increases the complexity of the final product and warrants an increase in both time and expense of navigating the regulatory pathway. Since they do not fulfil the definition of a medical device, such "combination devices" were previously evaluated simultaneously by multiple FDA centers including the Center for Radiologic Devices and Health (CDRH for medical devices), the Center for Biologics Evaluation and Research (CBER for biologics) and the Center for Drug Evaluation and Research (CDER for drugs) (Rados 2006, Adamovich *et al.* 2015). In order to streamline the process and push forward for personalized medical applications, the FDA has established the Office of Combination Products (OCP) under the Office of Special Medical Products as part of the Medical Device User Fee Modernization Act of 2002. The OCP achieves timely approval of combination products through the collaboration of experts from the three FDA Product Centers (Simoncelli 2013).

In 1976, the Medical Devices Amendment Act was passed in the United States which defined what constitutes a medical device and gave the FDA the power to determine and examine premarket safety of medical devices (FDA 2019b). As of 2019, the FDA regulated roughly around 6,500 different medical devices (Rathi and Ross 2019). This Act also separated medical devices into three classes: Class I, II and III. Class I medical devices include those with the least possible risk to the users (e.g. tongue depressor) while Class III has the highest risk (e.g. a cardiac pacemaker). All Classes, regardless of type, require General Controls which include Quality Systems Regulation (QSR) and Good Manufacturing Practices (GMP) (Adamovich *et al.* 2015). The QSR is in tandem with the risk caused by the device, its complexity and the complexity of its production process, as well as the size and complexity of the manufacturer itself (Tartal 2014). Medical devices legally marketed and sold before the 1976 Medical Devices Amendment Act (before May 28th, 1976) are exempted from re-

classification, as long as they were not changed or modified since then, and the FDA did not deem a Premarket Approval (PMA) application necessary. For the streamlining of the approval process, a certain fast-track pathway known as the 510(k) process or premarket notification, where the name is derived from Section 510(k) of the 1976 Medical Devices Amendment Act (i.e. there is no "510(k) form" but rather it is the interpretation of this section of the Amendment that got this process its name) (Jarow and Baxley 2015, Adamovich *et al.* 2015). Class I devices are generally exempt from a regulatory approval pathway but require General Controls. Class II requires Special Controls, which are device specific and are required to assure the safety and effectiveness of the device. Such special controls are typically outlined in guidance documents, available on the FDA website (https://www.fda.gov/). Typically, Class II devices are approved through the 510(k) pathway, in which the manufacturer establishes the safety and efficacy of the medical device by proving that such a device is substantially equivalent to a legally marketed predicate device. The predicate device can also be pre-Amendment approved. Although proving substantial equivalence generally requires bench testing and preclinical animal studies, special cases may even require human clinical data to be provided by the manufacturer prior to marketing. Usually the FDA decides in 510(k) pathway applications within 90 days (FDA 2018b). In instances where a predicate device is not available, the manufacturer will need to apply for a De Novo pathway, which is reserved for new, perceived low- or medium-risk medical devices (i.e. Class I or Class II medical devices). The De Novo pathway is a risk-based evaluation. Initially, manufacturers were required to fill in a 510(k) request, then wait for a decision from the FDA of "not substantially equivalent" (i.e. due to absence of predicate, introduction of a new intended use or a change of the technological characteristics of the device), then apply for a De Novo request. Before the implementation of this pathway, these devices would have proceeded to be re-classified as Class III devices and require a premarket approval. The FDA in 2012 further streamlined the process by allowing manufacturers to submit a De Novo request from the start, without waiting for decision on their 510(k) request, and within a 120-day timeframe. Moreover, once a medical device was granted an approval via a De Novo pathway, this medical device can be later

used as a predicate for future applications using the 510(k) pathway, saving on assessment time for the manufacturer (Rubalcaba 2018, FDA 2019c).

To push forward with innovation as well as protecting the safety of the public, the FDA in 2019 has finalized four new changes to better clarify the 510(k) pathway. These introduced the Special 510(k) program which could be used when the manufacturer wants to make well-defined device changes to their own, already approved devices. The Abbreviated 510(k) is to be used when the FDA deems that the approval relies on the demonstration of compliance to Special Controls requested by the FDA. The Refuse to Accept Policy for 510(k) is an accelerated pathway (within 15 calendar days) to check if the 510(k) submission is administratively correct and complete and to list missing application elements. And finally, the FDA introduced a guidance on how to correctly fill in an original submission to the traditional, special or abbreviated 510(k) submissions (Kelly 2019).

Finally, Class III devices require the most stringent controls in the form of a premarket approval (PMA). A PMA is the most sophisticated FDA regulatory pathway, requiring Phase I clinical trials (a limited clinical trial to establish safety) and a pivotal Phase II clinical trial (to establish efficacy of the device for treating the given clinical indication). Prior to performing the clinical trial, a manufacturer must receive approval to conduct the trial from the FDA by applying for an Investigational Device Exemption (IDE) based on pre-clinical testing results. Class III devices are those that are used in supporting and maintaining human life or are of great importance in prevention of illness or injury. Combination products (which are medical devices plus another effector, e.g. a drug or biologics) are usually treated individually by the FDA (Simoncelli 2013). In selected cases, the FDA can also approve medical devices based on special circumstances. First, there is the Expanded Access pathway, which is for life-threatening diseases or serious conditions, where a gold standard of therapy is not available. This pathway includes emergency use, compassionate use and the aforementioned IDE for clinical testing (FDA 2019d). Second, there is the Humanitarian Use Device (HUD) and is defined as a medical device aimed at the treatment or diagnosis of a disease or a condition that affects less

than 8,000 patients in the US per year. This is analogous to the Orphan Drug Designation which affects drugs and biologics intended for the treatment or diagnosis of a disease or condition affecting less than 200,000 persons in the US (FDA 2019e).

As more university research focuses on clinical translation, there is an increasing appreciation of and a need to understand the regulatory process for medical devices among academics (Pashuck and Stevens 2012). There needs to be a paradigm shift among researchers working on AM medical devices from what this novel technique can be used for, to how we can push this technique further to treat this or that condition (Castro *et al.* 2017). This way, more targeted research outcome can be achieved, and in the process, more AM medical devices built from the ground up with the necessary regulatory hurdles in mind. In 2017, there have been 21 companies in commercial production of TE-related products in the US market with approximately nine billion US dollars in sales. While this is an impressive statistic, this is less than half the number of companies that were identified in a study by Kim *et al.* of the TE-related companies in the US at that time (Kim *et al.* 2019). Of the success stories of TE medical devices (non-AM and non-polymeric) that received the FDA approval and saw widespread clinical use is the INFUSE™ bone graft (Hoffman *et al.* 2019). Widespread off-label use of the new device (Ong *et al.* 2010) forced the FDA to issue a warning for such practices (FDA 2008). This caused a limitation on the translation of other medical devices with growth factors to the clinic (Hoffman *et al.* 2019).

The complexity of getting a new medical device approved can limit innovative potential products to come out of TE research. A sound understanding of the regulatory process that is required to get a new medical device to the patient is needed by both physicians in the bed side and scientists in the bench side of research. An expedient approach to medical device research and design is to use already approved biomaterials to shorten and limit the regulatory work needed for approval. When such an approach is adopted, the 510(k) pathway can be employed, which can significantly cut down on time and cost of new medical device registration. This can bridge the gap between the researcher

working in a university setting or in the industry on one side and the clinician trying to treat his/her patients. This product timeline disconnect is what is commonly known as the “Valley of Death”. This is the period where many promising medical innovations ended, on account of failure of reaching the bedside (Hollister 2009a). Several other review papers have discussed such design parameters and implementation (Hollister 2009a, Hollister 2009b, Pashuck and Stevens 2012, Roberts *et al.* 2012, Hollister *et al.* 2015, Sastry 2014, Adamo *et al.* 2018, Hoffman *et al.* 2019, Kim *et al.* 2019).

2.3.1 510(k) criticism and surgical meshes

As previously mentioned, surgical meshes made from thermoplastic polymers are widely used to treat a wide range of conditions like abdominal hernia and pelvic floor prolapse. In recent years, there has been several complaints from patients regarding the occurrence of severe side effects, including chronic pain lasting more than three months, which is estimated to occur in ten percent of hernia patients (Fitzgibbons and Forse 2015). There has been a widespread fallout for these complaints, with surgical meshes being elevated by the FDA from Class II to Class III medical devices (Zargar and Carr 2018). The FDA also recalled several urogynecological meshes that were used in transvaginal repair of pelvic prolapse (FDA 2019f).

Interestingly, all US-marketed surgical meshes were found to be approved by the FDA through the 510(k) pathway (Zargar and Carr 2018). Zargar and colleagues traced the network of predicates to find out if the original medical devices were subjected to any form of rigorous testing. They found that 74 out of 77 cleared surgical meshes between 2013 and 2015 could be backtracked to surgical meshes that were marketed pre-Amendment, with three devices lacking any data on their predicate devices. Through tracking, they concluded that all the predicates traced back to six pre-Amendment surgical meshes that spawned 387 descendent meshes, 303 of them derived from just two meshes (Zargar and Carr 2018). While the 510(k) pathway could help innovation, the safety of the public could be harmed in the process, when medical devices were simply placed in predicate networks, where even the original device did not receive sufficient testing because it was sold pre-Amendment.

2.4 AM technologies and their current use in animal and clinical research

Recently the manufacturing of physical objects evolved into using layer-by-layer approaches. This fabrication concept is termed as 3D printing in the popular media and AM in scientific circles. We refrain from using the terms 3D printing, rapid prototyping and free-form fabrication when referring to AM to avoid confusion. AM is considered a disruptive technology, as the user can design and build their own customizable objects without the need for industrial output (Campbell and Ivanova 2013). Traditional manufacturing is, in retrospect, termed subtractive manufacturing, where objects are fabricated by machining, e.g. drilling or milling (Chhaya *et al.* 2015). The emergence of AM has provided new possibilities for designing and customizing medical devices; however, these AM medical devices must still comply with the regulations predominantly established for factory-made products.

While the focus in this chapter is on polymer melt-based AM approaches (namely, micro-extrusion, SLS and MEW), as these use an established building block for medical device production: melt processing of medical-grade polymers, there are many different classes of AM methods which are beyond the scope of this thesis. Some of them are mature technologies that saw long use, such as stereolithography (SLA), FDM, SLS and 3D printing (3DP). While others are relative newcomers, including two photon-polymerization (2PP) (Burmeister *et al.* 2015), EBM (Sing *et al.* 2016), continuous liquid interface polymerization (CLIP) (Tumbleston *et al.* 2015) and MEW. The coming section will describe the three melt-based approaches and mention relevant *in vivo* and/or clinical studies performed with constructs produced through them. Each of the following sections were reviewed in 2017 by us (Youssef *et al.* 2017) in a detailed topical review. The text has been improved and updated to reflect changes in the past three years. Summary tables for each of the three reviewed techniques up to the end of 2016 are available in the published review.

2.4.1 Micro-extrusion technologies

FDM is probably the most prototypical micro-extrusion AM technology used for manufacturing of medical implants. S. Scott Crump invented and patented FDM in 1989 (Crump 1992) and later founded Stratasys Inc. (https://www.stratasys.com). In basic principles, a solid polymer is extruded through a heated nozzle, which through a Cartesian coordinate robot, deposits the extruded polymer melt onto a collector in a layer-by-layer fashion, ultimately resulting in 3D objects. One of the most common thermoplastic polymers used for FDM is acrylonitrile butadiene styrene, which does not have a history of medical use. However, several biodegradable polymers including PCL and poly(L-glutamic acid) (PLGA) have been used to produce TE constructs (Hutmacher 2000, Yen *et al.* 2009). The polymer in case of FDM needs to be supplied as polymer filaments, but it can also be performed with syringe-based or screw extrusion, hence the umbrella term "micro-extrusion techniques" instead of using FDM (as the best known technique) to refer to this class of AM (**Figure 2.2A**). Micro-extrusion can prepare scaffolds that are similar to FDM-made ones, but with the added benefit of being able to customize the polymer by adding particles or drugs without needing to create a filament of their substrate prior to printing (Shor *et al.* 2007, Wang *et al.* 2004, Domingos *et al.* 2009, Dash and Konkimalla 2012, Ergun *et al.* 2011).

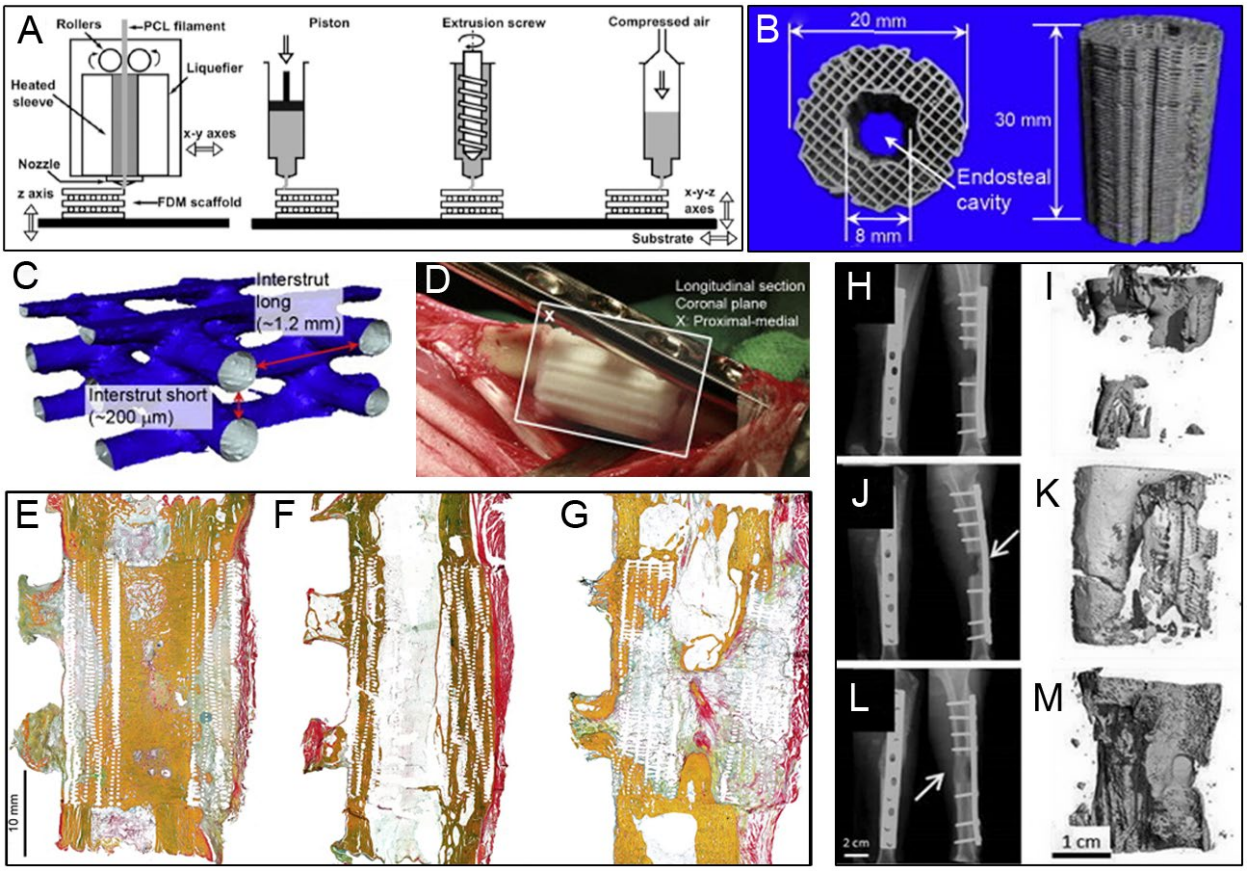

Figure 2.2. Selected *in vivo* animal experiments made using micro-extrusion technologies. (A) Summary of the different forms of micro-extrusion approaches, with FDM being the most focus in this chapter, reproduced form (Obregon *et al.* 2015) with permission from SAGE Publishing. (B-G) An Osteopore Inc. medical-grade PCL-TCP scaffold loaded with rhBMP-7 was used in a critical-sized tibial defect in sheep, reproduced from (Cipitria *et al.* 2015) with permission from Elsevier. (B) Digital rendering of the scaffold showing the honeycomb internal structure. (C) A micro-computed tomography (µCT) image of the repeating unit structure. (D) Surgical procedure in sheep. (E-G) Movat pentachrome micrographs of explanted scaffolds loaded with rhBMP-7 showing new bone formation after 3 months (E), 12 months (F) and after 12 months but with unmodified scaffold (G). (H-M) X-ray and µCT images of a critical-sized tibial bone defect in sheep filled with a PCL scaffold alone (H, I) or loaded with VEGF, PDGF and BMP-2 (J, K) or BMP-2 alone (L, M) – after 6 months post-surgery. Reproduced from (Kirby *et al.* 2016) under the CC BY 4.0 License.

The majority of the biomedical constructs made by micro-extrusion have been applied to studies involving hard TE (i.e. bone tissue), owing to the dimensions of the fibers drawn by the nozzle which are usually in the range of 160-700 µm (Zein *et al.* 2002). Bone is a dynamic tissue that is in a constant state of deposition and resorption (Feng and McDonald 2011). The purpose of a TE construct would be to provide osteoconductive (and when needed, osteoinductive) conditions for cellular proliferation while providing mechanical support (the scaffold has to be fixed by orthopedic fixation devices) until a sufficiently stable and calcified callus is obtained to try to restore the function of bone

(Hutmacher 2000). In 2000, Hutmacher described the first fabrication of a PCL FDM scaffold for TE bone application (Hutmacher 2000). The scaffold had a laydown pattern of 0°/60°/120° orientation and were put to extensive mechanical and physical characterization. These FDM scaffolds possessed porosity of more than 56% with pore sizes ranging between 380-590 µm. Fibroblasts and osteoblasts were seeded on these scaffolds and their growth pattern was observed, where they were found to proliferate from the periphery to the center, ultimately leading to the occupation of the pores in the structure (Hutmacher *et al.* 2001).

The early *in vivo* research with FDM scaffolds was mainly to detect signs of inflammation and observe new bone formation. To improve the osteoconductivity of the scaffolds, Schantz *et al*. experimented with blending PCL with hydroxyapatite (HA) to make scaffolds through FDM. Human calvarial bone chips were seeded inside the scaffolds and then the whole construct was implanted in nude mice (Schantz *et al.* 2002). No prominent foreign body reaction was detected while at the same time the seeded scaffolds showed improved bone formation at the defect site. Several other groups prepared the scaffold *in vitro* prior to the *in vivo* implantation. Such preparations included: coating with extracted bone marrow, seeding with bone marrow stromal cells (BMSCs), seeding with osteoblasts, or seeding with BMSCs overexpressing an important osteogenic transcription factor, Runx2. Functionalization of the scaffolds was achieved by compounding PCL with either HA or beta-tricalcium phosphate (β-TCP) or by incubating the PCL scaffold in simulated body fluid (SBF). Several groups used large animal models e.g. sheep to better convey the weight bearing situation in humans. Other animal models included rabbits, rats and beagle dogs (Youssef *et al.* 2017).

Osteopore Inc. (https://www.osteopore.com) was founded in 1996 in Singapore after a sustained research output on *in vivo* PCL FDM scaffolds from the National University in Singapore. The company was able to release to the market two FDM PCL products: Osteomesh™ and Osteoplug™ under GMP standards. Osteopore Inc. currently has FDA approval for its products as a Class II Medical Device for use in craniofacial bone defects using the 510(k) pathway (K051093).

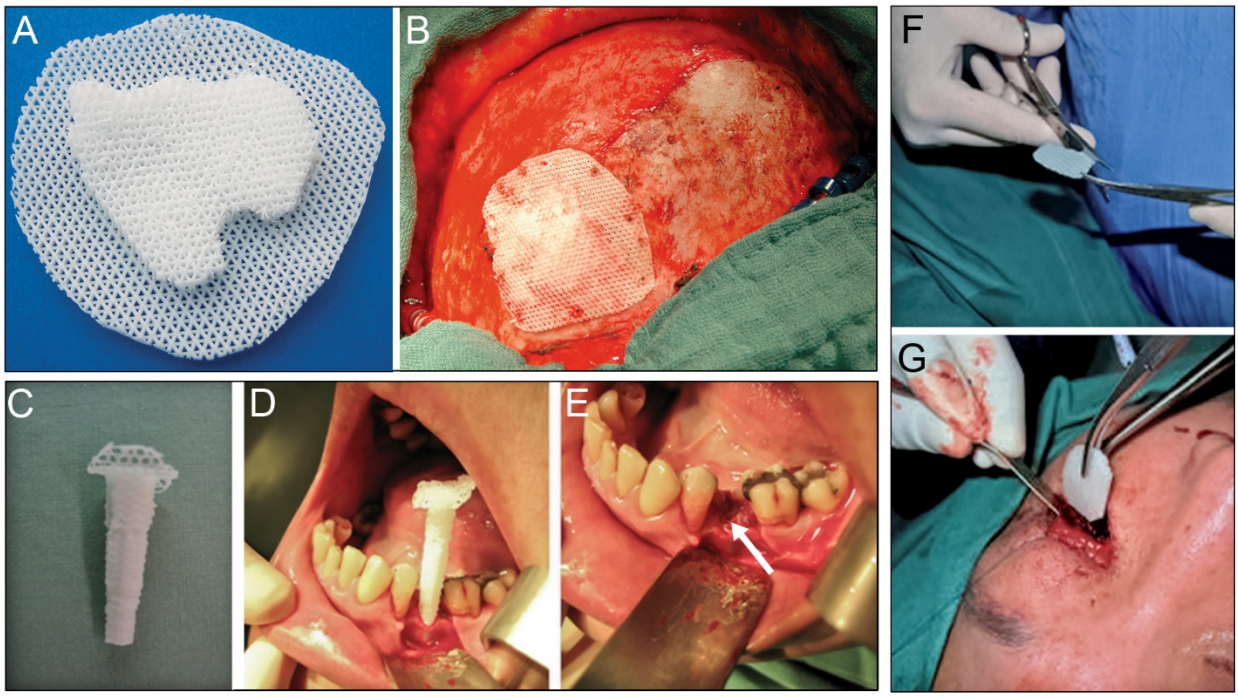

Figure 2.3. Examples of clinical FDM scaffold use. (A-B) An Osteopore Inc. customized, medical-grade PCL scaffold for calvarial defects, before (A) and after implantation in the patient (B), reproduced from (Probst *et al.* 2010) with permission from Georg Thieme Verlag KG. (C-E) An Osteopore Inc. PCL scaffold (C) is used to fill an extraction socket defect for a patient (D) to allow for insertion of a dental implant after removal of the excess scaffold parts (E). The white arrow shows the filled extraction socket, reproduced from (Goh *et al.* 2015) with permission from John Wiley and Sons. (F-G) An Osteomesh™ scaffold is used for a patient with a fracture of the inferior orbital wall. The commercial AM-produced scaffold needed to be trimmed down to size (F) and then implanted into the patient (G), reproduced from (Teo *et al.* 2015) with permission from Taylor & Francis.

Several research groups used additives in addition to the Osteopore Inc. scaffolds to promote cell proliferation and/or differentiation for a better healing response. These additives, in most cases, were also previously used clinically and approved for human use but for different purposes, for example, recombinant human bone morphogenetic proteins (rhBMP) and platelet-rich plasma (PRP). rhBMP-7 mixed with collagen has received a HUD approval from the FDA under the trade name OP-1 Putty™ for use in long bone non-unions when an autograft is not feasible or when alternative treatment modalities failed (H020008), while rhBMP-2 was approved, also as a HUD under the trade name INFUSE™ for lumbar spine fusion, open tibial fractures fixed with an intramedullary nail within 14 days of injury and in oral and maxillofacial uses (H040004). Cipitria *et al*. loaded PCL scaffolds with rhBMP-7 which were placed in critical size tibial defects in sheep. The rhBMP-7 group showed better bone formation after 12 months compared to the empty scaffold (**Figure 2.2B-G**) (Cipitria *et al.* 2015).

Abbah *et al*. compared a bone autograft to an Osteopore Inc. PCL/TCP scaffold loaded with rhBMP-2 in a spinal fusion surgery in pigs. The results showed superior bone formation in the scaffold group along with a less incidence of graft fracture post-surgery (Abbah *et al.* 2009). BMPs *in situ* pose the risk of ectopic bone formation because of diffusion to other tissues from the implantation site (Deutsch 2010). To counteract this side effect, Dupont *et al*. used a different approach where they coated a PCL Osteopore Inc. scaffold with a viral vector encoding rhBMP-2 and used them in a critical femoral bone defect in athymic nude rats. The group compared such scaffolds with other PCL scaffolds that were seeded with mesenchymal stem cells (MSCs) that were already transduced with the viral vector to over-express rhBMP-2. The results were in favor of the non-seeded scaffold group (Dupont *et al.* 2012). Kirby *et al*. used PLGA microparticles loaded with recombinant human vascular endothelial growth factor 165 ($rhVEGF_{165}$), recombinant human platelet-derived growth factor BB (rhPDGF-BB) and rhBMP-2 or rhBMP-2 alone (**Figure 2.2H-M**). They reported better mechanical properties in the growth factor group and in the rhBMP-2 group compared to scaffolds with empty microparticles (Kirby *et al.* 2016). Moving to PRP, Rai *et al*. submerged Osteopore Inc. PCL/TCP scaffolds in PRP derived from a rat for 30 minutes and then implanted them in critical femoral bone defects in rats and compared them to non PRP-treated scaffolds. The result was better vascularization and neo-bone stiffness in the PRP group (Rai *et al.* 2007). Such experiments show the potential of combining several modalities in treatment of challenging skeletal defects by using already existing and approved drugs/biologics. The challenge remains on how to make such combination medical devices across the regulatory bodies and available to surgeons and patients. Moreover, the Hutmacher group has recently published a detailed protocol for the validation of a pre-clinical large animal critical bone defect study using Osteopore Inc. PCL/TCP scaffolds (Sparks *et al.* 2020).

After such an extensive history of *in vitro* and *in vivo* experiments, especially with large animal pre-clinical studies, treating human patients was the next step for the development of these medical devices. Schantz *et al*. described in 2006 the first use of Osteoplug™ in human patients to cover burr holes from trephining, leading to filling of the calvarial defects when assessment was performed

12 months later (Schantz *et al.* 2006). Low *et al*. followed up 12 patients for a mean follow-up time of 16 months after the implantation of Osteoplug™ scaffolds to cover burr hole skull defects. They reported no complications with a satisfactory cosmesis (Low *et al.* 2009). Probst *et al*. used CT scan data from a patient to fabricate, via melt micro-extrusion, a PCL scaffold mixed with TCP (20%) using medical grade PCL from Osteopore Inc. (**Figure 2.3A-B**). The scaffold was used for a calvarial defect and followed up after 6 months (Probst *et al.* 2010). Goh *et al*. used PCL scaffolds from Osteopore Inc. in tooth extraction sockets in patients undergoing tooth extraction for a later replacement with a dental implant (**Figure 2.3C-E**). Compared to no filling of the defect, the treatment group had better bone quality in the extraction socket and better preservation of the alveolar ridge height (Goh *et al.* 2015). Teo *et al*. used Osteomesh™ PCL scaffolds to reconstruct fractures of the inferior orbital wall in patients (**Figure 2.3F-G**). It led to better healing of the bony defect with an improvement in binocular vision results, by restoring the level of the bulbus oculi compared to preoperative tests (Teo *et al.* 2015). Chhaya *et al*. described the use of an Osteopore Inc. PCL/TCP scaffold that was treated with autologous bone marrow and rhBMP-7 to treat a 70-year-old female patient with a complicated non-union tibial defect of 4 cm. After 18 months of follow up, the patient showed 75% new bone regeneration in the defect area (Chhaya *et al.* 2015).

In a report of novel clinical auricular reconstruction in five patients with microtia with a detailed description of the first case, Zhou and colleagues reported the reconstruction of an ear using a composite, PCL ear-shaped scaffold. The contralateral normal ear was CT scanned to provide a CAD model for the manufacture of negative molds for the compression molding of PGA unwoven fibers. The micro-extruded, ear-shaped PCL scaffold was pressed with the PGA part and together were coated by dichloromethane-dissolved PLA, followed by compression molding of the whole construct at 55 °C till solvent evaporation. The construct was tested for biocompatibility and then seeded with harvested autologous cells from the microtic cartilage of the patient. An expander was implanted into the subcutaneous tissue of the affected auricular region. After the implantation, the patient was followed up for 2.5 years, with two biopsies taken at 6 and 18 months to evaluate the cartilage formation post-

implantation. The surgery resulted in cartilage formation with preservation of landmark ear structure, similar to the normal contralateral side. The scaffold showed no signs of resorption or displacement (Zhou *et al.* 2018). While not exclusively an AM-made scaffold, this report fulfills a long standing aspire to reconstruct the human ear, which started with the now infamous Vacanti mouse in the late 1990s (Cao *et al.* 1997).

2.4.1.1 Micro-extrusion Summary

Micro-extrusion is ideally suited for the fabrication of TE scaffolds for bone regeneration. Osteopore Inc. showed great success with their products in both animal *in* vivo experiments, as well as clinical studies. This opens the door for further implementation of this relatively more readily available (in comparison with SLS and MEW) technology towards the translation of more patient specific, AM medical devices into the clinic. The establishment of large animal pre-clinical models paves the way forward towards more clinical translation.

2.4.2 Selective laser sintering (SLS)

SLS was invented in 1986 by Carl Deckard (Deckard 1989) who was, at that time, doing his Master's degree at the University of Texas Mechanical Engineering Department, to fabricate casting patterns for the production of machine parts using CAD (Department of Mechanical Engineering 2012). The configuration of a SLS device includes a housing, where the other device parts are located, as well as the powder material, which is kept at a temperature just below it melting point. There is an initial layer of powder on top of a piston, which moves down in the vertical direction, while a roller spreads a new thin layer of powder from a reservoir, as the existing layer on the piston is being sintered with the laser. This computer-controlled laser beam sinters (or fuses) the powder, with the remaining unfused powder behaving as a structural support for the scaffold being constructed (**Figure 2.4A**). The movement of the laser beam is controlled through galvanometers that replicate the forms created from sliced data extracted form an STL file (Gittard and Narayan 2010, Mazzoli 2013). Several different materials were described to have been used in scaffold fabrication using SLS, including

metals, ceramics, bioactive glass, polymers and composite materials (Shirazi *et al.* 2016, Mangano *et al.* 2014, van Noort 2012). The focus in this chapter will be on thermoplastic polymers.

The fabrication of TE scaffolds, as well as models for clinical applications have been performed using SLS across a range of thermoplastic medical polymers, whether alone or as composites with ceramics. SLS was used to process nylon (Berry *et al.* 1997), PVA with HA (Chua *et al.* 2004), PEEK with HA (Tan *et al.* 2003), poly(ether-ketone-ketone) (PEKK) (Adamzyk *et al.* 2016), high density polyethylene (HDPE) with HA (Hao *et al.* 2006), UHMWPE (Rimell and Marquis 2000), PCL (Williams *et al.* 2005), PCL with polysaccharides (Ciardelli *et al.* 2005), PCL with HA (Wiria *et al.* 2007), PCL with β-TCP (Liao *et al.* 2016, Lohfeld *et al.* 2012), polyamide (PA) with HA (Savalani *et al.* 2007), poly(L-lactide) (PLLA) (Bukharova *et al.* 2010), PLA with carbonated HA (Zhou *et al.* 2008) and poly(L-lactide-co-glycolide) with HA (Simpson *et al.* 2008).

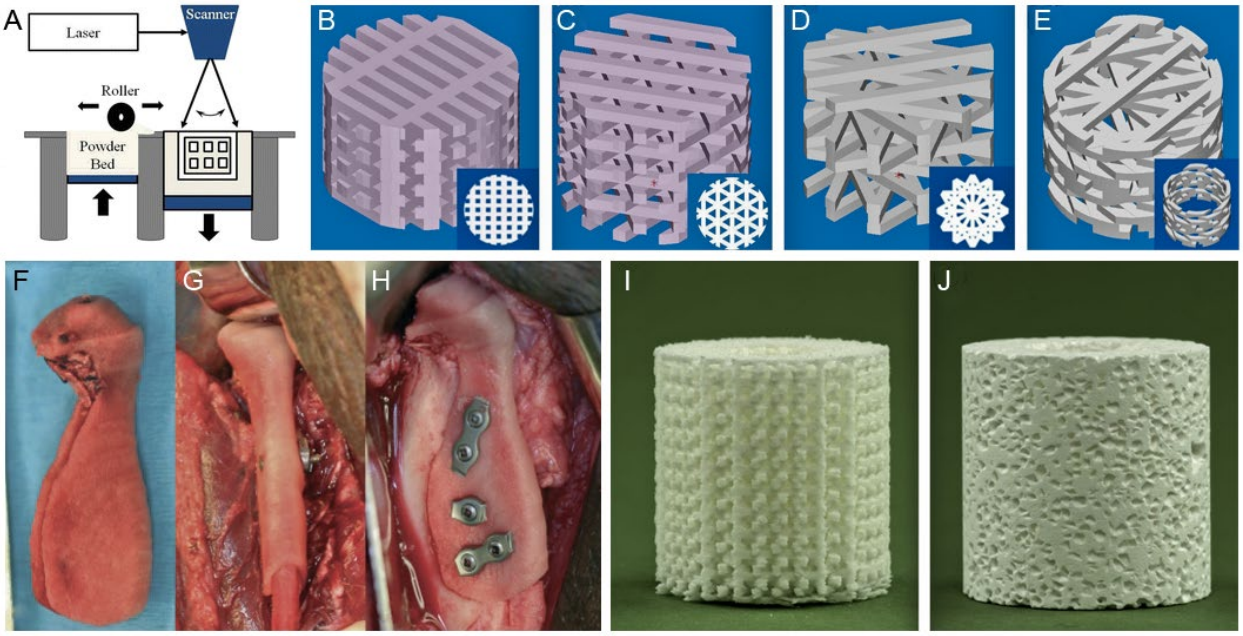

Figure 2.4. Summary of SLS technology and some of its applications. (A) A graphical representation of the SLS process, reproduced from (Gu *et al.* 2016) under the CC BY 4.0 Licence. (B-E) Diagrams of different complex scaffold shapes that are possible with SLS without support structures, reproduced from (Lohfeld *et al.* 2012) with permission from Elsevier. (F-H) Implantation of a SLS scaffold as a sleeve to the mandibular ramus in a minipig, reproduced from (Smith *et al.* 2007) with permission from John Wiley and Sons. (F) A SLS made sleeve that fit the condylar ramus of a minipig. (G) The scaffold fits into the remaining mandible. (H) Fixation of the scaffold with mini-plates. (I, J) Different scaffolds for weight-bearing bone defects made via SLS (PCL/TCP) (I) and with conventional approaches (pure TCP) (J), reproduced from (Lohfeld *et al.* 2012) with permission from Elsevier.

SLS has the benefit of fabricating complex 3D objects without the need for solvents or porogens (Meng *et al.* 2020). Moreover, compared to micro-extrusion or MEW, the process is not dependent on deposition, which gives the laser beam more freedom for more complex final constructs (**Figure 2.4B-E**). In principle, as long as the material is in powder form and can fuse but not decompose when heated using the laser beam, it can be SLS-processed (Williams *et al.* 2005). Optimal settings for the device parameters allow for the production of porous scaffolds for bone TE, with acceptable reproduction of the dimensions in the original 3D representation (Partee *et al.* 2006). There has been an interest in the topic of design and product optimization using SLS (Eshraghi and Das 2010, Eshraghi and Das 2012, Dias *et al.* 2014).

Williams *et al*. demonstrated the generation of PCL scaffolds that were seeded with human primary gingival fibroblasts expressing murine BMP-7, subcutaneously in mice. This resulted in bone formation on the surface and the inside of the scaffold, with a thin cortical layer of bone around the outer side of the scaffold. Moreover, the design of a mini-pig mandibular condyle based on CT scan data was shown to be possible through SLS (Williams *et al.* 2005). In another study, Smith *et al*. used CT data to produce a condylar ramus unit scaffold in a mini-pig model (**Figure 2.4F-H**). The scaffold acted as a shell and was filled with autologous bone marrow. Implantation was done after a condylectomy and the construct was fixed in the mandible using mini plates, with the intact contralateral tempromandibular joint serving as a control. The experiment resulted in bone formation, more on the exterior of the construct than in the interior, but overall, resembling the control on the contralateral joint (Smith *et al.* 2007). HA addition to PCL scaffolds made via SLS was investigated *in vitro* (Wiria *et al.* 2007) as well as both *in vitro* and *in vivo* (Xia *et al.* 2013). Xia and colleagues studied the ability of PCL-nano-HA scaffolds to adsorb rhBMP-2 and then release it in the cell culture medium. These scaffolds were later seeded with human MSCs and used in a critical femoral bone defect in rabbits. The group containing the PCL-nano-HA resulted in more extensive new bone formation and faster degradation of the scaffold after 9 weeks compared to PCL only. Lohfeld *et al*. investigated the *in vivo* effect of PCL/β-TCP scaffolds against a commercially available β-TCP scaffold

in sheep tibial critical bone defect model (**Figure 2.4I-J**) (Lohfeld *et al.* 2012). They demonstrated decreased bone formation in the PCL/TCP group compared to the pure TCP group when using 10% weight TCP mixed with PCL and they recommended further exploration of 50% TCP weight in future studies. Liao *et al*. studied PCL, PCL/TCP and PCL/TCP scaffolds coated with collagen type I. Several concentrations of TCP were investigated (10, 20, 30 and 40% weight), however, with 40% it was found that the scaffolds were too fragile and brittle. The authors also studied the *in vivo* performance in nude mice (intramuscular implantation) after seeding of the scaffolds with porcine adipose-derived stem cells and their osteogenic differentiation. The collagen type I coating of the PCL/TCP scaffolds improved the osteogenic differentiation and the volume of new woven bone formation *in vivo* (Liao *et al.* 2016). Similarly, coating of PCL scaffolds with collagen type II resulted in improved porcine chondrocyte proliferation *in vitro* and *in vivo* as well as improved extracellular matrix protein production as glycosaminoglycans (Chen, Lee*, et al.* 2014). This was also shown by PCL scaffolds loaded with porcine chondrocytes in a collagen type I hydrogel (Chen, Shyu*, et al.* 2014). Du *et al*. demonstrated an *in vivo* study where microspheres of PCL and HA are used in SLS instead of mixing PCL and HA powders for sintering (Du *et al.* 2015).

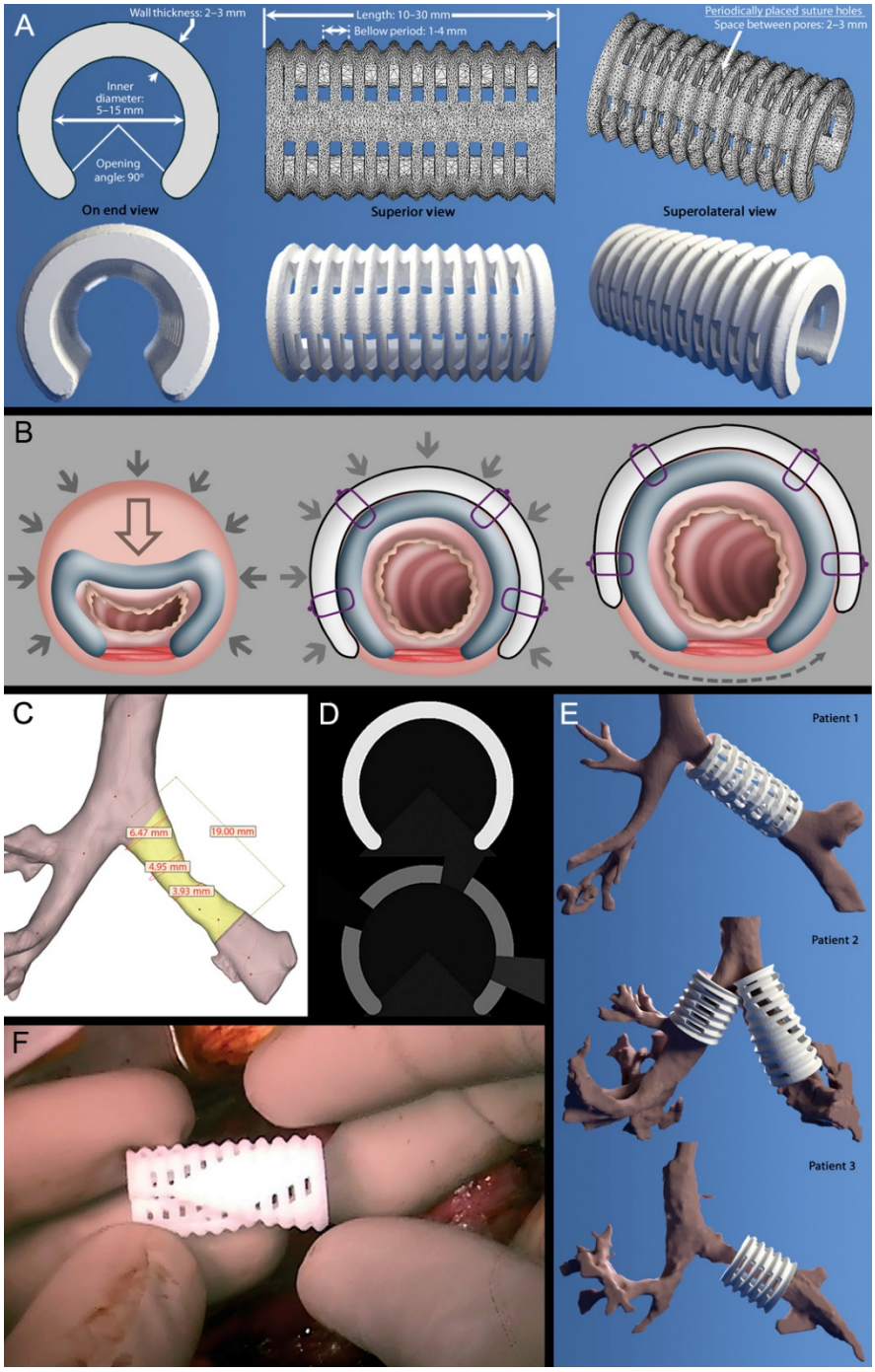

Figure 2.5. SLS-made tracheobronchial scaffold for tracheobronchomalacia, reproduced from (Morrison *et al.* 2015) with permission from The American Association for the Advancement of Science. (A) Digital rendering of the trachebronchial scaffold showing end, superior and superolateral views. (B) Graphical representation of the collapse caused by tracheobronchomalacia (left) and how the scaffold fixes this (middle), with possibility for peripheral expansion with growth (right). (C) 3D reconstruction of a patient's chest CT data. (D) An image slice of the design with light and grey areas representing the scaffold structure and dark areas as empty spaces. (E) 3D representation of how the scaffolds fit the respective patient pre-implantation. (F) Final scaffold prior to implantation during the surgical procedure.

In an important translational milestone, Zopf *et al*. produced a PCL scaffold via SLS for the surgical implantation in an infant suffering from tracheobronchomalacia (TBM) (Zopf *et al.* 2013). TBM is a potentially fatal, serious congenital respiratory condition in which there is airway collapse due to weak airway walls and cartilage (Tan *et al.* 2012). The implanted scaffold made it possible to remove the patient from life-saving endotracheal intubation after 21 days of surgery, with good follow up after one year. The procedure was performed after the institutional review board of the University of Michigan approached the FDA to acquire permission under the Emergency Use Exemption for medical devices (Code of Federal Regulations: 21CFR812.35). As previously discussed, this exemption can be granted when a medical device, which is still under investigation, can be used in the treatment of a life-threatening or serious condition, where there is no alternative therapy or a gold standard for the treatment. The scaffolds used were previously validated in a pre-clinical large animal study of a surgically created porcine model of TBM. However, the investigated animals did not survive the post-implantation phase due to the development of infection, probably attributed to the choice of the animal model itself and not the scaffold used. In the control animals, which had no iatrogenic surgical defects, but still had a scaffold implanted, showed no associated morbidity or mortality to the scaffold (Zopf *et al.* 2014). The study group then reported the results of similar procedures in three pediatric patients (**Figure 2.5**) with follow up data for up to 38 months for their first reported case (Morrison *et al.* 2015). A further report of 15 treated children from 2012 to 2018 was later published, with up to 77 months of follow up. A total of three mortalities were recorded, with only one of them from a scaffold-related complication. The tracheal scaffold was displaced and eroded into the esophagus causing a fatal upper gastrointestinal hemorrhage six months after the implantation (Les *et al.* 2019). They reported 36 hours as the time needed from patient presentation till the production of implantable scaffolds, along with 7 days that were needed to get the necessary regulatory and ethical approvals (Zopf *et al.* 2013). Such an achievement is a proof on the flexibility and possible future use of patient-customizable, AM scaffolds in the clinic to treat life-threatening and rare diseases, while accounting for the continued growth of the patient and the eventual resorption of the implant when it is no longer

needed. The same research group reported the treatment of a young woman with an adult-onset TBM using the same established method (Morrison *et al.* 2017).

In 2011, in what could be considered the first commercially available medical device from the melt processing of polymers using SLS, a US company, Oxford Performance Materials (OPM) (https://oxfordpm.com/), announced the availability of OsteoFab™, a SLS-made patient-specific calvarial implant made from PEKK (Oxford Performance Materials 2011). The company received FDA approval as a Class II medical device through the 510(k) Pathway (K121818). The company received two further 510(k) FDA approvals for other PEKK patient-specific SLS-made medical devices for facial bones (K133809) and the vertebrae (K142005). In a recent study, Adamzyk *et al.* characterized the *in vitro* and *in vivo* properties of OsteoFab™ scaffolds. PEKK scaffolds, prior to implantation in calvarial defects in sheep, were seeded with either autologous MSCs or *in vitro* osteogenically differentiated MSCs. In all scaffold groups, there was increased bone formation, compared to the empty defects in the control group. However, the presence or absence of seeded cells played no role, showing that the scaffolds themselves were osteoconductive enough to promote bone healing. The authors reported the formation of a foreign body fibrous capsule around the scaffold, which could potentially lead to decreased bone healing (Adamzyk *et al.* 2016). Another group investigated the potential poor implant-bone interface by functionalizing the SLS-made PEKK scaffolds from OPM with adipose-derived stem cells (ASCs) in a critical-sized mandibular defect in rabbits. The modified scaffolds showed a firm attachment to the surrounding bone tissue and a mix of both lamellar and woven bone tissue at the implant-bone interface (Roskies *et al.* 2017). A second commercial AM-produced PEKK spinal implants from RTI Surgical (https://www.rtix.com/), TETRAfuse™, was also introduced to the market (rti surgical 2019). The PEKK scaffolds were investigated and compared to commercial standard and titanium-coated PEEK and were found to have bone growth comparable to the titanium-coated PEEK scaffolds without the radiopacity from the titanium coating (Cheng *et al.* 2019).

2.4.2.1 SLS summary

SLS is a promising AM technique that can be used, and has been already used, for production of TE scaffolds for clinical application. The high cost of the commercially available devices could be the bottleneck for the adoption of this technique in a clinical environment (Chae *et al.* 2015). The availability of a commercial, on-demand, patient-specific AM medical device fabricated via SLS could introduce more clinicians to the technology and encourage further in-hospital spread, till ultimately, when it is economically viable, the full adoption of the technique and workflow.

2.4.3 Melt electrowriting (MEW)

The phenomenon of electrospinning of polymers, whether dissolved in solvents or molten, have traditionally resulted in haphazard fiber deposition to create a random mesh (Reneker and Yarin 2008). Melt electrospinning (MES) had the advantage over solution electrospinning (SES) in being solvent-free, but electrical instabilities meant that the control of the fiber deposition was not possible (Robinson *et al.* 2019). Several authors attempted to print aligned fibers using mandrels (Agrawal *et al.* 2015). Several thermoplastic polymers were previously melt electrospun, for example PCL blended with poly(ethylene oxide-block-caprolactone) (Dalton *et al.* 2006), PP (Lyons *et al.* 2004), PU (Karchin *et al.* 2011) and PLA (Yoon *et al.* 2013). MES provides an alternative processing route for polymers which cannot be dissolved in solvents, for example PP (Brown *et al.* 2016). With MES being particularly amenable to controlled direct-writing, MEW is a comparatively new inclusion on the list of AM technologies (Brown *et al.* 2011).

Since the inception of MEW in 2011 (Brown *et al.* 2011), there were obvious parallels between MEW and micro-extrusion technologies. First, a molten polymer is delivered to a nozzle/spinneret that is used to direct write a 3D structure, through the movement of a Cartesian coordinate robot. MEW uses applied voltages to produce much smaller filaments, with smaller spacing between fibers, using electrostatic drawing. In one respect, MEW could be described as “electrostatically assisted FDM” (Brown *et al.* 2016).

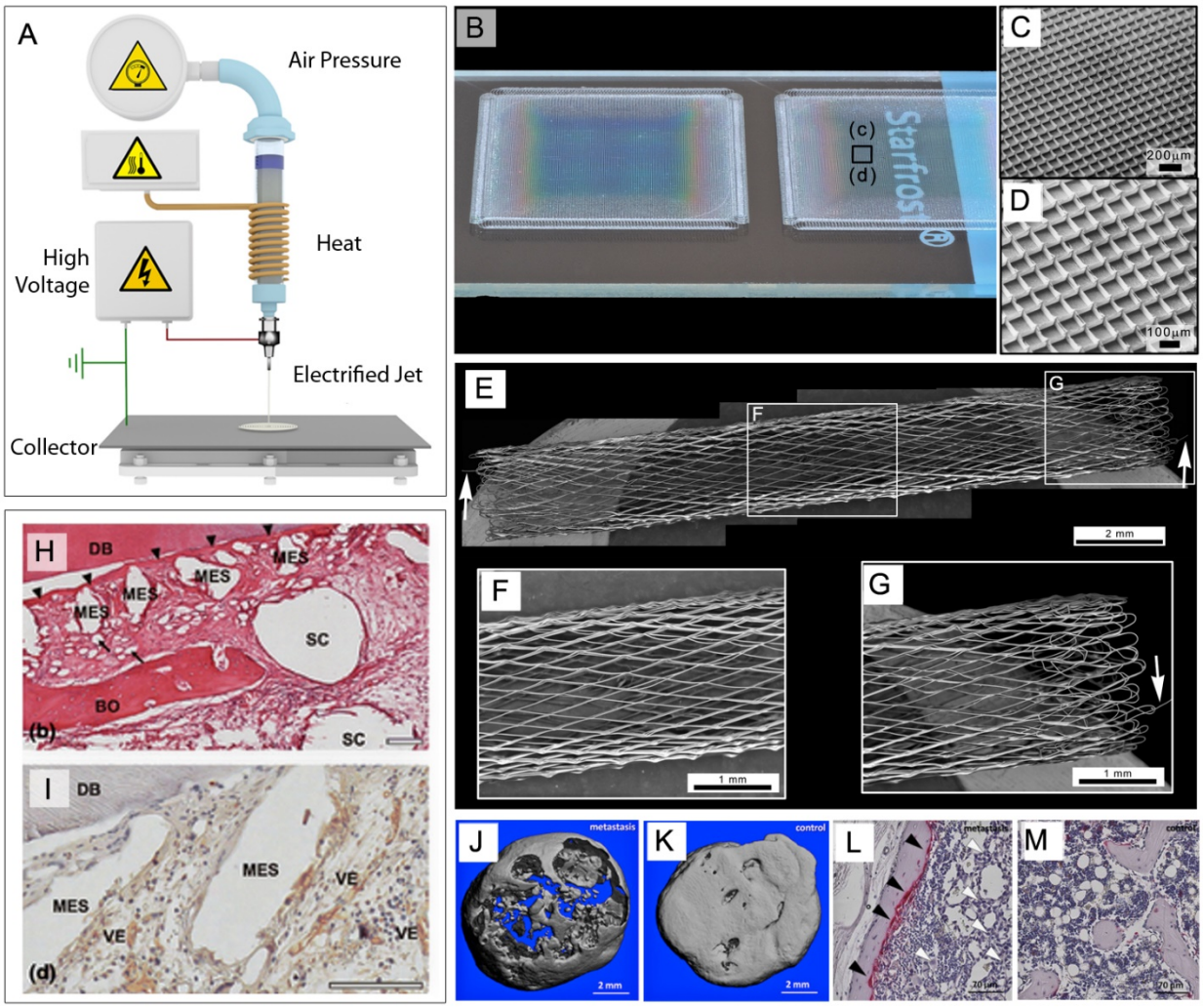

Figure 2.6. MEW process overview and sample scaffolds. (A) A schematic for a MEW device, reproduced from (Brown *et al.* 2016) with permission from Elsevier. (B-D) Representative box scaffold on a glass slide showing the macroscopic stacking of fibers (B) and with scanning electron microscope (C, D), reproduced from (Hochleitner *et al.* 2015) under the CC BY 3.0 License. (E-G) SEM images of a tubular scaffold reconstructed into a single stitched image of the whole construct (E) and magnification of the center (F) and the right edge (G), reproduced from (Jungst *et al.* 2015) with permission from John Wiley and Sons. (H, I) Histological representative images of an explanted hybrid scaffold made by FDM and MEW with hematoxylen and eosin (HE) (H) and immunohistochemical staining (I). MES – Space formed by MEW fibers, SC – Space formed by FDM fibers, BO – Bone, VE – vessel, small arrows – individual MEW fibers. Scale bar is 100 µm, reproduced from (Costa *et al.* 2014) with permission from John Wiley and Sons. (J-M) Humanized TE bone MEW constructs used for the study of prostate cancer metastasis. (J, L) Metastasis group (K, M) control group. (J, K) µCT images showing osteolytic lesions in the metastasis group. (L, M) HE image showing osteoclasts (white arrows) in resorption pits (black arrows) in the metastasis group, reproduced from (Holzapfel *et al.* 2014) with permission from Elsevier.

MEW follows the principles of electrohydrodynamic (EHD) processing and is described across the literature via a range of terminology, all stemming from the fabrication process itself, e.g. near-field melt electrospinning, direct-writing melt electrospinning, melt EHD 3D printing. Within our

research group, the terminology changed from melt electrospinning writing to melt electrowriting (while keeping the same acronym, MEW) to better distinguish between MEW in "electrostatic writing" or "electrostatic spinning" modes (Robinson *et al.* 2019).

A schematic of the MEW process is shown in **Figure 2.6A**. MEW involves melting a thermoplastic polymer inside a syringe, followed by using a force (pneumatic pressure in this instance) to drive the polymer melt to a flat-tipped nozzle. The syringe, heating elements and nozzle are all housed together in the printing head. The application of voltage creates an electric field between the nozzle and the collector plate. The result is a sustained ultra-fine jet with a predictable path that can be direct-written on a moving collector (typically in the x- and y-axes, but also possible in the z-axis, as well as in tubular mode), through computer-controlled Cartesian robot by the user-customizable G-Code. The polymer type, nozzle gauge, distance between the collector and the nozzle, applied voltage, melt temperature, feeding pressure, movement speed of the collector, deposition pattern (laydown pattern) and density (number of layers) are all variables that can be changed individually to create a wide range of scaffold types with different fiber diameters for scaffold design (Hochleitner *et al.* 2016, Youssef *et al.* 2019, Hrynevich *et al.* 2018). MEW, similar to MES, micro-extrusion techniques and SLS, is solvent-free and therefore no waiting time is needed before using the fabricated scaffold in a biological context (Dalton *et al.* 2013). Another difference between SES and MEW is that the scaffolds made from the former tend to have lower porosity scaffolds and smaller pores. The lower porosity and the small pores can decrease cell infiltration when the cells are cultured on the scaffold *in vitro* (Blakeney *et al.* 2011), this can potentially have an effect on vascularization and cellular infiltration when the scaffold is implanted *in vivo*. The design freedom of MEW scaffolds can be employed to generate precise, simple as well as complex scaffolds, and these can be characterized through non-destructive methods to ensure coherence between design and output (Youssef *et al.* 2019). The fiber diameter of MEW fibers ranges from sub-micron (Hochleitner *et al.* 2015) up to hundreds of microns (Mota *et al.* 2013) and can be changed on-the-fly during a single print (Hrynevich

et al. 2018). This contrasts with the fiber diameters obtainable from micro-extrusion technologies. MEW provides the ability to build regular, predefined, structured scaffolds (**Figure 2.6B-D**).

The MEW process faced several challenges since its inception in 2011, owing to the then, still new and unoptimized approach. Chief among them was the occurrence of fiber morphological abnormalities within the print, resulting in visible defects in the produced scaffolds, rendering them unusable. Hochleitner *et al.* investigated this issue and the phenomenon was termed fiber pulsing. This was due to an imbalance of the mass flow rates between the molten polymer coming out of the nozzle and the solidifying polymer being deposited on the collector. Through proper adjustment of the MEW device parameters, the quality of the produced scaffold and the phenomenon of fiber pulsing could be avoided (Hochleitner *et al.* 2016). It is important to point out that MEW is a comparatively new technique (in comparison to micro-extrusion and SLS) but still follows in the footsteps of much more established AM approaches. MEW printers are not yet widely available, and only a limited number of laboratories worldwide have the printers to produce such scaffolds (Robinson *et al.* 2019).

In consecutive reports, Wunner *et al.* was able to further improve the MEW process that prevented wider adoption of the technology, namely increasing build height (Wunner, Wille*, et al.* 2018), scale up (Wunner, Eggert*, et al.* 2019) and introducing in-process monitoring system (Wunner, Mieszczanek*, et al.* 2019). While MEW can produce micron-scale scaffolds with precise fiber diameters and spacing, the height of the scaffolds was typically less than 500 µm. The height increase was achieved through the computer control of the z-axis and adjusting the applied voltage as the printing head moves away from the collector. Using this approach, it was possible to achieve up to 7 mm in scaffold height (Wunner, Wille*, et al.* 2018). The second hurdle was the upscaling of scaffold production via MEW. Owing to the precise nature of the MEW process, the scaffold production time could be long, for example in Chapter 5, we discuss the fabrication of MEW scaffolds with a production time of 4.5 hours for each 12x12 mm scaffold. Wunner and colleagues addressed the issue by

implementing the vertical mounting of the collector plates, after the examination of the effect of gravity on the direction of printing (Wunner, Maartens*, et al.* 2018), simultaneously with the use of multiple printing heads. This has the potential to massively accelerate the production of new scaffolds for various projects, whether biomedical or otherwise (Wunner, Eggert*, et al.* 2019). The last hurdle to be overcome was the in-process control of the fabrication process. An automated MEW system which can monitor the fabrication in real time and allow for the direct analysis of changes in input parameters to the scaffold output (Wunner, Mieszczanek*, et al.* 2019). Such a system, together with *post-hoc* scaffold characterization (Youssef *et al.* 2019), is a breakthrough towards the development of quality assurance and process standardization, with the aim of using MEW for the production of medical devices that can navigate the waters of the complicated regulatory requirements.

MEW scaffolds have been already fabricated in tubular form (Jungst *et al.* 2015, Brown *et al.* 2012) (**Figure 2.6E-G**). Combination scaffolds were also made through MEW and SES and investigated for a potential use as vascular scaffolds (Pennings *et al.* 2019, Jungst *et al.* 2019). It was also possible to fabricate scaffolds using a dual-headed MEW printer in both melt electrowriting and electrospinning writing modes (Grosshaus *et al.* 2020). MEW scaffolds can be used as sacrificial scaffolds for creating pores inside a hydrogel structure (Haigh *et al.* 2015), or they can reinforce and improve the mechanical properties of a hydrogel (Visser *et al.* 2015, Castilho, Hochleitner*, et al.* 2018, Bas, De-Juan-Pardo*, et al.* 2017). The fiber reinforcement of hydrogels allows for the study of ultra-soft gels for neuronal migration assays (Schaefer *et al.* 2019, Janzen *et al.* 2020). The design freedom and fabrication precision of MEW made it possible to further reinforce hydrogels with out-of-plane fibers to increase the scaffold resistance to shear stress (de Ruijter, Hrynevich*, et al.* 2018). Moreover, hydrogels were also used as micropatterning templates for MEW PCL fibers (de Ruijter, Ribeiro*, et al.* 2018). PCL was blended with strontium-substituted bioactive glass to produce scaffolds for *in vitro* experiments with osteoblast-like cells (Ren *et al.* 2014). In further experiments, Hochleitner *et al.* processed a triblock copolymer of poly(lactide-block-ethylene glycol-block-lactide) (PLA-PEG-PLA), with the PLA part blended with different concentrations of bioactive glass (Hochleitner *et al.* 2017).

While PCL is the most used polymer in MEW (Brown *et al.* 2016), poly(2-ethyl-2-oxazoline) was successfully processed with this method (Hochleitner *et al.* 2014, Nahm *et al.* 2020), as was poly(L-lactide-co-ε-caprolactone-co-acryloyl carbonate) which was processed by MEW, then photo-crosslinked with UV light, producing a scaffold with favorable mechanical properties for soft TE (Chen *et al.* 2016, Hochleitner, Chen*, et al.* 2018). Poly(urea-siloxane), a thermoplastic polymer, was processed via MEW and could be applied to potentially optimized towards tendon and ligament TE (Hochleitner, Fursattel*, et al.* 2018). PVDF, which saw increased use in surgical meshes (Klinge *et al.* 2002), was also processed through MEW (Florczak *et al.* 2019).

Owing to the customizable nature of MEW, several authors have experimented with increasingly complex structures, in an attempt to mimic the complex and diverse ECM of different tissue types (No *et al.* 2020). Hrynevich *et al*. explored the ability to change the fiber diameter within the same printing process (Hrynevich *et al.* 2018). Liashenko and Hrynevich printed MEW scaffolds in sinusoidal configuration with changing tilt and amplitudes, further adding a customization layer towards soft TE scaffolds (Liashenko *et al.* 2020). Soft TE applications were further explored for tendon and ligament TE (Bas, D'Angella*, et al.* 2017), for heart valves (Saidy *et al.* 2019) and for cardiac patches (Castilho, van Mil*, et al.* 2018, Castilho *et al.* 2017). MEW fibers were also surface functionalized through the coating with calcium phosphate (CaP) particles through the immersion in SBF (Vaquette *et al.* 2013), as well as via dissolving HA with PCL before melting inside the MEW device (Abdal-hay *et al.* 2018). Plasma or sodium hydroxide (NAOH) treatment could also be applied to improve the hydrophobicity of PCL (Abbasi *et al.* 2020), which is by far the most commonly used polymer in MEW devices. The effect of plasma treatment on PCL polymer discs was thoroughly investigated in terms of the effect on CaP coating after SBF immersion (Tran *et al.* 2018).

MEW scaffolds were used *in vitro* for a variety of applications, each taking advantage of the customizable and precise nature of the technique. MEW scaffolds were used to grow fibroblasts (Farrugia *et al.* 2013), primary breast-derived mesenchymal cells (Weigand *et al.* 2016), spheroids

(Hrynevich *et al.* 2018, McMaster *et al.* 2019), osteogenic cells (Muerza-Cascante *et al.* 2016, Zaiss *et al.* 2016, Roder *et al.* 2015), chondrogenic cells (Bas, De-Juan-Pardo*, et al.* 2017, de Ruijter, Ribeiro*, et al.* 2018), periodontal cells (Farag, Hashimi, Vaquette, Volpato*, et al.* 2018, Fuchs, Youssef, Seher, Hartmann*, et al.* 2019, Fuchs, Youssef, Seher, Hochleitner*, et al.* 2019), MSCs (Hansske *et al.* 2017, Hrynevich *et al.* 2018, Blum *et al.* 2019), endothelial cells (Bertlein *et al.* 2018, Jungst *et al.* 2019, Pennings *et al.* 2019), primary prostate cancer-associated fibroblasts (Pereira *et al.* 2019) and macrophages (Tylek *et al.* 2020). Engineered bone MEW scaffolds were used as models for the investigation of prostate cancer bone metastasis *in vitro* (Bock *et al.* 2019, Paindelli *et al.* 2019).

Contrary to SLS and micro-extrusion, most *in vivo* MEW studies were all focused on a certain research questions, in which MEW served as a tissue model, developed *in vitro* and later implanted *in vivo*. Th characterization the implant itself or its local tissue reaction for the potential application of MEW scaffolds as a medical device were not done, especially with the choice of immunocompromised animal models. In other words, MEW implants were used as a research tool rather than a potential implantable medical device. An interesting observation: with few exceptions (Baldwin *et al.* 2016, Gonzalez-Gil *et al.* 2019), the only *in vivo* MEW studies which examined MEW scaffolds for a potential implantable medical device application involved multimodal constructs, where the implanted scaffold was made through MEW and either FDM or SES. We have previously reviewed all seven published *in vivo* MEW studies until the end of 2016 (Youssef *et al.* 2017). Currently the number of published *in vivo* studies from 2017 till today has more than doubled. It is worth noting that all *in vivo* studies were performed using medical-grade PCL, with only one study using, in addition, a PLLA FDM-fabricated component (Sudheesh Kumar *et al.* 2018). Most MEW scaffold implantation procedures published so far were performed on rodents and mostly involved subcutaneous implantation of scaffolds in immunocompromised animals, as part of achieving humanized animal models for the study of human cancers.

Some of these experiments involved multimodal, hybrid scaffolds (Dalton *et al.* 2020). In an interesting approach, Costa *et al*. described the use of a combined FDM and MEW scaffold where the FDM scaffold was heated to melt the first layers and then the MEW scaffold was pushed in to generate a bimodal scaffold for guided tissue regeneration of periodontal tissue (**Figure 2.6H-I**) (Costa *et al.* 2014). Jeon *et al*. investigated adding alginate gel to a composite scaffold of FDM and MEW and grow osteoblasts and chondrocytes in it for osteochondral defects repair (Jeon *et al.* 2014). Both studies were tested *in vivo* by subcutaneous implantation in athymic nude rats. Sudheesh Kumar *et al.* constructed an outer, hollow shell made by FDM to mimic cortical bone with an inner component through MEW with a hydrogel embedded with rhBMP-2. Both components were fabricated from PCL. The construct was placed inside a PLLA dome (also through FDM) acting as a structural support for the implant. The assembled construct was placed inside calvarial defects in rabbits (Sudheesh Kumar *et al.* 2018). Vaquette *et al*. performed what could be described as the first large animal (sheep) study using a MEW scaffold. A bimodal construct, with a MEW component and a SES one, was manufactured using medical-grade PCL and seeded separately with three different autologous cell types: gingival, MSCs and periodontal ligament cells (PDLCs) using the cell sheet culture method. The MEW scaffold was heated and then allowed to fuse with the SES one to create a barrier membrane. A dehiscence periodontal defect in sheep was surgically created and the different assembled scaffolds were used to fill it (Vaquette *et al.* 2019). In another study of periodontal defects in a rat model, a MEW PCL scaffold was seeded with cell sheets of human PDLCs and implanted inside mandibular defects in rats. The defects were lined beforehand with a SES PCL membrane to act as a barrier and protect the cell-seeded main MEW PCL scaffold (Farag, Hashimi, Vaquette, Bartold*, et al.* 2018).

The only study which specifically looked at the foreign body reaction to single fibers in tubular, CaP-coated MEW scaffolds using nonlinear multiphoton microscopy in mice with a dorsal skin fold chamber. The proliferation of macrophages and FBGCs were observed before and after treatment of the implant with either a vascular endothelial growth factor (VEGF) trap or clodronic acid. The authors

concluded that the foreign body reaction is aggravated by the release of VEGF in the implantation site (Dondossola *et al.* 2016).

MEW tubular scaffolds were used as a composite periosteal implant after cell seeding with MSCs with or without human umbilical cord vein endothelial cells (HUVECs) co-culture or VEGF-loaded, star-polyethylene glycol (star-PEG) incubation in immunocompromised non-obese diabetic, severe combined immunodeficient (NOD SCID) mice. The constructs were implanted as periosteal sleeves surrounding cortical defects in the femur. The authors reported a high number of FBGCs surrounding the PCL scaffold, in comparison to the hydrogel part (Baldwin *et al.* 2016). Critical sized femoral defects in rats were treated with MEW PCL tubular scaffolds seeded with either periosteum-derived or bone marrow-derived MSCs and compared to an allograft, a collagen scaffold with rhBMP-2 and acellular PCL MEW scaffolds. The periosteum-derived MSC-seeded MEW scaffold showed better defect healing compared to the bone marrow-derived ones (Gonzalez-Gil *et al.* 2019).

The remaining *in vivo* experiments were all part of a xenomorphic model to study metastasis, however the experiments provided insights as to tissue reaction for MEW scaffolds, albeit in immunocompromised, humanized mice. The Hutmacher group released a detailed protocol highlighting the use of tubular, CaP-coated MEW scaffolds as an *in vivo* humanized bone organ for the study of bone metastasis in various cancer models (Martine *et al.* 2017). The protocol involved a preparation process prior to implantation, in which tubular MEW scaffolds were coated with CaP and then seeded with human mesenchymal progenitor cells or osteoblasts. The scaffolds are then filled with rhBMP-7 and osteoblasts in cell sheets and sealed with fibrin glue prior to subcutaneous implantation in NOD SCID mice. The mice then are non-lethally irradiated and then injected with $CD34^+$ human bone marrow progenitor cells to allow for humanized hematopoiesis to commence in the construct as well as the mouse peripheral blood, spleen and bone marrow. These constructs were dubbed miniaturized tissue-engineered bone construct (mTEBC) (Martine *et al.* 2017). These mTEBC were then used as sites for ectopic human bone formation in mouse models, as a metastatic site of

prostate cancer (Holzapfel *et al.* 2014, Dondossola *et al.* 2018, McGovern *et al.* 2018, Landgraf *et al.* 2019, Pereira *et al.* 2019, Shokoohmand *et al.* 2019) and breast cancer cells (Thibaudeau *et al.* 2014, Thibaudeau *et al.* 2015, Quent *et al.* 2018, Shafiee *et al.* 2018, Landgraf *et al.* 2020) in a humanized mouse model (**Figure 2.6J-M**). The mTEBC model was also investigated with a different cell source, where human MSCs from fetal, term placenta as well as fetal, first trimester bone marrow were used instead of human osteoblasts (Shafiee *et al.* 2017). In another, unrelated, cancer model, Loessner *et al*. manufactured constructs out of MEW scaffolds seeded with human primary mesothelial cells and hydrogels with primary human ovarian cancer cells and investigated them *in vitro*. For the *in vivo* study, a xenograft intraperitoneal implantation model in NOD SCID mice was used, albeit not with primary human cells but rather with cell lines (Loessner *et al.* 2019).

In Chapter 5 the results of a study of the foreign body reaction to the implantation of ultra-fine PCL MEW flat scaffolds with fiber spacing of up to 50 µm and fiber diameter of 2.5 µm in outbred, immunocompetent Naval Medical Research Institute (NMRI) mice is shown. Moreover, there is an ongoing *in vivo* implantation study by our group in inbred BALB/c mice to understand tissue infiltration, vascularization and the foreign body reaction to more standard sized, implanted PCL MEW scaffolds. Both studies use non-treated, non-cell seeded, PCL-only scaffolds.

2.4.3.1 MEW summary

The *in vivo* experiments for MEW scaffolds performed indicate that such scaffolds are well integrated in animal models. The MEW scaffolds functioned as a promising, novel, expandable and modifiable research tool for understanding metastasis, tumor cell homing as well as drug action on such xenografts. Importantly, the small diameter of fibers within MEW scaffolds result in very soft and compliant objects, which can be functionalized and coated with biologically active molecules and growth factors. Most of these experiments were completed in immunocompromised mice via subcutaneous implantation and, to date, no clinical data from MEW-fabricated scaffolds are available.

The fact that FDM has achieved clinical use, and MEW uses similar principles but with the application of voltage, makes it a realistic candidate for AM of medical implants.

2.5 AM in tomorrow's clinic and biofabrication rooms

The past decades saw billions of dollars spent on scaffold-based TE research, however, very few products could clear the hurdles of regulatory approval and be available to patients (Hoffman *et al.* 2019, Kim *et al.* 2019). The promises made for the "revolution" that TE would usher into the clinical practice (Langer and Vacanti 1993) remain to be seen, even as the number of elderly people in developed countries increases. As was discussed earlier, the approach to the design of new medical devices (and hence, the complexity of the pathway needed for regulatory body approval) is one side of the equation, but another equally important side is the need for the input of the end-user; in this case the physician or the surgeon. AM can potentially solve this disconnect by giving the medical team the ability to design and actually "make" devices in-hospital in a multi-disciplinary team approach. This approach, in which specialized hospitals become AM-based medical device manufacturers, in so-called "biofabrication rooms", will be especially critical for patients with rarer disease and reconstructive needs or in niche markets like pediatrics for which it is difficult for the medical device industry to invest large sums of money in preparing manufacturing pipelines to produce very few implants. AM has the potential to revolutionize medical treatment for these scenarios as well as in creating patient-specific or personalized medical devices (Simoncelli 2013) with the much needed addition, in case of pediatric surgery, of accounting for the patient's growth (Hollister 2017). The adoption of AM in pediatric surgical practice is not only a technological possibility, but one of an ethical and economic necessity. The output from university-based research, which in some cases fails to find market breakthrough, could be reworked and adapted to such approaches, provided that all safety checks and quality assurances are met. The development and adoption of non-destructive, in-process quality assurance is a necessary step towards regulatory approval of AM medical devices (Youssef *et al.* 2019, Wunner, Mieszczanek*, et al.* 2019).

AM makes the inter-disciplinary approach towards patient treatment through medical imaging (the radiologist), the in-hospital AM laboratory (the biomedical engineer) and the operating room (the surgeon) possible. Another possible user of AM is the clinical pharmacist for on-demand, dose-adjusted drug products, a useful approach in pediatrics and drugs with short shelf life (Norman *et al.* 2016), or in case of rural-based, isolated patients during the current COVID-19 pandemic (Hsiao *et al.* 2020).

As discussed before, the generation of 3D objects through AM by means of STL files which were, in turn, created from the patient's own DICOM CT or MRI data is a reality. In today's medical practice, the availability of high-resolution, completely digital radiological data makes this approach increasingly within reach. With enough development and adoption in the medical community, such approaches can benefit, as an example, trauma patients in need of customized, acellular implants, which could be prepared in parallel to the patient preparation for surgery. A possible hurdle to the adoption of such workflows are economic ones, in terms of AM equipment availability. This could be solved by the sharing of resources among several teams inside the same or nearby hospitals (Martelli *et al.* 2016).

While the current, media-hyped "state of the art" of 3D organ printing is highly speculative; customized, safe and inexpensive acellular implants that can be made "on demand", is more likely to be realized over the next decade. In fact, as was shown and discussed above, it is already the case. Other more "regulatory-friendly" approaches are also discussed below.

2.5.1 Patient specific models and surgical tools

The imaging technologies (e.g. MRI, CT) required to patient-customize implants are established within hospitals and are already used in AM. Today, customized physical models of patients' organs are being additively manufactured to aid in surgical planning (**Figure 2.7A-E**), and the link between the surgeon and the AM workshop is becoming established. In this aspect, the physical models are not intended for implantation, but fabricated so that a surgeon can handle, look and plan

a surgical procedure on an organ that is patient-specific, especially in non-accessible or dangerous anatomical locations (Zeng *et al.* 2015, Wake *et al.* 2016, Ryan *et al.* 2016, Kondo *et al.* 2016).

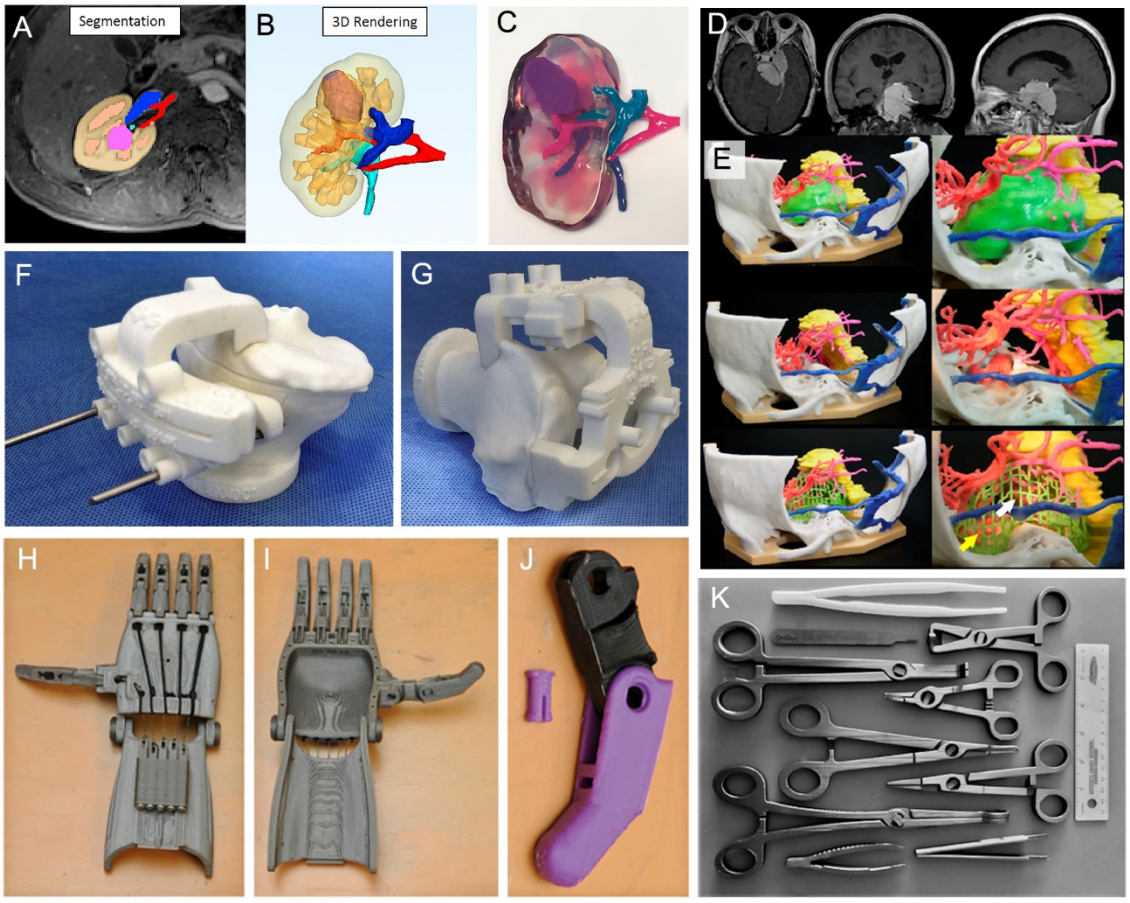

Figure 2.7. Further applications for AM in the clinic and beyond. (A-C) Fabrication of a renal tumor model from segmentation of a patient's CT scan data (A) through CAD (B) to obrain a phyiscal model for pre-surgical planning (C), reproduced from (Wake *et al.* 2016) with permission from Elsevier. (D, E) Using a patient's brain CT scan data (D) to produce a 3D model of a complicated skull base tumor (E), reproduced from (Kondo *et al.* 2016) with permission from Springer Nature. (F, G) Patient-specific intstumentation for knee arthroplasty with tibial (F) and femoral (G) cutting guides, reproduced from (Camarda *et al.* 2015) with permission from Springer Nature. (H-J) Prosthetic hand examples from Enabling the Future Project, with dorsal (H), palmar (I) views and a digit (J), reproduced from (Burn *et al.* 2016) with permission from Elsevier. (K) A set of surgical tools made via AM for a space mission, reproduced from (Wong and Pfahnl 2014) with permission from The Aerorspace Medical Association.

These physical models approximate the shape and size of the organ of interest, however for the surgeon, the tactile feel is an important criterion. Through the development of multi-material AM approaches, these physical models could gain a tactile aspect that would then allow the practice of a surgical procedure, even including the vasculature, bringing the organ model closer to a seemingly real, but non-functioning one. Such surgical planning and teaching models do not require sterilization or prior seeding with cells and can be built using non-clinically approved materials.

Patient specific instrumentation (PSI) or customized alignment cutting guides already exist and are manufactured from the patient's radiology data to form surgical tools that are placed into position allowing precise and efficient cutting of tissue. These medical devices are AM manufactured, but not necessarily from polymer melts. One example is to produce cutting guides for improving total knee arthroplasties (TKA), where patient-specific guides are positioned onto the femur and the tibia, complete with drilling locations and cutting positions (**Figure 2.7F-G**) (Mattei *et al.* 2016). While not considered an implantable medical device, the manufacture of such devices must comply with the current regulatory landscape. While certainly not for all patients, special patient groups can benefit from such devices, for example obese patients, where PSI helped in the restoration of the mechanical axis in obese patients undergoing TKA after a follow up period of up to one year (Anwar *et al.* 2016), preventing a possible complication like limb mal-alignment (Estes *et al.* 2013). PSIs are still manufactured by various orthopedic implant companies, potentially making them more expensive than in-house manufacture. It would make economic sense, in that case, that PSIs are only used for complicated primary cases and not to be used routinely, as routine use will add extra costs to the health care bill (Camarda *et al.* 2015). However, if PSIs are produced in-hospital using biofabrication rooms, it can be argued that in the future, it can be a routine procedure.

2.5.2 Emerging and future scenarios

AM provides the freedom of medical device production without relying on established supply chains. This is one of the reasons why AM is also regarded as a disruptive technology. In the current hospital supply chain systems, where the reliance on "just in time" supply, the occurrence of emergencies or disruptive situations could mean shortages and problems in the clinical practice (Global Trade Review 2020). Recently, the currently evolving COVID-19 pandemic has placed AM in hospitals again in the public perception (Banker 2020), with sensational headlines of the general community, the industry, as well as hobbyists, providing much needed personal protective equipment, fabricated through AM approaches, to healthcare providers at the forefront of the pandemic

(Wesemann *et al.* 2020). In other reports, AM was used to produce spare parts for ventilators, potentially saving patients life, without waiting for replacement parts from manufacturers (Sertoglu 2020, Carlota 2020). TE scaffolds as *in vitro* test systems can be used for the prompt investigation of potential vaccines (Tatara 2020).

In limited-resource countries, the adoption of AM technologies can save patient lives and decrease morbidity in already strained healthcare systems. AM has the potential to provide cost-effective solutions to medical device production and availability, without the need for huge costs and supply chain networks. The success of open-source and volunteer-based AM approaches to the design and fabrication of prosthetic hands (**Figure 2.7H-J**) is an early example of this (https://enablingthefuture.org, http://www.openhandproject.org).

In 2014, the National Aeronautics and Space Administration (NASA) in collaboration with Made in Space, Inc. started a two-phase project to assess 3D printing (here used to refer to AM) under zero gravity conditions. The overall aim was to explore the use of 3D printing for long duration, long endurance space missions. The use of 3D printing in this area can preserve crew and mission safety by enabling the crew to react rapidly in case of need. In each phase, select objects were 3D printed using an FDM device, which was brought to the International Space Station (ISS), and compared with identical printed ones, fabricated through ground-based, identical device. The 3D printed objects included tools, surgical instruments as well as special objects to be tested on return to Earth. The objects were subjected to intense physical and mechanical testing and in conclusion, the researchers found no engineering-significant effects to printing in space under microgravity (Prater, Bean*, et al.* 2017, Prater, Werkheiser*, et al.* 2019). Sustainability in such isolated scenarios is of great importance, therefore, NASA in collaboration with Tethers Unlimited Inc. (TUI) installed in 2019 the ReFabricator on board of the ISS. This is a device capable of recycling and reprocessing 3D printed objects, producing polymer filaments that can be reused in the FDM printer in the ISS. Testing of samples from this process is still pending. In another project, TUI developed a dry heat sterilization system, to recycle

polymers into food-grade and medical-grade polymer filaments, to be processed with the FDM printer again (Prater, Edmunson*, et al.* 2019). Another company, TechShot Inc., was tasked with the construction of the Fabrication Laboratory (FabLab) device. The FabLab can process a range of different materials, ranging from polymers and biomaterials to aerospace grade metals, e.g. Ti-6Al-4V. NASA is also investigating the development of inks to print integrated circuits for the 3D printing of wearable sensors to monitor crew health, e.g. cortisol, carbon dioxide or radiation sensors (Prater, Edmunson*, et al.* 2019). There has already been a variety of experiments to fabricate medical and surgical instruments for space missions (Rankin *et al.* 2014, Wong and Pfahnl 2014). In preparation for the first manned mission to Mars, there is a need to better optimize the logistic situation, safeguarding the human crew in the future Mars habitat, while dealing with weight and volume limitations. According to NASA estimates, 95% of spares will never be used. A logistical solution is to supply the tools to produce spares and medical devices in the case of an emergency, rather than supplying all the possible spares (or medical devices) themselves (**Figure 2.7K**) (Prater, Werkheiser*, et al.* 2017). In the context of MEW, which is the AM technology used in this thesis, it has been found that the forces generated by the electric field are more substantial than gravity (Wunner, Maartens*, et al.* 2018). It is therefore likely that MEW would also be unaffected when operated in microgravity, and the solvent-free manufacturing approach also brings advantages in the context of ventilation within a long-distance spacecraft.

2.6 Conclusion

In this chapter, a quick history of the use of polymer melts in medical devices was given, followed by a review of the FDA regulatory framework for medical devices, with a highlight of a special pathway that can accelerate the translation of AM melt-processed medical devices to the clinic. The state of the art of three polymer melt-based AM techniques was discussed, with a detailed discussion of the outcomes of their *in vivo* and clinical studies. A special emphasis was given to MEW, as this is

the scaffold fabrication method which will be used in the rest of this thesis. And finally, an account was given to the current and possible future uses of AM in clinics and beyond.

Chapter 3

A manuscript based on the work discussed in this chapter is in preparation:

Youssef, A., Tandon, B., Ziani, N. T., Groll, J., Jungst, T., Dalton, P. D. “The estimation of mass flow rate of melt electrowritten polycaprolactone scaffolds”.

3.1 Introduction

Melt electrowriting (MEW) is a relatively recent addition to the additive manufacturing (AM) family. Using principles from solution electrospinning (SES), melt electrospinning (MES) and micro-extrusion of polymer melts (mainly fused deposition modeling, FDM), MEW can fabricate customizable, solvent-free scaffolds, through the precise deposition of micron-scaled, polymeric fibers (Brown *et al.* 2011). The technique of MEW and a review of its applications were previously reviewed (Youssef *et al.* 2017, Robinson *et al.* 2019) and summarized in Chapter 2.

There are several parameters that can affect the shape and fidelity (fiber diameter, stacking height and quality, laydown pattern, spacing and turns) of the fabricated MEW scaffold: namely applied voltage, applied pressure, polymer melt temperature, collector speed, nozzle diameter, distance between nozzle and collector and laydown pattern (Hochleitner *et al.* 2016, Youssef *et al.* 2019). Contrary to those produced through its closest technological relatives, MES and FDM, the MEW scaffolds have fibers which accurately stack upon each other forming walls that can reach heights of up to 7 mm (Wunner, Wille*, et al.* 2018). While MEW fiber diameters can be produced as small as 820 µm (Hochleitner *et al.* 2015), their typical dimensions are within 5 to 45 µm (Hrynevich *et al.* 2018).

In order to preserve fiber placement fidelity, the printing parameters need to be controlled with the understanding which parameters have control over which morphological features of the fibers, and hence, the scaffold as a whole. We have previously reported on a phenomenon that occurred during the MEW process due to an imbalance between the applied voltage and the applied pneumatic pressure. This imbalance, termed fiber pulsing, deleteriously affects the printing process while altering the fiber diameter in the scaffold. The effects could be detected macroscopically as visible defects in the scaffold as well as changes in the regularity of the loops in the turns on the sides of the scaffolds. Microscopically, it manifested as fiber diameter change and fiber disruption (Hochleitner *et al.* 2016).

When the electrical field between the nozzle and the collector it too high, arcing can result. This is an electric discharge from the positively charged nozzle to the negatively charged or earthed collector and is a safety issue that can result in damage to the electrics of the printer. This discharge also interrupts the polymer jet, requiring the re-establishment of a new Taylor cone for the continuation of the printing process, leading to diameter inconsistencies and layer defects. Moreover, the intense electrical discharge leads to the fibers melting where it hits, and thus, a visible scaffold defect. Preventing arcing can be achieved through the optimization of the relationship between applied voltage and collector distance (from now on used to refer to the distance between the collector and the nozzle), or by printing onto a less electroconductive collector surface, e.g. glass slides.

A height limitation in MEW scaffolds has also existed due to poorly positioned fibers and which was recently overcome by Wunner and colleagues by using increasing electric fields during the printing process. In this instance, the applied voltage was dynamically increased with a change in the collector distance, avoiding the occurrence of fiber pulsing and arcing, so that a scaffold with a height of 7 mm was achievable (Wunner, Wille*, et al.* 2018).

As was observed with fiber pulsing, the discrepancy between the mass flow rate of the polymer passing through the nozzle and that landing on the collector is the reason for this phenomenon. This mass flow rate is determined through the pneumatic pressure and the applied voltage (Hochleitner *et al.* 2016). In their seminal report of MEW and the introduction of this novel AM method, Brown and colleagues described the relationship between the flow rate and the critical translation speed (CTS). The CTS is the lowest possible collector speed that matches the speed of the jet, resulting in the deposition of straight fibers. A reduction of the flow rate (the authors used unit volume per unit time, but the density of poly(ε-caprolactone) (PCL) is a known variable, so the mass could be calculated) by one order of magnitude from 50 to 5 µL/h resulted in a doubling of the needed CTS to get straight fibers, from 0.5 m/min to 1 m/min. This resulted from a decrease in the viscoelastic

mass at the charged nozzle, which is being accelerated downwards towards the grounded collector, leading to a faster jet speed, which needed a matching collector speed to get straight fibers. Moreover, the fiber diameter decreased by one third compared to the starting flow rate. It was also reported that when other parameters are kept constant, including the flow rate, but with an increase in collector speed, this lead to a decrease in fiber diameter, which could be attributed to a drawing effect on the molten polymer being extruded at the Taylor cone (Brown *et al.* 2011).

The setup used in this first description of MEW was equipped with a syringe pump to control the polymer extrusion from the syringe through the nozzle (Brown *et al.* 2011). The design of MEW devices now mostly excludes syringe pumps in favor for a more streamlined, controlled and programmable pneumatic air (or nitrogen) pressure controllers (Brown *et al.* 2016). To the best of our knowledge, in the current MEW literature, the flow rate of the polymer during printing using pneumatic conditions is not reported, and there are no reports on how other printing parameters affect the mass flow rate of the polymer. In our previous publication of the fiber pulsing phenomenon, it was assumed that the feeding pressure would be the most influential parameter on the mass flow rate of the polymer. However, mass flow rate itself is partly controlled through the feeding pressure, viscosity of the polymer melt and nozzle diameter as well as length (Hochleitner *et al.* 2016).

Therefore, in this chapter, we examined the effect of changing the collector speed on the mass flow rate of PCL during the fabrication of MEW scaffolds with box-shaped pores, while keeping the other conditions constant. It is important to establish this relationship to determine whether different collector speeds affect the mass flow rate to the nozzle, essentially producing a force that “pulls” the melt from the nozzle in addition to the pneumatic pressure. This would be a correlation to what Brown *et al.* already described (Brown *et al.* 2011), when they changed the collector speed and kept the flow rate through the syringe pump constant.

3.2 Materials and methods

3.2.1 Scaffold fabrication

A custom-made MEW device was used for the fabrication of scaffolds and was described in detail elsewhere (Hochleitner *et al.* 2016). Briefly, medical-grade PCL (PURASORB PC 12, Lot# 1412000249, 03/2015, Corbion Inc., Gorinchem, Netherlands) was used as received, with aliquots divided into 50 mL centrifuge tubes under argon atmosphere inside a glove box and stored at -80 °C, until used. The aliquot in active use was stored at room temperature. The polymer was added to disposable plastic syringes equipped with flat-tipped, 22G needle tips (Nordson EFD Deutschland GmbH, Pforzheim, Germany). The polymer was heated and used for up to four days and then the remainder was discarded.

The polymer was heated inside the printing head to 73.5 °C and then 1 bar of air pressure was applied to the syringe. The applied voltage was 6 kV (5 kV on the nozzle and -1.5 kV on the collector) while the collector distance was approximately 6 mm and kept constant throughout the experiments. MEW was performed at an ambient temperature of 23.4 ± 1.2 °C with a relative humidity of 35.5 ± 5.1 %. The following collector speeds were used in this experiment: 500, 750, 1500, 3000 and 6000 mm/min. Scaffolds with a sub-CTS collector speed (300 mm/min) were also printed for qualitative assessment.

The G-Code was based on one written by Mr. Joachim Liebscher and edited by Dr. Tomasz Jüngst and Mr. Andrei Hrynevich. An example of a G-Code file is listed in **Appendix 1**. The G-Code was further altered to print 20 fiber layers (2x10) in the 0/90° laydown pattern (box-shaped pores) with the planned fiber spacing of 250 µm and a scaffold size of 45 x 45 mm. Scaffolds with different layer counts (2x5 and 2x20) were printed for the qualitative assessment and were not included in the mass measurement. Since MEW is a continuous process once the jet starts, the movement from one fiber line to the next is done through a loop structure, where the collector moves in a circular movement

to translate to the next starting position for the new fiber. A pause of 0.1 second before the loop turn as well as another pause of 0.05 second after finishing the turn were introduced. The collector speed during the turn was 500 mm/min with a turn radius of 1.5 mm.

Manual stabilization of the jet was done once the Taylor cone was formed, followed by the start of the print process itself by running the G-Code in the IndraWorks Software (version 13.12) (Bosch Rexroth AG, Lohr am Main, Germany). A total of four different scaffolds were printed per run on the stainless-steel collector, with the first scaffold dedicated for jet stabilization (**Figure 3.1**).

3.2.2 Scaffold collection

The fibers leading from one scaffold to the other were cut. Scaffolds were sprayed with absolute ethanol to facilitate detachment from the collector, picked up with fine forceps and then stored in plastic Petri dishes, which were sealed off with Parafilm until used.

3.2.3 Scaffold characterization

Scaffolds were macroscopically inspected during collection. Those showing visible defects due to arcing or fiber pulsing were excluded from this study. The same was true when the fibers did not stack sufficiently to form regular walls.

A stereomicroscope (Discovery V20, Carl Zeiss Microscopy GmbH, Göttingen, Germany) with an attached 5-megapixel color camera (AxioCam ICc 5, Carl Zeiss) was used to inspect the scaffolds and capture images using both a 0.63x and a 1.5x lens. Fiber diameter measurement was performed on stereomicroscope images (ten measurements per scaffold, at least three scaffolds per collector speed) ($n \geq 30$). For scanning electron microscopy (SEM), a Crossbeam 340 (Carl Zeiss) was used for visualization of fine fiber details as well as correlating the stereomicroscope-measured diameters. Samples were not sputter-coated before being imaged and were mounted on aluminum stubs with 12.5 mm diameter and glued with conductive tape (Plano GmbH, Wetzlar, Germany). SEM measurements were done by Dr. Claus Moseke.

The mass of the scaffolds was measured using a fine balance (MC1 Research RC 210 P, Sartorius AG, Göttingen, Germany). The balance was tared with an empty Petri dish inside, on which the scaffold was placed. An antistatic gun (Zerostat, Sigma-Aldrich Chemie GmbH, Munich, Germany) was used to neutralize charges on the scaffold and the Petri dish and facilitate handling.

3.3 Results and discussion

3.3.1 Scaffold morphology

Four different scaffolds were printed per run on the stainless-steel collector (**Figure 3.1A**). The regularity of the fibers gave the scaffold a transparent aspect when detached from the collector and handled. A fiber was seen linking the scaffolds from the jet movement since MEW is not an on-and-off process and was considered when writing the G-Code for the scaffolds. The visual inspection of the scaffolds made it possible to exclude scaffolds, or sometimes whole runs, where anomalies occurred, for example fiber pulsing (black arrow; **Figure 3.1B**), caused by an imbalance of printing parameters.

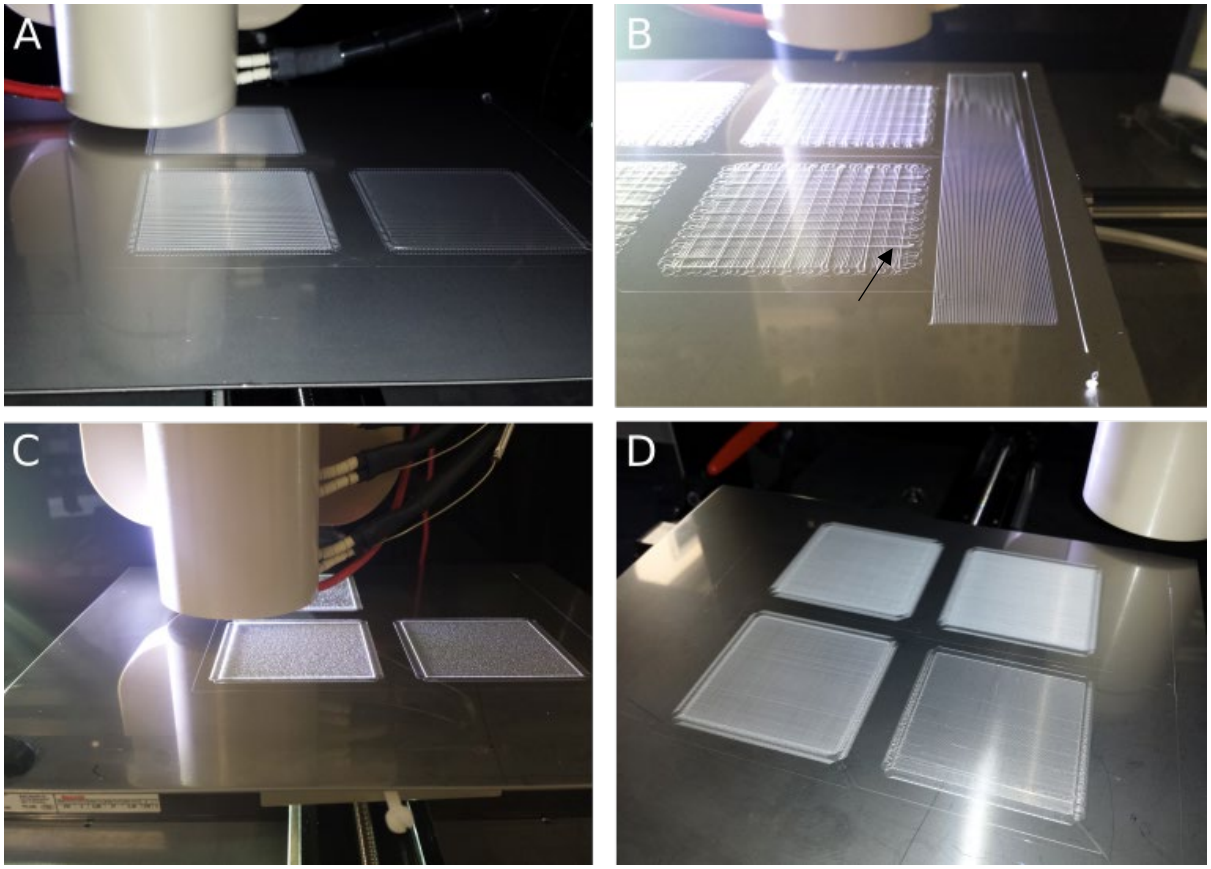

Figure 3.1. Melt electrowriting (MEW) of PCL scaffolds. Photographs of the MEW process under different parameters. (A) Optimized conditions result in regular and uniform scaffolds. (B) Imbalance in the mass flow rate results in fiber pulsing (black arrow). (C) Printing under the critical translational speed will lead to scaffolds with irregular fiber laydown patters. (D) Light parameter imbalances can result in poor stackability of fibers into walls.

Printing with 300 mm/min, which is below the CTS, resulted in an irregular mesh (**Figure 3.1C**) with fibers deposited in coiling, random paths. There is a stark contrast with the preciseness and regularity seen with higher collector speeds. **Figure 3.1A** shows scaffolds printed with a speed of 750 mm/min which was close to twice the estimated CTS, albeit in the scaffolds shown in the figure, the fiber spacing was set to 500 µm. Changing this parameter between 250 to 500 µm had no effect on fiber pulsing or scaffold regularity at the current collector speed (data not shown). Fiber spacing can affect scaffold morphology when there is a mismatch between fiber diameter and fiber spacing (Youssef *et al.* 2019).

When fiber pulsing occurred, similar to what was described before (Hochleitner *et al.* 2016), the diameter change in the fibers resulted in visible scaffold abnormalities (**Figure 3.1B**). The pulsing phenomenon appeared in this case, as a resulted of an increased feeding pressure, here 1.2 bar, instead of 1 bar throughout the experiment. The collector speed was set to 500 mm/min, which otherwise in the default experimental settings, resulted in regular scaffolds. In accordance to our previous observation (Hochleitner *et al.* 2016), an indicator of pulsing, other than the visual fiber diameter change, was the loop change during turning, where there was a clear positioning and size difference shown between periods where pulsing did not occur, and those when it did.

The failure of the fibers to properly stack on top of each other during printing led to visible scaffold changes, where the fiber distribution to form walls was not uniform. This means that instead of having regular walls, in certain areas in the scaffold the fibers form bundles away from the supposed laydown path (**Figure 3.1D**). When also complicated with pulsing, this led to unusable scaffolds. This was even more compounded with thicker scaffolds, i.e. those with more layer count, e.g. 2x20 layers (data not shown).

Using stereomicroscopy for all scaffold groups above the CTS, it was evident that the pause time before and after the turn loop needed further adjustment (**Figure 3.2 left column**). The long pause time was evident by slight fiber coiling at the loop, as a result of the change in collector speed

during deceleration before the pause and acceleration after it. Moreover, with higher collector speeds, starting from 1500 mm/min, as the fibers approached the loops, they tended to form bundles, which were repeated throughout the scaffold with relative regularity. The starting point of this occurrence relative to the scaffold edge, and hence the turns, was directly proportional to the collector speed; the faster it was, the longer the length of the fiber where this bundling happened. A possible cause of this phenomenon could be the electrostatic repulsion during fiber deposition, augmented with the acceleration and deceleration effects on the process (Wunner, Wille*, et al.* 2018).

Upon closer inspection under higher magnification with the stereomicroscope (**Figure 3.2 right column**), printing with a speed of 500 mm/min, resulted in fiber sagging between the intersections with other fibers, albeit while having a straight deposition path. The most regular and uniform scaffolds were obtained with a speed of 750 mm/min. With a speed of 6000 mm/min, the stacking of fibers forming walls tended to be less than that observed with slower speeds. In that group, the fibers could also be observed suspended between intersections (**Figure 3.2O**). MEW fibers were shown to suspend across gaps when the collector speeds were sufficiently high to overcome the sagging effect (Hrynevich *et al.* 2018).

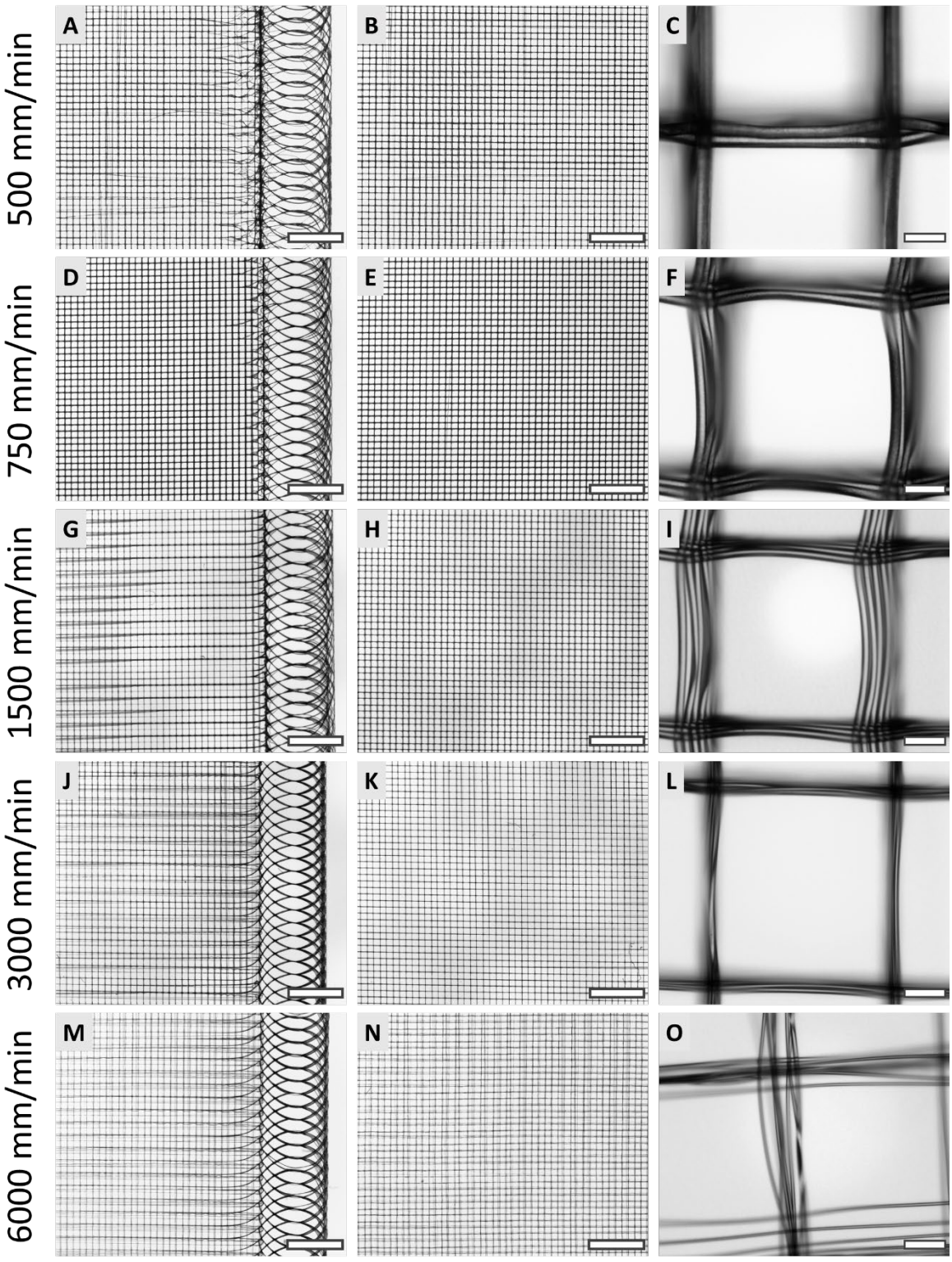

Figure 3.2. Stereomicroscopic examination of the different scaffold groups. (A-C) 500 mm/min. (D-F) 750 mm/min. (G-I) 1500/min. (J-L) 3000 mm/min. (M-O) 6000 mm/min. Left and middle column represent low magnification images with scale bars of 2 mm. Left column demonstrates the turn loops. Right column represents a higher magnification view with scale bars of 50 µm.

3.3.2 Fiber diameter measurement

As expected, the collector speed was inversely proportional to the fiber diameter. The maximum diameter measured was in the 500 mm/min group with a value of 17.1 ± 0.66 µm and on the other side of the spectrum, the least measured one was 4.2 ± 0.41 µm at a speed of 6000 mm/min. **Table 3.1** summarizes the diameters and masses of all experimental groups. All measurements were done with the stereomicroscope and the Zeiss Zen Pro 2012 software on at least three different scaffolds, each on ten different fibers (n ≥ 30). **Figure 3.3A** shows a graphical representation of the measured diameters in all scaffold groups.

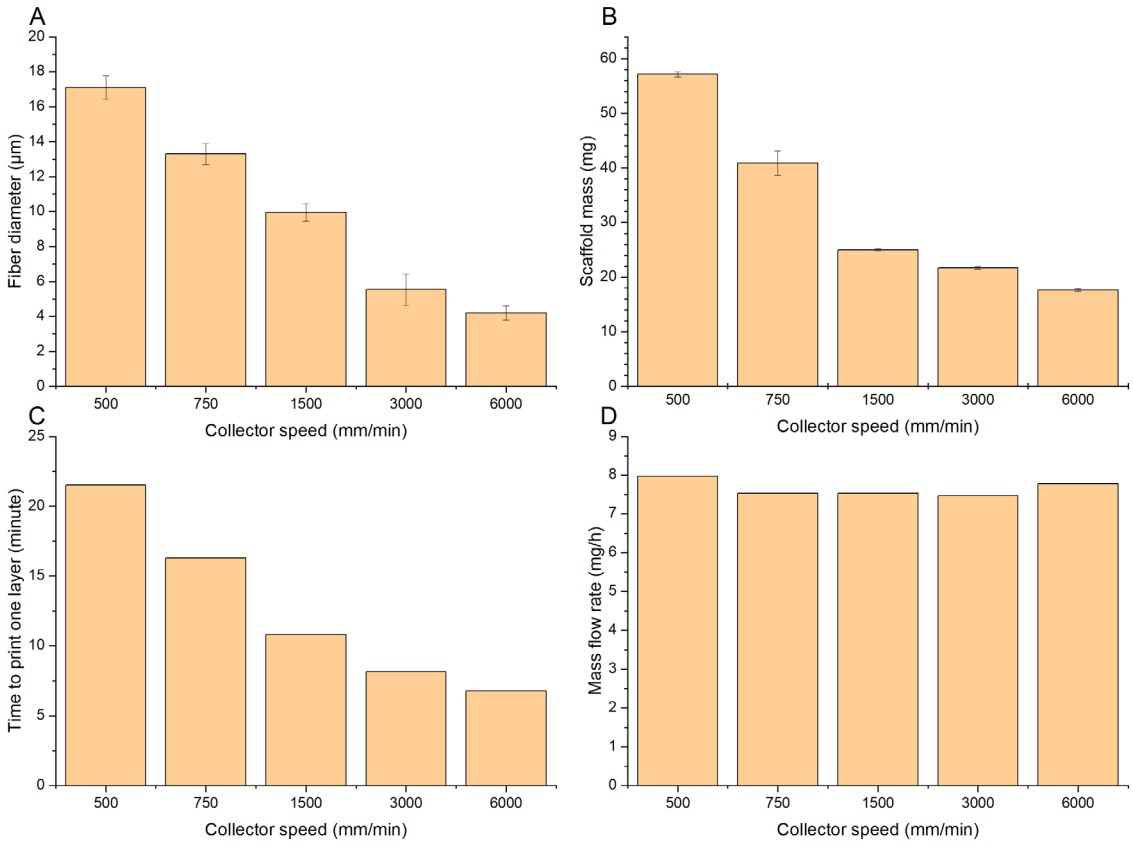

Figure 3.3. Graphical analysis of measured scaffold properties. (A) Fiber diameter. (B) Scaffold mass. (C) The amount of time needed to print a single layer in a scaffold. (D) Calculation of the mass flow rate by dividing the mass from (B) by the time needed to print the whole scaffold (calculated by multiplying (C) times the number of layers in the scaffold (10 layers)).

3.3.3 SEM examination

Only the 500, 750, 1500 and 6000 mm/min scaffolds were examined by the SEM (**Figure 3.4**). In case of the 6000 mm/min scaffolds, the thin fiber diameters presented a challenge for handling, which lead to scaffold damage during preparation for SEM visualization. Using the SEM, fiber diameters were categorically compared against the fiber diameter data obtained from the stereomicroscope. The fibers formed slightly flattened cylinders and showed little to no fusion between each other. The images were always taken from the middle of the scaffold, and those where the fibers showed accurate stacking in all the examined groups. While all groups showed a form of fiber sagging between the intersections of the fibers, the effect was more exaggerated in the 500 mm/min group. The smooth surface of the fibers showed the spherulite structure (representing a crystalline region; indicated in **Figure 3.4E**) of PCL, especially in the 500 mm/min group.

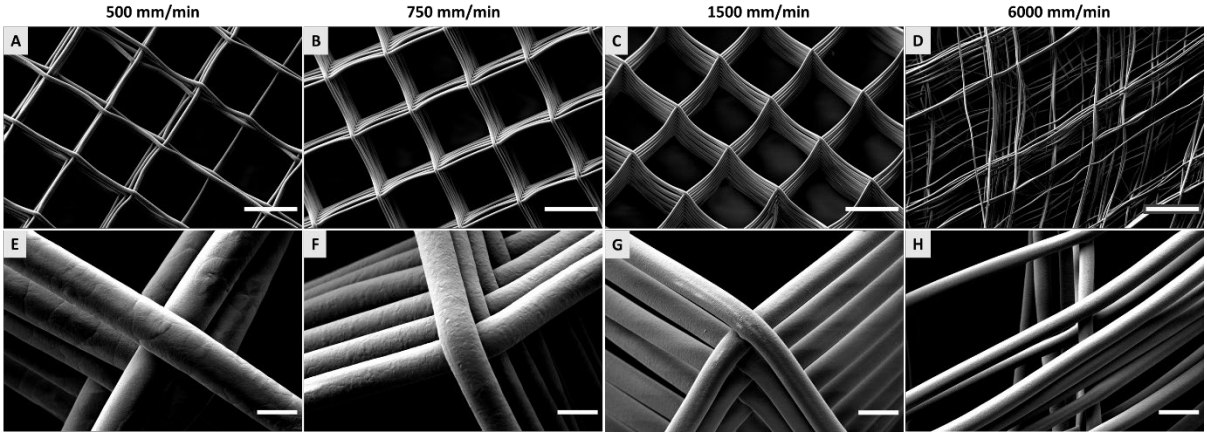

Figure 3.4. Scanning electron microscopy (SEM) images of scaffolds from four of the five investigated collector speeds. (A&E) 500 mm/min. (B&F) 750 mm/min. (C&G) 1500 mm/min. (D&H) 6000 mm/min. The 500 mm/min scaffolds show fiber sagging and PCL spherulite structures under higher magnification. Both the 750 and 1500 mm/min resulted in regular scaffolds with thinner fibers. Increasing the speed up to 6000 mm/min resulted in thinner fibers, fiber suspension at intersections and irregular fiber deposition away from the targeted walls. Image (C) was previously published in (Dalton 2017), reproduced with permission from Elsevier. All SEM images were taken by Dr. Claus Moseke.

3.3.4 Mass measurements

For the purpose of this study, the masses of the 2x10 layer scaffolds were weighed using a sensitive balance and compared (**Figure 3.3B**). The results showed that by decreasing the collector

speed, a larger fiber diameter is achieved, leading to an increase in the mass of the scaffold, provided the number of layers was kept constant.

Table 3.1. Summary of measured scaffold properties.

Measurement		Collector speed (mm/min)				
		500	**750**	**1500**	**3000**	**6000**
Fiber diameter (µm)	**Average**	17.1	13.3	10	5.53	4.2
	SD	0.66	0.6	0.5	0.89	0.41
Scaffold mass (mg)	**Average**	57.14	40.1	25	21.68	17.63
	SD	0.5	2.23	0.22	0.21	0.21

3.3.5 Mass flow rate calculation

In order to measure the mass flow rate, the time taken to print the scaffolds needed to be measured. For this, we measured the time taken to complete one full layer in the 0/90° laydown pattern (2x1 layers) (**Figure 3.3C**). The time measured was then multiplied by the number of layers in the scaffold (10 layers). It should be noted that this method of measurement also included the amount of time needed to complete the turn loops, in addition to the introduced pauses so that the printing quality is maintained.

The mass of the 2x10 layer scaffolds was divided by the time taken to print them. There was no change in the mass flow rate when the collector speed was increased (**Figure 3.3D**). This meant that increasing the collector did not result in the pulling of more material from the nozzle, but rather the increased speed led to more dragging of the polymer in the Taylor cone, which resulted in thinner fibers, but without the extrusion of more material. This result was in accordance with what Brown *et al.* described (Brown *et al.* 2011), when they kept the flow rate and other printing parameters constant, except the collector speed, they achieved thinner fibers. In the current experiment, there was no means to tell what the flow rate was beforehand (i.e. as an experimental parameter that can

be individually set). This could mean, that in the current MEW setup, where the polymer was pressed by a computer-controlled pneumatic pressure system, the flow rate of the melt did not depend on the collector speed and the dragging of the molten polymer jet.

3.4 Conclusion

The current experiment showed that the collector speed in MEW is an independent parameter which affects the fiber diameter, as well as morphological features. Printing below the CTS results in fiber features like coiling and sinusoidal configuration (Hochleitner, Chen*, et al.* 2018, Brown *et al.* 2011). When other printing parameters are kept constant, changing the collector speed did not result in a change in the mass flow rate of the polymer melt at the nozzle. While not applicable for polymer melts, the Hagen-Poiseuille equation could paint a picture on the candidate factors responsible for a change in the mass flow rate, namely; viscosity of the melt, length and diameter of the nozzle and the feeding pressure (Hochleitner *et al.* 2016).

Achieving complex, precise and customizable scaffolds are among the strengths of MEW and to provide quality scaffolds, the occurrence of fiber abnormalities needs to be prevented, as such an occurrence will result in unusable scaffolds, especially when the defect is located centrally. The characterization of the other mentioned parameters on the mass flow rate, and hence, the printing quality and fidelity, will need to be further assessed.

Chapter 4

This chapter was previously published as:

Youssef, A., Hrynevich, A., Fladeland, L., Balles, A., Groll, J., Dalton, P. D., Zabler, S. (2019). "The Impact of Melt Electrowritten Scaffold Design on Porosity Determined by X-Ray Microtomography." Tissue Eng Part C Methods **25**(6): 367-379. DOI: 10.1089/ten.TEC.2018.0373

Abstract: "Melt electrowriting (MEW) is an additive manufacturing technique using thermoplastic polymers to produce microscale structures, including scaffolds for tissue engineering. MEW scaffolds have, in general, high porosities and can be designed with different fiber diameters, spacings and laydown patterns. The need for a reliable method for scaffold characterization is essential for quality assurance and research purposes. Here we describe the use of sub-micrometer X-ray tomography for the generation of local thickness maps of volume porosity of 16 different scaffold groups, comprising of two diameter groups, two fiber spacing groups and four different laydown patters (0/90°, 0/60/120°, 0/45/90/135° and 0/30/60/90/120/150°), all made using a custom-built MEW printer with medical-grade poly(ε-caprolactone). The results showed a porosity range between 77.7 and 90.7% for all the scaffolds. Moreover, the influence of the scaffold regularity and flatness in the more regular pore shapes (0/90°, 0/60/120°) lead to the shift of the local thickness graph to one side, and thus the prevalence of one pore size. This non-destructive method for MEW scaffold characterization overcomes the limitations of microscopic methods of pore shape and size estimation."

The text of this chapter was edited, updated and extended with new, unpublished experiments, while the abstract above is quoted from the original publication, under the Creative Commons CC-BY-NC license. The publication has been cited a total of 6 times (Google Scholar; accessed 12.12.2020)

4.1 Introduction

The fabrication of three-dimensional (3D) scaffolds is a cornerstone of tissue engineering (TE) (Langer and Vacanti 1993, Hutmacher 2000). The scaffold acts as an artificial temporary support structure, which can act by itself to replace lost tissue parts or be seeded with cells or coated with effector molecules to cause a biological effect (Hutmacher 2000). These scaffolds are used within the field of TE both *in vitro* and *in vivo*. Based on the biomaterial selection and what the intended usage of the final product is, there has been, over the past few decades, many different fabrication methods to produce 3D scaffolds with a porous structure which can function as TE scaffolds (Moroni *et al.* 2018). However, in recent years and with the introduction of additive manufacturing (AM) concepts, the focus has shifted to defined, customizable and reproducible scaffolds (Dalton *et al.* 2020, Sharma *et al.* 2018). The production of such scaffolds through AM approaches represents several challenges to long established regulatory pathways and supply chains inside healthcare facilities, which are still based on a 20thCentury concepts of medical devices. The regulatory framework of the US Food and Drug Administration towards medical devices and a discussion of the application of AM technologies towards the production of patient-specific, safe and regulated medical devices were thoroughly given in Chapter 2 (Youssef *et al.* 2017).

Porous scaffolds aim to mimic the tissue structure by substituting for the extracellular matrix (ECM), which is a complex, fibrous network responsible for several biological functions and the formation of cell niches (Hynes 2009). Several methods were used to produce TE scaffolds using traditional manufacturing methods, e.g. electrospinning (Agarwal *et al.* 2009), salt leaching (Hou *et al.* 2003), gas forming (Salerno *et al.* 2009), phase separation (Guan *et al.* 2005) or sphere templating (Marshall and Ratner 2005), or AM techniques, e.g. micro-extrusion (Bartnikowski *et al.* 2014), stereolithography (Melchels, Bertoldi*, et al.* 2010), selective laser sintering (Roosa *et al.* 2010) and melt electrowriting (MEW) (Powell *et al.* 2014). The architectural design of the scaffold directly affects physical parameters of the scaffold, provided that the AM technique is of high enough resolution, such

as total porosity, pore size and interconnectivity and scaffold surface area (Melchels, Barradas*, et al.* 2010, Fuller *et al.* 2016). These parameters need to be quantified as a quality control method for the produced scaffolds, but it is often the case that they are difficult to be quantified (Ho and Hutmacher 2006). Several authors have proposed quantification methodologies to overcome these challenges, however, each method has its resolution and feature size limits (Ho and Hutmacher 2006, Lin *et al.* 2003, Loh and Choong 2013).

MEW produces flexible, structured, highly porous, customizable scaffolds, with precise and uniform fibers (Robinson *et al.* 2019), typically between 2 and 50 µm (Hrynevich *et al.* 2018) but can be as little as 820 nm (Hochleitner *et al.* 2015). The customizability of the scaffolds makes MEW suitable for many applications, whether as flat sheets for cell seeding *in vitro* experiments (Muerza-Cascante *et al.* 2015) and up to tubular constructs to be used in critical-sized bone defects in rodents (Gonzalez-Gil *et al.* 2019). The printing parameters control the overall morphology of the scaffold, through physical properties such as fiber diameter, spacing and laydown pattern. When parameters are optimized, scaffolds with different morphologies, porosities and pore shapes can be fabricated in a reproducible and customizable manner. The printing parameters can be tailor-made to have an effect on the mechanical properties of the scaffolds, opening the door to a plethora of applications (Bas, D'Angella*, et al.* 2017, Saidy *et al.* 2019, Liashenko *et al.* 2020).

In the published MEW literature, the 0/90° laydown pattern has been the most-used approach. This laydown pattern gives pores shaped like regular boxes with open base and top. The lateral walls of the box are made of fibers and the vertices are the intersections, or interdigitation of the fiber walls in the two laydown paths (Hochleitner *et al.* 2016, Tourlomousis *et al.* 2017, Wunner, Wille*, et al.* 2018). Another reported laydown pattern is the 0/60/120° one, where the pores are shaped like isosceles triangles (Bas *et al.* 2015, Farrugia *et al.* 2013, Tylek *et al.* 2020). When spacing is kept constant between the fibers in these box- and triangular-shaped pores, the result is a regular scaffold with a predictable architecture and a straightforward quality assessment method (Castilho,

Hochleitner*, et al.* 2018). The investigator will need to examine the scaffolds for the regularity of the pores, to have an overall view of the production fidelity. These symmetric and simple approaches to produce a structured scaffold do not simply correspond to how complex the ECM is, where pores are heterogeneously sized and arranged (Hynes 2009).

While MEW is capable of the fabrication of complex-shaped scaffolds with different laydown patterns, these produced scaffolds require a method of characterization that can describe and quantify the shape and size of the pores. Quality assurance is an important aspect of process validation with the ultimate aim of having a process and a product that can pass regulatory requirements for the production of medical devices under Good Manufacturing Process (GMP) (Hollister 2009a). Recent progress in MEW-related research led to in-process control and quantification by being able to inspect the fibers being printed and modify the printing parameters when and as needed (Wunner, Mieszczanek*, et al.* 2019). MEW also adds the possibility of multimodal scaffolds with a spectrum of different diameters with a single nozzle during a single print by changing the pressure (Hrynevich *et al.* 2018).

While MEW scaffolds had a general upper limit of a few millimeters thickness, it was only recently that this limit was overcome and scaffolds up to 7 mm in thickness were fabricated with MEW through dynamic parameter adjustment (Wunner, Wille*, et al.* 2018). However, the impression that MEW scaffolds are “flat” objects, led to many authors characterizing the pore size in such scaffolds with methods that generate two-dimensional (2D) images, e.g. stereomicroscopy or scanning electron microscopy (SEM) (Hochleitner *et al.* 2016). These 2D images are unsuitable for the analysis of complex 3D structures, and only report on the vertical pore size when looked at from an axial plane. Other methods like confocal microscopy have restrictions on how deep they can image (Shah *et al.* 2017). A promising technique that would alleviate these problems in a non-destructive way is the use of X-ray microtomography (μCT) for the quantitative analysis of volume porosity in MEW scaffolds.

Through the use of µCT, it is possible to capture the entire thickness of a typical MEW scaffold with micrometer accuracy within a field-of-view (FOV) which can reach several cubic millimeters (Hanke *et al.* 2016). Through the volume image analysis with modern software tools, the calculation of the average porosity, together with the quantification of several porosity-based properties, e.g. the distribution of local pore spaces, is now possible (Bradley *et al.* 2017). These quantification data make it possible to understand the available space for cell seeding in *in vitro* experiments as well as that for cellular infiltration in *in vivo* ones (Bradley and Withers 2016).

In this study, we investigate the use of µCT for the quantification of structural parameters of porosity in symmetric, highly ordered MEW scaffolds, while conducting a 2D stereomicroscopic image analysis to show the limits of such technique. The accuracy of the µCT methodology needed to be verified and the limits of spatial resolution for the technique needed to be investigated. Finally, after the accuracy of the determination of total porosity was verified, the influence of three different printing parameters were investigated, namely, fiber laydown pattern, diameter and spacing on porosity related parameters in 16 different scaffold types.

4.2 Materials and methods

4.2.1 Scaffold design and fabrication

The MEW setup used here is the same one described in Chapter 3. Briefly, a custom-made MEW printer was used for the scaffold fabrication as previously described (Hochleitner et al., 2016). Medical-grade poly(ε-caprolactone) (PCL) (PURASORB PC 12, lot number 1412000249, 03/2015, Corbion, Gornichem, The Netherlands) was heated to 73 ± 1 °C in a disposable plastic syringe with a 22G flat-tipped nozzle (both from Nordson EFD Deutschland GmbH, Pforzheim, Germany) under computer-controlled pneumatic pressure. The polymer was stored at -80 °C after aliquoting under argon atmosphere in a glove box. A positive voltage was applied to the nozzle while a negative one was supplied to the stainless-steel movable, computer-controlled collector. The net voltage value is the one provided in **Table 4.1**. Both the pressure and voltage differed between the different scaffold groups.

Table 4.1. Summary of different scaffold fabrication parameters. Due to the difference in diameter between both target diameter groups, the conditions had to be changed to fabricate scaffolds with the designed morphological properties of certain fiber spacings and laydown patterns.

Target diameter (µm)	Pneumatic pressure (bar)	Applied voltage (kV)	Collector distance (mm)	Collector speed (mm/min)
10	0.4	4.5	2.5	600
20	1.2	6	3.5	400

The scaffolds were designed to study the effect of fiber diameter, spacing and laydown pattern on porosity and pore size. Through adjusting the printer parameters, the target fiber diameter was either 10 µm or 20 µm. **Table 4.1** summarizes the printing parameters needed to fabricate the scaffolds with the different target diameters. The other two studied factors, fiber spacing and laydown pattern, did not require changes to the printing parameters, but rather changes to the G-Code to enable the changed collector movement. A sample G-Code file is listed in **Appendix 1**. To show the

effect of pore size on the scaffold morphology, two fiber spacing values were selected, 125 and 250 µm. Finally, to demonstrate the effect of pore shape, scaffolds with fibers in four different laydown patterns: 0/90°, 0/60/120°, 0/45/90/135° and 0/30/60/90/120/150° were printed.

Table 4.2. Scaffold nomenclature system. The scaffold naming system is derived from its shape, with a grouping of four different scaffolds with different laydown patterns in four different groups with different fiber diameters and spacings. Reproduced from (Youssef *et al.* 2019) under the Creative Commons CC-BY-NC license.

Scaffold	Laydown pattern (°)	Target fiber diameter (µm)	Fiber spacing (µm)	Layer count
10-125-2x5L	0/90	10	125	2x5 layers
10-125-3x4L	0/60/120	10	125	3x4 layers
10-125-4x3L	0/45/90/135	10	125	4x3 layers
10-125-6x2L	0/30/60/90/120/150	10	125	6x2 layers
10-250-2x5L	0/90	10	250	2x5 layers
10-250-3x4L	0/60/120	10	250	3x4 layers
10-250-4x3L	0/45/90/135	10	250	4x3 layers
10-250-6x2L	0/30/60/90/120/150	10	250	6x2 layers
20-125-2x5L	0/90	20	125	2x5 layers
20-125-3x4L	0/60/120	20	125	3x4 layers
20-125-4x3L	0/45/90/135	20	125	4x3 layers
20-125-6x2L	0/30/60/90/120/150	20	125	6x2 layers
20-250-2x5L	0/90	20	250	2x5 layers
20-250-3x4L	0/60/120	20	250	3x4 layers
20-250-4x3L	0/45/90/135	20	250	4x3 layers
20-250-6x2L	0/30/60/90/120/150	20	250	6x2 layers

For more clarity, the scaffold nomenclature from now on is based on their architecture, with the first number indicating the targeted fiber diameter, the second number the fiber spacing, and the

last two numbers being the number of fiber rotations in a single repeat of the scaffold and the number of total repeats in the whole scaffold (e.g. 10-250-3x4L). **Table 4.2** outlines the nomenclature of the 16 different scaffold types investigated in this study and **Figure 4.1** shows schematic illustrations of the four different laydown patterns (done by Mr. Andrei Hrynevich), these served as guidelines when writing the G-Code. Apart from the 2x5L scaffolds, the number of layers in the all the other scaffolds was kept at 12 layers in total (3x4, 4x3 and 6x2 all equal 12). The base G-Code prior to editing was originally written by Mr. Andrei Hrynevich and adopted to the current experiment.

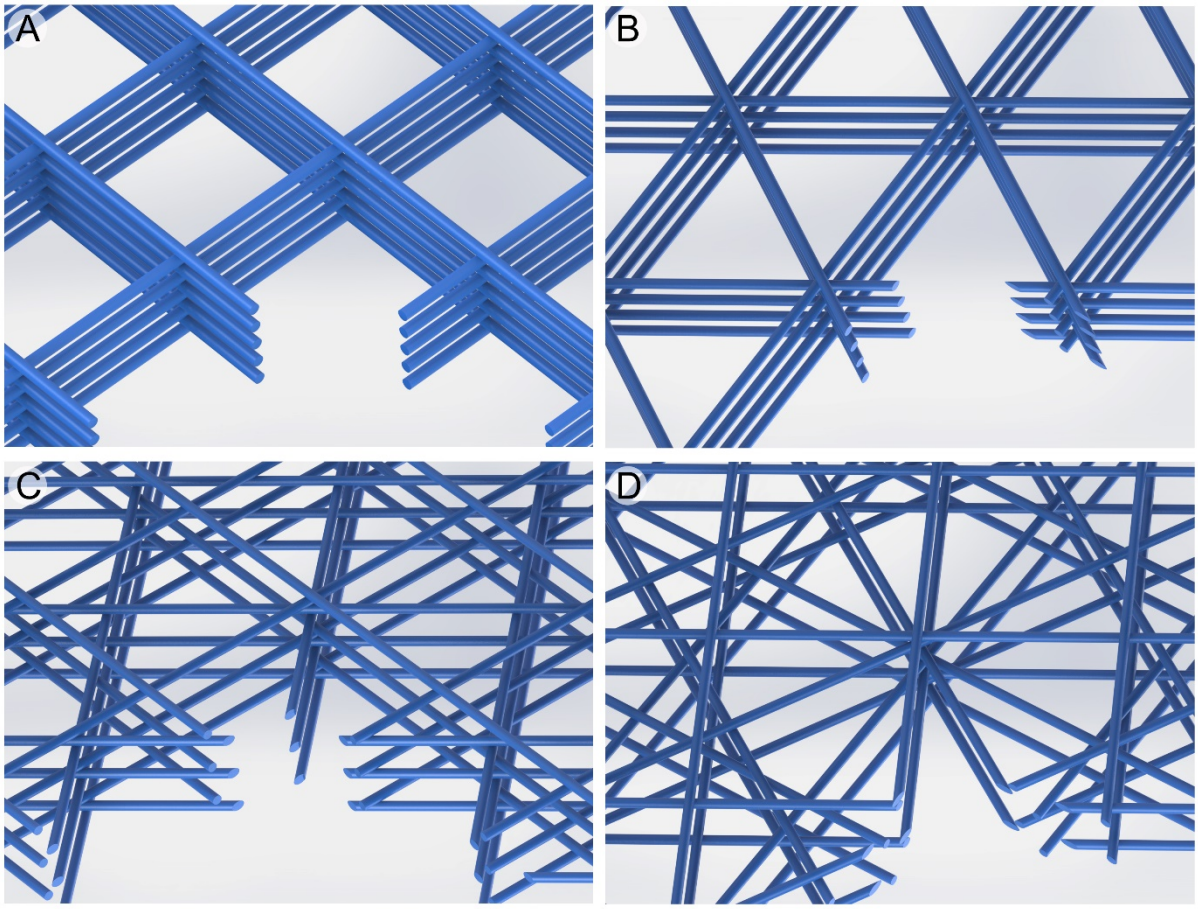

Figure 4.1. Computer renderings of the four different fiber laydown patterns. (A) 0/90° (2x5L), (B) 0/60/120° (3x4L), (C) 0/45/90/135° (4x3L) and (D) 0/30/60/90/120/150° (6x2L). Reproduced from (Youssef *et al.* 2019) under the Creative Commons CC-BY-NC license. Renderings were done by Mr. Andrei Hrynevich.

After fabrication, the scaffolds were sprayed with absolute ethanol to facilitate separation from the stainless-steel collector, then stored in plastic Petri dishes and sealed with Parafilm until used. Before collection, the scaffolds were checked with a Zeiss stereomicroscope (Discovery V20, Carl

Zeiss Microscopy GmbH, Göttingen, Germany) for defects like fiber pulsing. Fibers with visible defects were discarded.

4.2.2 Scanning electron microscopy (SEM)

A Zeiss Crossbeam 340 SEM (Carl Zeiss Microscopy GmbH, Göttingen, Germany) was used for the qualitative and quantitative analysis of the scaffold micro-structure and morphology. The scaffolds were mounted on aluminum stubs and glued with conductive tape (both from Plano GmbH, Wetzlar, Germany). Prior to SEM visualization, the scaffolds were sputter coated with a layer of 4 nm of platinum using a Leica EM ACE600 sputter coater (Leica Microsystems GmbH, Wetzlar, Germany). The SEM preparation steps were previously reported in detail (Hochleitner *et al.* 2016). Ten different scaffolds from each diameter group were imaged and the diameters of ten different random fibers per scaffold were (n=100). SEM imaging was performed by Mr. Andrei Hrynevich.

4.2.3 2D image analysis

Although SEM images have higher magnification and are better resolved than stereomicroscope ones, but they have a lower FOV. Pore size analysis using 2D stereomicroscopic images of the scaffolds was done using the open-source software package Fiji (Schindelin *et al.* 2012), which is a modification of ImageJ (Abràmoff *et al.* 2004). The base ImageJ version underneath was v1.52p (National Institute of Health, USA). From each of the 16 different scaffold groups, three scaffolds were imaged and from each, three different images were taken from the scaffold center with a polarizer-equipped 0.63x lens using a Zeiss AxioCam ICc 5 color camera (Carl Zeiss Microscopy GmbH, Göttingen, Germany).

In Fiji, the images were converted into binary ones through the application of a threshold. This was followed by the measurement of local thickness, which is a measurement of the diameter of a sphere (here, a circle) that fits inside the pore space, outlined by the thresholding process. An ImageJ macro script was written based on individual measurements and used to batch process the images

from each scaffold group (the ImageJ macro code is listed in **Appendix 2**). The grey value threshold was different among the groups but remained the same inside the group itself. During the optimization of the experiment, it was evident that selecting one threshold for the 16 groups would result in too much or too little closure of the pore space, leading to inaccurate measurements. The measurement outcome was the frequency of diameter measurements of the pores. The images represented 4x3.5 mm rectangular areas of the center of the scaffold.

4.2.4 X-ray microtomography (µCT)

The µCT scans were recorded on a detector-based sub-micrometer custom-built CT scanner which is based on a liquid metal-jet anode and was previously described in detail (Fella *et al.* 2017). Scaffolds were placed in a plastic, radiolucent sleeve to keep them from vibrating and moving during the scan. The voxel sampling in all scans was 2.83 µm/voxel, the volume of interest was a cylinder of 6.1 mm diameter and 7.2 mm height. For simplicity, this scanning mode will be called medium resolution. For evaluating the accuracy of the present method, one scaffold was measured at a very high resolution: 0.53 µm/voxel sampling. However, the FOV at this resolution is much smaller: a cylinder that is only 1.2 mm in diameter and 1.4 mm in height. Initial scaffold scanning was done by Dr. Simon Zabler and Mr. Andreas Balles for the establishment of the methodology. The rest of the samples were scanned by Mr. Logan Faldeland. Detailed description of the imaging protocol and the reconstruction steps for the phase contrast images is available elsewhere (Baranowski *et al.* 2019, Fella *et al.* 2017, Ullherr and Zabler 2015, Youssef *et al.* 2019).

4.2.5 Volume image analysis

A high-resolution X-ray phase contrast image was generated after scanning the region of interest (ROI). To transform into a binary volume image, a global threshold value had to be applied to the pixels which were cast from floating point numbers to 16-bit grey values [0-65535]. The threshold was set to the 50% grey level between fibers and surrounding air. To evaluate the sensitivity of these results on the choice of the grey value, the value of the threshold was changed for all scaffolds by

± 12.5% of the entire grey value interval. The 12.5% range was chosen as an arbitrary number. Changes in total porosity of the scaffold were assessed. The pore size was measured by the generation of a local thickness map of the 3D image stack of each scaffold measured. The image analysis was also performed using Fiji, based on ImageJ v1.52c. For the 3D renderings of the µCT scans, Avizo v9.0 (ThermoFischer, Waltham, Massachusetts) was used. Volume image analysis was done by Dr. Simon Zabler and Mr. Logan Faldeland.

4.3 Results

4.3.1 Scaffold characterization with SEM

The MEW printer parameters used for each of the fiber diameter were previously empirically tested and selected based on previous experience with MEW scaffold fabrication. However, SEM measurement of fiber diameters was performed to verify the actual diameters of the printed scaffolds. The fiber diameter measured using SEM for the 10 µm target group was 11.15 ± 0.45 µm, while for the 20 µm one, it was 22.69 ± 0.52 µm. The direct-written fibers were uniform throughout the scaffolds with no fiber pulsing observed due to the appropriate adjustment and validation of the MEW printer parameters before scaffold production (Hochleitner *et al.* 2016). A collage of representative SEM images of all the 16 different scaffold groups with different fiber diameters, spacings and laydown patterns is shown in **Figure 4.2**. Except for the 20-125-6x2L group, the fibers stacked well upon each other into walls. The accurate placement of fibers within the 20-125-6x2L sample was likely affected by electrostatic attractions towards fibers already deposited (refer to Chapter 3).

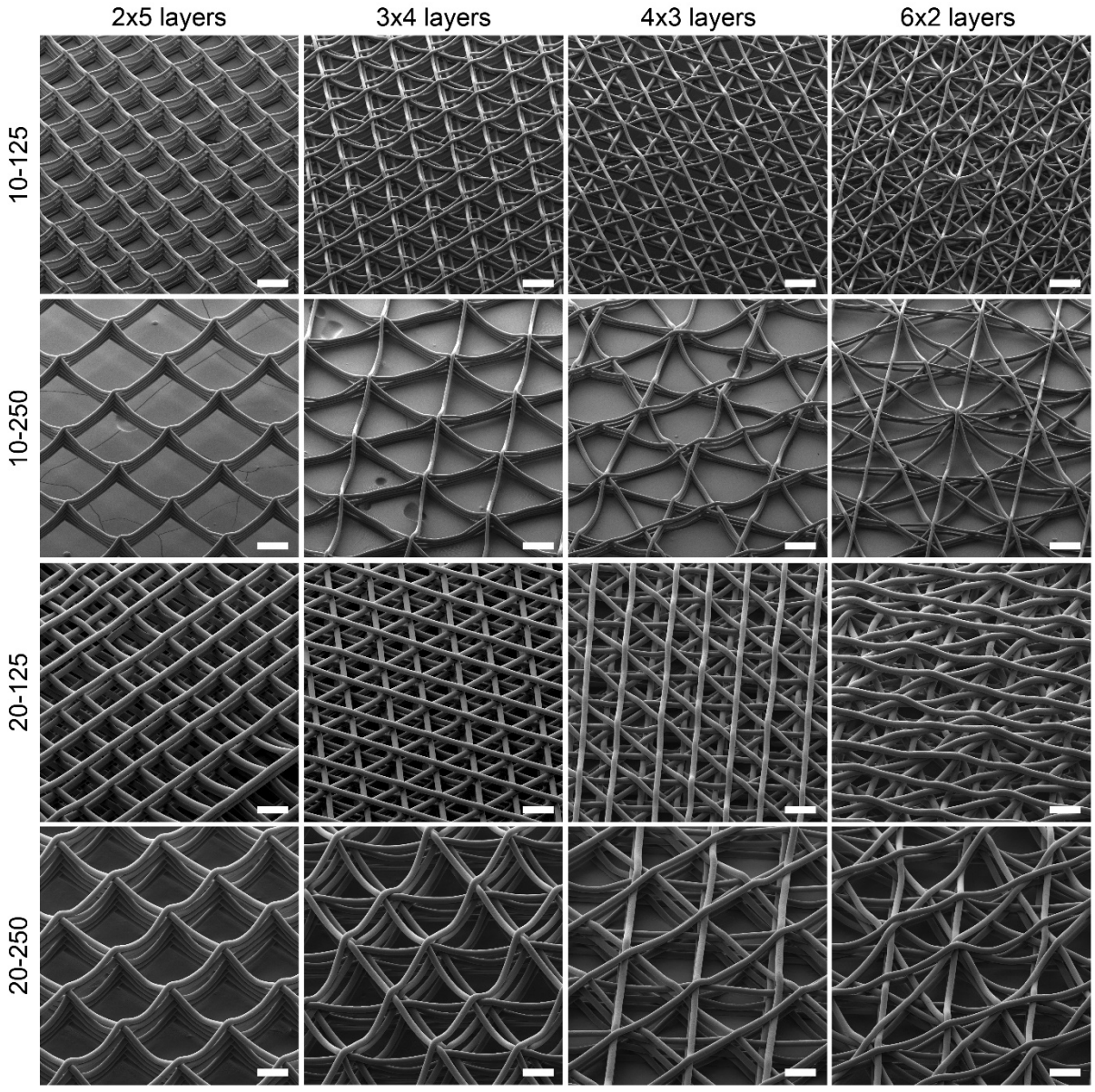

Figure 4.2. Scanning electron microscopy images of the 16 different scaffold types investigated in this study. The different fiber diameters, spacings and laydown patterns are shown. Scale bars are 100 µm. Reproduced from (Youssef *et al.* 2019) under the Creative Commons CC-BY-NC license. Images were taken by Mr. Andrei Hrynevich.

In general, the fibers were regular and round with a smooth surface. The more complex fiber laydown patters (4x3L and 6x2L) had a heterogenous distribution of pore sizes and shapes compared to the more regular ones (2x5L and 3x4L). The 2x5L laydown pattern represented the most regular and reproducible pore shape, followed by the 3x4L one. The center point in the 6x2L scaffolds had the intersection point of the six fibers forming a single repetition (1L) of the scaffold and represented the most regular point. These scaffolds had two repetitions in total, making the central point that of the interdigitation of 12 different fibers stacking in the vertical plane.

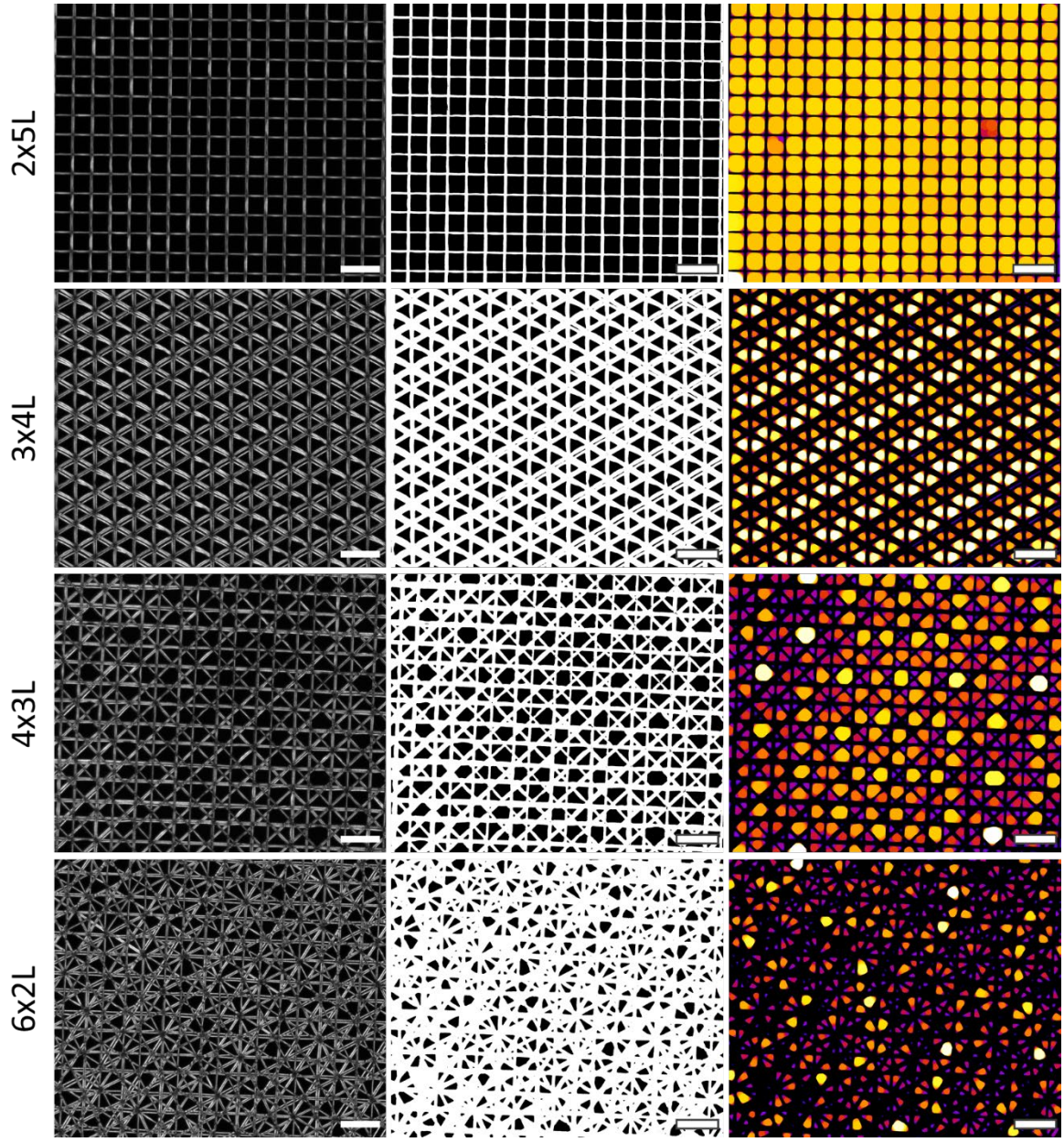

Figure 4.3. Workflow of the two-dimensional local thickness analysis (2D-T_{loc}) of steromicroscopy images. Here is an example of the measurement process in the four different fiber laydown patterns in the 20-250 group. Briefly, stereomicroscopy images (left side) were captured, then converted to a binary image by applying a thresold (middle). The binary image is used to calculate the 2D-T_{loc} of the detected pores. Colour coding of the right column: yellow: large pore, dark blue: small pore, black: scaffold fibers. Scale bars are 500 µm.

4.3.2 2D local thickness measurement (2D-T_{loc})

The stereomicroscope images were taken with a polarizer-equipped lens to create sufficient contrast between the fibers and background, for a more uniform and reproducible thresholding. The local thickness analysis resulted in the diameter of a theoretical sphere (in the case of a 2D image, a circle) that would fit a given pore space. An overview of the measurement workflow is shown in **Figure**

4.3 with all the laydown patterns of the scaffolds of the 20-250 groups. The mean, standard deviation and maximum of 2D-T_{loc} values are listed in **Table 4.3**. **Figure 4.4** shows a graphical summary of the pore size distribution using the 2D measurement method. The selection of the grey value threshold is considered the main source of error in this measurement. A higher value would entail lower 2D-T_{loc} and *vice versa*.

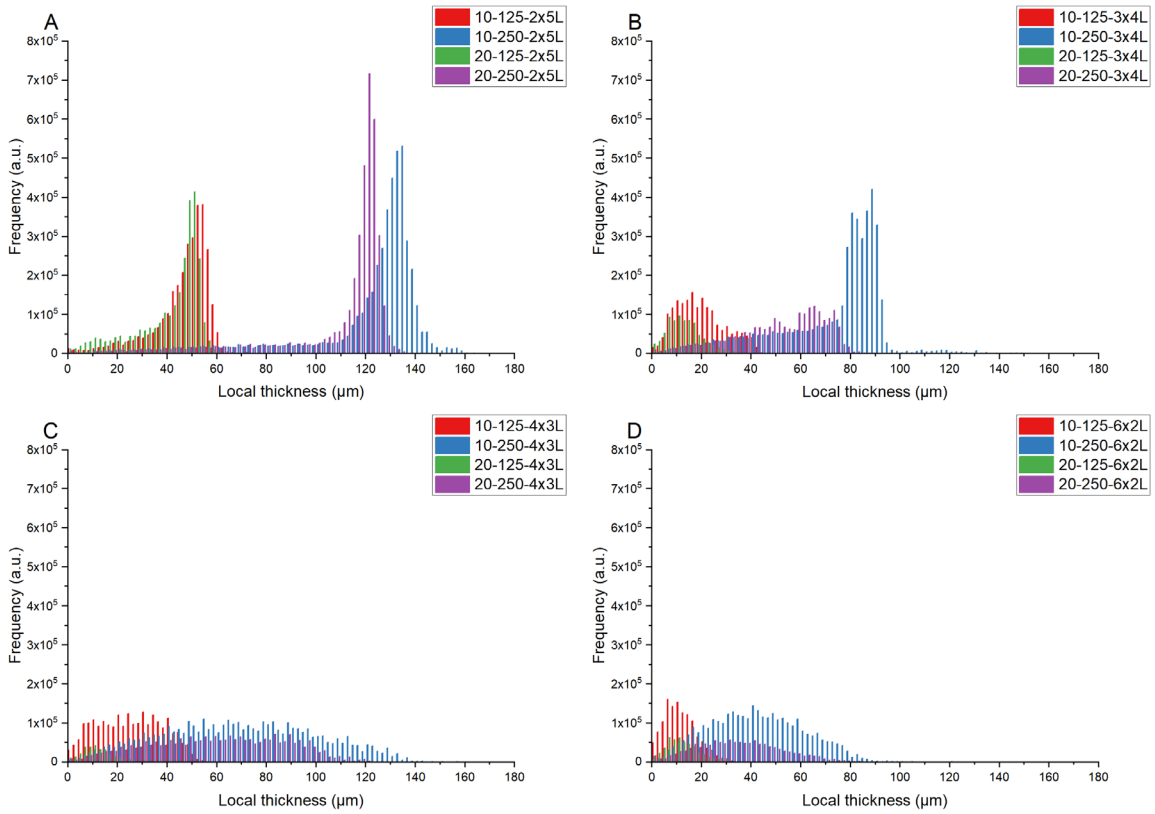

Figure 4.4. Graphical summary of the two-dimensional local thickness measurements for each of the investigated 16 scaffold types grouped under laydown pattern. (A) 2x5L, (B) 3x4L, (C) 4x3L, (D) 6x2L. Each graph shows the four different combinations of fiber diameters and fiber spacings per laydown pattern (10-125, 10-250, 20-125 and 20-250).

4.3.3 µCT scanning of the scaffolds

The µCT imaging of the scaffold resulted in X-ray phase contrast images as shown in **Figure 4.5A**. The data from these images are the basis for the reconstruction and the further analysis of the scaffold morphology. In **Figure 4.5B**, the 20-125-6x2L scaffold is shown from an axial and in a cross-sectional view, as an example of the output of an X-ray phase contrast image. This scaffold type,

based on a dodecagonal unit design, represented the most fiber-dense and irregular one, as previously mentioned.

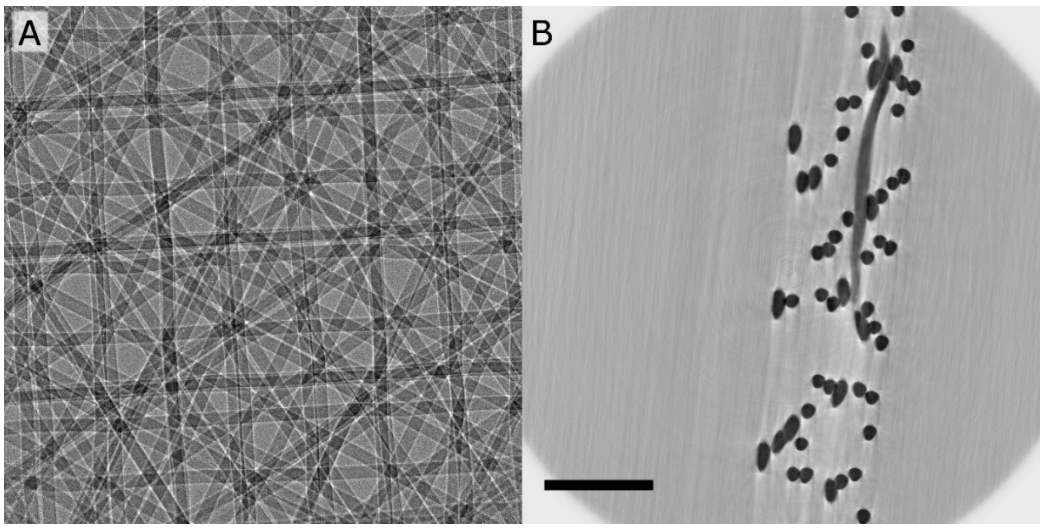

Figure 4.5. X-ray phase contrast imaging of melt electrowritten scaffolds. (A) High-resolution X-ray phase contrast image of a 20-250-6x2L scaffold in flattened view. (B) Axial view of a section of the reconstructed volume image of the same scaffold in (A). Contrast is inverted for better visibility of the scaffold fibers. Scale bar is 200 µm. Reproduced from (Youssef *et al.* 2019) under the Creative Commons CC-BY-NC license. Images were taken by Dr. Simon Zabler.

Figure 4.6 represents 3D graphical renderings from the µCT data of the four laydown patterns in the 20-250 group. Through the rendering, it was possible to visualize, in 3D, the underlying fibers of the scaffolds and observe their ability to stack upon each other, especially in tilted views, which is also technically possible with the SEM but only to a certain depth and is limited by how the sample is mounted inside the SEM vacuum chamber. Excessive tilting of the sample inside the SEM can result in damage to the device and the sample.

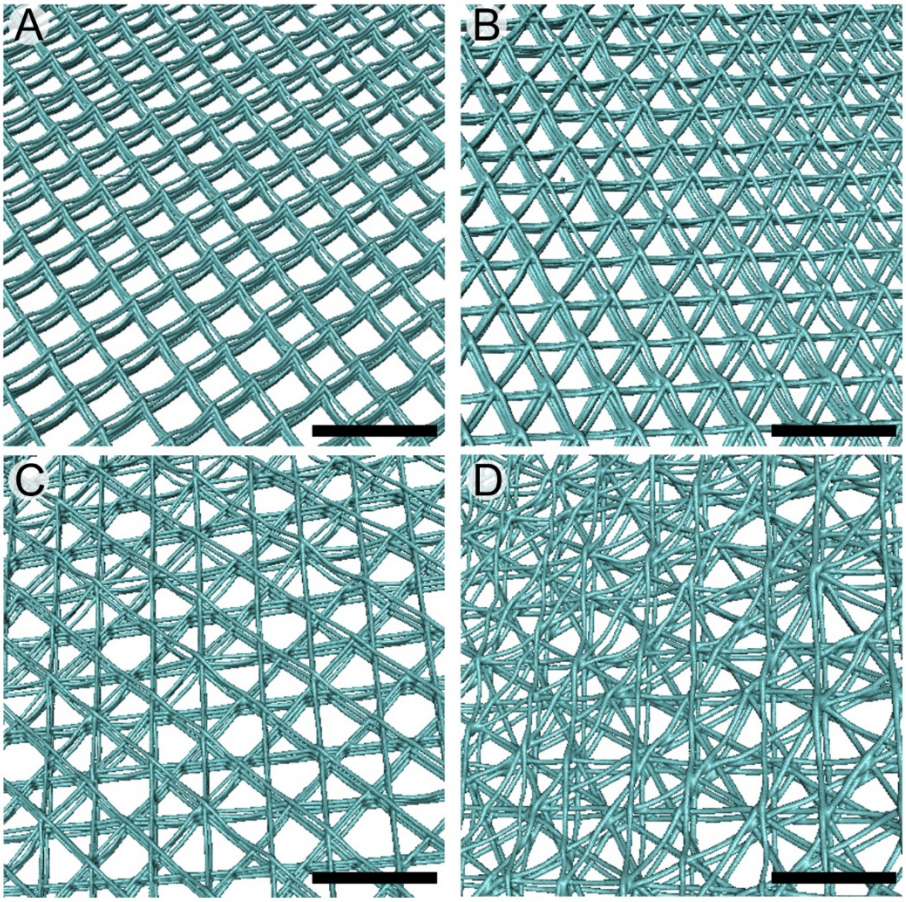

Figure 4.6. Graphical renderings using X-ray microtomography (µCT) scans of the four investigated laydown patterns. All images are from the 20-250 group. (A) 2x5L, (B) 3x4L, (C) 4x3L and (D) 6x2L. Scalebare are 500 µm. Reproduced from (Youssef *et al.* 2019) under the Creative Commons CC-BY-NC license. Renderings were generated by Dr. Simon Zabler.

4.3.4 Porosity calculation

Once the binary volume image was set, part of the scanned volume (V_0) (which is a volume mask of the volume of the space between the upper- and lowermost borders in a cross section of the MEW scaffold, i.e. excluding the air above and below the scaffold), which also included the volume of the fibers (V_F) and on which total scaffold porosity (P_{tot}), needed to be defined and calculated through the following equation:

$$P_{tot}=(V_0-V_F)/ V_0 \,.\, 100\% \quad (1)$$

Defining V_0 was achieved through a binary closing operation. The result of this process is illustrated in **Figure 4.7**, where the scaffold and surrounding space are shown, followed by the closing of the open spaces on the upper and lower borders of the scaffold and finally the generation of local

thickness map. This process was optimized and evaluated for the different scaffold groups on account on the different fiber diameter and spacing, and hence, the complexity. These optimizations when changed had no more than a difference in 2% in the value of P_{tot} (Youssef *et al.* 2019).

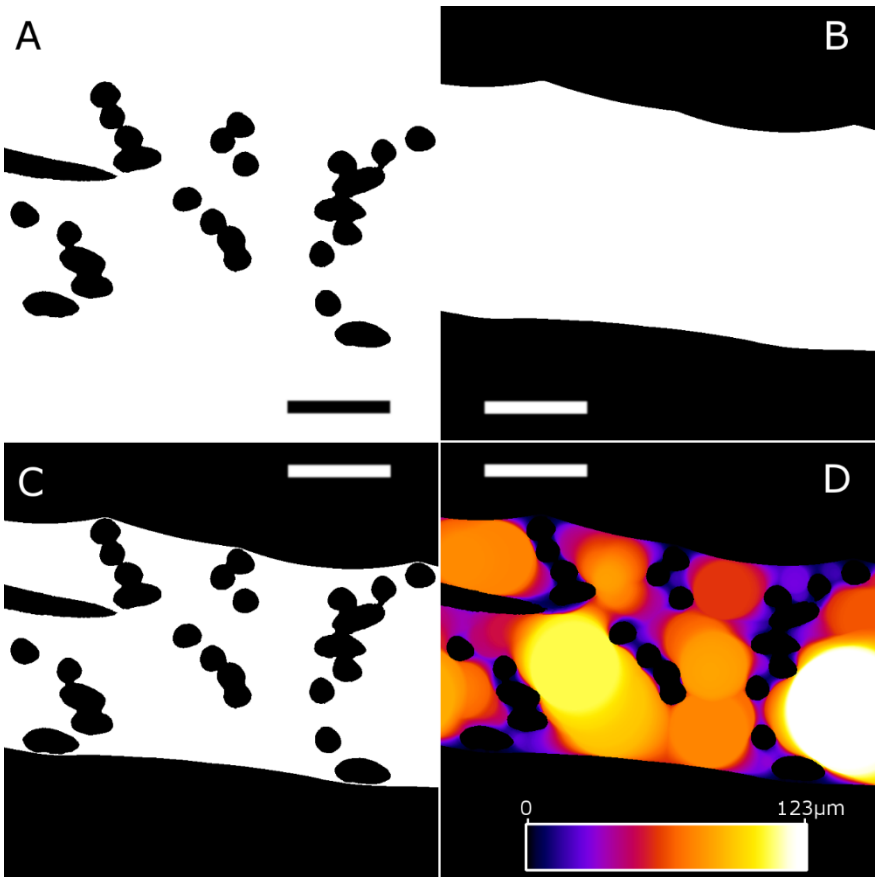

Figure 4.7. Workflow of the three-dimensional local thickness analysis (3D-T_{loc}) of reconstructed X-ray microtomography (µCT) scans. All images represent the same 20-125-6x2L scaffold. (A) A binary volume image of the scaffold in axial view highlights the position of the fibers inside the scaffold. (B) A mask is created by binary closure to remove empty volume above and below the scaffold. (C) The binary volume image and the mask are superimposed on each other to create a pore volume image. (D) Local thickness analysis is performed to display the sphere with the largest diameter that would fit a given pore space. Scale bars are 100 µm. The color scale for local thickness is linear and ranges from 0 to 123 µm. Reproduced from (Youssef *et al.* 2019) under the Creative Commons CC-BY-NC license. Images were taken by Dr. Simon Zabler.

4.3.5 Total porosity of the different scaffolds

Using a 50% grey value threshold between the fibers and air (**Figure 4.8A**), the calculation of P_{tot} ranged between a maximum of 90.7% for the 10-250-2x5L scaffold and a minimum of 77.7% for 10-125-6x2L. By changing the grey value threshold by ± 12.5%, the resulting change in P_{tot} was to be regarded as the upper and lower limits of the scaffold porosity measurement. **Figure 4.8D** shows these

changes as the error bars in the graph. The choice of the grey value threshold was the principle source of error in the current study.

Despite these perceived subjectivity in the measurement, **Figure 4.8D** shows that the least dense scaffolds (10-250 group) had the largest porosity whereas the densest (20-125 group) had the lowest. In terms of laydown patterns, the most regular (2x5L) scaffolds had the largest values of P_{tot}, whereas the group with the most complex structure (6x2L group) yielded the smallest value for every fiber spacing and fiber diameter groups. The two intermediate structures (4x3L and 3x4L) featured very similar values of P_{tot}, which was between the two values of those of the 2x5L and 6x2L groups. There was a slight tendency of 4x3L scaffolds towards having larger porosities in the 20-250 group, compared with the 3x4L ones.

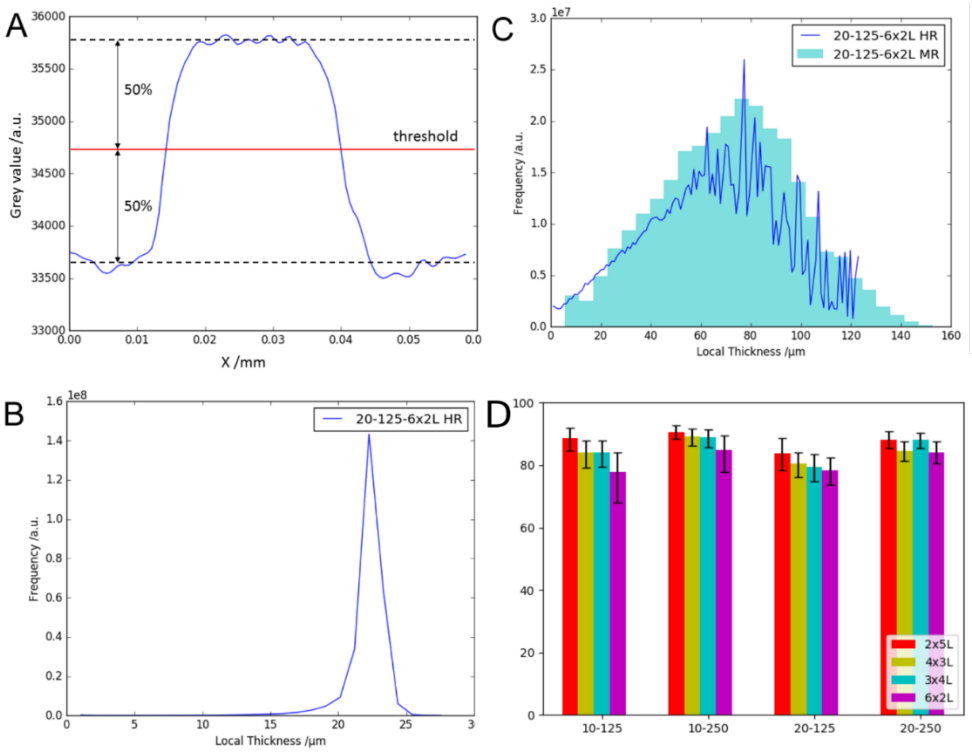

Figure 4.8. (A) Grey value range over a single PCL fiber. For binary segmentation, the selected grey value threshold is set to 50% of the range. (B) Applying the local thickness (3D-T_{loc}) analysis to the fiber instead of the pores can be used to measure the fiber diameter. (C) An overlap of 3D-T_{loc} of a 20-125-6x2L scaffold measured using high resolution (HR, line plot) on a medium-resolution (MR, histogram) one. Reproduced from (Youssef *et al.* 2019) under the Creative Commons CC-BY-NC license. Graphs were made by Dr. Simon Zabler.

4.3.6 3D local thickness measurement (3D-T_{loc})

Compared to the measured 2D-T_{loc}, the corresponding 3D variant was 3D-T_{loc} and is computed using the pore volume shown in **Figure 4.7C**. To every detected pore, the diameter of the largest sphere which could fit that space was measured (**Figure 7D**). The diameter of these spheres was given in voxels and was converted from voxels to micrometer by multiplying by the voxel size in micrometer, which was 2.83 for medium and 0.53 for high-resolution scans. **Figure 4.9** is a graphical representation of the 3D-T_{loc} of all 16 scaffold variants. **Table 4.3** summarizes 3D-T_{loc} for all scaffold types (as well as total porosity and 2D-T_{loc}).

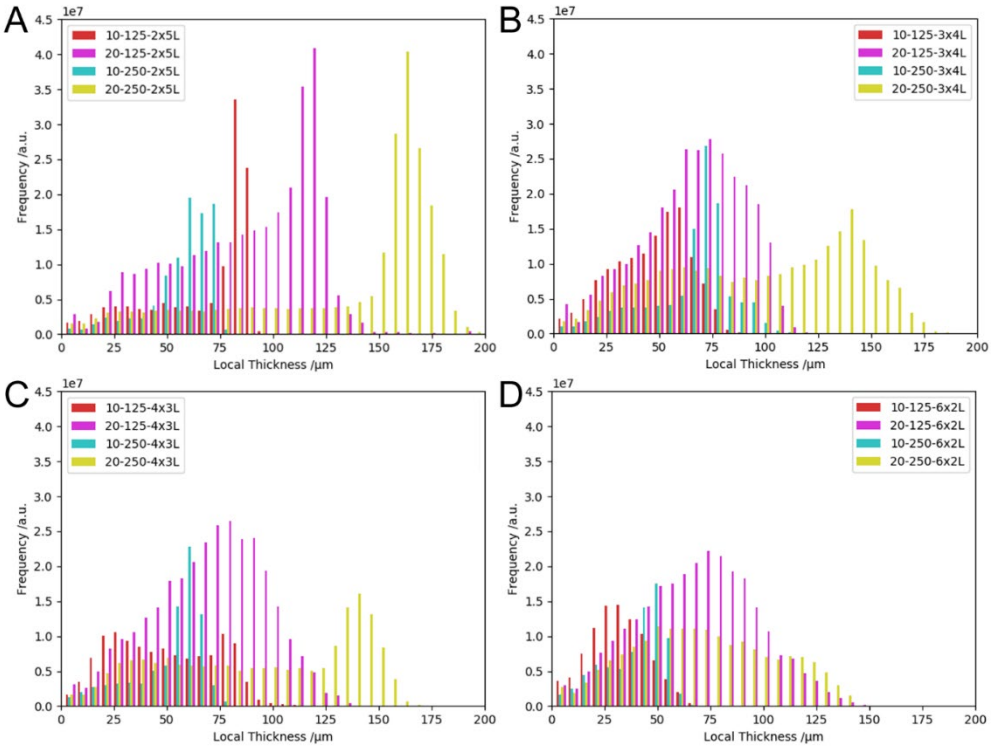

Figure 4.9. Graphical summary of the three-dimensional local thickness measurements for each of the investigated 16 scaffold types grouped under laydown pattern. (A) 2x5L, (B) 3x4L, (C) 4x3L, (D) 6x2L. Each graph shows the four different combinations of fiber diameters and fiber spacings per laydown pattern (10-125, 10-250, 20-125 and 20-250). Reproduced from (Youssef *et al.* 2019) under the Creative Commons CC-BY-NC license. Graphs were made by Dr. Simon Zabler.

Table 4.3. Summary of the calculated values for each of the 16 different scaffold types. Adapted from (Youssef *et al.* 2019) under the Creative Commons CC-BY-NC license. Table initially made by Dr. Simon Zabler.

Group	Sample	Total Porosity (P_{tot})	3D local thickness (3D-T_{loc})			2D local thickness (2D-T_{loc})		
			Maximum (µm)	Mean (µm)	SD (µm)	Maximum (µm)	Mean (µm)	SD (µm)
2x5L	10-125-2x5L	$88.6\%^{+3.4\%}_{-4.0\%}$	96.22	69.01	24.54	79	40	23.38
	10-250-2x5L	$90.7\%^{+2.1\%}_{-2.3\%}$	85.09	58.95	14.98	163	82	47.63
	20-125-2x5L	$83.8\%^{+4.9\%}_{-5.4\%}$	200.03	88.26	32.73	97	49	28.58
	20-250-2x5L	$88.2\%^{+2.6\%}_{-2.8\%}$	198.75	135.19	47.98	163	82	47.63
3x4L	10-125-3x4L	$84.1\%^{+3.8\%}_{-4.6\%}$	96.39	48.05	17.95	47	24	14.14
	10-250-3x4L	$89.0\%^{+2.5\%}_{-3.4\%}$	119.40	66.75	20.42	149	75	43.59
	20-125-3x4L	$79.5\%^{+4.0\%}_{-4.5\%}$	131.16	65.99	23.72	39	20	11.83
	20-250-3x4L	$88.0\%^{+2.4\%}_{-2.7\%}$	185.14	99.33	43.55	107	54	31.46
4x3L	10-125-4x3L	$84.0\%^{+3.9\%}_{-4.8\%}$	131.16	50.86	24.25	65	33	19.34
	10-250-4x3L	$89.2\%^{+2.5\%}_{-2.9\%}$	82.41	52.73	16.74	157	79	45.9
	20-125-4x3L	$80.4\%^{+3.8\%}_{-4.2\%}$	135.84	70.02	26.34	31	16	9.52
	20-250-4x3L	$84.6\%^{+3.0\%}_{-3.4\%}$	169.23	95.67	44.36	121	61	35.51
6x2L	10-125-6x2L	$77.7\%^{+6.3\%}_{-9.6\%}$	79.24	33.26	13.47	45	23	13.56
	10-250-6x2L	$84.9\%^{+4.5\%}_{-7.2\%}$	90.21	40.69	14.22	121	61	35.51
	20-125-6x2L	$78.2\%^{+4.1\%}_{-4.5\%}$	154.49	68.84	27.64	35	18	10.68
	20-250-6x2L	$84.0\%^{+3.7\%}_{-3.5\%}$	144.75	73.01	32.87	83	42	24.54

4.3.7 Scan resolution

To validate the high-resolution scan method, an attempt to measure the fiber diameter using the high-resolution scan data was performed (**Figure 4.8B)**. The µCT-measured fiber diameter for the targeted 20 µm fiber diameter was 22.6 ± 1.8 µm, which corresponds with that measured using SEM: 22.69 ± 0.52 µm. Moreover, to compare the accuracy of the measurements taken from the medium-resolution scans, the 20-125-6x2L scaffold was also scanned by the high-resolution method. **Figure 4.8C** shows a comparison of the distribution of 3D-T_{loc} between both scan methods on the same scaffold.

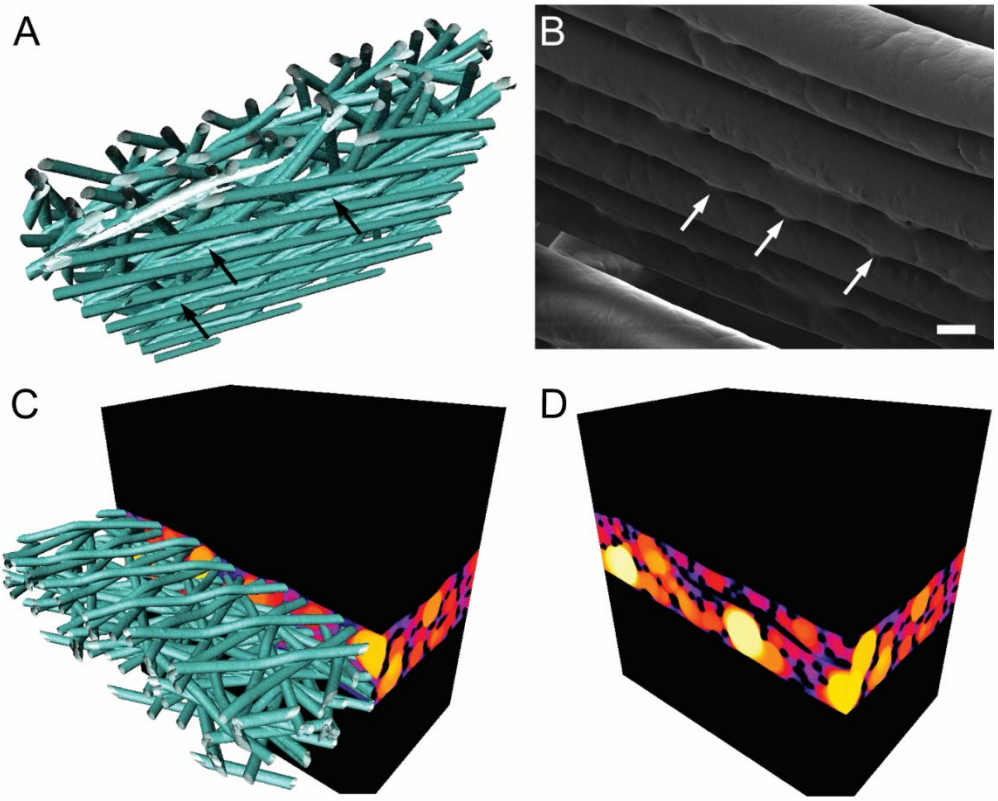

Figure 4.10. (A) A 3D rendering of a high-resolution scan of a 20-125-6x2L scaffold with partial fusion between two fiber layers (black arrows). (B) A SEM image of a different scaffold showing the same partial melting effect (white arrows). To take the image, the sample had to be significantly tilted inside the SEM. (C) An overlap of a 3D rendering of a 20-125-6x2L scaffold with its local thickness analysis. (D) is similar to (C) after the removal of the scaffold rendering and replacement with black spaces. Reproduced from (Youssef et al. 2019) under the Creative Commons CC-BY-NC license. (A), (C) and (D) were rendered by Dr. Simon Zabler. (B) was taken by Mr. Andrei Hrynevich.

4.4 Discussion

4.4.1 MEW scaffolds and their design

MEW is a new technology that is a recent addition to the AM family (Brown *et al.* 2011). PCL is a slowly degrading polymer that has been the polymer of choice for much of the reported MEW literature for both *in vivo* and *in vitro* applications (Muerza-Cascante *et al.* 2016, Baldwin *et al.* 2016, Martine *et al.* 2017, Delalat *et al.* 2017a). It is already available in medical-grade purity and is in use for several approved medical devices produced through other AM approaches (Youssef *et al.* 2017, Woodruff and Hutmacher 2010). Contrary to other melt micro-extrusion AM approaches, MEW can produce scaffolds with small fiber diameters in a reproducible and precise manner. These small-diameter PCL MEW scaffolds require a characterization method, which the use of µCT could fulfill. The method could quantitatively and quantitatively characterize MEW scaffolds of different fiber diameters, spacings and laydown patterns.

4.4.2 Effect of scaffold design on porosity

The total porosity calculation showed a clear trend indicating that larger values of fiber spacing lead to higher porosity. Concerning laydown patterns, less complex scaffolds (e.g., 2x5L) have higher porosity, whereas more complex structures (e.g., 6x2L) have a lower porosity. Due to the very large specific surface of the layer-by-layer printed structures, changing the value of the grey value threshold, which estimates the volume space between air and the PCL fibers, by 12.5% can alter the measured scaffold porosity by approximately 5% in total. We previously mentioned that this step was the main cause of error in the experiment. This effect was present, although the same measurement routine, initial grey value threshold estimation and data analysis were systematically applied to all samples by one person (Mr. Logan Fladeland). On the other side, by changing the closing radius by up to 50% for the generation of the binary mask, the effect on porosity was ten times less pronounced than changes to the grey value threshold.

4.4.3 Effects of scaffold design on pore size

4.4.3.1 2D local thickness analysis

The 2D-T_{loc}, shown in **Figure 4.4**, represents a 2D measurement of a 3D property. Pores are 3D empty spaces inside solid objects. In the MEW literature, it has been a long-standing tradition to describe pore size by mentioning the targeted fiber spacing between in the layer-by-layer fabrication of the scaffold. This methodology did not fully accommodate more complex scaffolds with irregular, but ordered architecture, similar to the 4x3L and 6x2L groups in the current study.

The use of local thickness measurement in 2D, however, came with limitations. First, the 3rd-dimension is absent with this approach, which is increasingly important with higher order structures that result in small, suspended, fibers within the morphology (Hrynevich *et al.* 2018). Second, by using the stereomicroscope to do the imaging, this meant that the raw images were not of high magnification. The use of SEM images would require an extra step before thresholding to digitally subtract the stub surface (bottom of the image) from the image. MEW scaffolds are typically 2-3 mm in height and usually are easily visualized under an optical microscope, although, recently, heights of up to 7 mm were described, but this approach is not yet practiced in the majority of laboratories with MEW devices, as it required z-axis and electric field computerized control (Wunner, Wille*, et al.* 2018). Using stereomicroscopy, the choice of the ROI for imaging and the application of the grey value threshold to create the binary images were the only manual and subjective input in the analysis (similar to the µCT measurement, disregarding the closing radius adjustment).

The analysis showed in the more complex scaffolds a bell-shaped distribution of the pore sizes, compared with the localized peaks of the more regular scaffolds. The 2x5L group, as well as the 10-250-3x5L scaffold, all showed peaks to the right side of the graph, indicating a preference for the increased frequency of large-sized pores, of similar diameter. In the other scaffold groups, the bell-shaped distribution indicated a spread of pore diameters across a wide range, owing to the complex scaffold architecture. The limitations of the image acquisition method should always be taken into

consideration when viewing the results of this method. But through the estimation of 2D-T_{loc}, an overall, arguably, more accurate understanding of the available pore spaces in the scaffold can be achieved, other than the target fiber spacing in the G-Code as an indication of pore size.

4.4.3.2 3D local thickness analysis

Repeating the local thickness analysis in 3D using the µCT reconstructed, thresholded sliced images overcame the resolution limitation of the stereomicroscope, without the background and tilting limitations of the SEM. Similar to the measurements in 2D-T_{loc},, the 3D-T_{loc} histograms of the 2x5L scaffold groups (**Figure 4.9A**) all showed a peak to the right-hand side of the distribution. The scaffolds with 10 µm targeted fibers had smaller pores than those with 20 µm fibers. From a visual inspection of the structure (compare with SEM images in **Figure 4.2**), it appeared that pore size measured was limited by the flat scaffold, meaning that, on account of the flat MEW scaffold, the 3D-T_{loc}, could not be higher than the diameter the sphere that would fit the height of the scaffold. In this case, even in the more porous group, the 10-250-2x5L, the measured 3D-T_{loc} did not approach the theoretical limit of 250 µm, which is the maximum pore size possible. Instead, in this group, the maximum was 85.09 µm and the mean was 58.95 ± 14.98 µm, while in the 20-250-2x5L group, where the scaffold is higher than that in 10-250-2x5L, on account of the doubled fiber diameter, the maximum was 198.75 µm and the mean was 135.19 ± 47.98 µm.

The impression that was obtained from the 3x4L structures (**Figure 4.9B**) was similar to the 4x3L ones where there is a right-hand side peak of the distribution of 3D-T_{loc} for the 10-250 scaffolds, i.e. the groups with the highest porosity. Unlike the other three groups in this laydown pattern, the 20-125 scaffold appeared to be unaffected by the flatness of the structure and hence, provide a more varied distribution of 3D-T_{loc}. The mean pore diameter here was 66.0 ± 23.7 µm, while the largest pore was 131.2 µm, which is larger than the target fiber spacing in the scaffold. Furthermore, the distribution of 3D-T_{loc} for the 10-125 scaffold appeared to follow the 20-125 one up to a pore diameter

of approximately 60 µm, afterwards the 10-125 scaffold displayed a decreased distribution, most likely caused by flatness effects, as it was less thick than the 20-125 one.

We observed the same trend for the 4x3L structures (**Figure 4.9C**) where the distribution of 3D-T_{loc} for the 10-250 scaffold had the same pronounced peak on the right side of the graph. The 20-250 and the 10-125 structures, however, featured a bimodal distribution, where there were peaks on the left and right of the graph, indicating a more varied pore size in the scaffolds. This could be attributed to only partial limitation by the flatness effect. The 20-125 scaffold finally showed a broad continuous distribution of pores with little effects from the flatness of the structure. Here, similar to 20-125-3x4L, the scaffold had a maximum pore size greater than the targeted fiber spacing (135.84 µm). The 12-125 scaffold also showed a maximum higher than 125 µm (131.16 µm).

Finally, the distribution of the 6x2L structures (**Figure 4.9D**) supported the observation that the pore size in more complex structures was hardly affected by the flatness of the scaffold. Only the 10-250 structure showed a right-handed peak in the distribution of 3D-T_{loc}. While the 20-250 distribution appeared more evenly distributed, it featured a little elevation towards the right, the 10-125 and 20-125 scaffolds appeared to be more affected by their architectural pattern. The 20-125 scaffold had the broadest distribution of all the 6x2L scaffold groups. Here, the maximum pore size was 154.5 µm, much higher than the targeted 125 µm. The height effect could be an explanation to the smaller pore sizes observed in the 10-125 compared to the 20-125 one.

4.4.3.3 Local thickness analysis summary

The 3D nature of µCT scans allowed for the analysis of the pore space by calculating the 3D-T_{loc}, in a precision that is not possible using 2D methods. Unlike calculations of P_{tot}, the analysis of the 3D- T_{loc} took a closer look at a design-influenced property: pore size. Using the 3D µCT scans, it was evident that for less complex scaffolds, e.g., 2x5L or in particular, those printed with a target fiber diameter of 10 µm, the pore size was essentially limited by the flatness of the scaffolds, i.e. the fiber spacing is larger than the height of the entire scaffold thickness. This prevented the calculation of pore

sizes which correspond to the planned fiber spacing, as the generated pore, in this instance, is not as big as a sphere with a diameter equal to the fiber spacing. For the more complex structures, e.g., 6x2L and for the scaffolds with a target fiber diameter of 20 µm, a continuous pore distribution was found, which could be used as a morphological fingerprint for the 3D characterization of porosity. Furthermore, this flatness effect is totally invisible when T_{loc} is calculated using a 2D method, e.g. the calculation of 2D-T_{loc} through stereomicroscope images. Such 2D images disregard the fact that MEW scaffolds are 3D AM scaffolds which are made layer-by-layer, through translation in the x-, y- and z-axes. The perception that MEW scaffolds are mostly flat sheets could limit the spread and application of MEW scaffolds as medical devices. It is worth noting that, as discussed in Chapter 2 (Youssef *et al.* 2017), almost all the MEW *in vivo* experiments were performed using tubular MEW scaffolds, which provided more structured 3D pore spaces that allowed tissue ingrowth and infiltration (Martine *et al.* 2017).

4.4.4 High-resolution scanning

The spatial resolution accuracy of this analysis can be addressed by comparing the distribution of 3D-T_{loc} in the 20-125-6x2L scaffold to a high-resolution scan that was recorded in addition to the medium-resolution one. As mentioned before, the scaffold with the least fiber stacking, compared to the other scaffolds was the 20-125-6x2L sample. This resulted in a more irregular fiber deposition highlighted by multiple suspended fibers rather than stacked ones. By scanning this scaffold with the high-resolution mode and then calculating the 3D-T_{loc} based on the new values, a broad continuous distribution (**Figure 4.8C**), with a maximum of 123.2 µm (slightly smaller than the fiber spacing) and a mean of 66.0 ± 29.3 µm, was observed.

The abrupt cut off seen in the high-resolution scan after the 3D-T_{loc} value of approximately 120 µm was probably caused by the narrow FOV of this scanning modality (**Figure 4.8C**). The high-resolution method also was able to describe smaller pores in the scanned section, and this explains the difference in mean and SD values between the high- and medium-resolution scans for the same

20-125-6x2L scaffold, 66 ± 29.03 µm and 68.8 ± 27.6 µm, respectively. Apart from this limited volume effect, both distributions showed a congruent linear slope at the smaller pores, which is an indication that medium-resolution scans in this regime were equally valid, despite the lower spatial resolution, compared to the high-resolution scan. The maximum pore size of 80 µm for this scaffold (20-125-6x2L) was accurately reproduced from both scans (**Figure 4.8C**).

The high-resolution scan mode made it possible to visualize the fibers, pores and the surface of the fibers using 3D reconstruction of the µCT data. **Figures 4.10** show a capture of a graphical rendering of a high-resolution scan of the 20-125-6x2L scaffold with both the fiber surface (**Figure 4.10A**) and a scaffold cross section, showing the pores (**Figure 4.10C**) and the 3D-T_{loc} map (**Figure 4.10D**). These reconstructions depicted fine surface details of the fibers such as the occasional fusion between two fibers, seen during deposition of the upper fiber on the lower one, before the former has cooled down and solidified. These details could only be visualized with the SEM after significant tilting and/or cutting of the scaffold (**Figure 4.10B**). The creation of a 3D-T_{loc} map (**Figure 4.10C**) and the subsequent subtraction of the scaffold (**Figure 4.10D**) in the 3D reconstructions, provided a dynamic and accessible approach to visualizing a porous MEW scaffold, which could provide a feedback loop to the design and finally, the potential application of the scaffold.

4.4.5 The potential of µCT scanning in MEW

Through MEW, it is possible to print precise scaffolds in a variety of complex and reproducible geometric shapes and patterns (de Ruijter, Hrynevich*, et al.* 2018, Liashenko *et al.* 2020), using fiber diameters that span the gap between solution electrospinning and micro-extrusion techniques (Hrynevich *et al.* 2018), all with medical-grade polymer and without the use of solvents (Youssef *et al.* 2017). However, the desire for perfect geometrical shapes might not represent the native ECM that the whole objective of scaffolds for TE was to mimic. Using µCT scanning, it was possible to observe the effect of the scaffold flatness on the local thickness in the 2x5L and 3x4L fiber laydown groups (and to some extent, the 10-250 group in the 4x3L and 6x2L fiber laydown groups). This disappears in

the rest of the groups of the 4x3L and 6x2L, indicating that the pore size distribution was becoming more dependent on the complex architecture of the scaffold. Complex but defined and reproducible porous scaffolds could be potentially more physiologic when used *in vitro* and *in vivo*, than flat, simple ones.

While µCT analysis of MEW scaffolds was previously described for porosity estimation (Powell *et al.* 2014), explanted MEW scaffolds as a TE bone model for the study of metastasis (Holzapfel *et al.* 2014), analysis of particles in fibers (Ren *et al.* 2014), and the creation of a finite element model for mechanical properties (Castilho, Hochleitner*, et al.* 2018, Bas *et al.* 2018), none so far analyzed the effect of the three scaffold properties that were discussed in this chapter (fiber diameter, spacing and laydown pattern) on the total porosity and pore size distribution of the scaffold (Youssef *et al.* 2019). By changing the laydown pattern and coupled with the possibility of changing the fiber diameter in a single print (Hrynevich *et al.* 2018), as well as the offset and tilt of the fiber walls (Liashenko *et al.* 2020), the complexity of the scaffold could be tailored to fit a target structure for an *in vitro* or *in vivo* application. As it was recently possible to produce MEW scaffolds that were up to 7 mm in thickness (Wunner, Wille*, et al.* 2018), the work discussed here could help in the design and quality assurance of the produced scaffolds, for the potential biomedical application. With such scaffold thickness, determining and assessing the morphology of the scaffold could be challenging. With in-process quality control of printed fibers now a possibility (Wunner, Mieszczanek*, et al.* 2019), post-production, non-destructive quality assurance using µCT scanning could benefit the spread and acceptance of MEW scaffolds towards development of medical devices. For MEW scaffolds, this data might help in the design optimization, feedback loops and characterization of printed scaffolds, in the aim to optimize cellular infiltration both *in vitro* and *in vivo* by changing the scaffold porosity. Moreover, using the same method, which was applied to the empty PCL scaffolds, it could be possible to quantify the volume of deposited tissue (*in vivo*) or cells (*in vitro*) in MEW scaffolds, as part of TE research.

4.5 Conclusion

This work explored the non-destructive, 3D quantitative analysis of porosity in MEW scaffolds using µCT. The 3D analysis of porosity in thin fibrous scaffolds or in any other open porous structure is potentially more difficult compared to the analysis of closed pores (e.g., foams or rocks). A set of 16 different scaffolds with different fiber diameters, spacing and laydown patterns was produced via MEW. The produced scaffolds were characterized using SEM to check their morphological similarity to the intended design. A 2D method for the evaluation of pore size was tested and finally, µCT scanning of the scaffolds was conducted, partly using a high-resolution scanner to compare the validity of the main, medium-resolution method. After scanning, the X-ray phase contrast images were processed and images masked and thresholded, with the local thickness of the entire pore space calculated and analyzed for its histographical distribution. Scaffold morphological parameters like total porosity and pore size distribution were obtained by this routine. Using the high-resolution scan mode, it was possible to examine additional parameters, e.g., the fiber diameter and it was possible to obtain values that were comparable to those obtained using the SEM.

The precision in calculating P_{tot} has been shown to depend on the accuracy of the grey value threshold which separates voxels belonging to the scaffold from the surrounding air. However, with this error margin in mind, it was possible to show that µCT accurately and quantitatively characterized porosity and pore sizes in all scaffolds.

The use of µCT is suited for analyzing and comparing volume porosity and related parameters in PCL scaffolds and can be potentially used for creating a unique fingerprint of their 3D structure. This non-destructive method could be applied for MEW scaffold quality assurance, to verify that the AM structure fabricated, is indeed the one that was designed. There is the potential for using the same approach for MEW scaffolds used in *in vitro* and *in vivo* experiments, with the aim of translating MEW to the production of precise, on-demand and customizable medical devices.

Chapter 5

A manuscript based on the work discussed in this chapter is in preparation:

Youssef, A., *et al.* "The foreign body reaction to micro-scale melt electrowritten flat polycaprolactone scaffolds."

5.1 Introduction

The surgical procedure typically required for the implantation of a medical device usually creates a traumatic event that requires a regenerative reaction, which is, at its core, an innate immune-mediated one (Huber-Lang *et al.* 2018). Furthermore, the presence of a medical device inside the body, which is immunologically regarded as a foreign material, prevents the completion of healing and leads to the formation of the foreign body reaction (FBR) (Kastellorizios *et al.* 2015). The FBR is defined as a chronic inflammatory, persistent reaction of vascularized tissue to a foreign material in the body (Anderson 1988). This includes a spectrum of objects, from the aforementioned medical devices (Anderson *et al.* 2008) to deposited crystals (Nakayama 2018), stones and parasite eggs (Ozkanli *et al.* 2014).

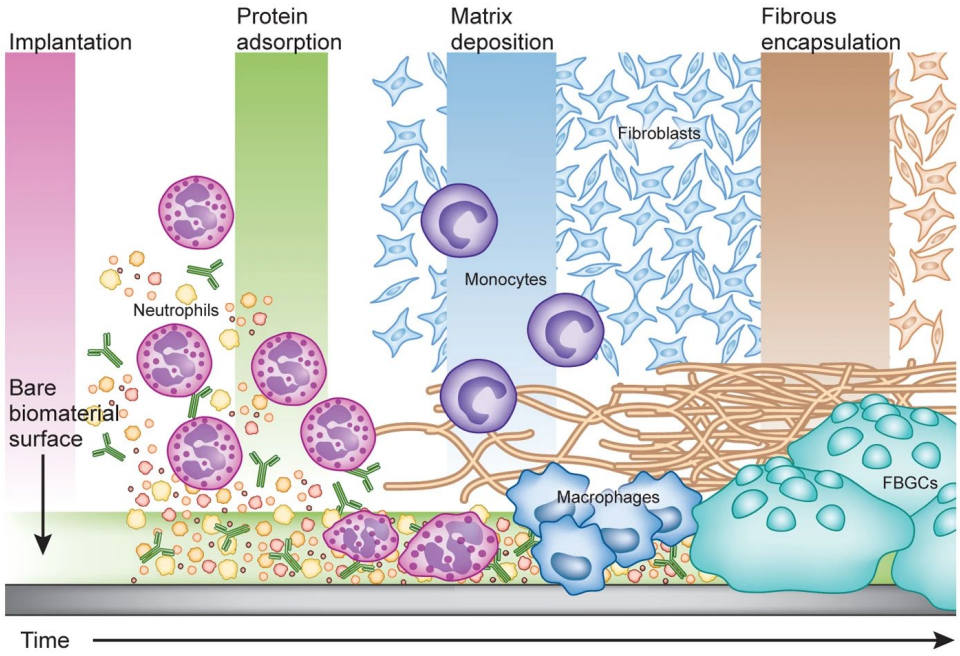

Figure 5.1. Graphical representation of the events occurring after the implantation of a foreign material into the body. The first events after the implantation and the exposure of the material to blood and plasma proteins is the non-specific protein adsorption to the surface. This is followed by the migration of granulocytes and tissue-resident macrophages to the implant surface. Blood monocytes home towards the implantation area and differentiate into macrophages. Fibroblasts will start to infiltrate the region and deposit collagen. When the macrophages are unable to remove the foreign body, the fuse together and form foreign body giant cells. As a last resort, the body seals off the implant with a thick fibrous capsule to protect against potential harm. Reproduced from (Grainger 2013)[1], with permission from Springer Nature.

[1] Grainger, D. W. (2013). "All charged up about implanted biomaterials." Nat Biotechnol **31**(6): 507-509.

The FBR is mostly conserved in mammals and follows the same cascade (Klopfleisch and Jung 2017). In this chapter, the focus is on the FBR to implantable medical devices, which in this case constitute the foreign material which stimulates the inflammatory reaction (**Figure 5.1**). The cascade starts with the exposure of the bare biomaterial surface to plasma proteins and the interstitial, as well as extracellular fluid, leading to non-specific protein adsorption (Anderson *et al.* 2008). This event is the starting point and results in the activation of the complement system. This step of protein adsorption is potentially a controllable bottleneck for the whole cascade, for example, through the use of zwitterionic polymers or coatings (Blackman *et al.* 2019). The innate immune system responds by mobilizing the acute inflammatory cells to the implantation site (Huber-Lang *et al.* 2018). These cells include neutrophils, tissue resident macrophages and monocytes (Varol *et al.* 2015). The acute reaction gives rise to a chronic one with the abundance of macrophages, lymphocytes, plasma cells and fibroblasts (Sheikh *et al.* 2015). The macrophages fuse together and form foreign body giant cells (FBGCs). FBGCs attempt to further phagocytose the foreign body, often leading to "frustrated phagocytosis", where FBGCs release damaging phagocytic enzymes into the implant-tissue interface (Junge *et al.* 2012), a step which could complicate implant infection in case a biofilm has already formed on the implant surface (Patel *et al.* 2012). Giant cells are usually found in granulomata of different origins and as osteoclasts in bone (Miron *et al.* 2016, ten Harkel *et al.* 2015, Zhang *et al.* 2019), but in the case of a foreign body granuloma, the giant cells are usually of the foreign body type and not the Langhans variant (Pritchard *et al.* 2003, Al-Maawi *et al.* 2017). The distinction between both is usually through the arrangement of nuclei (Al-Maawi *et al.* 2017). Giant cells can have up to hundreds of nuclei and reach up to 120 µm in size (Gupta *et al.* 2014).

Further inflammation leads to the encapsulation of the foreign body with a fibrous capsule made of newly deposited collagen to seal off the offending agent away from the body. This step serves to shield the body away from any potential effects of this foreign, unremovable and indigestible foreign body (Kastellorizios *et al.* 2015). Once formed, the foreign body reaction persists for the lifetime of the implant, independent of the biomaterial from which it was made (Anderson 1988). The

collagen is primarily produced from the fibroblasts which migrated during the initial inflammation, as well as fibrocytes, which are cells of mesenchymal origin, originating, most probably, from monocytes (Reilkoff *et al.* 2011).

The FBR can lead to implant dysfunction, fibrosis, pain and swelling, and the functional effect on the implant can be detrimental, e.g. in case of pacemakers (Yoko *et al.* 2013). Conversely, the scar tissue formation can play a vital role in tissue reinforcement, such as for hernia repair using surgical meshes (Schumpelick *et al.* 2006). The contraction of the fibrous capsule can also lead to positional changes of the implant as well as adhesions and chronic pain (Prantl 2009).

There has been a significant research output on the analysis of the FBR towards polymeric flat meshes, as these have been used for decades for the treatment of hernias and pelvic floor prolapse (Klinge *et al.* 2014). The ideal mesh is the one that allows the integration of new tissue inside the mesh pores with deposition of new collagen fibers, blood vessels and a decreased FBR. The search for such a "perfect" surgical mesh, however, is an ongoing process (Serafini *et al.* 2020). One aim of hernia repair using surgical meshes is to avoid the formation of a scar plate, which is a layer of stiff, poorly integrated connective tissue, ultimately leading to mesh shrinking and recurrence (Amato *et al.* 2015). Instead, the goal is to use a mesh that will lead to tissue ingrowth through its pores, with proper integration of the implant, followed by resorption (Jordan *et al.* 2018). It was reported that large pores and thick fibers produce a favorable FBR in vascular scaffolds compared to small pores and thinner fibers (Wang *et al.* 2014). Likewise, the same result was reported in surgical meshes, where the use of low-weight, large-pore meshes leads to better tissue integration compared to high-weight, small-pore ones (Junge *et al.* 2012). The implantation of high-weight meshes was associated with scar plate formation and "a bridging scar", where the proximity of the formed foreign body granulomata to each other, lead to a reduction of the effective porosity and a decrease in tissue infiltration (Cobb *et al.* 2005).

The effect of size and topography was also noticed for microsphere implantation, with better biocompatibility of spheres of 1.5 mm diameter compared to those with a diameter of 0.5 mm or less. The larger spheres had little fibrous capsule and appeared to escape the foreign body reaction, compared to smaller ones. Moreover, a spherical shape dictated a milder reaction than other geometrical shapes, independent from the total implanted surface area, as well as independent from the material (Veiseh *et al.* 2015). The size of the implant also affected the fusion of macrophages, where particles larger than 10 μm can be deemed non-phagocytosable and in turn, surrounded by FBGCs and a fibrous capsule (Sheikh *et al.* 2015). It is worth noting that when pores are less than 10 μm in size, this can provide a site for bacterial infiltration and biofilm formation. Bacteria can infiltrate these pores, however macrophages and neutrophils will be excluded, giving such microbes immunity against phagocytosis (Amid 1997, Falagas and Kasiakou 2005).

It has been shown, mostly *in vitro*, that the scaffold topographical cues can influence the macrophage behavior (Chen *et al.* 2010, Sridharan *et al.* 2015), including polarization from the pro-inflammatory M1 type towards anti-inflammatory M2 type (Zhang *et al.* 2017, Sussman *et al.* 2014). There has been a sustained research output from the group of Prof. Buddy Ratner in Washington University to develop poly(2-hydroxyethylmethacrylate) (polyHEMA) scaffolds with spherical 40 μm pores which are interconnected through 16 μm inlets. These scaffolds were found to induce little FBR (Bhrany *et al.* 2013) and a shift of the macrophage phenotype to the M2 type (Sussman *et al.* 2014) when compared to solid scaffolds from the same material or to controls. It should be noted that such implants are considered as hydrogel scaffolds (Fukano *et al.* 2010) and are not fibrous.

Melt electrowriting (MEW) is an additive manufacturing (AM) technique which can produce fibrous, highly porous scaffolds with controllable, micro-scale fiber diameters and spacings, using medical-grade, solvent-free thermoplastic polymers. The freedom of scaffold design and fabrication presented by MEW, enable further research possibilities on the effect of scaffold morphology on the FBR, with the aim of producing scaffolds that can downregulate the FBR with anti-inflammatory

features. To date, there have been no fundamental *in vivo* studies on the FBR of empty, unaltered MEW scaffolds. Most of the *in vivo* MEW literature focused on the application of calcium phosphate-coated MEW tubular scaffolds as a model for the study of metastasis in prostate and breast cancer (Dondossola *et al.* 2016, Holzapfel *et al.* 2015, Martine *et al.* 2017).

Our group has recently shown a change in macrophage polarization from M1 to M2 when macrophages were cultured on MEW scaffolds with a box pore shape and a size of 40 µm (Tylek *et al.* 2020). Part of this *in vivo* study was the analysis of the effect of the pore geometry of the scaffold on the macrophage polarization between M1 and M2 types by other members of our group. However, the work done for this thesis and presented in this chapter will only discuss the FBR to the implanted constructs, with both geometrical pore shapes (box and triangle), without focusing on macrophage polarization.

5.2 Materials and methods

5.2.1 Study design

To investigate the *in vivo* response to the subcutaneous implantation MEW scaffolds, four different experimental groups were planned (box, triangle, PCL film and sham). Two groups were implanted subcutaneously in every mouse on either side. Study animals had box scaffolds on the right side and triangular scaffolds on the left one and control animals had a PCL film on the right side and an empty pocket (sham group) on the left side. The terminology of the scaffolds is explained in the next subsection.

Prior to the start of the experiment, both cryosectioning and formalin-fixed, paraffin-embedded (FFPE) samples were tested as a method for tissue processing and done on *in vitro* cell-seeded MEW scaffolds, as well as excised mouse tissue (skin and subcutaneous tissue and spleen). Ultimately, FFPE was chosen owing to better preservation of morphological details and the ability to process a larger number of samples in a faster way.

A pilot experiment was performed with eight of the planned 60 mice. The pilot phase was used to check for the effectiveness of the implantation technique, the establishment of histological and immunostaining methods as well as microscopy techniques.

5.2.2 MEW scaffold fabrication

5.2.2.1 Groups

This *in vivo* experiment was planned as a proof of principle of an ongoing in *vitro* experiment, featured in (Tylek *et al.* 2020). Accordingly, the scaffold design was carried over from the *in vitro* experiment, albeit with modifications. The scaffold designs used were the samples with the laydown patterns and fiber spacing which showed the highest effect during the *in vitro* phase. These scaffolds were with a laydown pattern of 0/90° and a 50 µm fiber spacing (herein referred to as “box scaffolds”)

and with a laydown pattern of 0/60/120° and a 60 µm fiber spacing (referred to as “triangular scaffolds”).

5.2.2.2 Scaffold design

The identical scaffold designs used in the *in vitro* experiments, however, could not be adopted for the *in vivo* component. Changes in the scaffold design had to be implemented, to accommodate the need for increased handling, sterilization and manipulation steps before and during the surgical procedure. Consequently, the scaffolds were thicker and had a reinforcing ring surrounding the sample.

The initial scaffold production for the pilot phase was done by Dr. Carina Blum, who printed the scaffolds for the *in vitro* experiments, based on G-Code produced by Mr. Joachim Liebscher, similar to that used in Chapter 3, for the box scaffolds and by Mr. Andrei Hrynevich for the triangular scaffolds. The scaffold parameters were similar to what was previously used in the *in vitro* phase of the experiments (Tylek *et al.* 2020). The layer count was increased to a more handleable 42 intersecting fiber layers (2x21 for box and 3x14 for triangular scaffolds). A frame was printed on the outer edges of the scaffold to reinforce the scaffold and improve handling.

The modified scaffold production was based on a G-Code produced by Mr. Andrei Hrynevich that include a circular motion to reposition the jet when a complete layer is finished, to avoid build-up of fibers on the first line of fibers during repositioning to start a new layer, both in the x- and y-axes. Automation and modulation of the MEW process was maximized so that the same code was used to print the box as well as triangular scaffolds. This allowed proper and precise positioning of the frames on top of the already printed scaffolds without trial and error. In total, 42 layers were printed (2x21 for box scaffolds and 3x14 for triangular scaffolds), similar to what was produced during the pilot phase. In general, scaffolds were printed first and stored for a few days (during which quality assurance was also performed) and then frame production was done *en masse*.

5.2.2.3 MEW process

MEW was performed on a custom-built MEW printer that was designed and built by Dr. Tomasz Jüngst and Mr. Andrei Hrynevich (**Figure 5.2A**). The printer is similar in design to that which was used for scaffold productions in Chapters 3 and 4 and previously described in (Hochleitner *et al.* 2016). However, the difference was the addition of a computer-controlled z-axis, and a collector that accommodated glass slides in fixed positions. Medical-grade PCL (PURASORB PC 12, Lot# 1412000249, 03/2015, Corbion Inc., Gorinchem, Netherlands) was heated inside the printing head in a plastic disposable syringe equipped with a 30G nozzle (Nordson EFD Deutschland GmbH, Pforzheim, Germany) to 73 °C for 30 minutes then allowed to cool down in room temperature (RT) for 15 minutes and then reheated to 66 °C for another 30 minutes. A pneumatic pressure of 2 bar was used to force the molten PCL through the nozzle. The printing head was positioned 1.8 mm above the surface of a normal (non-charged and non-coated) glass slide (VWR International, Radnor, PA, USA), on which printing of 12x12 mm scaffolds was done (**Figure 5.2B**). The glass slides, the metal collector and the underside of the printing head were all cleaned with absolute, undenatured ethanol before printing followed by wiping with a fiber-free clean-room wipe to minimize dust particles. Voltage was set to 0 kV for the collector and +4 kV using negative (LNC 10000-5 neg) and positive (LNC 10000-5 pos) high voltage sources (both from Heinzinger Electronic GmbH, Rosenheim, Germany).

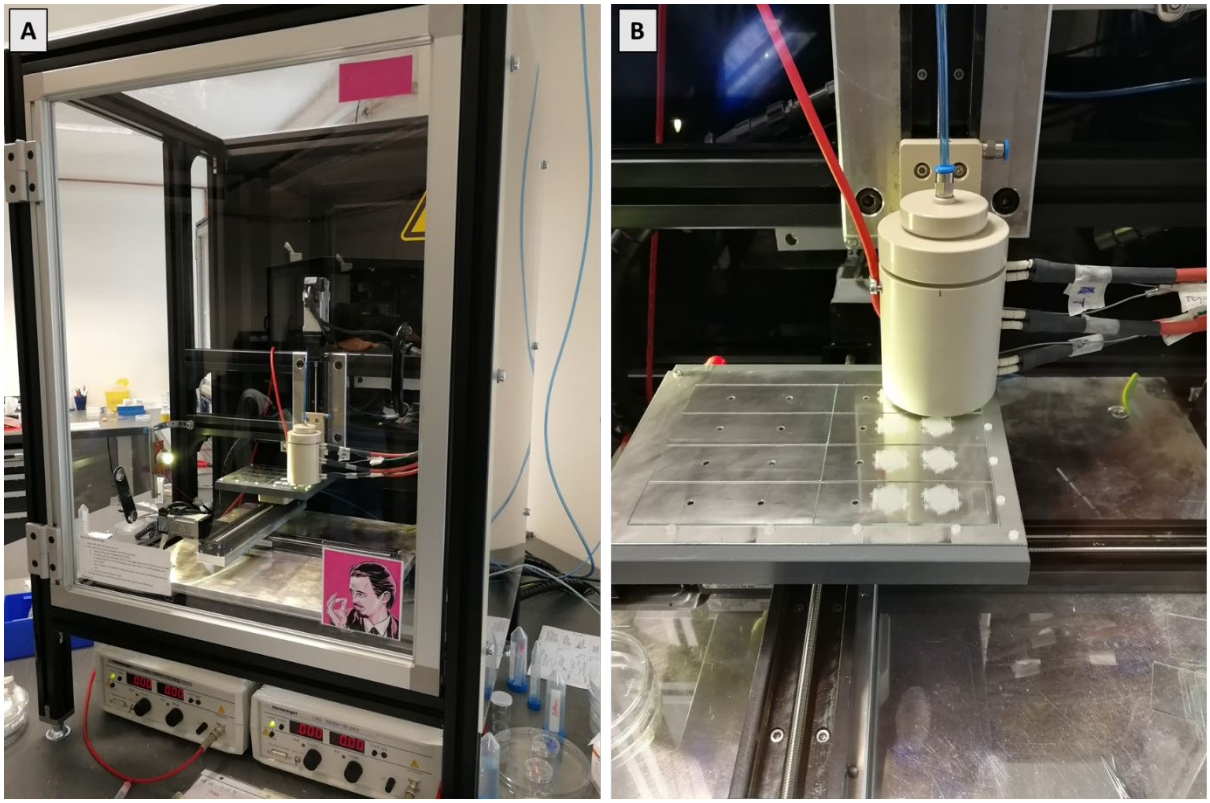

Figure 5.2. **The MEW printer setup.** A) The MEW printer inside the polycarbonate protective housing with the two voltage devices at the bottom. Inside is the printing head and the moving collector with the computer-controlled axes. B) Close up of the printing head with the two-column arrangement of glass slides on the metal collector. Triangular scaffolds were being printed at that moment.

In the pilot *in vivo* experiment scaffolds, the linear collector speed was 1050 mm/min, with a turn speed of 600 mm/min and pauses of 20 and 10 ms before and after the turns, respectively. For the main experiment scaffold, collector speed was set to 1050 mm/min for the linear motion and 950 mm/min for the turns, with pauses of 50 and 1 ms before and after the turns, respectively. The G-Code used in the production of the main experiment scaffolds is annotated and listed in **Appendix 1**. After printing, scaffolds (while still on top of the glass slides) were stored under dust free conditions in Petri dishes or glass slide boxes until the frames were printed on top of them.

5.2.2.4 Frames

The glass slides with the scaffolds on top were repositioned back into the MEW printer, in the same slide position and printing order. To fulfil a minimum target scaffold surface area of approximately 1 cm^2, a frame with an inner radius of 6 mm and an outer radius of 7 mm was printed with a 22G nozzle using a melting temperature of 73 °C and 2 bar pneumatic pressure. The collector

speed was adjusted to 35 mm/min to print irregularly deposited fibers below the critical translation speed. The collector distance was kept at 8.2 mm and -1.5 kV applied to the collector and 8 kV to the nozzle.

5.2.2.5 Final scaffolds and quality assurance

The diameter of the final scaffolds was 14 mm. Scaffolds were individually inspected via stereomicroscope while they are still on the glass slides and given a score regarding the presence of structural defects that would prevent their use. An empirical scoring system of "+", "-" or "+/-" was adapted from Dr. Carina Blum and used. A scaffold with a "+" score was perfect without any visible defects. A one with "-" had either multiple small defects, like fibers not stacking upon each other, tilted walls or the presence of large structural defects, caused by, for example, a dust particle or a fiber pulsing incident. A scaffold with a "+/-" had 1-2 small jumping fiber defects that were away from the center of the scaffold. Only scaffolds with a "+" or "+/-" score were used. The decision to use "+/-" scaffolds was to improve scaffold yield, as the combined "+" and "+/-" scaffolds constituted less than 50% of the printed scaffolds. A single scaffold took almost 4.5 hours to be printed, without a frame.

5.2.2.6 Scaffold collection and sterilization

After printing of both the scaffold and the frame into the composite scaffold (from now on, simply referred to as scaffold), absolute undenatured ethanol was pipetted on top of the scaffold to separate it from the glass slide. The scaffold was then moved via forceps into a Petri dish with absolute denatured ethanol. After all the scaffolds were collected, the Petri dish was moved under a sterile laminar air flow hood. The scaffolds were then moved to a new sterile Petri dish with 70% ethanol (prepared from absolute undenatured ethanol with autoclaved double distilled water (ddH_2O) under sterile conditions) for 15 minutes. Then the scaffolds were moved to a new Petri dish using new sterile forceps for another round of sterilization in fresh 70% ethanol for another 15 minutes. The scaffolds were then washed in three changes of sterile phosphate-buffered saline (1X PBS), each for 5 minutes.

This was followed by moving into sterile 100 mL containers in 1X PBS to be stored until used at 4 °C. Films were sterilized in the same way, in the same session.

5.2.3 PCL film preparation

To prepare PCL films as one of the two control groups, a film casting device (Film Applicator 510, Erichsen GmbH, Hemer, Germany) was used. A glass surface was cleaned twice with chloroform, twice with acetone and twice with absolute ethanol, then an metal applicator (cleaned in the same way) with a clearance of 200 µm was filled with medical-grade PCL (same as that used for MEW) and manually heated using a heat gun at full power, held from a distance of 20 cm. Temperature was controlled using an infrared thermometer and was between 80 and 110 °C. The applicator progressed at 1 mm/s. The film was left to solidify for one hour and then absolute ethanol was used to separate it from the glass undersurface (**Figure 5.3**). The film thickness was then measured using a digital caliper.

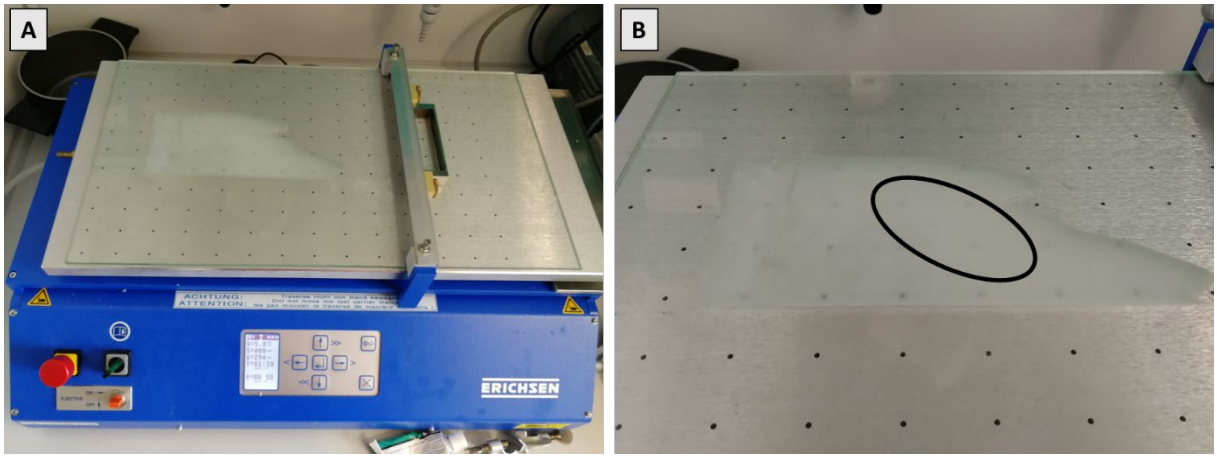

Figure 5.3. **Fabrication of the film scaffolds.** A) The melt drawing device with the already melted PCL film on top of the glass substrate. B) Close up of the produced film showing the area used for the punching out of circular, 14 mm wide film scaffolds (ellipse).

The films were then punched with a stainless-steel hollow sharp punch with a diameter of 14 mm. The punch was initially cleaned by submerging in chloroform, followed by acetone and finally absolute ethanol. Punched-out films were then collected and placed in a Petri dish under dust-free

conditions and sealed by Parafilm until sterilized. Sterilization was done in the same way as with the MEW scaffolds.

5.2.4 Scaffold characterization

5.2.4.1 Scanning electron microscope (SEM) analysis

Representative samples were selected and imaged using a stereomicroscope (Zeiss Discovery V.20, Carl Zeiss, Oberkochen, Germany) to measure total scaffold diameter and the width of the frame. Other samples were sputter-coated with 4 nm of platinum (Leica EM ACE600, Leica Microsystems, Wetzlar, Germany) and then imaged using a Zeiss Crossbeam 340 SEM (Carl Zeiss, Oberkochen, Germany) to check scaffold structure and measure fiber diameter. Measurements were performed by Mr. Andrei Hrynevich. For the measurement of fiber diameters, three scaffolds per group were selected and in each, the diameters of ten different fibers were measured (n=30). Tilted images in a 45° angle were also acquired to characterize the fiber walls in the scaffolds. Sterilized scaffolds were also characterized to check if the sterilization process had an effect on scaffold morphology, albeit with a lower number of measurements (n=7). PCL films were similarly characterized.

5.2.4.2 2D local thickness

The established routine used in Chapter 4 to measure the two-dimensional local thickness (2D-T_{loc}) as a correlation to pore size was used with the current scaffolds. Briefly, using high magnification with the 1.5x lens of the stereomicroscope, three images from three different scaffolds from each scaffold group were taken (n=9). Using the open-source software package, Fiji (Schindelin *et al.* 2012), running ImageJ v1.52p, the images were thresholded and analyzed with the function local thickness to give the diameter of a circle that will fit inside the available pores. The ImageJ macro code is listed in **Appendix 2**.

5.2.5 *In vivo* study

5.2.5.1 Study design and animals

The animal experiments were approved by the Government of Lower Franconia, Germany (ID: 55.2-DMS-2532-2-482). 60 Naval Medical Research Institute (NMRI) outbred female mice were ordered from the company Charles River (Sulzfeld, Germany). For each of the four time points (2-, 4-, 7- and 14-days post-implantation), 15 mice were used. These mice were divided into 10 mice for the scaffold groups and 5 as controls. **Table 5.1** summarizes the design of the experiment. Mice were delivered to the animal facility of the Department of Functional Materials in Medicine and Dentistry, University of Würzburg at 11 weeks of age and were left for two weeks before the start of the experiment to acclimatize. The mice were caged, under controlled temperature and humidity, in groups before the surgery and then individually afterwards. Food and water were supplied *ad libitum* and a 12-hour light/dark cycle was applied. Enrichment elements were added in the cages for the welfare of the animals. The average preoperative weight of the animals was 34.27 ± 2.72 g.

Table 5.1. Summary of the experimental setup. The mice were distributed in four different time points with two experimental groups in each.

Group	Day 2	Day 4	Day 7	Day 14
Control (Right side: Film, left side: sham)	5	5 (3 done in Pilot)	5	5
Scaffold (Right side: box, left side: triangle)	10	10 (5 done in Pilot)	10	10
Group total	15	15	15	15
Grand total	60			

5.2.5.2 Surgical procedure

All surgical procedures were performed under aseptic conditions, and by the same operator (Almoatazbellah Youssef). The surgical technique that was used was previously described for a different implant (Pavia-Jimenez *et al.* 2014). Dr. Andrea Ewald performed the anesthesia. The mice were weighed then anesthetized. For induction of anesthesia, the mice were placed in an air-tight

chamber with 4% isoflurane and then for maintenance, 1-3% isoflurane was delivered through a mask. Subcutaneous injection of 25 mg/kg of tramadol was given preoperatively as an analgesic.

The skin on both flanks was shaved using an electric razor. Skin disinfection was done using Octenisept (Schülke, Norderstedt, Germany). The animal was then covered with sterile surgical drapes, on top of a thermal pad adjusted to 30 °C. A skin incision 10 mm in length was performed using Metzenbaum scissors in the lateral side (flank) of the animal between the costal margin and the inguinal area. Blunt dissection was performed with scissors to create a pocket in the subcutaneous tissue superficial to the abdominal muscles of approximately 15x15 mm in dimension, then irrigated with sterile 0.9% sodium chloride solution. The sterilized scaffold was then taken out of the sterile PBS solution and placed in the pocket, according to the group distribution. For the scaffold groups, the side of the scaffold that was in contact with the metal collector of the MEW printer (smooth side) was placed on the floor of the pocket (superficial to the abdominal muscles), similarly for the PCL films, the side in contact with the glass surface of the film casting device (smooth side) was also placed on the floor of the pocket. For the sham group, just the pocket was created without implanting anything inside. The surgical procedure is summarized in **Figure 5.4**.

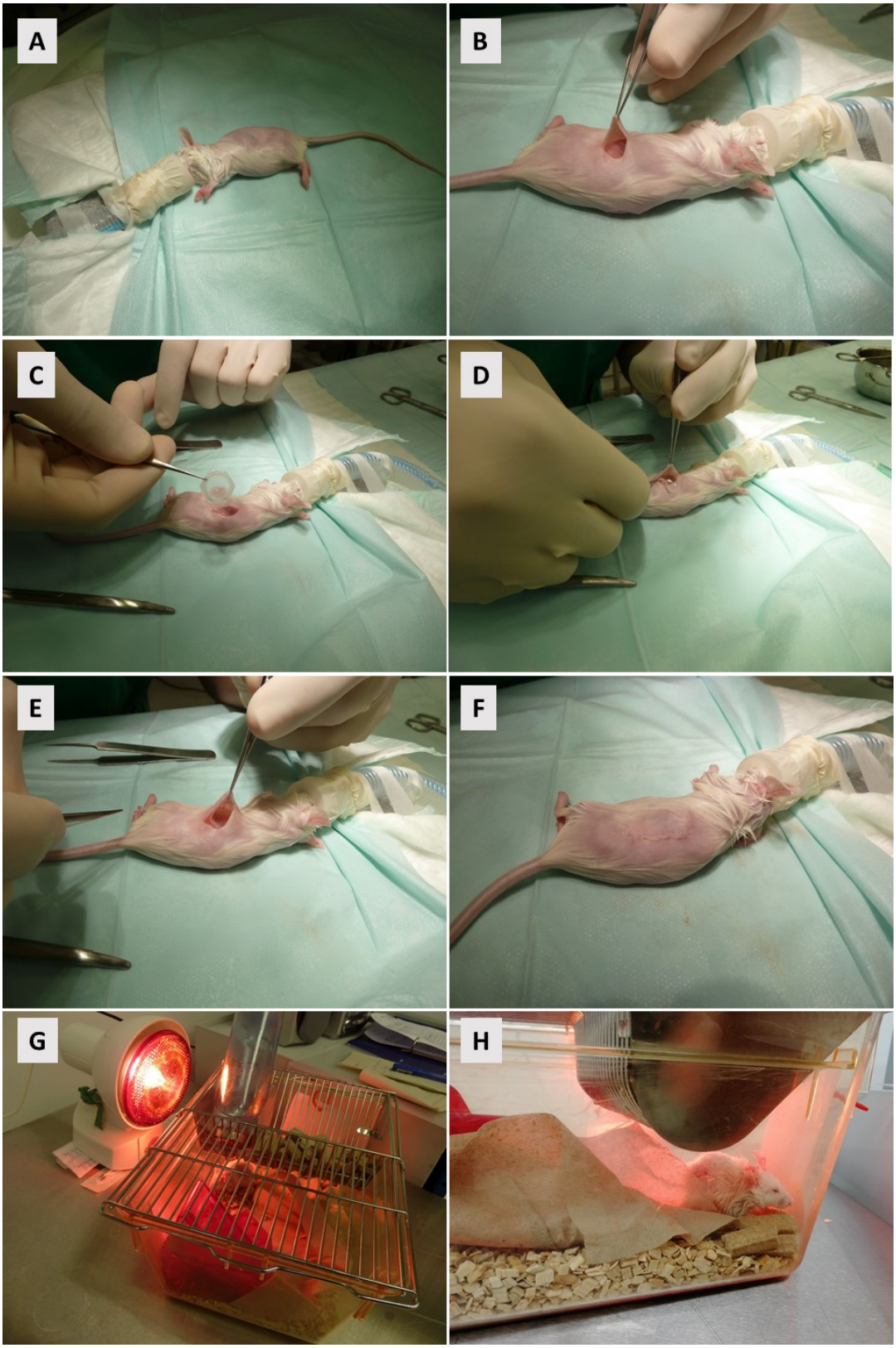

Figure 5.4. Steps of the implantation procedure. (A) Mice are anesthetized, and the surgical site is disinfected and prepared. (B) A lateral incision is made, and a subcutaneous pocket is created through blunt dissection. (C-E) The scaffold is implanted in the pocket and checked for correct positioning and flatness. The wound is checked for hemostasis. (F) Closure of the wound in a single layer. (G and H) Mice are allowed to recover under an infrared lamp before being caged individually.

Appropriate positioning of the implants was checked before closing the wound to make sure that the scaffolds, as much as possible, were flat without folding, as well as to check for proper hemostasis. The wound closure was done in one layer (skin and subcutaneous tissue) with Vicryl 6-0 uncoated, undyed sutures equipped with a reverse cutting needle (Ethicon, Somerville, NJ, USA). After both sides were operated on, the mouse was allowed to recover in an individual cage, warmed by an infrared lamp. In general, five mice were operated on per day.

The wound closure technique was altered twice during the course of the study. During the pilot phase, an inverted running suture was chosen to close the wounds. During the main experiment, the technique was changed to a simple interrupted one, however, this was accompanied by a high complication rate, and the original inverted running technique was reused again, albeit with decreased suture tension.

5.2.5.3 Follow up and animal care

The mice were followed up 4-5 hours postoperatively and then daily until the day they were to be sacrificed. In case of open wounds within the first 24 hours postoperatively, re-suturing was attempted, under complete aseptic conditions and under general anesthesia (isoflurane inhalation, same protocol as in the surgery). Tramadol in drinking water (20 mg/mL) was administered for 7 days postoperatively in the Day 14 group, or until euthanasia in Day 2, Day 4 and Day 7 groups.

5.2.5.4 Sacrifice and sample collection

On the assigned day for sacrifice for each group, the mice were individually euthanized by carbon dioxide inhalation, confirmation of death was done by checking the corneal reflex, followed by cervical dislocation. The implantation site was carefully inspected (and when any abnormality was detected, photographed) and then shaved with an electric razor. The mouse is then placed in the supine position and pinned down through the limbs for fixation. **Figure 5.5** provides a summary of the sample excision steps.

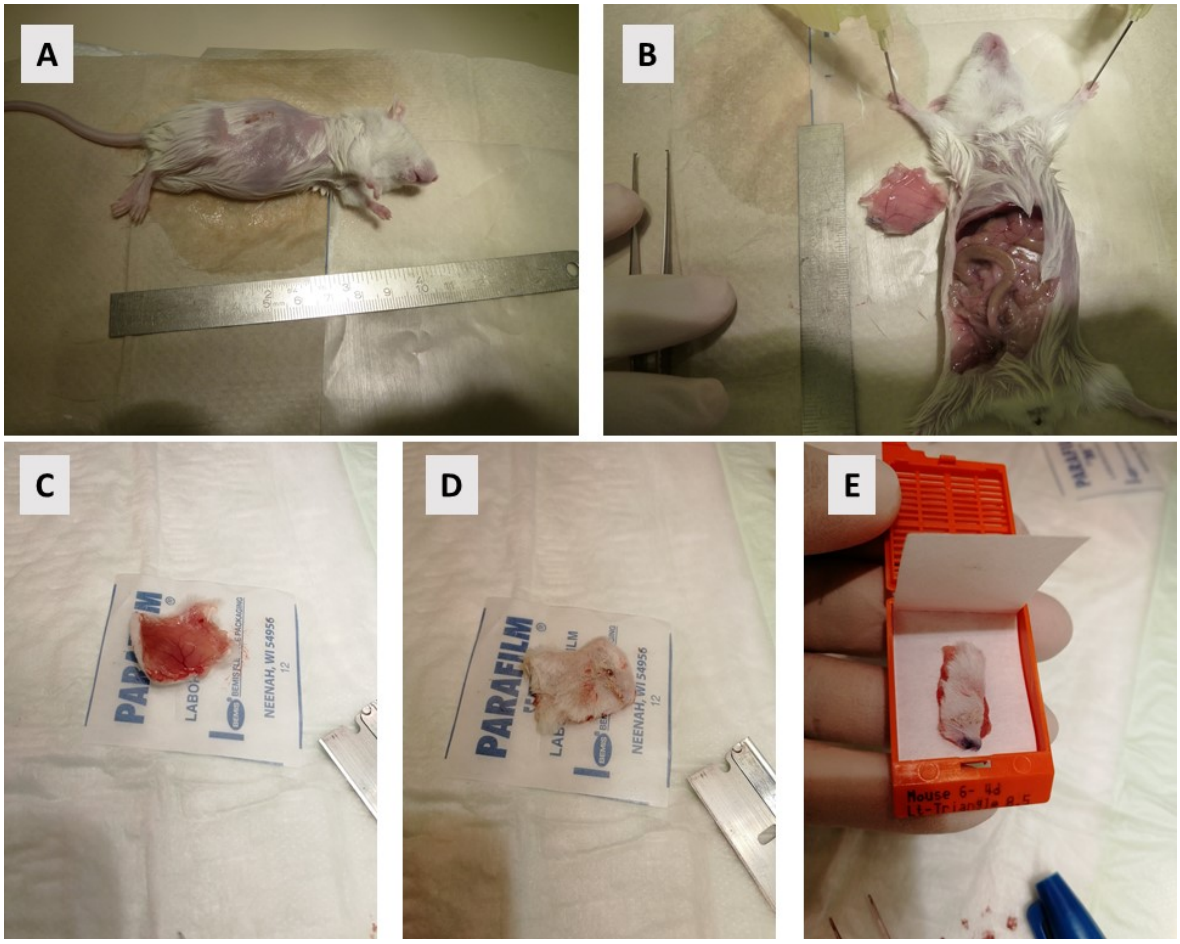

Figure 5.5. Steps of sample excision. (A) Mice are euthanized with CO_2 inhalation and cervical dislocation. The excision site is wetted for easier dissection. A tissue block is excised (B), inspected (C and D) and cut in two parts. One part is placed inside a standard histology cassette for fixation in formaldehyde solution (E).

A median abdominal incision through the skin, subcutaneous tissue, abdominal muscles and peritoneum was done and extended cranially till the xiphoid process and caudally till the urethral orifice. The incision was then extended laterally on both sides till the scapular line. When possible, the implantation site of the constructs was superficially identified through the contour of the implanted scaffold frame, or the film. If this was not possible, then the suture line was used as a landmark for the excision. A tissue block of approximately 20x20 mm was dissected out, composed of the overlying skin, subcutaneous tissue (with the scaffold, film or empty pocket inside), and the abdominal muscles. The gross appearance of the tissue block was noted in terms of vascularization and inflammation. The remaining subcutaneous tissue around the excision site was then thoroughly inspected to make sure that the no constructs were left behind. Finally, the tissue block was cut into two halves using a razor

blade in one move. One half was handed over for further experiments for RNA isolation. The other half was placed between two pieces of filter paper, inside a standard histology cassette to preserve the flat shape of the tissue block. During the pilot phase, tissue was fixed in a commercial, methanol-stabilized 4% formaldehyde solution (Merck 1.00496.5000), while in the main experiment in also a similar, commercial, methanol-stabilized, albeit 4.5% formaldehyde solution (Roti Histofix, Carl Roth 2213.6).

One additional NRMI mouse was sacrificed for tissue collection without undergoing any surgeries. A tissue block corresponding to that taken from the study animals, as well as spleen and liver tissue parts were collected to be used as normal controls in the immunohistochemical staining.

5.2.5.5 Tissue processing

The tissue was kept in the fixative solution at RT for 48 hours during the pilot phase and 24 hours during the main experiment. Afterwards, the tissue, while still inside the cassette, was washed twice with ddH_2O, before being placed in an automatic tissue processor (Thermo Scientific Mircrom STP 120, Thermo Fischer Scientific Inc., Schwerte, Germany) for a 14-hour program of immersion in: one change of each of 50%, 70%, 80%, 99% ethanol, two changes of 2-propanol, one change of 2-propanol/xylene 1:2, two changes of xylene, and two changes of paraffin. The cassettes were then collected, and the tissue taken out to be embedded into a paraffin block using an embedding system (MEDITE TES Valida, Burgdorf, Germany) with molten paraffin at 65 °C, then left to cool down in RT. Embedding was always done in the same way, so that the sharp edge that resulted from cutting the tissue block in two halves was placed down first to be at the paraffin block outer surface, i.e. sectioning should be from central part of the scaffold to the periphery.

5.2.5.6 Sectioning

A manual rotary microtome (microTec CUT 4060, Forchheim, Germany), equipped with disposable low-profile microtome blades (SLEE Medical GmbH, Mainz, Germany, article number: 28407000), was used to first surface the blocks using 10 and 20 µm steps, then to cut 5 µm sections

that were floated in ddH_2O at 42 °C and mounted on positively charged glass slides (R. Langenbrinck SuperFrost Plus, Emmendingen, Germany). Slides were left overnight inside a 37 °C oven to dry. The blade movement to section the paraffin block was always from the muscle layer (deep) towards the skin layer (superficial) to decrease the paraffin ribbon fragmentation. Mr. Esteban Ceballos assisted in the sectioning of the paraffin blocks. Sequential sections were used in all experiments.

5.2.6 Staining

5.2.6.1 Histochemical staining

The protocols for the various histochemical staining methods were kindly provided by Ms. Purificación Ripalda Cemborain from the University of Navarra, Pamplona, Navarra, Spain. The protocols were individually adapted for use and updated from the literature (Riedelsheimer and Büchl-Zimmermann 2015). The detailed staining protocols for each method are summarized in **Appendix 3**.

A common step in all protocols is the deparaffinization step. Slides were deparaffinized by placement in a 60 °C oven for 15 minutes, followed by submerging in two changes of xylene, one for 15 minutes and the other for five minutes, then two minutes in each of a graded series of ethanol concentrations (100% twice, 96%, 80%, and 60%). Slides were rehydrated in ddH_2O for five minutes. Histological staining was then performed using hematoxylin and eosin (HE), as well as picrosirius red (PSR) stains (Riedelsheimer and Büchl-Zimmermann 2015). Following staining, dehydration was performed in an ascending concentration of ethanol (96% twice, 100% twice) then two incubations in xylene. Coverslipping was done with a synthetic resin, Roti-Histokitt (Carl Roth 6638.2) and 24x60 mm coverslips, with a thickness of 0.13-0.16 mm (R. Langenbrinck, Emmendingen, Germany). Slides were left overnight under a fume hood for drying. Afterwards, excess resin from coverslipping was removed with a razor blade, if any.

5.2.6.1.1 Hematoxylin and eosin

The standard HE stain was used as the primary stain to assess the sections and decide if further sectioning was needed to find the region of interest (ROI) of the implant inside the tissue block. After deparaffinization and rehydration, the slides were incubated in Mayer's hematoxylin (Sigma-Aldrich MHS32-1L) for 15 minutes, then briefly rinsed in tap water. Bluing was done by either washing for ten minutes in running tap water or incubation in 0.1% sodium bicarbonate solution (w/v, in ddH_2O) for two minutes. Using either method, two minutes of washing in ddH_2O followed, before incubation in 0.5% Eosin-Y solution (Carl Roth X883.2) for two minutes. Slides were briefly washed in running water, before being dehydrated and coverslipped, as mentioned above.

5.2.6.1.2 Picrosirius red

PSR was used to assess the collagen deposition around the scaffold/film and the new collagen formation inside the scaffolds. After deparaffinization, the slides were placed in ddH_2O for five minutes, then for one hour in a solution of 0.5 g sirius red (Direct Red 80, Sigma-Aldrich 365548) dissolved in 500 mL of 1.3% saturated picric acid solution (Sigma-Aldrich P6744-1GA). Two quick washings (dipping for three times for each) in 0.5% acetic acid solution (in ddH_2O) were done followed by rapid dehydration and coverslipping, as previously mentioned.

5.2.6.2 Immune staining

5.2.6.2.1 General

Several iterations and optimization steps to reach a final working protocol for immunohistochemistry (IHC) were performed. This included multiple antigen retrieval methods, primary and secondary antibodies and detection systems. Moreover, immunofluorescence was also attempted. Ultimately, the protocol presented in this chapter was the most robust one and with the best reproducible results. The detailed staining protocols are listed in **Appendix 3**.

5.2.6.2.2 Immunohistochemistry

The working protocol was partly based on protocols from Ms. Purificación Ripalda Cemborain and later adapted to the manufacturer (Vector Labs, Abcam and Dianova) recommendations for the IHC detection system and antibodies, resepctively.

5.2.6.2.2.1 Antigen retrieval

Owing to the use of FFPE, antigen retrieval (AR) was deemed necessary to unmask antigens after being crosslinked by formaldehyde during fixation (Shi *et al.* 2011, Webster *et al.* 2009). The two available retrieval methods, heat-induced and proteolytic-induced epitope retrieval (HIER and PIER, respectively) were tested (Webster *et al.* 2009). For PIER, treating the sections with trypsin (Sigma Aldrich T7168-20TAB) and proteinase K (Merck 21627) was done. For HIER, heating the sections in 10 mM citrate buffer (pH 6) (Carl Roth X863.1) or Tris-Ethylenediaminetetraacetic acid (EDTA) buffer (TE buffer) (pH 9) inside a domestic, electric pressure cooker or a domestic microwave was tested. After thorough testing, the method of choice was HIER with citrate buffer inside the pressure cooker. The duration of the heating and amount of pressure inside the cooker were empirically tested until proper settings were reached, where the tissue sections did not sustain damage or were washed away due to the process.

5.2.6.2.2.2 Antibodies and controls

Based on previous literature, IHC was used to visualize macrophage infiltration of the implants, as well as blood vessels in and around the constructs (Roman Regueros *et al.* 2014, Slezak *et al.* 2018). To identify macrophages and giant cells in the tissue sections, a pan-macrophage anti-CD68 polyclonal rabbit anti-mouse antibody (1:500, Abcam ab125212) was selected. While for endothelial cells, a monoclonal anti-CD31 rat anti-mouse antibody (1:50, clone SZ31, Dianova DIA-310) was used.

Secondary antibodies were part of a horseradish peroxidase (HRP) polymerized reporter enzyme staining system from Vector Labs (Burlingame, CA, USA). The detection kit included secondary

antibodies, which were raised in goat against the respective species of the primary antibodies and were conjugated to micropolymeric HRP, allowing a one-step detection system with amplification.

As positive controls, mouse liver tissue was used. As negative controls, three controls were used: 1) normal mouse skin (with subcutaneous tissue and abdominal muscle), 2) omission of primary antibody and overnight incubation with PBS instead, and 3) immunoglobulin isotype control in the same concentration as the primary antibodies (Rabbit IgG or Rat IgG, Vector Labs I-1000 or I-4000, respectively) (Hewitt *et al.* 2014). Representative images of all different controls are shown in **Appendix 4**.

5.2.6.2.2.3 Staining

After the deparaffinization, samples were immersed in ddH_2O for five minutes followed by five minutes in PBS. Antigen retrieval with 10 mM citrate buffer (pH 6) was performed in a domestic electric pressure cooker (SAGE SPR700BSS4EEU1) for five minutes with pressure set to 50 kPa. Slides were allowed to cool down to RT for 20-30 minutes before being washed again in PBS for five minutes. Quenching of endogenous peroxidases was done in 3% hydrogen peroxide (in ddH_2O) for 15 minutes followed by another five-minute wash in PBS. Blocking of non-specific protein binding was done with a 2.5% normal goat serum solution (from Vector ImmPRESS HRP Kit, Vector Labs MP-7444 for anti-rat kit and MP-7451-15 for anti-rabbit kit) for 45 minutes. Excess blocking solution was removed, and then primary antibodies (diluted in PBS) were applied and incubated overnight in 4 °C in a humidified chamber.

The following day, slides were washed for ten minutes in PBS, then secondary antibodies from the respective HRP detection kits against either rabbit or rat primaries were applied as is without dilution (Vector ImmPRESS HRP, Vector Labs, see above) in a humidified chamber at RT for 30 minutes. Afterwards, the slides were washed three times for ten minutes each in PBS. As an HRP substrate, Vector ImmPACT NovaRED Kit (Vector Labs SK-4805) was incubated for three minutes, followed by incubation in ddH_2O for five minutes. Counterstaining was done for seven seconds in Modified Harris'

hematoxylin solution (Sigma-Aldrich HHS32-1L), washed with tap water and then dehydrated and coverslipped, as previously described.

5.2.7 Microscopy

HE-stained slides were checked using a Zeiss Imager.M1 microscope (Carl Zeiss, Oberkochen, Germany) for the presence of the implanted constructs inside the tissue block. When no construct was visible, the paraffin block was sectioned again, and the staining process repeated. Initial slide checking was done with a 10x lens. Imaging was achieved with the 20x lens for an overview and with 40x for high-powered field (HPF) images. When needed, the automated microscope stage was used to capture tiled images of the tissue sections, which were auto-stitched, to capture a greater area of the slide. The capture settings were kept constant during imaging of the IHC images (same illumination and exposure time) using the brightfield mode of the microscope. In addition, all slides were scanned at 40x with a 3DHISTECH Panoramic SCAN II (3DHISTECH, Budapest, Hungary) for archiving and further image analysis.

5.2.8 Image analysis

5.2.8.1 Histomorphological analysis

5.2.8.1.1 Hematoxylin and eosin

HE-stained were qualitatively analyzed with a focus on the scaffold integrity, presence and type of inflammatory cells at implant-tissue interface and inside the scaffold pore spaces.

5.2.8.1.2 Picrosirius red

PSR-stained slides from all groups were examined with brightfield microscopy for the presence of collagen deposits (appears red in the stained tissue) inside the pore spaces and at the scaffold-tissue interface. The slides from the Day 7 and Day 14 groups were qualitatively analyzed.

5.2.8.2 Quantification of CD68 staining

At least ten representative HPF micrographs from a representative slide per sample were used. Images were saved in the proprietary Carl Zeiss format (CZI). A custom macro was written for the open-source image processing package Fiji (Schindelin *et al.* 2012), running ImageJ v1.52n, to automate the analysis, reducing user bias (The ImageJ macro code is listed in **Appendix 2**). User interaction was only needed to adjust the position of the ROI, which was a rectangle of the same size in all images (120x150 µm), whether by simple placement adjustment or by rotating the ROI to coincide with the rotating scaffold segment. Briefly, based on published methods for image analysis (Fusser *et al.* 2019) and for color deconvolution (Fuhrich *et al.* 2013), stain separation for the CD68 stained IHC micrographs was done on the truecolor (RGB) image (converted from the 8-bit color CZI original image) to separate the NovaRED-stained structures from the blue hematoxylin counterstain, and then a threshold was applied to create a binary mask to the image. ROI selection was done on the RGB image and saved to be used on the masked binary image. The threshold was empirically selected and was the same in all analyzed images. The stained area of CD68 was calculated as a percentage of the selected ROI (120x150 µm).

5.2.8.3 Qualitative analysis of CD31 staining

The slides were examined for the presence of CD31-positive vascular structures around the implants and inside the pore spaces of the scaffolds as previously reported (Slezak *et al.* 2018). Although not factored into the analysis, the difference in vascularization between the scaffold and its reinforcing frame was also observed.

5.2.9 Statistical analysis

For the IHC quantification, the mean and standard deviation (SD) were presented. Statistical analysis was performed using OriginPro 2020 (OriginLab, Northampton, MA, USA). A two-way analysis of variance (ANOVA) test followed by Tukey test were performed, although the data showed a non-

normal distribution using the Shapiro-Wilk test. It was previously shown that ANOVA was robust enough and can accept as input non-parametric data (Blanca *et al.* 2017) when sample size is high enough. For IHC quantification, after exclusion of defective samples, at least n=40 per control group (4 mice and at least ten HPF images per implant) or n=80 per scaffold group (8 mice and at least ten HPF images per implant) were used in the statistical analysis. Statistical significance was defined as $p < 0.05$.

5.3 Results

5.3.1 Scaffold characterization

5.3.1.1 Gross appearance

The PCL MEW-fabricated scaffolds as well the PCL films had on one side a smooth, shiny surface, which was the surface in contact with the glass surface during production. The upper side in the case of scaffolds had multiple intersections of the fiber walls, creating small, projecting domes, as well as the outer frames, which were visibly thicker than the scaffold they were reinforcing. The upper side of the film was in contact with the metal applicator used to cast it and had a matt, whitish surface. The different side for both types of implants could be readily visualized.

The cross section of the scaffold was not possible to directly measure whether by a caliper or by cutting and vertical mounting for SEM measurement. Instead a calculation was done, based on the fiber diameter (see below) and the layer count. The frame, however, was possible to be measured directly by a caliper, and had a thickness of approximately 450 µm. The film was measured also by a digital caliper and a thickness of 250 µm was recorded.

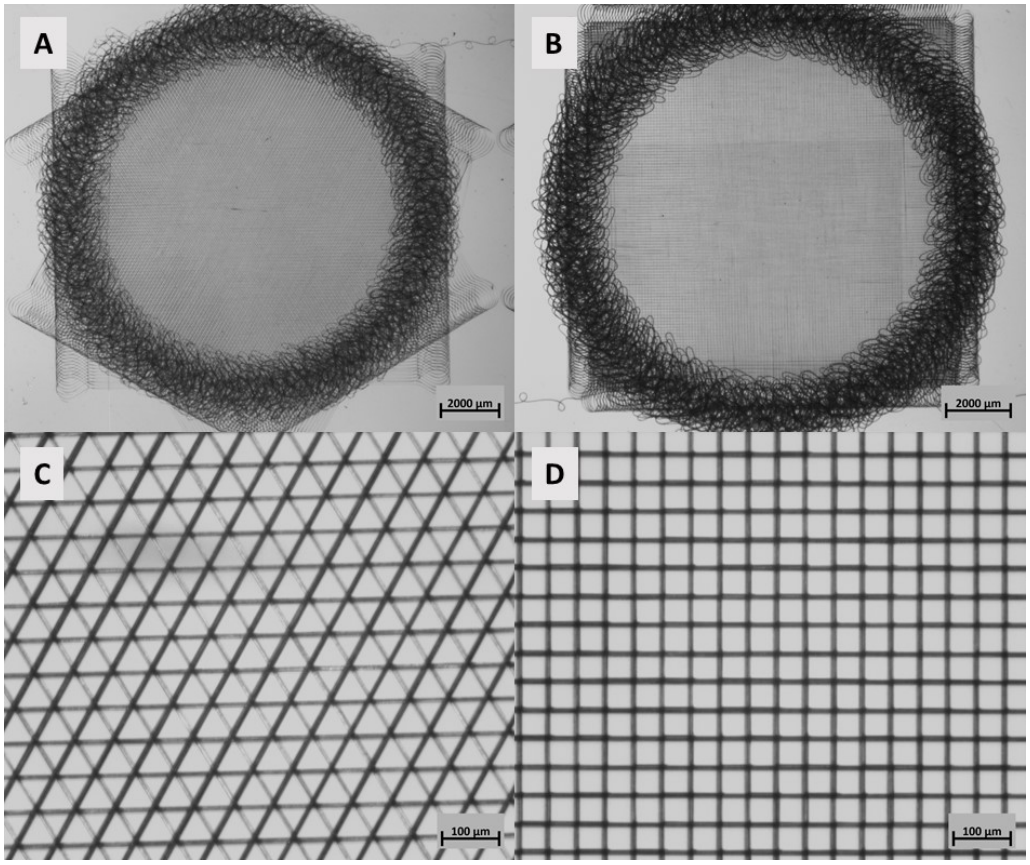

Figure 5.6. Stereomicroscope images of the scaffold groups. (A) shows a sample triangular scaffold with the frame and (B) a box one (Scale bar is 2 mm). (C) and (D) are higher magnification images of (A) and (B), respectively (Scale bar is 100 µm).

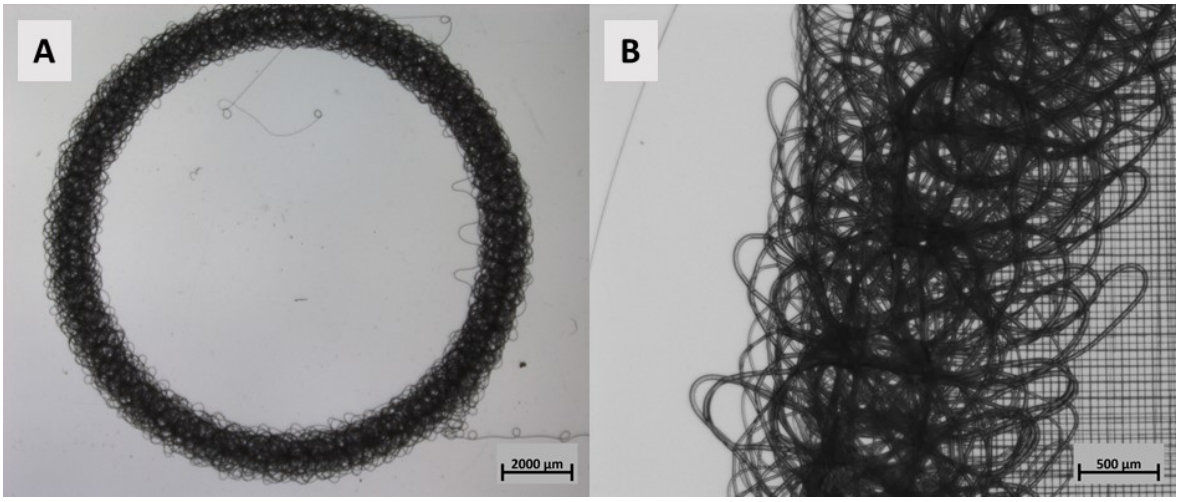

Figure 5.7. Printing of the frame around the scaffold for support. (A) shows the circular frame without a scaffold, while (B) is a higher magnification of a different scaffold showing the frame on top of a box scaffold. Scale bar is 2 mm in (A) and 500 µm in (B).

5.3.1.2 Stereomicroscopy

The individual examination of scaffolds rendered many scaffolds unusable due to the presence of defects that landed them in the "-" category. The overall success rate of printing a scaffold that was fit for implantation was less than 50%. **Figure 5.6** shows a representative scaffold from each of the box and the triangular groups. There was a visible difference between the scaffold itself and the frame, which was composed of thicker fibers with irregular spacing, by design. The frame fibers were deposited on top of the scaffold on the outer edges in a random coiling writing mode (**Figure 5.7**). The diameter of the scaffold with the frame was approximately 14 mm. In the box scaffolds, the corners of the scaffolds could still be observed outside the four quadrants of the circular frame, while in the triangle scaffolds, the six corners could still be observed, but to a lesser extent. **Figure 5.8** shows examples of rejected scaffolds with defects.

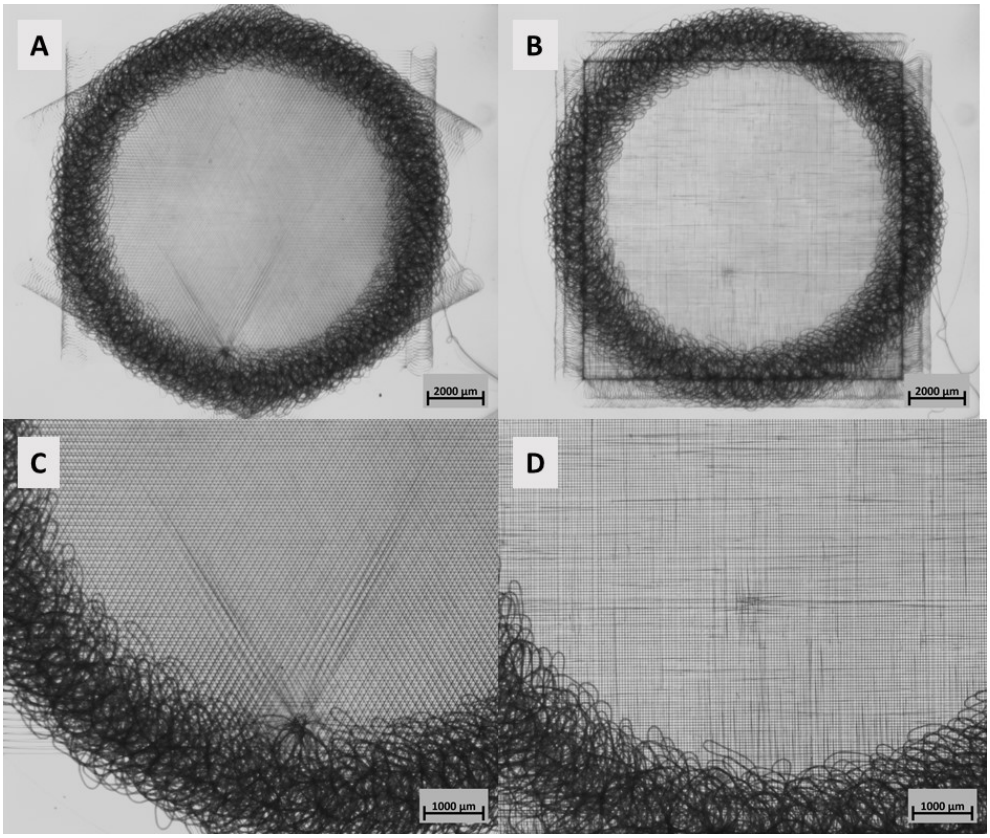

Figure 5.8. Examples of rejected scaffolds. (A) and (B) show scaffolds that would be rated as - in the three-rating system (+, - and +/-) in low magnification and (C) and (D) in a higher magnification. (A) and (C): Box scaffolds. (B) and (D): Triangular scaffolds. Scale bar in (A) and (B) is 2 mm and in (C) and (D) is 1 mm. Scaffolds were rejected when the defective morphology affected the intended design of the scaffold.

5.3.1.3 SEM

5.3.1.3.1 Pilot scaffolds

Using the SEM, the pilot experiment scaffolds, produced by Dr. Carina Blum, revealed an average diameter of 2.34 ± 0.25 µm for the triangular scaffolds and 2.32 ± 0.2 µm for the box scaffolds (n=30, three scaffolds from each type with ten random fiber measurements from the center). Sterilized samples showed diameters of 2.48 ± 0.12 µm and 2.5 ± 0.2 µm for triangular and box scaffolds, respectively (n=7 for each). The limited number of measurements were due to the limited number of scaffolds available, after excluding ineligible scaffolds. The morphological examination of scaffolds (**Figure 5.9**) showed that the fiber spacing was 62.46 ± 3.08 µm and 48.93 ± 2.83 µm for triangular and box scaffolds (n=7), respectively. The unsterilized box scaffolds had regular box-shaped pores (**Figure 5.9A**), while the triangular scaffolds had pores which were mostly triangular (**Figure 5.9E**). In some cases, there was a slight translation of the fiber walls, this resulted in pores with a quadrilateral part and a small triangular one at its apex. These small triangles were occasionally blocked by partially molten fibers from the intersecting fiber wall (**Figure 5.9G**). This translation was likely caused by a minor shift in the axis of the MEW printer. The sterilized samples from the pilot group were not as straight as the non-sterile ones and showed visible waviness and relaxation of the fibers (**Figure 5.9 A-B and E-F**). There were signs of fusion of the fibers with those beneath them (**Figure 5.9E, G**), especially in the triangular groups. The fibers in both box and triangular scaffolds of the pilot samples showed a slightly rough surface with some banding (**Figure 5.9C**), except when melting was observed (**Figure 5.9G**). Some crystalline structures were also visible on the surface of the fibers in the sterilized group, probably due to the salt precipitation from the PBS solution, in which they were washed and stored (**Figure 5.9D, H**).

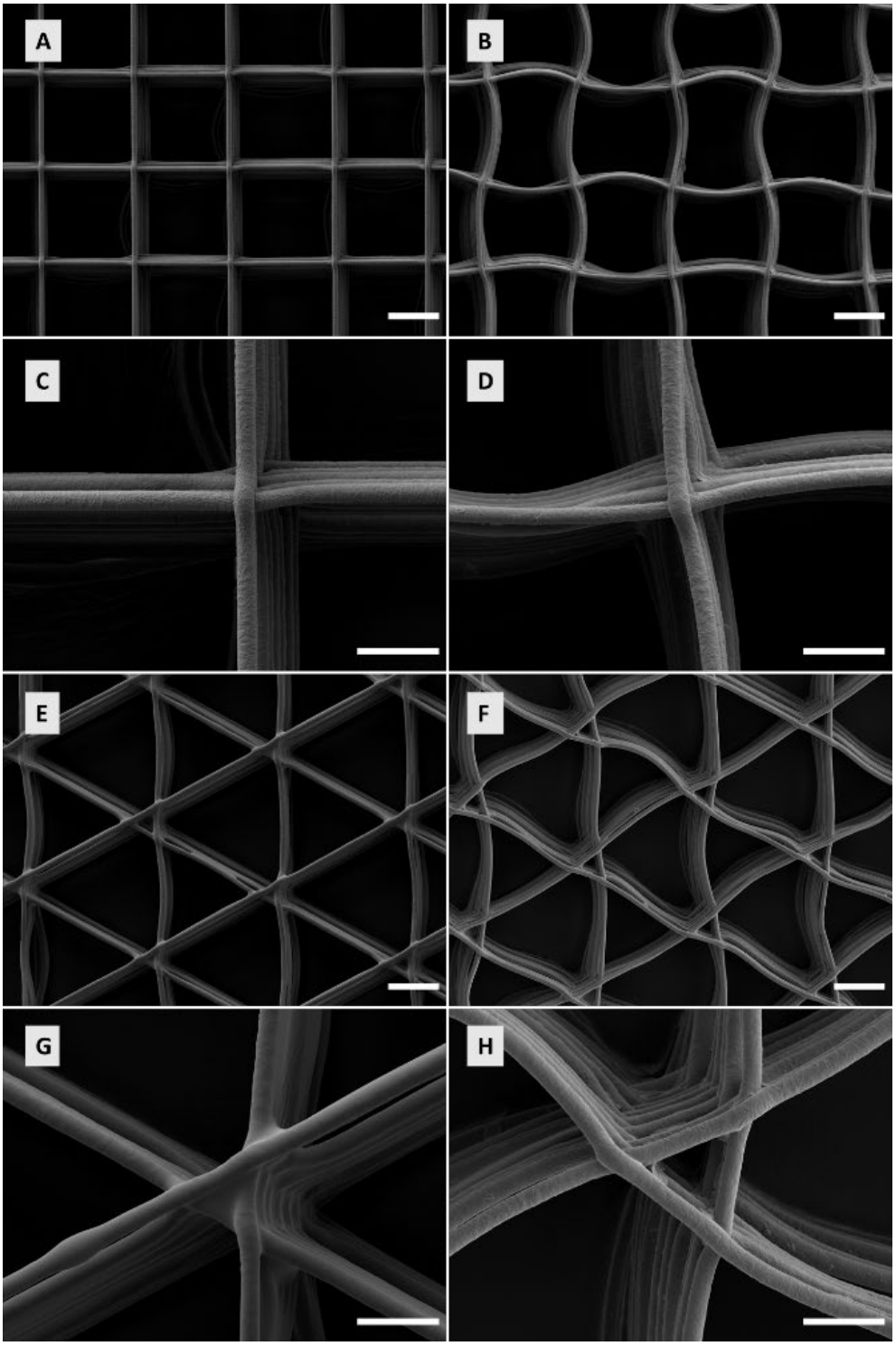

Figure 5.9. SEM images of MEW scaffolds from the pilot experiment. (A) shows a box scaffold before sterilization in two changes of 70% ethanol and washing multiple times in 1X PBS and (B) afterwards. (C) and (D) are higher magnification images of the intersection points of the fiber walls, before and after sterilization, respectively. (E) and (F) are images of a triangular scaffold before and after sterilization, respectively, with (G) and (H) representing higher magnification images of the intersection points of the fiber wall at one of the apices of the triangular pores, before and after sterilization, respectively. Scale bar is 25 µm in (A), (B), (E) and (F). Scale bar is 10 µm in (C), (D), (G) and (H). Relaxation of the fibers could be seen after sterilization. In (G), the intersection points showed melting of the fibers and fusion. Scaffolds were produced by Dr. Carina Blum. SEM images were captured by Mr. Andrei Hrynevich.

5.3.1.3.2 Main experiment scaffolds

Fiber diameters of the box and triangular, non-sterilized scaffolds from the main experiment were 2.47 ± 0.25 µm and 2.48 ± 0.15 µm, respectively (n=30). Qualitive evaluation of the constructs using the SEM revealed scaffolds with uniform pore shapes for the box scaffolds (**Figure 5.10A-B**). In the triangle scaffolds (**Figure 5.10C**), similar to what was seen in the pilot phase, the apex of the triangular pores was isolated by the fiber walls, creating a small triangle in the apex and a larger quadrilateral below it (**Figure 5.10D**). This was uniformly present in the samples and could not be removed at the time of the experiments by changing printing parameters (**Figure 5.10C**). It was probably due to a minor shift in the axis of the MEW printer.

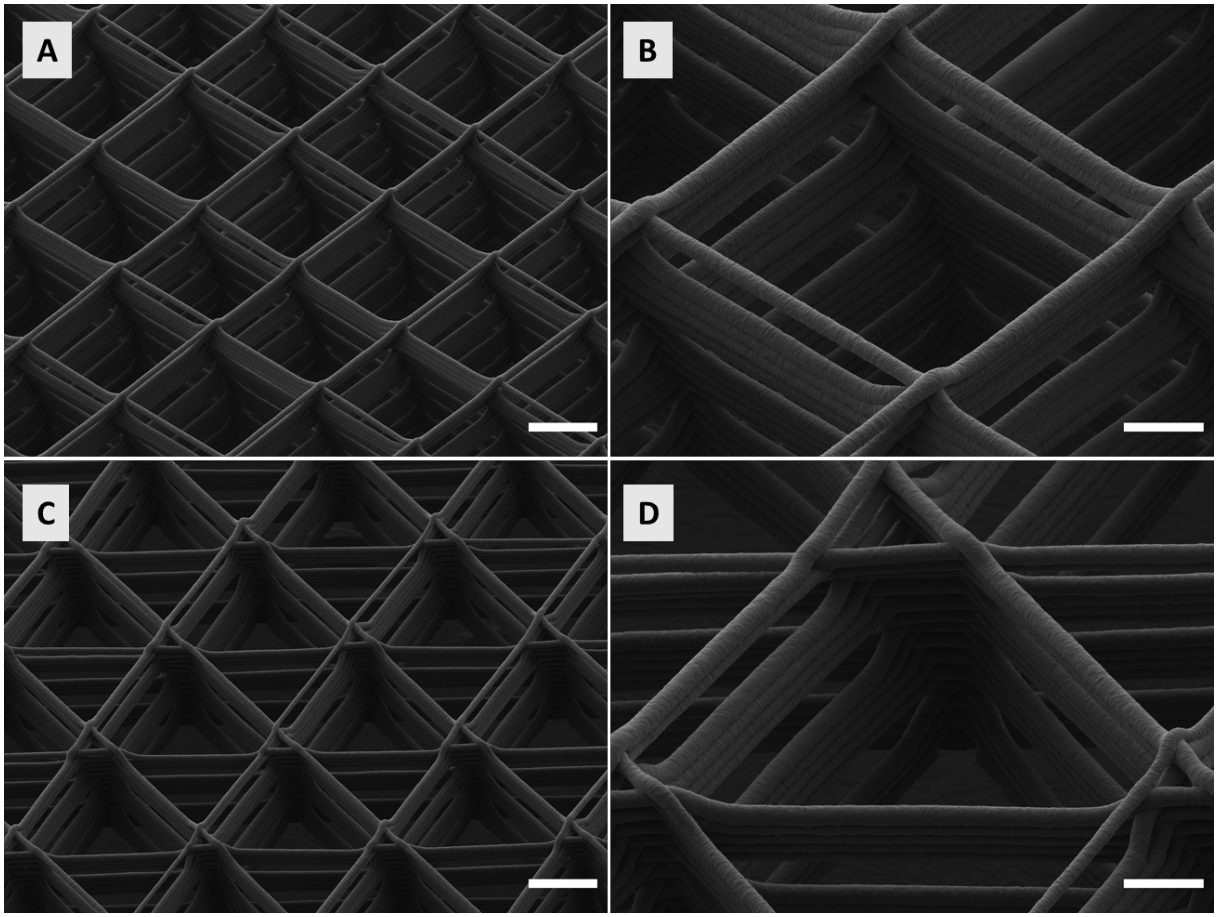

Figure 5.10. SEM images of the main experiment scaffolds. (A-B) Box scaffolds. (C-D) Triangular scaffolds. The box scaffolds showed regular box-shaped pores, while the triangular ones had a larger quarilateral pore and a smaller triangular one at the apex. Scale bar is 25 µm in (A) and (C) and 10 µm in (B) and (D). SEM images were captured by Mr. Andrei Hrynevich.

The fiber walls fused incompletely and at isolated foci. This meant that some sections of the fiber wall were made of clustered, fused fibers, forming mini-walls. These in turn were separated from each other by lateral pores (**Figure 5.10B, D**). This phenomenon was observed in both box and triangular scaffolds and was probably related to the low collector distance that was used for the printing. This could be caused directly through the melting of the top of the just-printed fiber by the proximity of the heated printing head, or through the small collector distance, where the short travel distance of the molten polymer jet might not have allowed for proper solidification before being deposited on the previous fiber. However, individual fibers could still be observed in the fiber walls in other sections of the scaffolds. The relaxation effect observed in the pilot scaffolds after sterilization was not seen in the main experiment scaffolds when examined under the SEM, which could mean that the effect could be handling-related during sample preparation for SEM visualization (**Figure 5.11A-B and E-F**). The fibers in both box and triangular groups showed a rough surface and occasional banding (**Figure 5.11C-D and G-H**), similar to what was already observed with the pilot scaffolds. Furthermore, some crystalline structures were detected on the fiber surface of the sterilized scaffolds, similar to what was seen in the pilot, and was probably due to some PBS remnants on the surface from the wash steps after sterilization (**Figure 5.11D, H**).

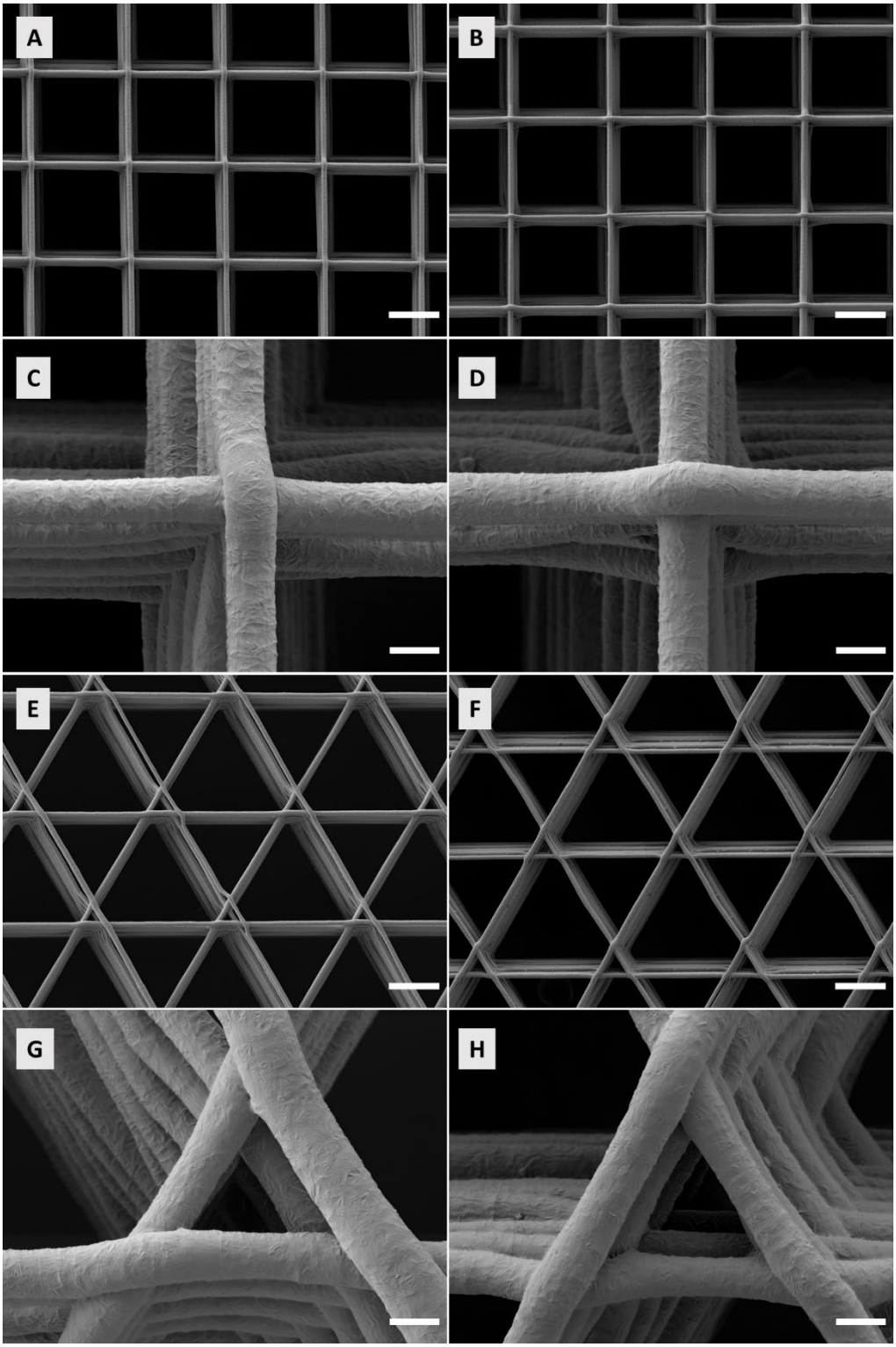

Figure 5.11. Further SEM images of main experiment scaffolds. (A-D) Box scaffolds. (E-H) Triangular scaffolds. The non-sterile scaffolds (A), (C), (E) and (G) and the 70% ethanol-sterilized scaffolds (B), (D), (F) and (H) show identical morphology with the exception of some crystal diposition on the fibers at higher magnification (D) and (H), compared to the already rough fiber surface in the non-sterile scaffolds (C) and (G). Scale bar is 25 µm in (A), (B), (E) and (F) and 2.5 µm in (C), (D), (G) and (H). SEM images were captured by Mr. Andrei Hrynevich.

SEM analysis of both sides of the film were also conducted (**Figure 5.12**). For the matt surface, the spherulite arrangement of the polymer were evident with gaps at the meeting point of adjacent spherulites (**Figure 5.12A-B**). For the smooth side of the film, it was challenging to focus the SEM, as the surface was too smooth with only occasional depressions in the film (**Figure 5.12C-D**). The same observation regarding the precipitation of crystals in the sterilized scaffold samples was also noted in the film samples (**Figure 5.12B, D**).

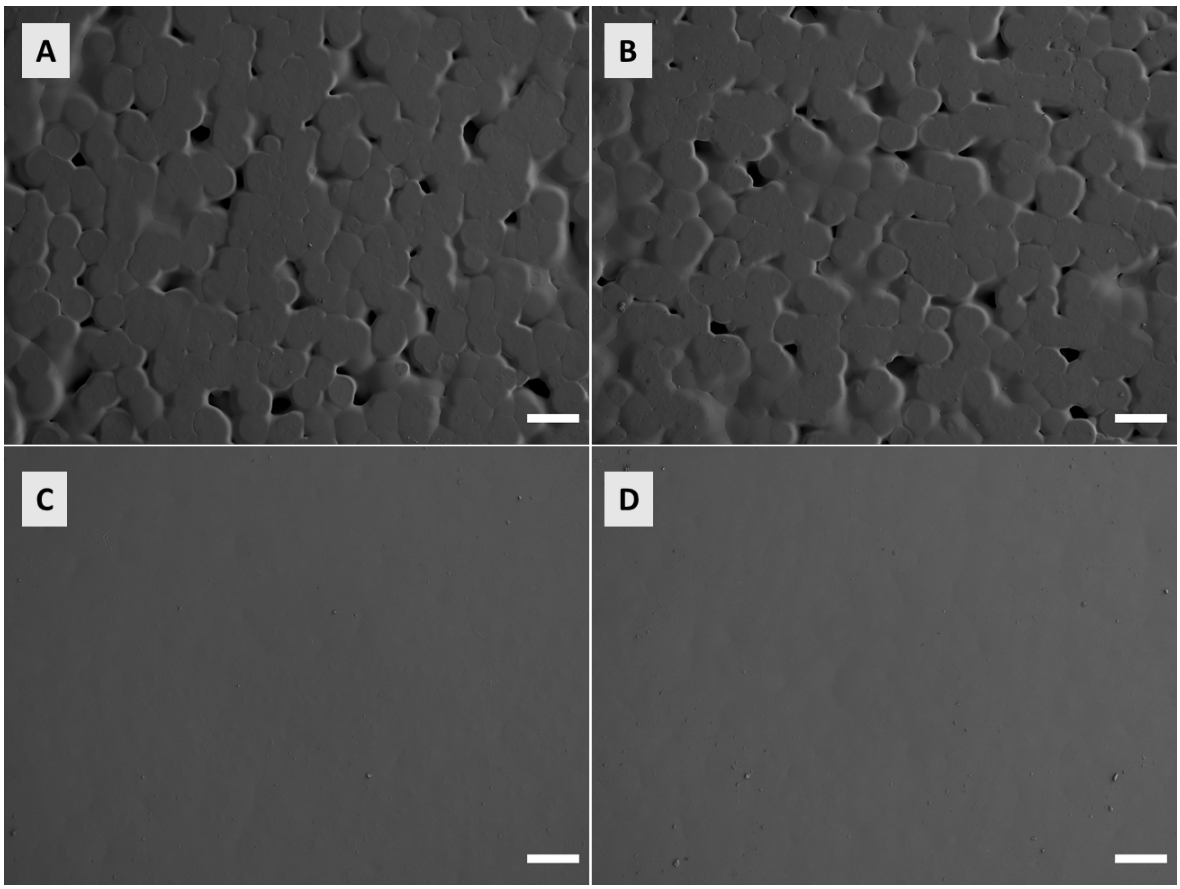

Figure 5.12. Scanning electron microscopy of PCL films. The melt drawn PCL film had a rough side that was in contact with the metal spacer (A) and (B) and a smooth side, that was in contact with the glass surface (C) and (D). (B) and (D) show films after sterilization in 70% ethanol and washing in 1X PBS. SEM images were captured by Mr. Andrei Hrynevich.

5.3.1.4 2D local thickness analysis

The analysis of the pore spaces in the images taken with the stereomicroscope gave 2D local thickness (2D-T_{loc}) maps which gave the diameter of the largest sphere (here, as the images are in 2D and not a 3D stack, a circle) which would fit a given pore space. **Figure 5.13** shows the workflow of the

measurement process for both the box and triangular scaffolds. The mean, standard deviation and maximum values of the measurement are listed in **Table 5.2**. The assignment of the grey value threshold to create the binary mask for the image is considered the main source of error in this measurement, as it was given subjectively, however, it remained the same for all measurements. **Figure 5.14** shows a graphical representation of the pore size distribution in both scaffold types.

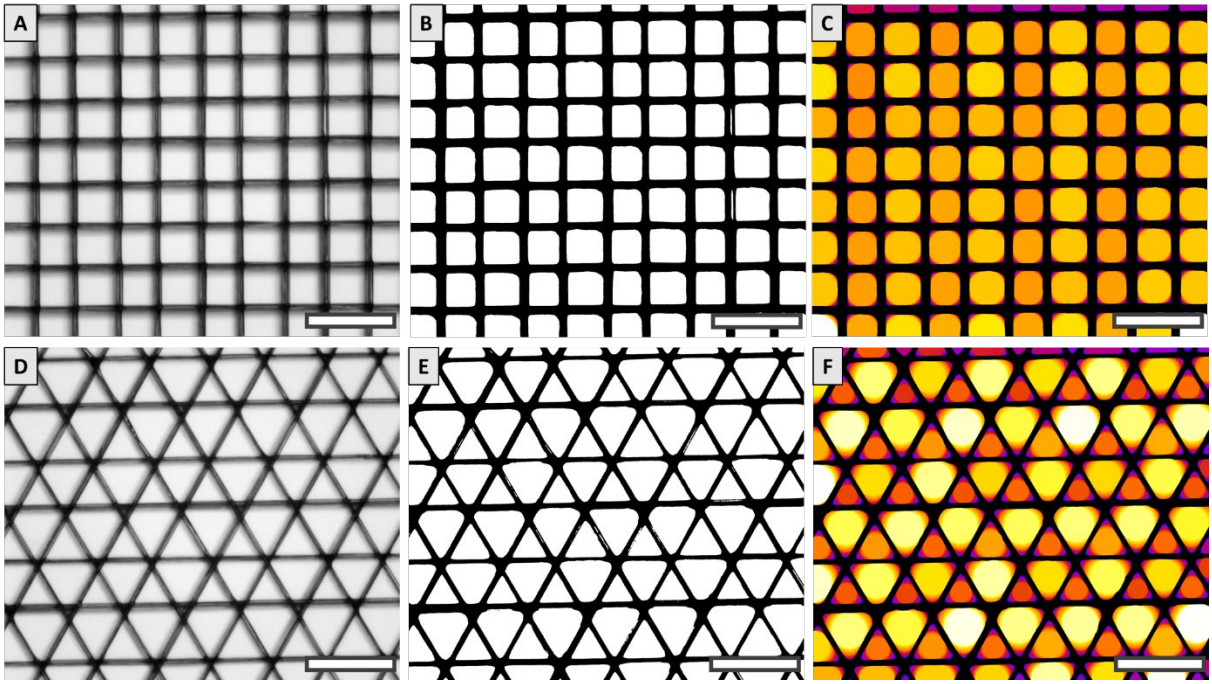

Figure 5.13 Workflow of the two-dimensional local thickness analysis (2D-T_{loc}) of stereomicroscopy images. The measurement process is shown for box scaffolds (A-C) and for triangular ones (D-F). Briefly, stereomicroscopy images (left side) were captured, then converted to a binary image by applying a thresold (middle). The binary image is used to calculate the 2D-T_{loc} of the detected pores. Colour coding of the right column: yellow: large pore, dark blue: small pore, black: scaffold fibers. Scale bars are 100 µm.

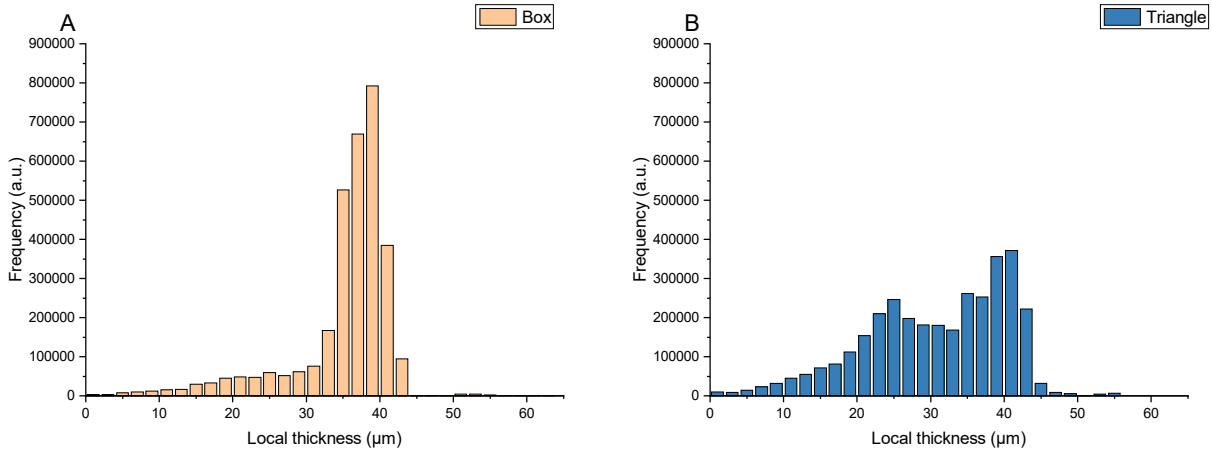

Figure 5.14 Graphical summary of 2D-T_{loc} for box (A) and triangular (B) scaffolds. Box scaffolds show a higher frequency of repeating pore sizes compared to triangular ones with a wider distribution.

Table 5.2. Summary of 2D-T_{loc} results for box and triangular scaffolds.

Scaffold	2D local thickness (2D-T_{loc})		
	Maximum (µm)	Mean (µm)	Standard deviation (µm)
Box (50 µm spacing)	63	32	18.76
Triangle (60 µm spacing)	55	28	16.45

5.3.2 Animal surgery

5.3.2.1 Pilot experiment surgical outcome

During the pilot experiment (all from the Day 4 group), the control group of animals (with PCL film on one implantation pocket and a sham surgery in the other) handled the surgery well, there were no local wound complications with no signs of inflammation or hemorrhage at the wound site. For the scaffold group, one mouse completely pulled the suture material from the wound, however the wound remained closed. On the assigned day for sacrifice, the wound was seen to be partially open, however, the implant was not externally visible. Another mouse had the wound completely open, although there were no signs of inflammation or hemorrhage, and the general condition of the mouse was normal. On excision, the wound was also partially open, and the scaffold could be seen in the wound floor. This mouse (both sides) was excluded from the analysis.

5.3.2.2 Main experiment surgical outcome

Two mice from Day 7 group bit off their sutures after 48 hours (excluding them from secondary closure by re-suturing) of the surgery and started to lose weight, so according to the humane endpoints of the study they had to be euthanized and the surgery was repeated with two new mice. However, when the surgery was redone, one mouse completely bit off the wound open on the day of the sacrifice (Day 7). After euthanasia, no scaffold was detected in the subcutaneous pocket, and it is presumed that the mouse took the scaffold out of the pocket. It is worth mentioning that in all these cases, the affected side was the right side in a scaffold group mouse (i.e. involving a box scaffold).

5.3.2.3 Re-suturing of open wounds

When the single interrupted sutured technique was used during the main experiment, 8 out of 15 animals required re-suturing of one or both sides. The affected side was the right side in two cases, the left side in another three and both sides were involved in the remaining three. A wound that required re-suturing was that which had more than two sutures missing, and this happened less than 24 hours from the primary closure. **Figure 5.15** summarizes the number of animals that suffered from complications and required re-suturing. All cases requiring re-suturing were in Day 2 or Day 7.

Once the running inverted suture technique (as in the pilot) was used again, with decreased suture tension, there were no further cases requiring re-suturing, except in the previously mentioned (see above) two cases in the Day 7 group but there, re-suturing was not performed as the injury occurred after 24 hours from the surgery. Once the animals were re-sutured, the wounds were considered closed, but afterwards they were, as with the rest of the mice, subjected to daily follow up and inspected thoroughly at the time of excision for further wound complications.

5.3.2.4 Wound complication

In total, 14 out of 62 mice (the two extra mice were to replace those euthanized from Day 7) had wound complications, observed at the time of sacrifice. At the time of excision, the right side was the site of the most complications in 10 of 14 animals (72%), followed by the left side in 3 of 14 animals (21%) or both sides in 1 of 14 animals (7%). Out of the ten mice that had an injury in the right side at excision, only one of them was in a control group mouse (1 of 14) (here, containing a PCL film). All the remaining nine mice contained box scaffolds. The definition of an injury at the time of excision was when more than two sutures were missing. Usually the wound was sutured close with at least five sutures. No mice from the sham group had any wound complications.

While it could be attributed to the change in the suturing technique, most of the complications were in the Day 2 and Day 7 animals. Day 14 had the least rate of complications. All of the five mice that were re-sutured in the Day 2 group had wound complications at the time of excision, compared to one of the three mice from Day 7. In total, six mice in Day 2, three in Day 4, four in Day 7 and one in Day 14 had wound complications. **Figure 5.15** summarizes the overall rate of complications that were faced in all the groups.

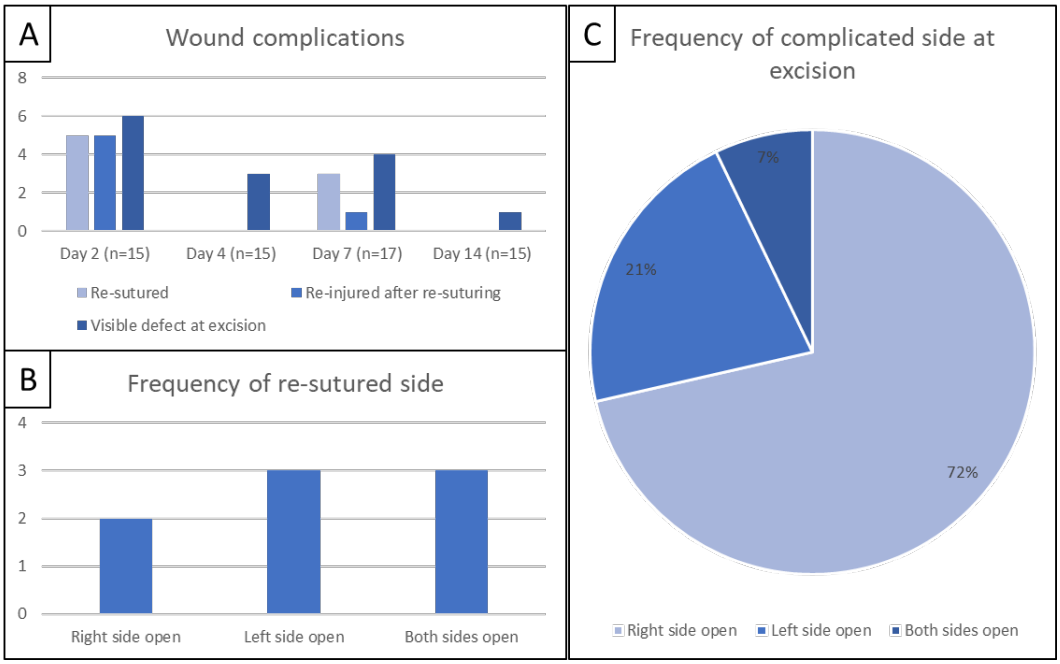

Figure 5.15. Graphical summary of the overall complications observed after surgery. (A) Wound complications were analyzed across the different time points regarding the performed counter measures and whether the wound was still problematic at the time of animal sacrifice. (B) The frequency of the need for re-suturing per side. (C) The right side was the most observed side with complications at the time of excision.

5.3.2.5 Gross evaluation of excised tissue

An uncertainty in the experiment was pinpointing the location of the scaffold for excision (**Figure 5.16A**). Attempting to relocate based on the contour of the frame was not always reliable (**Figure 5.16B**). The reliance on observing the slight elevation in the skin (or the muscle layer when looking from inside the abdominal cavity, was not always possible. It was not desired to dissect the constructs away from the tissue block, as it would nullify the sham group, and possibly cause damage to the scaffold-tissue interface or introduce artefacts. To work around this issue, a large tissue part of the abdominal wall was excised and then trimmed down, while taking care not to cut through where the implant was thought to be (**Figure 5.16C-F**). The other safety measure was to check for scaffold remnants in the remaining skin and subcutaneous tissue of the mouse. Another issue was dividing the scaffold into two parts, for RNA analysis. Although this was done in one motion with force and with a sharp, fresh razor blade, the exact location of the scaffold in the tissue block was not initially certain.

Moreover, the cutting could have led to lateral movement of the constructs inside the block, potentially causing detachment, if there was no sufficient tissue ingrowth in the constructs.

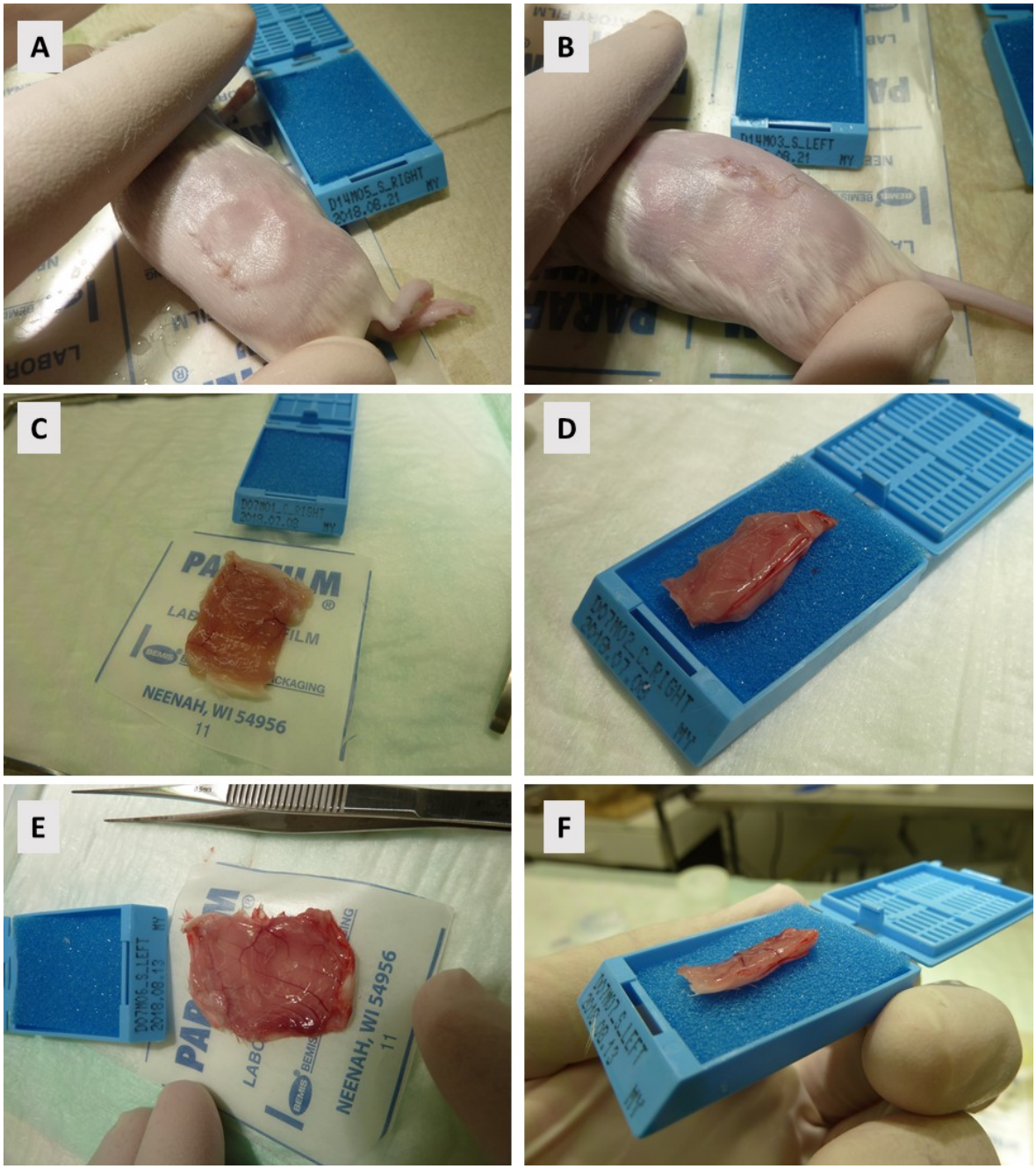

Figure 5.16. Sacrifice and sample excision. (A) Visualizing the implanted scaffold by observing the raised edges of the frame, while in (B) the results of this maneuver were not as successful. (C) An example of an excised film sample, with (D) showing the result of cutting the sample in two parts. The rigid film was not stationary inside the tissue block and was seen moving after the cutting. (E) An example of an excised scaffold sample (here a triangular one). (F) An example of a cut scaffold sample (different scaffold than the one in (E)).

The excised tissue with film implants showed poor tissue integration, as the film was freely movable inside the pocket and when the tissue block was cut, it tended to move out of the pocket (**Figure 5.16D**). In the scaffold groups, noticeable swelling in the region where the scaffold should be (by means of locating the circular frame) probably would signify folding of the scaffold in the pocket (**Figure 5.16E-F**). In all time points, the sham group tissue samples were excised using the suture lines as landmarks for the subcutaneous pocket location, as there were no bulging or contour changes from the scaffold frame or the PCL film. **Figure 5.16** shows examples of excised tissue and illustrates several challenges related to localization and cutting of different implants. **Figure 5.17** shows an assortment of wound sites from all the different groups.

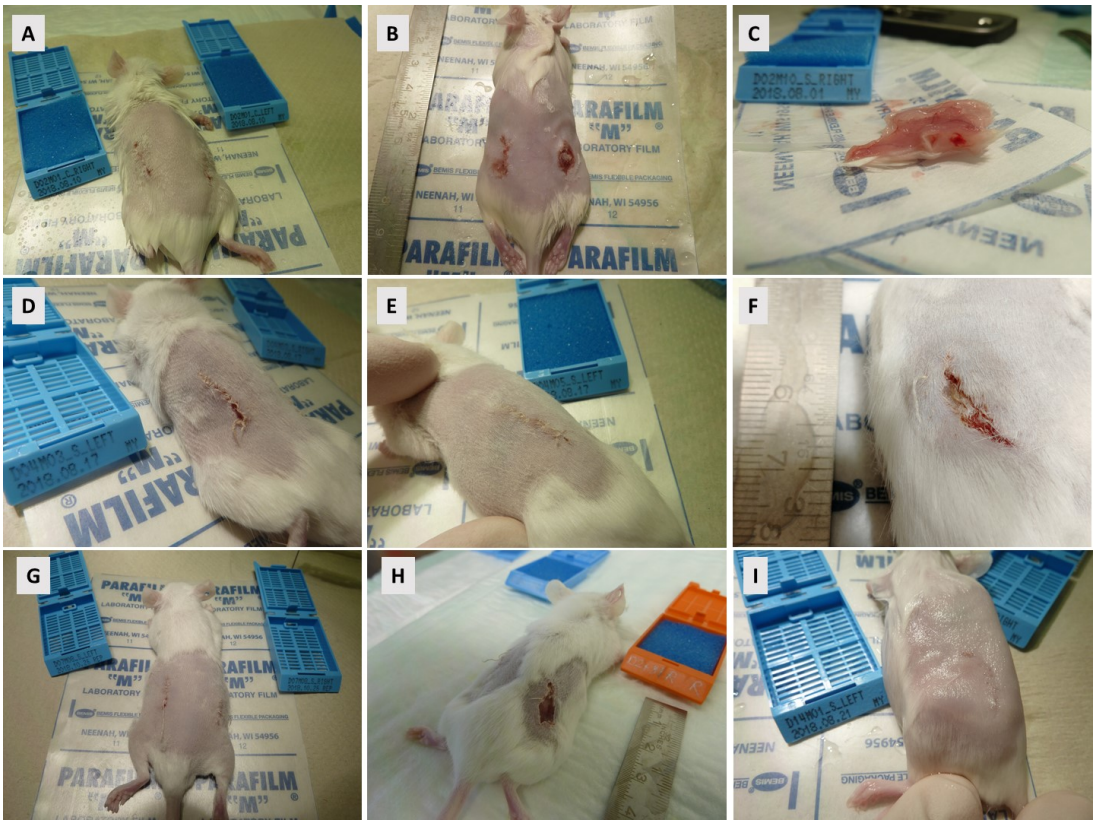

Figure 5.17. Wound sites at the time of excision. (A) Non-complicated wounds in a Day 2 mouse. (B) Partially open Day 2 wound on the right side. (C) The wound shown in (B) after excision of the tissue block containing the scaffold. (D) Day 4 mouse showing two bitten sutures with closed, non-complicated wound. (E) Closed, non-complicated Day 4 wound. (F) Open, complicated Day 4 wound showing scaffold in the wound floor. No signs of infection or exudate are seen. (G) Non-complicated Day 7 wounds. (H) One of the two mice that had to be euthanized early after sustaining the wound on the right side after 48 hours postoperative. (I) Non-complicated, healed Day 14 wound.

5.3.3 Histology

5.3.3.1 Sectioning

The initial identification of the implants in the paraffin blocks was challenging, owing to the uncertainty in macroscopically locating the implantation area during excision. Moreover, no inking of the samples was performed before fixation or microtomy. Approximately half of the paraffin blocks (57 out of 120) required further resurfacing to achieve deeper sections from the block until the implant appeared. This was done based on the initial HE staining and screening. In 16 out of 120 blocks, the paraffin blocks had to be melted and re-embedded, as it was discovered that the tissue was embedded in the other direction (frame side), instead of the cut side from the center. Although strict microtomy technique was followed, it could not prevent the dissociation of tissue layers from each other in some of the sections, especially in Day 2 samples, where tissue ingrowth was expected to be at the least. The scaffolds or films were not the cause of the ribbon dissociation, as they dissolved during paraffin embedding. The same was true for the Vicryl sutures used in wound closure, as the majority of dissociation was located at the implant-tissue interface, while suturing was further superficial to that site.

5.3.3.2 HE staining

5.3.3.2.1 General findings

The PCL MEW scaffolds, as well as the PCL films, dissolved during the paraffin embedding of the scaffolds, leading to the presence of a scaffold phantom, where the fibers were seen as empty spaces, and fiber walls were a stack of these empty spaces upon each other. The standard HE staining confirmed the location of the implants in the intended implantation site: subcutaneous between the external abdominal muscle (deep) and the dermis (superficial) (**Figure 5.18**). In most sections, the panniculus carnosus muscle could be clearly seen superficial to the implant. Across several samples from all time points, there was a variation in the presence or absence of adipose tissue, often with

mammary tissue (all mice used in the experiments were female). Oftentimes, the adipose layer was superficial to the scaffold, below the panniculus carnosus muscle, but it could also be found deep to the scaffold, superficial to the epimysium of the external abdominal muscle. The sham and film samples also captured this diversity. Occasionally, lymphoid tissue whether skin-associated lymphocyte aggregates (SALT) or inguinal lymph nodes were seen around the construct area. **Figure 5.19** presents a summary of some of the common findings related to the positioning of the constructs inside the tissue block.

Scaffolds in all time points tended to show several grades of folding (Figure **5.19A-B**) while being integrated in the tissue, i.e. the folding happened when the animal was alive and is not caused by excision and processing, from a simple "wave", to an isolated folded segment, followed by a straight segment, to finally the frame itself folding on top of the scaffold or on top of itself. Another morphological finding in the scaffolds, was the rotation in some areas, meaning that instead of seeing the scaffold in a transverse section, one could see it in a longitudinal one, with the vertical pore spaces visible. All these variations happened across all time points and seem to be caused by the structure of the scaffolds, on account of the small diameter fibers (approximately 2.5 µm across both scaffold types) and the fiber layer count (42 layers). In total, the scaffolds were calculated to be approximately 105 µm thick at the fiber wall intersections. **Appendix 5** includes additional representative images of the frame parts of the scaffold, which were not assessed during the qualitative analysis of HE-, PSR- and CD31-stained images or the quantitative one of CD68-stained images.

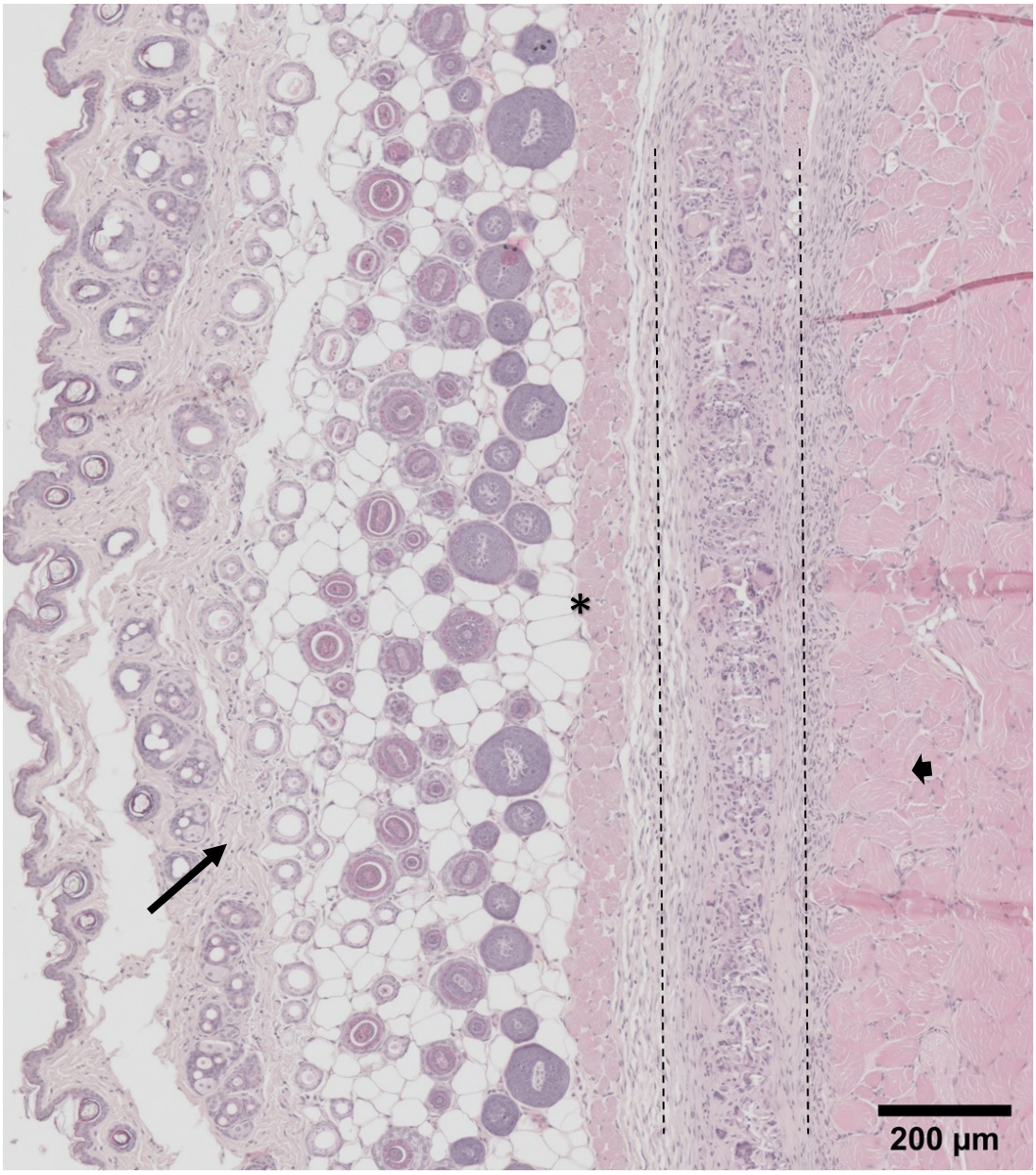

Figure 5.18. HE staining of a typical Day 14 box scaffold. The scaffold (between the dotted lines) is seen implanted in the intended position: subcutaneously, deep to the dermal layer (arrow) and above the striated abdominal muscle layer (arrowhead). The panniculus carnosus (asterisk) is seen superficial to the scaffold. In all figures shown later, the skin is always to the left (superficial layer) while the abdominal muscles are always to the right (deep layer). The scaffold material itself (PCL) is fully dissolved during the paraffin embedding in the tissue processing machine, by the effect of xylene. FBGCs shown are both the classic FBR type as well as the Langhans type.

The healing skin wound was occasionally visible with or without suture material. The wound granuloma consisted of a dense infiltration of inflammatory cells in a fibrin matrix with blood vessels in the periphery. The suture material could be identified through the presence of partially empty spaces, and by polarized light during microscopy. The Vicryl (polyglactin 910) braided suture lines partially dissolved during paraffin embedding.

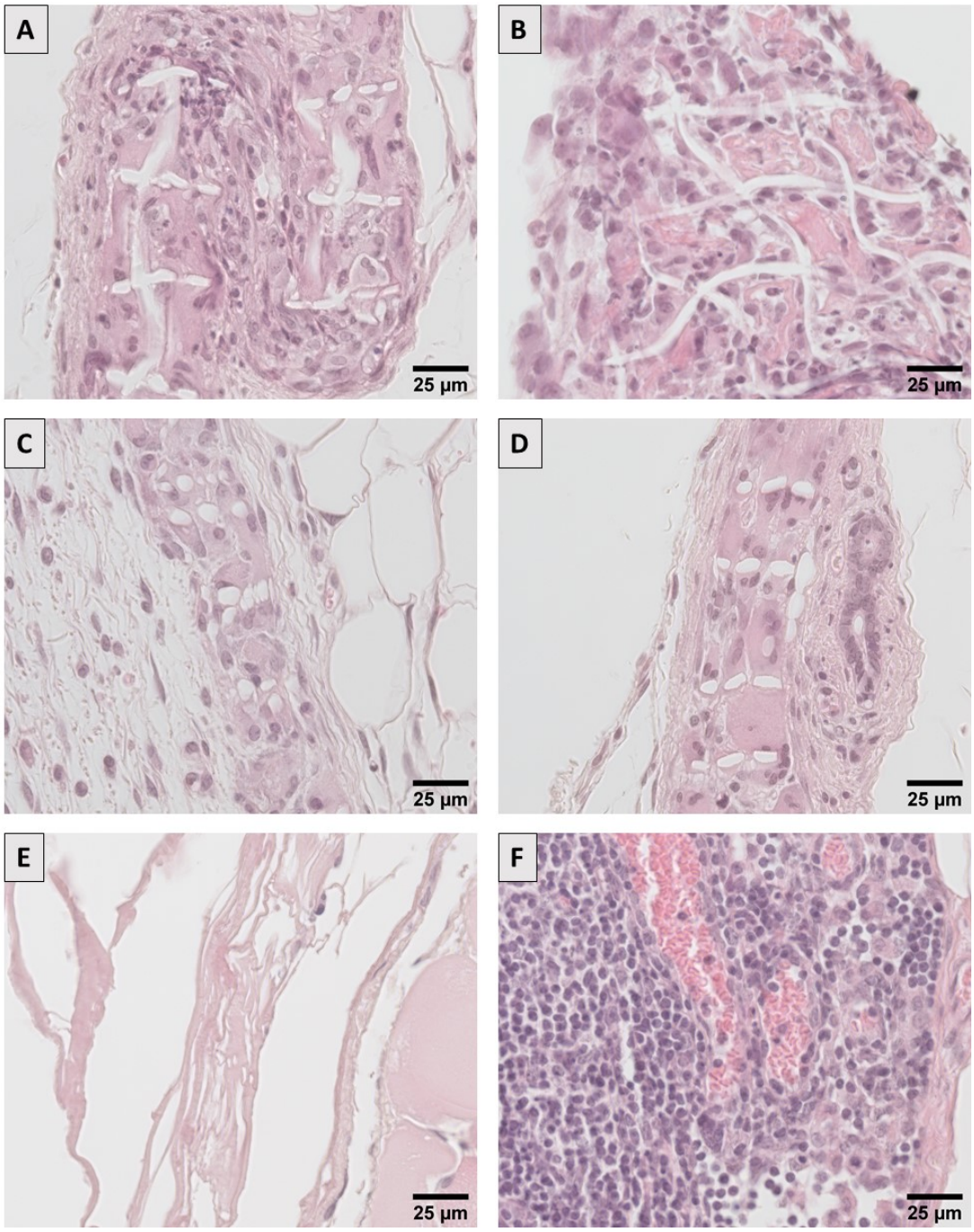

Figure 5.19: A summary of variations seen during the examination of HE stained sections. (A) A scaffold folded on itself twice and both segments could be seen. This creates layers in between that allow for cellular infiltration between the individual segments. (B) The scaffold rotated so that when sectioned, the cut shows a longitudinal section (with pores visible, surrounded by walls) instead of a transverse section. (C) The scaffold is seen implanted on top of fat tissue (right) instead of directly on the abdominal muscle. (D) The scaffold was implanted on mammary tissue instead of the abdominal muscles. (E) In Day 2 scaffolds, the scaffold was not properly supported by extracellular matrix, and during the dissolution of the scaffold during paraffin embedding resulted in loss of potential cellular elements. Excessively damaged samples were excluded from analysis. (F) Lymphocyte aggregates could be seen in several blocks.

5.3.3.2.2 Day 2

The scaffold groups showed similar results to each other (**Figure 5.20A-F**). The scaffolds were mostly not infiltrated by inflammatory cells throughout the full length of the cross-section of the scaffold (**Figure 5.20B-C**). The cellular infiltration occurred occasionally at the scaffold-tissue interface and more on the deep side (**Figure 5.20E-F**). The pore spaces could be seen with an acidophilic, homogenous material inside, which is probably fibrin from the post-implantation hematoma (**Figure 5.20B-C and E-F**). In the non-infiltrated scaffold parts, the skeleton of the dissolved fibers could be seen either partially or completely broken apart (**Figure 5.19 E** and **Figure 5.20B**). This could be due to the dissolution of the scaffold in xylene during paraffin embedding, without the presence of cellular and extracellular matrix elements which could hold the integrity of the structure, as seen at later time points. When the scaffolds were focally infiltrated with acute inflammatory cells, there were neighboring empty parts of the scaffold, where no infiltration occurred. The region of the frames appeared either completely non-infiltrated or with individual cells scattered in the random pore spaces between the frame fibers. The decreased cellular infiltration in the scaffold groups could be explained with the presence of air bubbles inside the scaffold pores which originated during implantation.

For the films, a hematoma could be seen both superficial (**Figure 5.20G**) and deep (**Figure 5.20H**) to the space previously occupied by the film. Surrounding this layer was an infiltration of inflammatory cells, which also infiltrated the subcutaneous fat and the septa between the adipocytes. Some skeletal muscle cells were seen undergoing necrosis (data not shown).

The sham samples showed a mild infiltration of inflammatory cells like neutrophils, eosinophils, macrophages and lymphocytes (**Figure 5.20I**). The cells are found in the loose areolar connective tissue, with occasional interstitial hemorrhage (evident by the presence of erythrocytes in multiple levels of the connective tissue layers). The reaction seemed more intense around the epimysium of the abdominal muscles. Excessive inflammatory cell accumulation was seen surrounding

hair particles which got erroneously implanted and were treated as a foreign body by the mouse immune cells (data not shown). No FBGCs were seen in any of the four groups at this time point.

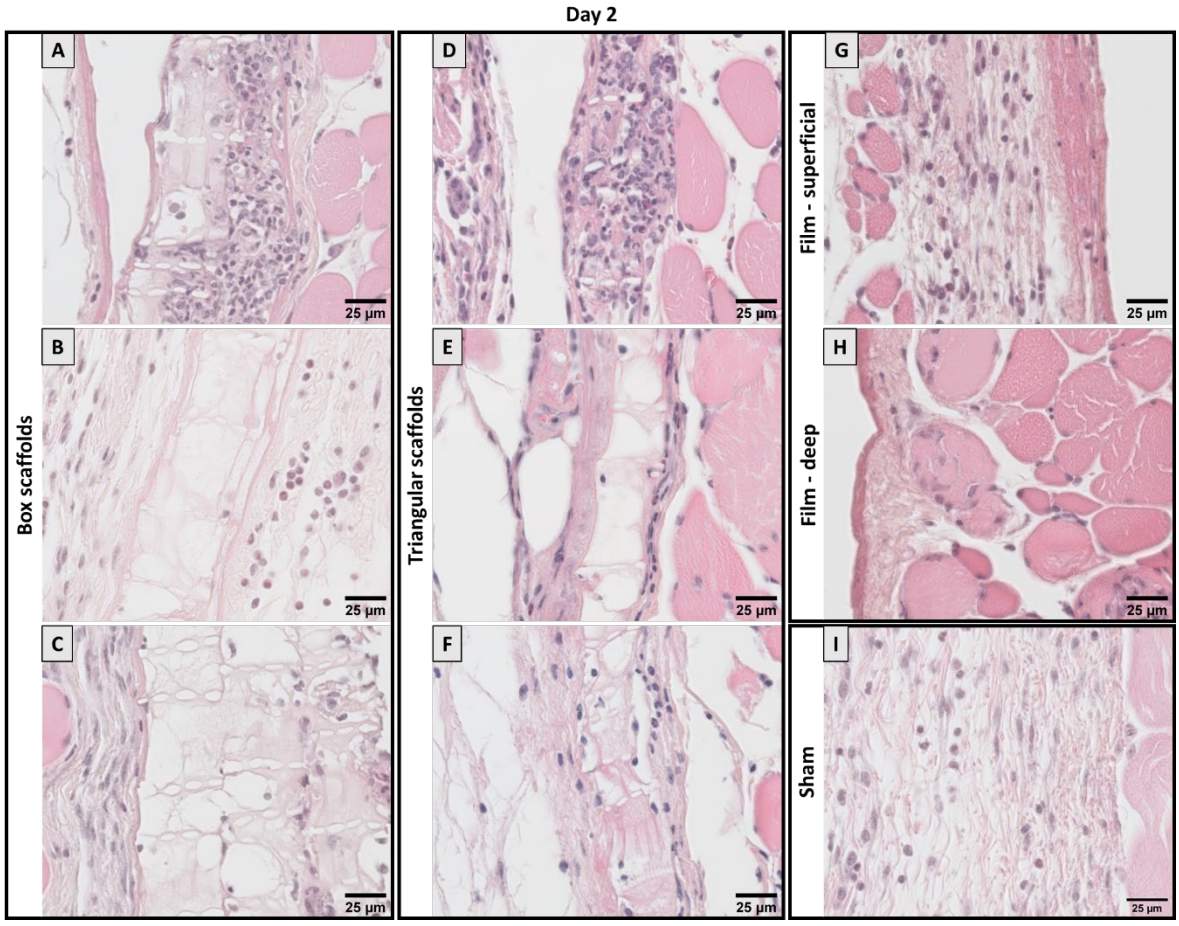

Figure 5.20. HE-stained sample micrographs of all study groups at Day 2. (A-C) Box scaffolds. (D-F) Triangular scaffolds. (G-H) PCL film. (D) Sham group with no implant. At Day 2 there was little cellular infiltration (A and D) of the full length of the scaffolds, with most pores empty or filled with fibrin (B-C and E and F). Cellular infiltration could be seen along the scaffold-tissue interface (E-F). In the film group, the implant-tissue interface had an organized hematoma with few inflammatory cells (G-H). In the sham group (I), the empty pocket had infiltrating acute inflammatory cells. Scale bars are 25 µm.

5.3.3.2.3 Day 4

The scaffold samples were more populated with inflammatory cells, compared to the Day 2 samples (**Figure 5.21A-B and D-E**), although empty parts of the scaffolds still managed to occasionally appear (**Figure 5.21C**), but even then, they were surrounded by a denser layer of inflammatory cells at the scaffold-tissue interface (**Figure 5.21F**). FBGCs started to appear, engulfing fused segments of the fiber wall, but not the whole wall (**Figure 5.21D**). Because of the overlap with other mononuclear cells like macrophages and lymphocytes, it was not possible to accurately count the number of FBGCs

per HPF, especially that FBGCs are multinuclear. Qualitatively, the triangular scaffolds had more FBGCs compared to the box ones (Figure 5.21D). There were no FBGCs detected in either the film or the sham groups.

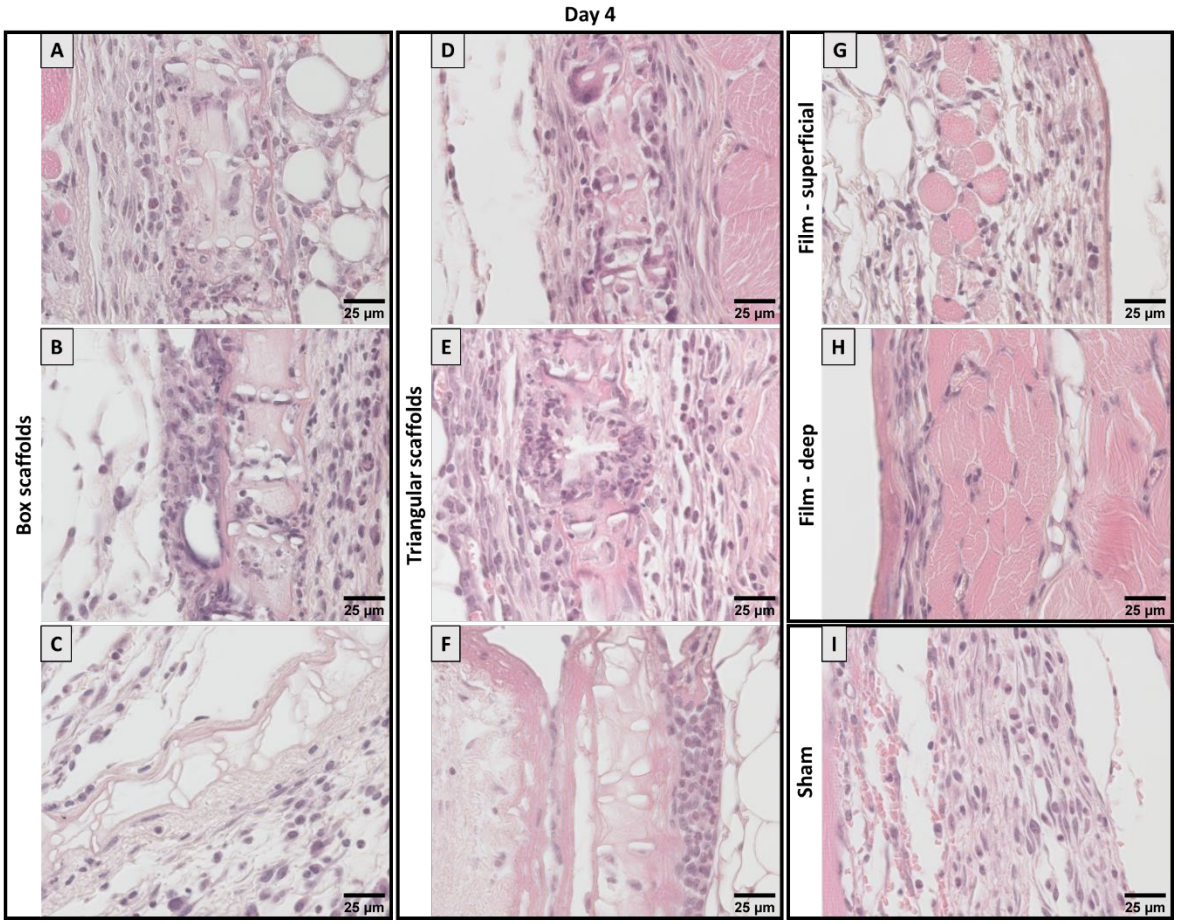

Figure 5.21 HE-stained sample micrographs of all study groups at Day 4. (A-C) Box scaffolds. (D-F) Triangular scaffolds. (G-H) PCL film. (D) Sham group with no implant. At Day 4 the scaffold groups showed a massive increase in mononuclear inflammatory cellular infiltration in the box scaffolds (A-B) and more prominently in the triangular ones (D-E), including the appearance of FBGCs (D). Scaffolds still showed non-infiltrated regions (C, F). Film samples (G-H) still had the organized hematoma at the implant interface with more pronounced cellular infiltration with fibrosis. The sham group (I) had fibroblasts as well as inflammatory cells in the empty pocket. Scale bars are 25 µm.

In the film samples, the organized hematoma layer was less in thickness and the inflammatory cellular reaction was more condensed and in a more organized connective tissue layer, where it integrated with the epimysium of the abdominal muscles. This connective tissue layer appeared thicker, but more areolar in the superficial layer, directly below the panniculus carnosus muscle.

Sham samples of Day 4 had, similar to the ones from Day 2, acute inflammatory cellular infiltration and fibroblasts in the loose areolar connective tissue (**Figure 5.21I**). Also, some skeletal muscle fibers underwent necrosis and were surrounded by macrophages (data not shown).

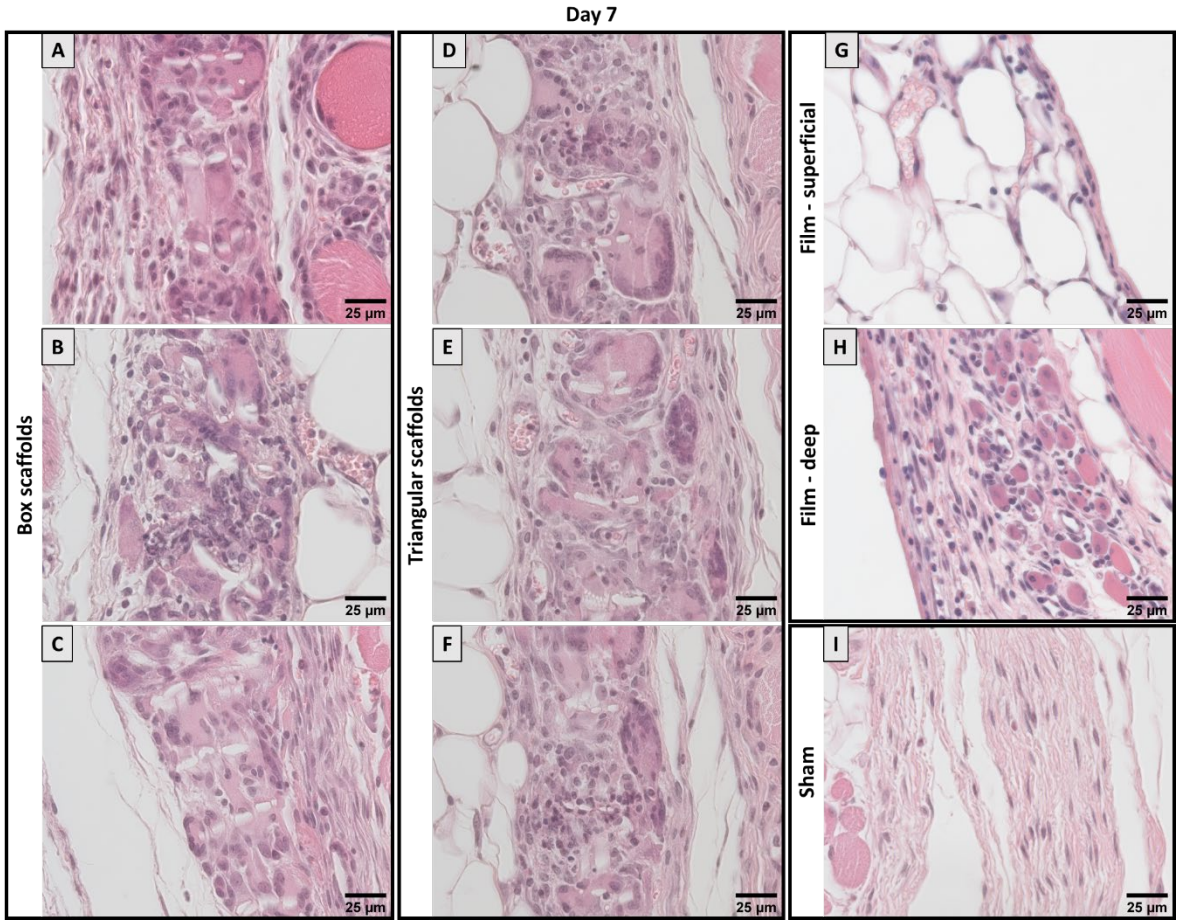

Figure 5.22. HE-stained sample micrographs of all study groups at Day 7. (A-C) Box scaffolds. (D-F) Triangular scaffolds. (G-H) PCL film. (D) Sham group with no implant. At Day 7 there were no more non-infiltrated pores in both scaffold types. Mononuclear inflammatory cells infiltrated the pores (A, B and F) while large FBGCs engulfed the fiber wall (C-E), with some reaching a size of almost 50 µm (D). The film group had fewer inflammatory cells (G) with visible blood vessels, fibrosis and muscle necrosis deep to the implant (H). The sham group had less inflammation and more fibroblasts and collagen deposition (I). Scale bars are 25 µm.

5.3.3.2.4 Day 7

The scaffold samples represented an increase in cellular infiltration compared to what was seen before in Days 2 and 4 (**Figure 5.22A-F**). There were no more non-infiltrated areas detected, with the frames showing a relatively moderate infiltration of mostly mononuclear cells with occasional FBGCs stretched around and trying to engulf the large diameter fibers of the frame. The frequency of FBGCs increased towards the scaffold itself away from the frames. In the scaffold center, FBGCs were

seen around entire fiber walls or segments of the wall (**Figure 5.22C-E**), with some reaching sizes as large as the pore itself (> 50 µm) (**Figure 5.22D**). Again, a FBGC quantification was not possible here as well. A qualitative difference between box and triangular scaffolds was not detected. No FBGCs were detected in film or sham samples.

The inflammatory infiltration around the implanted films was less than Day 4 (**Figure 5.22G**). Persistent neutrophils and eosinophils could still be observed, along with fibroblasts, and macrophages. Blood vessels could be seen in the implantation bed, deep to the film (**Figure 5.22H**).

The sham samples showed less inflammation with increased collagen deposition and fibroblasts. The number of inflammatory cells dropped and became mostly localized close to the epimysium of the abdominal muscles (**Figure 5.22I**).

5.3.3.2.5 Day 14

The clearest feature of the Day 14 scaffold samples (**Figure 5.23A-F**) was the presence of large FBGCs (of both the classic type, as well as the Langhans one) that were larger than the whole thickness of the scaffold, or they tended to engulf several walls and occupy several pores, simultaneously. In this regard, there was no difference, qualitatively, between both the box and the triangular scaffolds. When pores were not occupied by FBGCs, they had signs of neovascularization in or through them, which was mostly observed near the frame areas. Other visible cells in or around the scaffolds were lymphocytes, plasma cells as well as still-persistent neutrophils and eosinophils. The large diameter fibers of the frame (**Appendix 5**) were also engulfed by FBGCs but the number of cells and the number of nuclei per cell were less than those seen in the scaffold center. This even extended to the parts of the scaffold situated beneath the frame (at the edges of the scaffold, where the large-diameter fibers of the frame were printed).

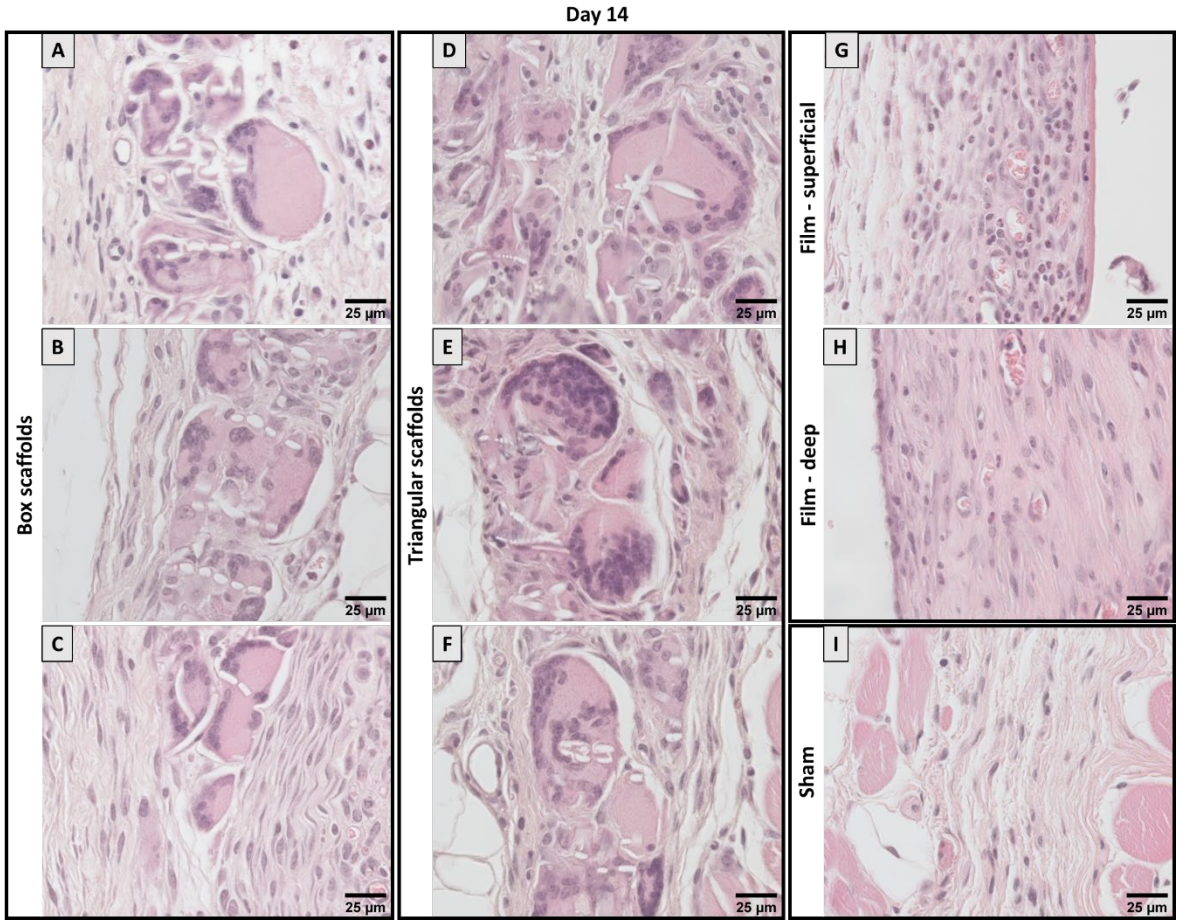

Figure 5.23. HE-stained sample micrographs of all study groups at Day 14. (A-C) Box scaffolds. (D-F) Triangular scaffolds. (G-H) PCL film. (D) Sham group with no implant. At Day 14 regardless of either scaffold type (A-F), they were infiltrated with large FBGCs reaching the size of several pores. The FBGCs are of both the Langhans type (D) and classic type (E). Film samples had peri-implant new blood tissue formation and fibrosis (G-H). The sham group had fibroblasts and fibrosis with few signs of inflammatory cells (I). Scale bars are 25 µm.

The film samples of Day 14 continued the trend of having no morphologically detectable FBGCs, with the inflammatory cells and fibroblasts in a fibrotic layer directly above and below the space once occupied by the film. These cells showed no histomorphological signs of being fused together (**Figure 5.23G-H**).

The sham group showed a resolution of the inflammatory reaction with almost no inflammatory infiltration. The empty pocket site showed collagen fibers with fibroblasts (**Figure 5.23I**). In samples where the cutaneous wound was seen, there was wound granuloma formation with chronic inflammatory cells, as well as persistent FBGCs around the suture material.

5.3.3.3 PSR staining

PSR staining (**Figure 5.24**) was only analyzed for Days 7 and 14, as it was expected, according to the literature (Anderson *et al.* 2008), that formation of the foreign body capsule to be a late event in the FBR. While there was a detectable increase in the thickness of the deposited collagen layer around the scaffolds or the film groups between Day 7 and Day 14, an objective quantitative assessment of the thickness of this layer was not possible without a significant amount of doubt. The problems already described with shredding and tissue separation at the implant-tissue interface during microtomy, prevented an objective measurement of the capsular thickness because of possible tissue expansion. Moreover, the collagen layer surrounding the constructs was seen in continuity with that surrounding nearby fibrous layers, for example, the epimysium deep to the implant or the adipose tissue septa superficial to it. However, qualitatively, it was evident that the Day 14 scaffolds had more collagen deposition inside the frame part surrounding the scaffold, and to a lesser extent, inside the scaffolds itself, when the pores were not completely blocked by FBGCs, compared to the Day 7 groups. When collagen deposition did occur inside the scaffold pores, it was inbetween the FBGCs. The same observation was seen in the film samples, where the superficial and deeper layers to the film space had thicker collagen deposition in Day 14 compared to Day 7. Given the binary contrast in the PSR staining (collagen red, cells yellow), it was shown that the layers around the film implants in Day 7 and Day 14 had more cellular infiltrates, compared to the layers around both kinds of scaffolds. In the sham group, there was no detectable difference between both timepoints, or between either and control tissue (normal mouse skin and subcutaneous tissue from the same anatomical location, data not shown).

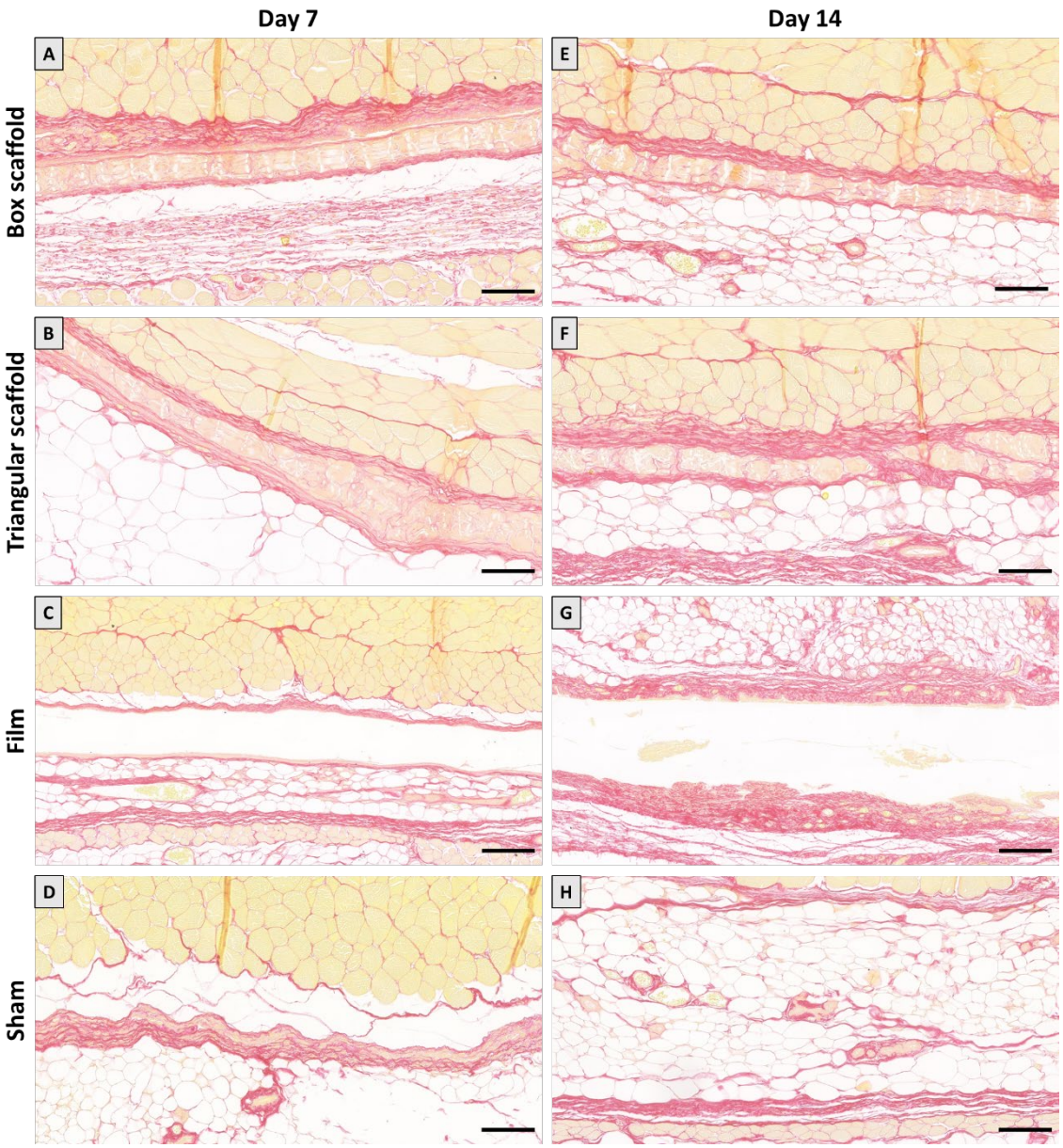

Figure 5.24. Representative images of PSR staining of Days 7 and 14. Day 7 samples (A-D) exhibited collagen deposition around, with little to none inside the scaffolds (A-B). There was mild collagen deposition around the film (C) and in the empty pocket (D). Day 14 scaffold samples had collagen around the implants as well (E-F) with limited deposition inside the pores due to the FBGCs. Due to sectioning artefacts like shredding, as well as the fusion of the deposited collagen with surrounding connective tissue layers, it was not possible to quantitatively measure the thickness of the new deposited collagen. Scale bars in A-B, D-F and H are 100 µm. Scale bars in (C) and (G) is 200 µm.

5.3.3.3 IHC staining

5.3.3.3.1 CD68 staining

For the quantification of macrophages in the available sections, the percentage of the area positively stained for CD68 was used (**Figure 5.25**). Because of the tight packing of the FBGCs in Days

7 and 14 and the morphological changes seen in all groups within the scaffolds, it was not possible to do a cell count for CD68 positive cells. **Figure 5.26** displays representative CD68 IHC staining results across all implant groups at all time points.

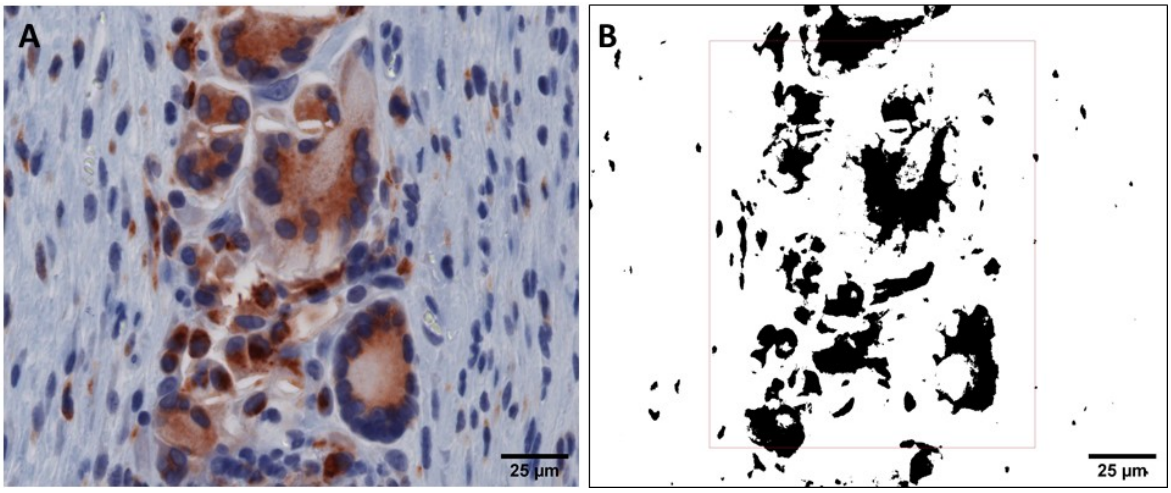

Figure 5.25: Workflow of the IHC quantification for the CD68 positively stained area. A custom-written script for the image processing suite Fiji was written to first pick a region of interest (ROI) and then do color deconvolution, thresholding of the image, mask creation, smoothing and finally area measurement within the ROI (as shown in B). User interaction was needed before every image was processed to place the ROI accurately and rotate it if needed. ROI dimensions: 120x150 µm. Scale bar is 25 µm.

Table 5.4: Summary of mean and SD values of the area stained positive with CD68 across all samples. "N" refers to the number of mice investigated, for every mouse, at least 10 HPF were analyzed.

Group	Area positively stained with CD68 (%)			
	Day 2	Day 4	Day 7	Day 14
Box	3.31 ± 3.55 (N=9)	20.46 ± 14.96 (N=9)	23.84 ± 10.27 (N=9)	32.66 ± 10.89 (N=9)
Triangle	3.38 ± 3.18 (N=8)	15.34 ± 11.04 (N=9)	32.43 ± 10.03 (N=10)	34.43 ± 9.63 (N=10)
Film	7.04 ± 3.70 (N=5)	3.38 ± 2.57 (N=5)	3.91 ± 2.82 (N=5)	4.31 ± 3.30 (N=4)
Sham	7.04 ± 5.38 (N=5)	7.97 ± 4.49 (N=5)	1.24 ± 0.88 (N=5)	1.92 ± 1.53 (N=5)

Table 5.4 shows a summary of the mean and standard deviation values of positively stained areas with CD68 across all groups and all time points. **Figures 5.27 and 5.28** show a box plot of the results of the CD68-positive area percentage across timepoints and implant type.

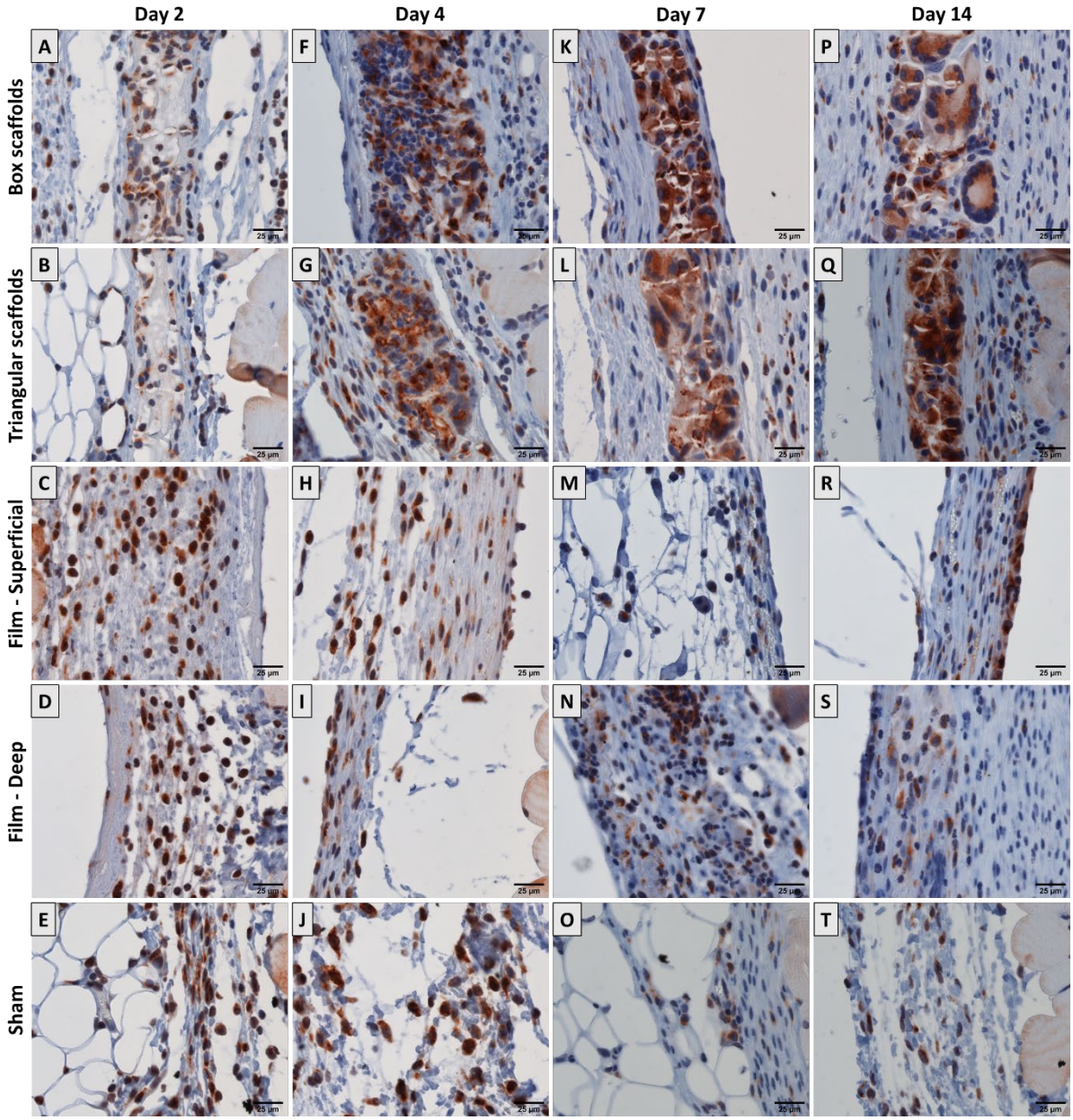

Figure 5.26. Representative images for IHC staining for CD68 as a pan-macrophage marker. In the scaffold groups number of positively stained cells increased with time from Day 2 (A-E), Day 4 (F-J), Day 7 (K-O) to Day 14 (P-T). Macrophages and FBGCs stain positive (reddish brown, Vector NovaRED). Some weak non-specific staining can be observed in skeletal muscles. Scale bars are 25 µm.

While looking at the individual groups in the different timepoints, in the box scaffold groups, there was a highly significant ($p \leq 0.001$) increase of the percentage of CD68-stained areas across the time points except from Day 4 to Day 7. The Day 4 box scaffold group was the one with the most outliers of all the scaffold groups. In the triangular scaffold groups, a similar picture could be seen, where there was a highly significant ($p \leq 0.001$) increase in the stained area, until Day 7, then the increase between Day 7 and Day 14 groups was not significant anymore. In the film groups, there was

no significant change across all timepoints. In the sham groups, the increase was moderately significant ($p \leq 0.01$) between Day 4 and Day 7, and mildly significant ($p \leq 0.05$) between Day 2 and Day 7, as well as between Day 4 and Day 14 (Figure 5.27).

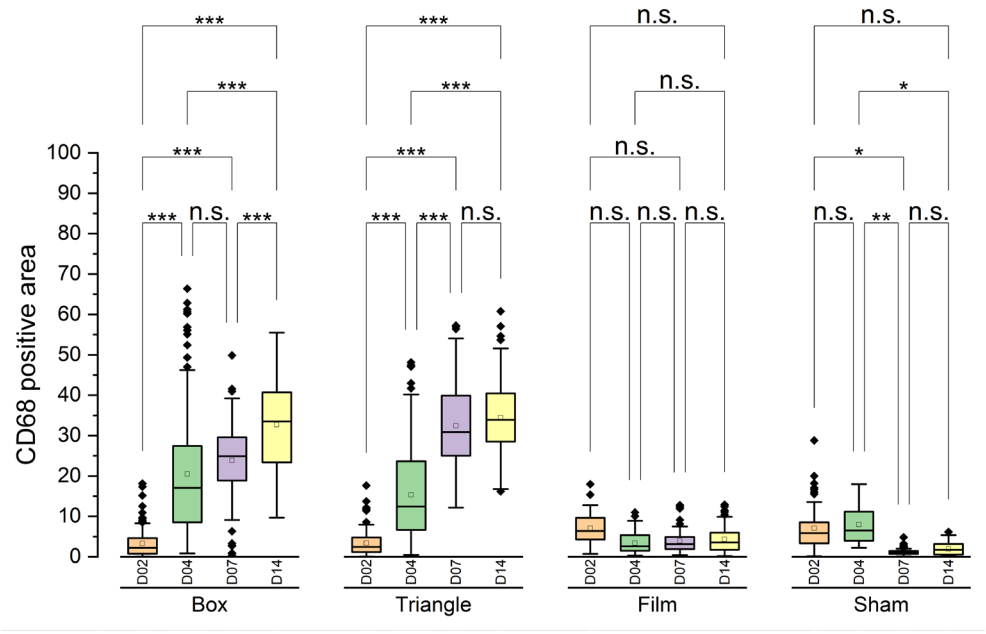

Figure 2.27. Box plot of the CD68-positively stained area per implant type across the four timepoints. There was a significant increase in the CD68-positvely stained area across the timepoints in the box and triangular scaffold groups except for from Day 4 to Day 7 in the box scaffold group and from Day 7 to Day 14 in the triangular one. There was no significant change due to the presence of the film implants across all time points, while for the sham group, there were mild increases with time. A two-way ANOVA was performed with a *post hoc* Tukey test. n.s.: not significant; * = $p \leq 0.05$; ** = $p \leq 0.01$; *** = $p \leq 0.001$.

When comparing the different groups in individual timepoints, there was no significant difference between any of the implant groups as well as with the sham group in Day 2. In Day 4, the increase of the percentage of the CD68-positive area was highly significant ($p \leq 0.001$) between box and triangular scaffolds, as well as between each of them and the sham and film groups. However, there was no significant difference between the film and the sham groups. In Day 7, the mean in the triangular scaffolds group was seen significantly higher ($p \leq 0.001$) than that of the box scaffolds, correlating with the morphological findings in HE staining. As with Day 4, there was a highly significant increase ($p \leq 0.001$) between each of the scaffold groups and the film and sham groups, as well as between each other (with the triangular scaffolds having a higher positive area for CD68). Finally, on Day 14, there was no significant difference between the box and triangular scaffolds, or between the

film and sham groups. However, the interactions between each of the box scaffolds or the triangular scaffolds with either the film or the sham groups, were highly significant ($p \leq 0.001$).

Except in Day 2, the presence of either the box or the triangular scaffolds led to a highly significant increase in the percentage of CD68-positive area relative to either the film or the sham groups. This indicated that both scaffold types evoked a strong macrophage- and FBGC-rich foreign body reaction in comparison to a comparatively sized solid film of the same material (PCL). The surgical procedure itself did not cause the reaction as there was also a significant increase between the scaffold groups and the empty surgical pocket. In this regard, the sham group is comparable to the PCL film.

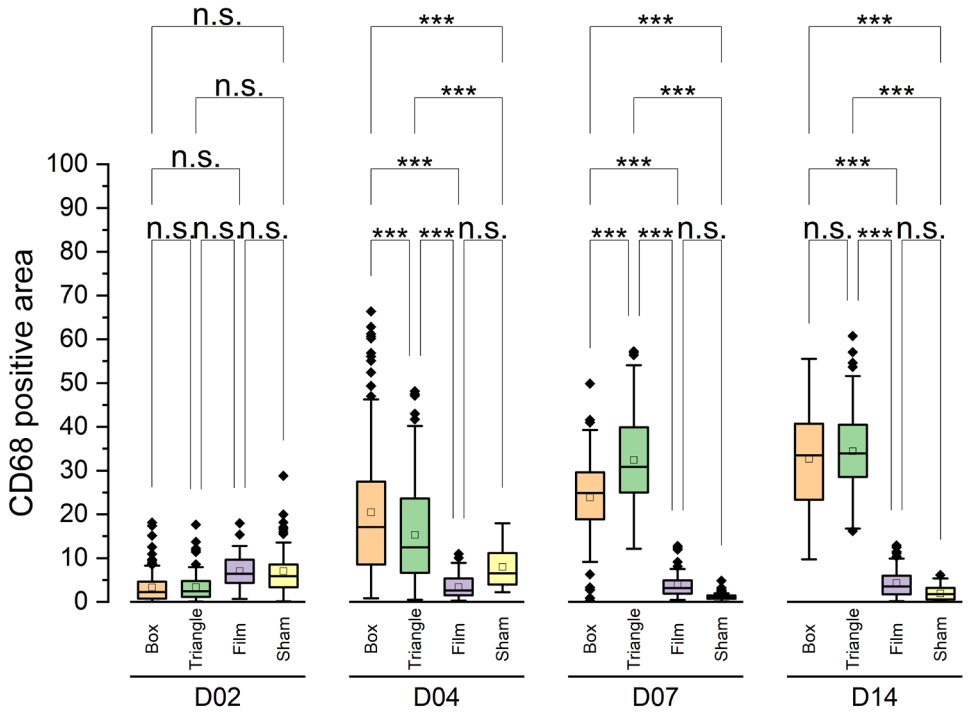

Figure 5.28. Box plot of the CD68-positively stained area in all time points per implant type. There was no significant effect of the presence of any of the implants at Day 2. At all timepoints, there was no difference between sham and film groups. The presence of either the box or the triangular scaffolds always led significant between either the film or the sham groups. There were significant differences between each of the box and triangular scaffolds at Day 4 and Day 7, with the box group and the triangular one taking the lead, respectively. At Day 14, there was no difference between either scaffold groups. There was always a significant difference between the scaffold groups and film or sham groups. A two-way ANOVA was performed with a *post hoc* Tukey test. n.s.: not significant; * = $p \leq 0.05$; ** = $p \leq 0.01$; *** = $p \leq 0.001$.

5.3.3.3.2 CD31 staining

The CD31 immune staining of endothelial cells was used as an indicator to vascularization around or inside the constructs (only around in case of the film group). No positive staining for endothelial cells was detected in any of the scaffold groups (both box and triangular) in Day 2, both in the scaffold center or in the frame (**Figure 5.29A-B**). Blood vessels were seen in the surrounding tissues, but not in direct proximity of the scaffold. This was also true to the film and the sham groups (**Figure 5.29C-E**). In the sham group, there were no blood vessels in the implantation area.

In the Day 4 group, there were little to no blood vessels seen in the centers of the box or triangular scaffolds or in the frame. There were single instances of blood vessels seen across only one scaffold, within proximity of the frame. The blood vessels around the scaffolds were more prominent and were more proximal to the scaffold, compared to those seen in the Day 2 group.

Moving to Days 7 and 14 groups, vascularization was observed in random manner with more vessels observed inside the scaffold, but only in that part of the scaffold adjacent to the frame. The frames themselves were generally well vascularized, especially in the Day 14 group (**Appendix 5**). Similar to Days 2 and 4, blood vessels surrounding the scaffolds were more prominent than those inside the scaffolds themselves.

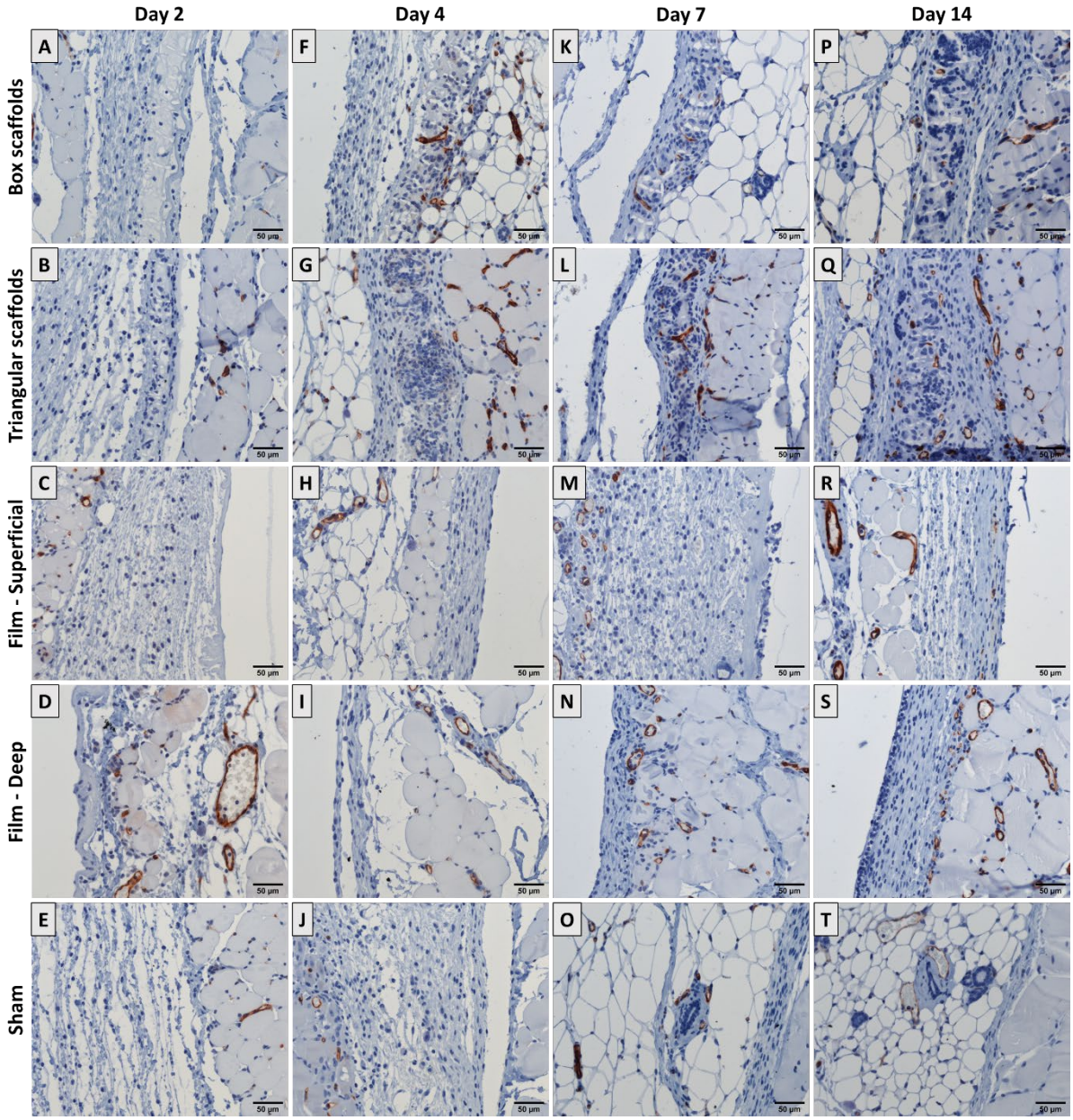

Figure 5.29. Representative images for IHC staining for CD31 as an endothelial marker. The number of new blood vessels increased over time from Day 2 (A-E), Day 4 (F-J), Day 7 (K-O) to Day 14 (P-T). The increase was mainly in the area surrounding the scaffolds (box and triangular), as well as the film and in the empty pocket in the sham group. Infiltration of new blood vessels was higher in the frame area and directly next to it (data not shown) compared to the scaffold itself. Endothelial cells stain positive (reddish brown, Vector NovaRED). Scale bars are 25 µm.

5.4 Discussion

Controlling the extent of the FBR around implanted medical devices can lead to significant improvement in patient morbidity and a decrease in the need for reoperation, especially in case of surgical meshes for the treatment of hernias and pelvic prolapse (Bringman *et al.* 2010). The promise of AM for the design of medical devices can lead to such flexibility and customizability of design and fabrication, producing better medical devices for better surgical outcomes, towards the long-term goal of achieving personalized medicine (Baylon *et al.* 2017, Serafini *et al.* 2020).

MEW scaffolds bridge the gap between already clinically used micro-extrusion techniques and solvent-using solution electrospinning (Robinson *et al.* 2019). MEW uses medical-grade thermoplastic polymers to produce defined, high resolution structures (Youssef *et al.* 2017) that can be further used to study the effect of scaffold architecture on the FBR (Dondossola *et al.* 2016). Compared to micro-extrusion scaffolds, MEW ones are highly porous, albeit with smaller heights and thinner fibers (Youssef *et al.* 2019). MEW was used to process polypropylene (Haigh *et al.* 2017), which has seen decades of use in the clinic as a non-degradable polymer in hernia meshes (Cortes *et al.* 2008b) and suture lines (Greenberg and Clark 2009) as well as polydioxanone (unpublished data, Hochleitner *et al*.) and poly(vinylidene difluoride) (Florczak *et al.* 2019) as examples of degradable ones (Pillai and Sharma 2010).

Previous work has shown that MEW scaffolds could be used *in vitro* to promote the polarization of macrophages towards the healing M2 type (Tylek *et al.* 2020), thus, theoretically, producing a milder reaction when implanted *in vivo*. In the current experiment, similar scaffolds were used but with a higher number of layers, to produce scaffolds which could be easily manipulated for the surgical procedure, as well as more easily visualized in histological sections using standard brightfield microscopy. The characterization of the scaffolds showed that the final product matched the designed one, with scaffolds of two different pore shapes, either box- or triangular-shaped, with fiber laydown patterns of 0/90° and 0/60/120°, respectively. The fiber diameter in both scaffold types

was approximately 2.5 μm, and the spacing, was as designed, approximately 50 μm in the box scaffolds and 60 μm in the triangular ones. The decision to use such spacing, which meant that the two scaffolds types did not have the same pore size, as seen through the 2D-T_{loc} analysis, was based on the decision that this *in vivo* study was a proof of principle to the, then, on-going *in vitro* experiment investigating macrophage polarization on MEW scaffolds by Tylek and colleagues (Tylek *et al.* 2020).

The current experiments were planned to examine the effect that the group of Prof. Buddy Ratner described, where hydrogel scaffolds with identical 40 μm spherical pores were found to induce a mild FBR (Bhrany *et al.* 2013) and induce a shift to M2 macrophages when implanted *in vivo* (Sussman *et al.* 2014). The difference between these scaffolds and what was used in the current experiment is first of all the material (polyHEMA *versus* PCL), the fabrication method (multi-step hydrogel casting *versus* one-step, solvent-free MEW) and scaffold "type" (partially solid, partially porous *versus* totally porous, fibrous scaffold). The fibrous nature of MEW scaffolds meant that the scaffolds are porous in 3D with lateral communicating pores between the fiber walls and across fiber intersections at crossing points. These lateral pores are poorly reported and characterized in the current MEW literature. In Chapter 4 we have discussed this limitation and offered a potential solution by using non-destructive X-ray microtomography to analyze the 3D local thickness of the scaffolds and determine the interconnectivity of MEW scaffolds (Youssef *et al.* 2019).

The research output originating from the field of surgical meshes has led to very important progress in the understanding of the biology of flat polymeric implantable scaffolds, with access to an incredible amount of tissue material as well as archival samples (Klinge and Klosterhalfen 2012, Klosterhalfen and Klinge 2013). Hernia repair using surgical meshes has been performed since the 1890s (Baylon *et al.* 2017). Inguinal hernia repair is the most performed general surgical procedure (Berger 2016). A definitive classification of surgical meshes does not exist (Klinge and Klosterhalfen 2012). However, there have been attempts to classify them based on the pore size (Amid 1997). This led to four classes: Class I with macropores of more than 75 μm, Class II with macropores and

micropores of less than 10 µm, Class III with micropores, and finally Class IV with sub-micropores. Class IV meshes were found to be unsuitable for use as hernia repair implants. Class II and III were associated with the potential for bacterial infection, as immune cells were not able to penetrate biomaterials with pores less than 10 µm in size (Amid 1997). Large pores were associated with better fibrovascular tissue formation between the pores and less chances of infection (Bringman *et al.* 2010, Klosterhalfen and Klinge 2013). It is challenging to position the scaffolds used in the current study into a classification of hernia meshes, but they could fit into the Class II meshes with a mixture of macro- and micropores. This could potentially indicate a tendency to cause a surgical site infection, in case a contamination occurred during implantation or afterwards.

While most MEW *in vivo* experiments reported to date were performed on immunocompromised mice (refer to Chapter 2), the current experiment was performed on immunocompetent, outbred NMRI mice. This provided an opportunity to analyze the FBR of these micro-scale MEW scaffolds, which was not the intended scope of most of the previously published *in vivo* experiments. Moreover, the implantation of pure, medical-grade PCL was not the focus of most of the *in vivo* MEW studies, with scaffold pore sizes of 100 µm (Dondossola *et al.* 2016). The results showed that the animals handled the procedure and the implantation sufficiently well. However, the frequency of wound complications on the right side, which harbored the box scaffolds could be explained to either an increased reaction to the box scaffolds *per se*, which was not seen with CD68 staining as well as HE sections, or an operator error. The same operator performed the surgeries in all the mice in the same exact manner, excluding the difference in skin closure techniques which was thoroughly discussed in the results section. What pointed to an adverse reaction towards the box scaffolds, was the fact that there were hardly any wound complications in the PCL film groups, which were also implanted in the right side of the mice in exactly the same technique as that for the box scaffolds. Anderson has described that solid, smooth implants, such as breast implants, generate a FBR in the form of one- to two-layer proliferation of macrophages, while those with a rough surfaces, such as poly(tetrafluroethylene) vascular scaffolds, had macrophages and FBGCs at the tissue-material

interface (Anderson 1988). Moreover, he and colleagues have shown that PCL films had the best healing process with the least inflammatory response, when compared to aligned and non-aligned electrospun PCL nanofibers (Cao *et al.* 2010). In the current experiment, we have not detected, at any time point, the presence of FBGCs surrounding the PCL film implants. Ideally, the location of the constructs would have been randomized to mitigate such uncertainties in the analysis. Another potential solution would have been to adopt a dorsal midline implantation approach, where more (at least two) scaffolds could be implanted through the same dorsal incision. The dorsal implantation technique has the added benefit of keeping the suture lines away from the reach of the mouse, so potential gnawing on the sutures could be avoided. Ideally, the surgical procedure should provide very mild irritation to the mouse that it warranted no gnawing from the host.

The HE-stained sections showed, as expected, a timewise increase in the inflammatory reaction as we moved from Day 2 to Day 14. The appearance of macrophages from Day 4 was also accompanied by early fusion to form FBGCs with a lower number of nuclei, compared to the FBGCs seen later in Day 7 and Day 14, where the number of nuclei greatly increased, although in all cases, the number of nuclei per FBGC was not quantitively assessed. The minimal cellular infiltration observed in the Day 2 scaffolds, which is a described and expected early outcome of the FBR (Anderson 1988), led to the loss of structural integrity of the scaffolds when it was processed for paraffin embedding, making histological evaluation difficult. This could have been due to the inability of the deposited fibrin in the formed hematoma inside the scaffolds in Day 2 to be retained, once the skeleton of the scaffold was dissolved in xylene during paraffin embedding. This led to Group 2 being the one with the highest number of excluded scaffolds, as that effect led to tissue sections where the scaffold area could not be properly identified without significant doubt.

The position of the scaffold and film was as intended in the subcutaneous space, superficial to the abdominal muscles and deep to the dermis. The panniculus carnosus muscle in the subcutis also served to histologically identify the implantation area in both the implant as well as the sham

groups. The use of IHC as the immunological staining technique also provided a more secure method of associating the histomorphological and immunological results, as it was possible to perfectly locate and align the ROIs in relation to the implant location, compared with immunofluorescence. In the latter case, the navigation of the slides had to be done with reliance on the autofluorescence, which was not always a reliable method when performed during the pilot phase of the study.

The computerized analysis of the percentage of the CD68-positive area in a fixed-sized ROI across all samples allowed the objective analysis of all groups in terms of macrophage infiltration. CD68 is a pan-macrophage marker which could also potentially stain fibroblasts positively (Gottfried *et al.* 2008). However, as the same methodology was applied to all the slides analyzed, the effect of the side staining could be mitigated. Proper immunohistochemical controls were employed with positive tissue control (liver) and two negative controls (IgG control and omission of primary antibody) (**Appendix 4**). Moreover, normal mouse skin was also added as an extra control, as CD68 staining was observed to cause non-specific staining in sweat glands, keratin and occasionally in skeletal muscles. The addition of skin as a control insured that these non-specific staining effect could be excluded from the study samples. The analysis showed that, except at Day 2, the presence of either scaffold types led to a highly significant increase in the percentage of the CD68-positive area compared to either the film or the sham group. Across all timepoints, the film groups showed very minimal reaction that was comparable to that of the sham group. This indicated that the implanted material, medical-grade PCL, was not the cause of the massive reaction seen in the MEW scaffold groups, but rather the scaffold micro-architecture. While there were significant differences between both the box and triangular scaffolds in the early timepoints, with box scaffolds having a higher stained-area percentage, this effect reversed in Day 7, with the triangular scaffolds having a higher area percentage. The difference between both groups was not detected in the Day 14 groups, which could also be morphologically correlated with the HE staining.

The presence of higher FBGC infiltration in small pore scaffolds was already reported in the literature and described as the development of a scar plate or a bridging scar (Cobb *et al.* 2005), where the foreign body granulomata around adjacent fibers would merge together and prevent cellular and vascular infiltration of the pores. In both HE and IHC staining, there is a stark difference between the center of the scaffold itself and the area with the frame in the periphery. The frame was not subjected to the same quantitative analysis in the IHC section for a number of reasons. First, the frame total area was much less compared to the total area of the scaffold. The scaffolds were designed with a total area of 1 mm^2, with the frame forming a 2-2.5 mm outer, thicker rim. Second, the frame was always located at the periphery of the scaffold and was used for manipulation using forces, which could have caused potential structural changes to the frame fibers. Third, the frames could not be always demonstrated in each slide (Ideally the frames would be seen on either side of the scaffold, but this was not always readily available). Fourth, because how the assembled scaffold was fabricated, there is always a part of the scaffold beneath the frame part, which could affect the results. Finally, there is a substantial thickness difference between both the scaffold and the frame (calculated 105 µm for the scaffolds *versus* digital caliper-measured 450 µm for the frames). With all these reasons in mind, with HE staining, the frame part showed more fibrovascular growth in the later timepoints and earlier cellular infiltration in the earlier ones. The collagen deposition was also relatively higher in the frame area using the PSR stain. With IHC, the number and size of FBGCs ingulfing the fibers was less than that in the scaffold itself. The effect seen in the scaffold, where one FBGC would ingulf a whole fiber wall, or may extend to multiple adjacent walls, potentially simultaneously blocking several pores, was not seen in the frames at all. Finally, with CD31 staining, there were more observed blood vessels in the frame part compared to the scaffold starting from Day 4 onwards.

The reason for the scaffolds not being well vascularized, in comparison to the frame, could also be due to the thickness of the constructs. The theoretical thickness of the scaffold is approximately 105 µm, while that of the frame was approximately 450 µm. This meant that there was less of a need for vascularization across the scaffold, as it was less than the 200 µm diffusion limit for

vascularized tissues (Lovett *et al.* 2009). Moreover, the frames were always externally located, compared to the center of the scaffold, which also meant that if vascularization was happening in a radial manner, moving towards the center of the scaffold, the frame would be first to be vascularized, followed by the scaffold regions close to it, which was what we observed (**Appendix 5**).

The formed FBR due to the implantation of these two scaffold types would fit the scar plate that was described in hernia meshes-related research. This plate would ultimately lead to the fibrous capsule contraction and shrinkage of the mesh (Cobb *et al.* 2005, Jordan *et al.* 2018). While in many sections, it was evident that the scaffold was deformed through folding or rotation, the highest observed timepoint (Day 14) would not be a proper timepoint to make a conclusion that the FBR led to morphological changes of the scaffolds. However, it is described in the literature that implantation of flat surgical meshes leads to scaffold shrinkage by means of the FBR (Amid 1997, Cobb *et al.* 2005).The observed FBR in the scaffold group could ultimately lead to a higher degradation rate of the PCL used in the scaffolds. Previous research has shown PCL particles using electron microscopy inside macrophages and fibroblasts post implantation, with all PCL particles smaller than 10 µm cleared after six months (Woodward *et al.* 1985) (Refer to Chapter 2). While the individual fibers of the implanted scaffolds in the current study was around 2.5 µm, the fibers almost always fused together in walls (or bands) due to the MEW parameters used. A proper investigation of the effect of 2.5 µm fibers would require them to be individually implanted, probably across a support frame or through the cage system, which some groups reported to use (Anderson 1988). Previous research in single polymeric fibers showed that smaller fibers (1-5 µm thick) could be surrounded by a significantly smaller FBR capsule compared to thicker one (6-10 or 11-15 µm thick) (Sanders *et al.* 2002). However, the implantation of single fibers is beyond the scope of this project and would be of no practical value within the scope of the development of an implantable polymeric medical device.

The poor tissue ingrowth that was observed in the scaffold groups could be the reason for the sectioning artefacts observed, where dissociation of tissue layers happened. This prevented a

quantitative analysis of the thickness of the deposited collagen fibers around the scaffolds using the PSR stain. However, due to the merging of the new collagen layers with the already present epimysium and adipose tissue septa, it was not possible to do an objective analysis, without choosing a cutoff point between both. Such dilemma could be prevented by using a cage system (Anderson 1988, Anderson *et al.* 2008), where the cage would keep the surrounding tissue and the scaffold separate.

There has been a growing interest in using biomaterial scaffolds as drug or vaccine delivery tools (Weber and Mule 2015, Zhang *et al.* 2018). Through the modification or coating of scaffolds, it could be possible to achieve local delivery of substances in a controlled manner (Chen *et al.* 2018). This could also be applied to the field of vaccine research, where the scaffold serves to attract dendritic cells to the drug of interest (Ali *et al.* 2009). In our research, the MEW PCL scaffolds generated a strong immune reaction that could be further adapted for such research purposes. However, the pores would need to be more microporous enough to allow for more tissue ingrowth and vascularization (Junge *et al.* 2012). In the field of immune therapy, MEW scaffolds have already been used as an expansion medium for chimeric antigen receptor T-cell therapy (Delalat *et al.* 2017b). It is worth mentioning that the sphere-templated scaffolds from the Ratner group have already been used for the scaffold-mediated delivery of mRNA vaccines (Chen *et al.* 2018).

Several limitations of the current study have already been discussed above. However, MEW PCL scaffolds have so far not been implanted with such high definition *in vivo.* To reach a definitive conclusion regarding the severe FBR that the scaffolds seem to have induced would require the repeat of the experiments with some modifications. First, the scaffolds would need to be with comparable effective pore size across box and triangular scaffolds, and objectively characterized using X-ray microtomography, as established in Chapter 4, before implantation, and potentially also after excision. Second, the scaffolds would need to be fabricated with a higher layer count. This was previously a challenging aspect for MEW scaffolds, but Wunner and colleagues have recently showed that it was possible to print thicker MEW scaffolds (Wunner, Wille*, et al.* 2018). However, this will need to be

established in fiber spacings as low as 50 µm. Third, the different groups will need to include scaffolds with larger diameters, to determine if the recorded effect was a pore or a diameter effect. Fourth, a group composed of randomly written fibers with the same characteristics as the frame will need to be included in the analysis. Finally, the experiment will probably need to be extended past 14 days, at least to 21 days to reach a comparable implantation period to the Ratner group (Sussman *et al.* 2014).

5.5 Conclusion

MEW can be used to fabricate customizable, precise scaffolds through an AM technique that can be easily translated to medical device production. The *in vivo* implantation of MEW scaffolds for analysis of adverse effects as a validation towards potential medical device applications is under reported in the literature, where the focus has been on the creation of cancer study models. In the current experiment, the implantation of two types of scaffolds with different fiber laydown patterns and spacing and the analysis of the resulting FBR, led to the conclusion that the combination of small pores and small fibers led to a massive FBR (observed up to 14 days post implantation) compared to a flat sheet of the same material, medical-grade PCL. The FBR could be due to either the small pores or the thin fibers or both, as the current experiment could not isolate the cause of that effect. Here, we reported that the presence of either scaffold types led to massive increase in CD68-positive stained areas, as well as an increase in size and frequency of FBGCs compared to flat films of the same material or empty pockets. This immune reaction prevented proper tissue ingrowth and vascularization of the scaffold.

To our knowledge, this is the first reported *in vivo* study using highly resolved flat MEW scaffolds. There needs to be further optimization steps towards the scaffold design for *in vivo* experiments that is built on previous knowledge from comparable mesh systems. The reliance on the translation of *in vitro* results to *in vivo* experiments does not always work as expected. *In vitro* systems lack many of the unique properties of implantation (Jannasch *et al.* 2019), chief among them the lack of the injury hematoma and the hemostasis that occurs as a result of the implantation process. From a classical tissue engineering perspective, the investigated scaffolds do not appear to be suitable for regenerative strategies, and the outcomes deviate substantially from previous MEW PCL scaffold *in vivo* experiments. The mechanism for this immune response is not apparent and would need to be investigated in future research.

Chapter 6

Additive manufacturing (AM) represents a new promising field for the development and manufacture of medical devices (Youssef *et al.* 2017, Touri *et al.* 2019). Contrary to conventional, factory-based manufacturing, AM makes it possible to produce patient-customized implants, while providing solutions for niche markets, like pediatric implants (Les *et al.* 2019). The regulatory framework governing traditional manufacturing still, however, applies to AM. The best strategy for the quick introduction of new AM-based solutions to the market would be to adapt materials and fabrication modalities (e.g. melt processing) which have proved their efficacy and safety over decades of use in the clinic, and take them forward towards patient-specific customization. Through the use of the US Food and Drug Administration 510(k) pathway, and its equivalent in other regulatory bodies, AM-based medical devices can survive the so-called "Valley of Death" and move ahead to the bedside (Hollister 2009a, Hollister 2009b, Pashuck and Stevens 2012).

The focus of this thesis was the development and application of melt electrowriting (MEW) as a AM fabrication method to produce solvent-free scaffolds from medical-grade thermoplastic polymers, followed by the optimization of the printing process, the non-destructive characterization of the scaffolds, and finally, the implantation of such constructs subcutaneously in mice. The structure of the thesis intentionally mimicked the road which a new medical device must take to gain regulatory approval for wider market distribution.

MEW is a new addition to AM technologies (Brown *et al.* 2011), and it bridges the gap between micro-extrusion technologies, which already witnessed a successful translation to the bedside (Probst *et al.* 2010), and solution electrospinning, which uses toxic solvents in its operation (Robinson *et al.* 2019). Although MEW devices can produce tubular scaffolds, the focus here is on highly resolved flat meshes and while MEW scaffolds were used in several *in vivo* experiments, those were with larger fiber dimensions and pore sizes. Furthermore, the aims of previous MEW *in vivo* studies were mainly the development of a platform for cancer research (Martine *et al.* 2017).

The *in vivo* experiment described in Chapter 5 aimed at evaluating the foreign body reaction (FBR) of high-resolution MEW scaffolds with 50 and 60 μm fiber spacings and 2.5 μm fiber diameters in two different laydown patterns, 0/90° and 0/60/120°. This experiment was mainly influenced by pioneering work done by Prof. Buddy Ratner's group in Washington University (Marshall and Ratner 2005), where sphere-templated poly(2-hydroxyethylmethacrylate) (polyHEMA) scaffolds with 40 μm spherical pores induced very little FBR (Bhrany *et al.* 2013) and a shift in macrophage polarization from the inflammatory M1 phenotype to the healing M2 one (Sussman *et al.* 2014). This inspired our group to undergo *in vitro* experiments with MEW scaffolds with up to 40 μm fiber spacing in an attempt to shift the macrophage polarization towards the M2 phenotype (Tylek *et al.* 2020). The experiment in Chapter 5 demonstrated how *in vitro* outcomes are not always indicative of *in vivo results*, especially for the complex immune system. The analysis of the FBR is provided here as an endpoint to the experiment, which is difficult to recapitulate *in vitro* (Chen *et al.* 2010, Jannasch *et al.* 2019).

The results in Chapter 5 showed an extensive immune reaction that was driven by the scaffolds themselves and not by the poly(ε-caprolactone) (PCL) material or the surgical procedure. Whether either the fiber spacing, diameter, or both were responsible for this effect, will need to be further investigated in future research. The laydown pattern led to conflicting results in Day 4 and Day 7 groups, with no significant differences in Day 2 and Day 14 ones. *In vitro* experiments have no established method to mimic the FBR to MEW implants, especially that cell seeding is a challenging procedure in MEW scaffolds (Blaudez *et al.* 2020). However, the results from Chapter 5 seem to be in agreement with the extensive literature from decades of surgical meshes research (Jordan *et al.* 2018, Amid 1997, Cobb *et al.* 2005, Klinge and Klosterhalfen 2012). Flat surgical meshes are used in one of the most performed surgical interventions, hernia repair. It is estimated that 20 million hernia repair surgeries are performed annually (HerniaSurge Group 2018). This provided a wealth of available material for histopathological research and evaluation in the search for the ideal mesh (Klinge and Klosterhalfen 2012). The design of future MEW *in vivo* experiments could benefit from the surgical mesh literature more than from polyHEMA hydrogel implants, as such implants are physically different

from each other (Refer to Chapter 5). What could prove imperative to the success of such experiments, is, ultimately, the intended application of such flat MEW scaffolds. This thesis provides a framework for the qualitative assessment of future MEW scaffolds, as well as a histopathological basis for the qualitative and quantitative evaluation of the *in vivo* performance.

Biomaterial research started through collaboration between pioneering physicians with clinical problems and engineers who could solve them. The field saw multiple revolutions with the development of new biomaterials and tissue engineering approaches. This led to a growing trend of interdisciplinarity, which might have led to a lack of focus in this research field. There have been tens of thousands of research articles on a multitude of biomaterial and tissue engineering solutions, but the translation to the clinic remain extremely and unproportionally slow, echoing an apparent disconnect between the clinical needs and the research outputs, and a lack of appreciation of the regulatory guidelines that control the introduction of new medical devices into the market (Ratner 2019). The general thinking should shift from "what the new technologies can be used for" to "what the current problems that can be solved with this approach are" (Castro *et al.* 2017).

As previously discussed in Chapter 2, AM medical devices as bronchotracheal pediatric implants addressed a real clinical need, while using a clinically approved AM technique (selective laser sintering) and a medical-grade, clinically approved thermoplastic polymer (PCL) (Zopf *et al.* 2013). The same could be said about micro-extrusion techniques (Schantz *et al.* 2006). MEW as a technology is in a position where a direct (and relatively easy) translation pathway to the clinic can exist, if the research questions target the strengths of MEW, while avoiding the weaknesses. MEW scaffolds are mainly non-woven fibrous meshes, which as implants could see potential use in several tissue types, using thermoplastic polymers without the use of solvents (Kade and Dalton 2020, Robinson *et al.* 2019). MEW scaffolds, however, are probably not suitable for load-bearing applications in a way similar to micro-extrusion scaffolds, like the Osteopore ones (Chhaya *et al.* 2015). Tubular MEW scaffolds were, nonetheless, investigated *in vivo* in a critical-sized bone defect in rats (Gonzalez-Gil *et al.* 2019). The

limitations that faced MEW at its start have been more or less addressed in the past few years, one at a time (Wunner, Wille*, et al.* 2018, Wunner, Eggert*, et al.* 2019, Wunner, Mieszczanek*, et al.* 2019). The dual approach of in-process control of the MEW device (Wunner, Mieszczanek*, et al.* 2019) and the use of non-destructive volumetric analysis using X-ray microtomography (µCT) (Youssef *et al.* 2019) could prove crucial for quality control of produced scaffolds. The vertical mounting of MEW devices could reduce the needed footprint (Wunner, Maartens*, et al.* 2018, Wunner, Eggert*, et al.* 2019), opening the door for a potential implementation in operating theaters or clean rooms where space is at a premium.

Through continuous innovation, characterization and troubleshooting of the technique, investing in making new, medical-grade polymers printable, following the research established by similar, approved and clinically tested implants, fabricated using traditional methods and finally the careful planning of *in vivo* work using the appropriate designs, MEW may be the next prime candidate for translation into the clinic.

Appendix 1
G-Code listings

Chapter 3 codes

Code written by Mr. Joachim Liebscher and modified by Dr. Tomasz Jüngst, Mr. Andrei Hrynevich and the author.

Main code

```
;------------------------------------------------------------
; Construct 1  - stabilizing of parameters (2L)
; Construct 2-4 prints
; 0.250 mm
; +5.00 kV -1.50 kV
; F750
; pause for 0.10 s before loop
; PURAC 1 days at 85 °C;
; 24 °C 35% rH
; 22 G
;------------------------------------------------------------


; Temperature and pressure configuration

T1=850
T2=850
DRUCK=10

; Number of layer pairs per construct
1 DIM #LC (4)
1 #LC (1)  = 2 :       #LC (2)  = 5   :       #LC (3)  = 10  :       #LC (4)  = 40


; Construct description
; - lines:
1       #LLENGTH       = 45
1       #LSPEED        = 750
1       #LDIST  = 0.25
1       #LNUM          = INT(#LLENGTH / (2*#LDIST))

; - turns:
1       #TRADIUS       = -1.5
1       #TSPEED        = 500
1       #TIPAUSE       = 0.1
1       #TOPAUSE       = 0.05



; Initialize time measurement
1 #GSTART      = CLOCK
1 #GLINES      = (#LC(1)+#LC(2)+#LC(3)+#LC(4))*#LNUM*2
1 #GFLINES     = 0

; Part 1 - starting position
G17 G90
G1 X210 Y160 F800

; Construct 1
LP BUILDLAYER [1]



; Position construct 2
G90
```

```
G1 X150 Y160 F800

; Construct 2

LP BUILDLAYER [2]


; Position construct 3

G90
G1 X90 Y160 F800
G1 X90 Y100 F800
G1 X150 Y100 F800

; Construct 3

LP BUILDLAYER [3]

; Position construct 4

G90
G1 X210 Y100 F800

; Construct 4

LP BUILDLAYER [4]


; Parking position with movement

; Move to parking positon

G90
G1 X215 Y100 F800
G1 X215 Y165 F800

; Movement parking position
1 FOR I%=1 TO 2000
1 WAIT
LP PARKLOOP
1 WAIT
1 NEXT I%


; Programm END
DRUCK=0
T1=0
T2=0
M30


;-------------------------------------------------------------

; Function: Build X-Layer, then Y-Layer
LPS BUILDLAYER
        ;move in
        G91
        G1 X-8 Y-8 F800
        G4 F0.5

        ;build
        1 FOR I%=1 TO #LC(P1)
                1 WAIT
                LP DOXLAYER
                LP DOYLAYER
                1 WAIT
        1 NEXT I%

        ;move out
        G91
        G1 X8 Y8 F800
PEND



; Function: Build a X-layer
LPS DOXLAYER
```

```
1 FOR I%=1 TO #LNUM
        G1 X[-#LLENGTH]        Y0                              F[#LSPEED]
        G4 F[#TIPAUSE]
        G3 X0                          Y[-#LDIST]    R[#TRADIUS] F[#TSPEED]
        G4 F[#TOPAUSE]

        G1 X[#LLENGTH] Y0                               F[#LSPEED]
        G4 F[#TIPAUSE]
        G2  X0                         Y[-#LDIST]    R[#TRADIUS] F[#TSPEED]
        G4 F[#TOPAUSE]
1       WAIT

        ; Time Calculations:
1       #GFLINES = #GFLINES+1
1       DIFF    = (CLOCK - #GSTART)/ 1000 : DIFFH = INT(DIFF/3600) : DIFFM = INT((DIFF-
DIFFH*3600)/60) : DIFFS = INT(DIFF-DIFFH*3600-DIFFM*60)
1       EST     = DIFF/#GFLINES*#GLINES - DIFF  : ESTH = INT(EST/3600) : ESTM = INT((EST-
ESTH*3600)/60) : ESTS = INT(EST-ESTH*3600-ESTM*60)
1       PRN#(0, "Elapsed time: ##h ##min ##s, est. remaining time: ##h ##min ##s", DIFFH,
DIFFM, DIFFS, ESTH, ESTM, ESTS)
1 NEXT I%
G1   X[-#LLENGTH]    Y0           F[#LSPEED]
G4 F0.05
PEND


; Function: Build a Y-Layer
LPS DOYLAYER
1 FOR I%=1 TO #LNUM
        G1 X0                          Y[#LLENGTH]                   F[#LSPEED]
        G4 F[#TIPAUSE]
        G2 X[#LDIST]           Y0             R[#TRADIUS]    F[#TSPEED]
        G4 F[#TOPAUSE]

        G1 X0                          Y[-#LLENGTH]                  F[#LSPEED]
        G4 F[#TIPAUSE]
        G3 X[#LDIST]           Y0             R[#TRADIUS]    F[#TSPEED]
        G4 F[#TOPAUSE]
1       WAIT

        ; Time Calculations:
1       #GFLINES = #GFLINES+1
1       DIFF    = (CLOCK - #GSTART)/ 1000 : DIFFH = INT(DIFF/3600) : DIFFM = INT((DIFF-
DIFFH*3600)/60) : DIFFS = INT(DIFF-DIFFH*3600-DIFFM*60)
1       EST     = DIFF/#GFLINES*#GLINES - DIFF  : ESTH = INT(EST/3600) : ESTM = INT((EST-
ESTH*3600)/60) : ESTS = INT(EST-ESTH*3600-ESTM*60)
1       PRN#(0, "Elapsed time: ##h ##min ##s, est. remaining time: ##h ##min ##s", DIFFH,
DIFFM, DIFFS, ESTH, ESTM, ESTS)
1 NEXT I%
G1   X0          Y[#LLENGTH]      F[#LSPEED]
G4 F0.05
PEND


; Function: Movement at parking position
LPS PARKLOOP
1 FOR I%=1 TO 100
        G1 G91 Y-130 F500
        G4 F0.05
        Y130
        G4 F0.05
1       WAIT
1 NEXT I%
PEND
```

Chapter 4 codes

Code written by Mr. Andrei Hrynevich and modified by the author.

Main code

```
; Scaffolds for µCT.
; Log: Printing with ~ 20 µm fiber diameters with 250 µm spacing
; 12 mm scaffold, 2x5 - 6x2 - 250 µm spacing
; 3.5 mm working distance
; external SRs: SRRBv1, SRXLv1, SRRSQv3
; duration measurement, written in the file "TM"
; Turn radius is 1 turn speed is 400
; -1,5+4.5 kV; ~3.5 mm
; 22G; 1.2 bar
; 23.3 °C, 35% rH; 85 °C
; shifted XMIN, YMAX
; PURAC PCL 3 Days 85° C
;Parameters
(----------------------------------------------------------------------)
; Temperature and pressure configuration
T1=850
T2=850
P=12

;Working area
1 #XMAX=230
1 #XMIN=90
1 #YMAX=185
1 #YMIN=30

1 #CSIZE=16
1 #SPACING=20

;Base feedrate for the linear and circular movement
1 #FEEDF=400
1 #FEEDR=400
1 #ECTS=300

;Turn radius
1 #XRAD=1.5

;Pause
1 #TI=0.04
1 #TO=0.00


;main program
(----------------------------------------------------------------------)

N010 G17 G8 G90
;Starting time
0015 STARTTIME%=CLOCK

;First glass slide for stabilization;
N020 G1 X[#XMAX]       Y[#YMAX]       F[#FEEDF]
N030 G91
0040 CALL SRRBv1 (10, 1,1,12,28,800)

1 NDROWS%=INT((#YMAX-#YMIN)/(2*(#CSIZE+#SPACING)))
1 NCOLUMNS%=INT((212-#XMIN)/(#CSIZE+#SPACING))

1 FOR I%=1 TO NDROWS%
1       FOR J%=1 TO NCOLUMNS%
N045            G90
N050            G1      X[212-(J%-1)*(#CSIZE+#SPACING)]              Y[#YMAX-(2*I%-
2)*(#CSIZE+#SPACING)]  F[#FEEDF]
N060            G91
1 CALL SRRSQv3(16,0.25,3,4)
;P1 - size, P2 - spacing, P3 - number of rotations, P4 - Height
1       NEXT J%
```

```
1       FOR J%=1 TO NCOLUMNS%
N045            G90
N050            G1      X[212-(#CSIZE+#SPACING)*(NCOLUMNS%-1)+(J%-1)*(#CSIZE+#SPACING)]
        Y[#YMAX-(2*I%-1)*(#CSIZE+#SPACING)]   F[#FEEDF]
N060            G91
1 CALL SRRSQv3(16,0.25,6,2)
;P1 - size, P2 - spacing, P3 - number of rotations, P4 - Height
1       NEXT J%
1 NEXT I%

;Measure the time, switch off the pressure and go to initial position
0145 ENDTIME%=CLOCK
0150 TIMEH%=INT((ENDTIME%-STARTTIME%)/3600000)
0160 TIMEM%=INT((ENDTIME%-STARTTIME%-(TIMEH%*3600000))/60000)
0165 OPENW(1, "TM")
0163 REWRITE(1)
0170 PRN#(1, "Running time was:",TIMEH%,"h",TIMEM%,"min")
0180 CLOSE(1)

P=0
N210 G90
N220 G1 X[#XMAX] Y[#YMAX-70] F[#FEEDF]
N220 G1 X[#XMAX] Y[#YMAX] F[#FEEDF]
M30
```

Subroutines

SRRBv1

```
;Rectangular construct with width in X- and length in Y-direction
;Parameters: P1-hight(layers), P2 - X-direction fiber pitch, P3 - Y-direction fiber pitch
;P4 - Size in X-direction, P5 - size in Y-direction, P6 - linear speed
;!!!!! diagonal entering movement cancelled


1 H=P1
1 XPITCH=P2
1 YPITCH=P3
1 XSIZE=P4
1 YSIZE=P5
1 FEEDL=P6

1 #XRAD=1
1 #YRAD=1

;Pause calculation


;G1 X-3 Y-3     F[#FEEDF]
1 FOR I%=1 TO H
        LP XLAYER_ST[XPITCH, XSIZE, YSIZE, FEEDL]
        LP YLAYER_ST[YPITCH, XSIZE, YSIZE, FEEDL]
1 NEXT I%
;G1 X3          Y3      F[#FEEDF]
PEND


LPS XLAYER_ST
;SWP with the lines parallel to the X-axis;
; P1 - lines spacing, P2 - X-dimension, P3 - Y-dimension; P4 - linear speed

1 FOR I%=1 TO INT(P3/(2*P1))
        G1 X[-P2]               Y0                      F[P4]
        G4 F[#TI]
        G3 X0                   Y[-P1]  R[-#XRAD]       F[#FEEDR]
        G4 F[#TO]
        G1 X[P2]                Y0                      F[P4]
        G4 F[#TI]
        G2 X0                   Y[-P1]  R[-#XRAD]       F[#FEEDR]
        G4 F[#TO]
```

```
1 NEXT I%
G1 X0   Y[2*P1*INT(P3/(2*P1))] F[P4]
G4 F[#TI]
PEND


LPS YLAYER_ST
;SWP with the lines parallel to the Y-axis;
;P1 - lines spacing, P2 - X-dimension, P3 - Y-dimension; P4 - linear speed

1 FOR I%=1 TO INT(P2/(2*P1))
       G1 X0                 Y[-P3]                F[P4]
       G4 F[#TI]
       G2 X[-P1]             Y0      R[-#YRAD]     F[#FEEDR]
       G4 F[#TO]
       G1 X0          Y[P3]                        F[P4]
       G4 F[#TI]
       G3 X[-P1]             Y0      R[-#YRAD]     F[#FEEDR]
       G4 F[#TO]
1 NEXT I%
G1 X[2*P1*INT(P2/(2*P1))]     Y0      F[P4]
G4 F[#TI]
PEND
```

SRRSQv3

```
;rotated linear arrays, even angular distribution
;external SR for the "CALL" command
;P1 - size, P2 - spacing, P3 - number of rotations, P4 - Height
;Used External SRs: SRXLv1
G91
G1 X-8  Y-8     F[#FEEDF]
1 WAIT
1 POLECX= MCS(1) - P1/2
1 POLECY= MCS(2) - P1/2
POP([POLECX], [POLECY])
PLS(X[POLECX], Y[POLECY])
1 FOR J%=1 TO P4
1       FOR I%=1 TO P3
               ROT([180*(I%-1)/P3])
1              CALL SRXLv1(P2, P1, P1, #FEEDF)
               ;P1 - lines spacing, P2 - X-dimension, P3 - Y-dimension; P4 - linear speed
               ROT()
               G90
               G1 (POL) Y[P1/SQRT(2)] A[-45+(180*I%/P3)]    F[#FEEDF]
               G91
1       NEXT I%
        G90
1       IF P3<5 THEN
        G1 X=IC(0)             Y[POLECY+P1/2] F[#FEEDF]
           X[POLECX+P1/2]      Y=IC(0)
1       ELSE
        G1 X[POLECX+P1/2]      Y=IC(0)        F[#FEEDF]
           X=IC(0)             Y[POLECY+P1/2]
1       ENDIF
        G91
1 NEXT J%
G1 X8   Y8      F[#FEEDF]
M30
```

SRXLv1

```
;SWP with the lines parallel to the X-axis;
; P1 - lines spacing, P2 - X-dimension, P3 - Y-dimension; P4 - linear speed

1 FOR I%=1 TO INT(P3/(2*P1))
       G1 X[-P2]              Y0                    F[P4]
       G4 F[#TI]
       G3 X0                  Y[-P1]  R[-#XRAD]      F[#FEEDR]
       G4 F[#TO]
```

```
        G1 X[P2]               Y0                     F[P4]
        G4 F[#TI]
        G2 X0                  Y[-P1]  R[-#XRAD]      F[#FEEDR]
        G4 F[#TO]
1 NEXT I%
G1 X0   Y[2*P1*INT(P3/(2*P1))] F[P4]
G4 F[#TI]
```

Chapter 5 codes

Code written by Mr. Andrei Hrynevich and modified by the author.

Main code

```
; Scaffolds for D2H in vivo experiments
; 12x12 mm Box scaffolds
; 2.9 mm from metal to head working distance (Z=0.9)
; external SRs: SRRBv1, SRXLvP4, SRRSQvPx2 (loop radius changed)
; duration measurement, written in the file "TM"
; Turn radius is 0.5
; 0 +5.0 kV; ~2.9 mm
; 30G; 2.0 bar
; 23.3 °C, 37% rH; 77 °C
; shifted XMIN, YMAX
; PURAC PCL 0 Days 77 °C - Heated to 85 °C for 30 minutes and then 77 °C for 30 minutes
;Parameters
(----------------------------------------------------------------------)
; Temperature and pressure configuration
T1=770
T2=770
P=20

;Working area
1 #XMAXR=218
1 #XMINR=150
1 #XMAXL=148
1 #XMINL=80
1 #YMAX=206
1 #YMIN=102

1 #CSIZER=12
1 #CSIZEL=12
1 #SPCX=10
1 #SPCY=26-#CSIZER

;Base feedrate for the linear and circular movement
1 #FEEDF=1100
1 #FEEDR=1000
1 #ECTS=300

;Turn radius
1 #XRAD=1.5
1 #LR=0.6

;Pause
1 #TI=0.05
1 #TO=0.001


;main program
(----------------------------------------------------------------------)

N010 G17 G8 G90
;Starting time
0015 STARTTIME%=CLOCK

;Start of Right Side: Box

;First glass slide for stabilization;
N020 G1 X[#XMAXR]      Y[#YMAX]       F[#FEEDF]
N030 G91
0040 CALL SRRBv1 (5,0.2,0.2,6,14,1100)

1 NDROWS%=INT((#YMAX-#YMIN)/(2*(#CSIZER+#SPCY)))
1 NCOLUMNS%=INT(((#XMAXR-11)-#XMINR)/(#CSIZER+#SPCX))

1 FOR I%=1 TO NDROWS%
1       FOR J%=1 TO NCOLUMNS%
N045           G90
```

```
N050           G1      X[(#XMAXR-11)-(J%-1)*(#CSIZER+#SPCX)]        Y[#YMAX-(2*I%-
2)*(#CSIZER+#SPCY)]    F[#FEEDF]
N060           G91
1 #TI=0
1 #TO=0
1 CALL SRRSQvPx2(12,0.06,3,14,#TI,#TO)
;P1 - size, P2 - spacing, P3 - number of rotations, P4 - Height, TI - pause before loop, TO -
pause after loop
1       NEXT J%

1       FOR J%=1 TO NCOLUMNS%
N045           G90
N050           G1      X[(#XMAXR-11)-(#CSIZER+#SPCX)*(NCOLUMNS%-1)+(J%-1)*(#CSIZER+#SPCX)]
        Y[#YMAX-(2*I%-1)*(#CSIZER+#SPCY)]     F[#FEEDF]
N060           G91
1 #TI=0
1 #TO=0
1 CALL SRRSQvPx2(12,0.06,3,14,#TI,#TO)
;P1 - size, P2 - spacing, P3 - number of rotations, P4 - Height, TI - pause before loop, TO -
pause after loop
1       NEXT J%
1 NEXT I%

;Docking after Right Side:
N210 G90
N220 G1 X[#XMAXR] Y[#YMAX-70] F[#FEEDF]
N220 G1 X[#XMAXR] Y[#YMAX] F[#FEEDF]


;Start of Left Side: Triangle

;First glass slide for stabilization;
N020 G1 X[#XMAXL]      Y[#YMAX]       F[#FEEDF]
N030 G91
0040 CALL SRRBv1 (1,0.2,0.2,6,14,800)

1 NDROWS%=INT((#YMAX-#YMIN)/(2*(#CSIZEL+#SPCY)))
1 NCOLUMNS%=INT(((#XMAXL-11)-#XMINL)/(#CSIZEL+#SPCX))

1 FOR I%=1 TO NDROWS%
1       FOR J%=1 TO NCOLUMNS%
N045           G90
N050           G1      X[(#XMAXL-11)-(J%-1)*(#CSIZEL+#SPCX)]        Y[#YMAX-(2*I%-
2)*(#CSIZEL+#SPCY)]    F[#FEEDF]
N060           G91
1 #TI=0
1 #TO=0
1 CALL SRRSQvPx2(12,0.06,3,14,#TI,#TO)
;P1 - size, P2 - spacing, P3 - number of rotations, P4 - Height, TI - pause before loop, TO -
pause after loop
1       NEXT J%

1       FOR J%=1 TO NCOLUMNS%
N045           G90
N050           G1      X[(#XMAXL-11)-(#CSIZEL+#SPCX)*(NCOLUMNS%-1)+(J%-1)*(#CSIZEL+#SPCX)]
        Y[#YMAX-(2*I%-1)*(#CSIZEL+#SPCY)]     F[#FEEDF]
N060           G91
1 #TI=0
1 #TO=0
1 CALL SRRSQvPx2(12,0.06,3,14,#TI,#TO)
;P1 - size, P2 - spacing, P3 - number of rotations, P4 - Height, TI - pause before loop, TO -
pause after loop
1       NEXT J%
1 NEXT I%

;Measure the time, switch off the pressure and go to initial position
0145 ENDTIME%=CLOCK
0150 TIMEH%=INT((ENDTIME%-STARTTIME%)/3600000)
0160 TIMEM%=INT((ENDTIME%-STARTTIME%-(TIMEH%*3600000))/60000)
0165 OPENW(1, "TM")
0163 REWRITE(1)
0170 PRN#(1, "Running time was:",TIMEH%,"h",TIMEM%,"min")
0180 CLOSE(1)

;Docking after Left Side
P=0
N210 G90
```

```
N220 G1 X[#XMAXL] Y[#YMAX-70] F[#FEEDF]
N220 G1 X[#XMAXL] Y[#YMAX] F[#FEEDF]
M30
```

Subroutines

SRXLvP4

```
;rounded connnection btw the circles and lines via splines
;Parameters: P1-hight(layers), P2 -fiber spacing, P3 - size
;P4 - linear speed, P5 - turn speed
;to be called with the "CALL" command
;!!!!!Pause switched off

;SR executable code
(--------------------------------------------------------------------)

1 H=P1
1 PITCH=P2
1 SIZE=P3
1 FEEDL=P4
1 FEEDR=P5
1 TIPAUSE=P6
1 TOPAUSE=P7

SplineDef(1213)

;radius calc
1 IF PITCH<0.5 THEN
1       RAD=#LR
1       ELSE
1       RAD=PITCH
1 ENDIF

1 APPD=0.4*RAD

1 FOR J%=1 TO H
1       FOR I%=1 TO INT(SIZE/(2*PITCH))
                G1 X[-SIZE]           Y0             F[FEEDL]
                G4                                                          F[TIPAUSE]

                G6 X[-APPD] Y[APPD]                          F[FEEDR]
                G3 X0          Y[-PITCH-2*APPD]      R[-RAD] F[FEEDR]
                G6 X[APPD] Y[APPD]                           F[FEEDR]
                G4                                                          F[TOPAUSE]
                G1 X[SIZE]     Y0                            F[FEEDL]
                G4                                                          F[TIPAUSE]
                G6 X[APPD]     Y[APPD]                       F[FEEDR]
                G2 X0          Y[-PITCH-2*APPD]      R[-RAD] F[FEEDR]
                G6 X[-APPD] Y[APPD]                          F[FEEDR]
                G4                                                          F[TOPAUSE]
1       NEXT I%
        G1 X0   Y[2*PITCH*INT(SIZE/(2*PITCH))]       F[FEEDL]
        G4                                                                  F[TIPAUSE]
1 NEXT J%
M30
```

SRRSQvPx2

```
;rotated linear arrays, even angular disribution
;external SR for the "CALL" command
;P1 - size, P2 - spacing, P3 - number of rotations, P4 - Height
;Used External SRs: SRXLv3
G91
G1 X-2  Y-2     F[#FEEDF]
1 WAIT
1 POLECX= MCS(1) - P1/2
1 POLECY= MCS(2) - P1/2
```

```
POP([POLECX], [POLECY])
PLS(X[POLECX], Y[POLECY])
1 FOR J%=1 TO P4
1       FOR I%=1 TO P3
                ROT([180*(I%-1)/P3])
1               CALL SRXLvP4(1, P2, P1, #FEEDF, #FEEDR, P5, P6)
                ;P1-hight(layers), P2 -fiber spacing, P3 - size, P4 - linear speed, P5 - turn
speed, PauseIN, PauseOUT
                ROT()
                G90
                G4 F[P5]
                G3 (POL) Y[P1/SQRT(2)] A[-45+(180*I%/P3)] R[P1/SQRT(2)]     F[#FEEDF]
                G4 F[P5]
                G91
1       NEXT I%
        G90
1       IF P3<5 THEN
        G3 X[POLECX+P1/2]      Y[POLECY+P1/2] R[-P1/SQRT(2)] F[#FEEDF]
        G4 F[P5]
1       ELSE
        G2 X[POLECX+P1/2]      Y[POLECY+P1/2] R[-P1/SQRT(2)] F[#FEEDF]
        G4 F[P5]
1       ENDIF
        G91
1 NEXT J%

;1 CALL FRML (1.5, 0.25, 10, 10, 10)
; P1 -  width, P2 - spacing, P3 - inner size Y, P4- inner size X, P5 - speed

G1 X8   Y8      F[#FEEDF]
M30
```

Frame main code

```
; Scaffolds for D2H in vivo experiments
; Log: Printing of frames around scaffolds - SRFRLSv2 (6, 2, 7, 3, 35, 1)
; 12x12 mm Box scaffolds
; XXX mm working distance (Z=7)
; external SRs: SRRBv1, CFRAMEv2, SRFRLSv2
; duration measurement, written in the file "TM"
; Turn radius is 0.5
; -1.5 +8.0 kV; ~XXX mm
; 22G; 2.0 bar
; 22.7 °C, 34% rH; 85 °C
; shifted XMIN, YMAX
; PURAC PCL 5 Days 77-85 °C
;Parameters
(----------------------------------------------------------------)
; Temperature and pressure configuration
T1=850
T2=850
P=20

;Working area
1 #XMAXR=218
1 #XMINR=150
1 #XMAXL=148
1 #XMINL=80
1 #YMAX=206
1 #YMIN=102

1 #CSIZER=12
1 #CSIZEL=12
1 #SPCX=10
1 #SPCY=26-#CSIZER

;Base feedrate for the linear and circular movement
1 #FEEDF=500
1 #FEEDR=300
1 #ECTS=300

;Turn radius
1 #XRAD=1.5
```

```
1 #LR=0.5

;Pause
1 #TI=0.1
1 #TO=0.05


;main program
(-----------------------------------------------------------------)

N010 G17 G8 G90
;Starting time
0015 STARTTIME%=CLOCK

;Start of Right Side: Box

;First glass slide for stabilization;
N020 G1 X[#XMAXR]      Y[#YMAX]       F[#FEEDF]
N030 G91
0040 CALL SRRBv1 (5,0.5,0.5,6,14,800)

1 NDROWS%=INT((#YMAX-#YMIN)/(2*(#CSIZER+#SPCY)))
1 NCOLUMNS%=INT(((#XMAXR-11)-#XMINR)/(#CSIZER+#SPCX))

1 FOR I%=1 TO NDROWS%
1       FOR J%=1 TO NCOLUMNS%
N045            G90
N050            G1      X[(#XMAXR-11)-(J%-1)*(#CSIZER+#SPCX)]        Y[#YMAX-(2*I%-
2)*(#CSIZER+#SPCY)]    F[#FEEDF]
N060            G91
1 #TI=0.05
1 #TO=0.001
1 CALL CFRAMEv2
;SRFRLSv2 (6, 2, 7, 3, 35, 1)
1       NEXT J%

1       FOR J%=1 TO NCOLUMNS%
N045            G90
N050            G1      X[(#XMAXR-11)-(#CSIZER+#SPCX)*(NCOLUMNS%-1)+(J%-1)*(#CSIZER+#SPCX)]
        Y[#YMAX-(2*I%-1)*(#CSIZER+#SPCY)]     F[#FEEDF]
N060            G91
1 #TI=0.05
1 #TO=0.001
1 CALL CFRAMEv2
;SRFRLSv2 (6, 2, 7, 3, 35, 1)
1       NEXT J%
1 NEXT I%

;Docking after Right Side:
N210 G90
N220 G1 X[#XMAXR] Y[#YMAX-70] F[#FEEDF]
N220 G1 X[#XMAXR] Y[#YMAX] F[#FEEDF]



;Start of Left Side: Triangle

;First glass slide for stabilization;
N020 G1 X[#XMAXL]      Y[#YMAX]       F[#FEEDF]
N030 G91
0040 CALL SRRBv1 (1,0.2,0.2,6,14,800)

1 NDROWS%=INT((#YMAX-#YMIN)/(2*(#CSIZEL+#SPCY)))
1 NCOLUMNS%=INT(((#XMAXL-11)-#XMINL)/(#CSIZEL+#SPCX))

1 FOR I%=1 TO NDROWS%
1       FOR J%=1 TO NCOLUMNS%
N045            G90
N050            G1      X[(#XMAXL-11)-(J%-1)*(#CSIZEL+#SPCX)]        Y[#YMAX-(2*I%-
2)*(#CSIZEL+#SPCY)]    F[#FEEDF]
N060            G91
1 #TI=0.05
1 #TO=0.001
;1 CALL CFRAMEv2
;SRFRLSv2 (6, 2, 7, 3, 35, 1)
1       NEXT J%
```

```
1       FOR J%=1 TO NCOLUMNS%
N045            G90
N050            G1      X[(#XMAXL-11)-(#CSIZEL+#SPCX)*(NCOLUMNS%-1)+(J%-1)*(#CSIZEL+#SPCX)]
        Y[#YMAX-(2*I%-1)*(#CSIZEL+#SPCY)]     F[#FEEDF]
N060            G91
1 #TI=0.05
1 #TO=0.001
;1 CALL CFRAMEv2
;SRFRLSv2 (6, 2, 7, 3, 35, 1)
1       NEXT J%
1 NEXT I%

;Measure the time, switch off the pressure and go to initial position
0145 ENDTIME%=CLOCK
0150 TIMEH%=INT((ENDTIME%-STARTTIME%)/3600000)
0160 TIMEM%=INT((ENDTIME%-STARTTIME%-(TIMEH%*3600000))/60000)
0165 OPENW(1, "TM")
0163 REWRITE(1)
0170 PRN#(1, "Running time was:",TIMEH%,"h",TIMEM%,"min")
0180 CLOSE(1)

;Docking after Left Side
P=0
N210 G90
N220 G1 X[#XMAXL] Y[#YMAX-70] F[#FEEDF]
N220 G1 X[#XMAXL] Y[#YMAX] F[#FEEDF]
M30
```

Frame subroutines

CFRAMEv2

```
;rotated linear arrays, even angular disribution
;external SR for the "CALL" command
;P1 - size, P2 - spacing, P3 - number of rotations, P4 - Height
;Used External SRs: SRFRLSv2
G91
;G1 X-8 Y-8     F[#FEEDF] (Disabled,not needed)

G91
G1 X-1 Y-8     F[#FEEDF]
;X2 for the 2mm thickness of the construct, Y-6 is to go to the middle of the construct
1 CALL SRFRLSv2 (6, 2, 7, 3, 35, 1)
; P1 - Inner radius, P2 - number of spiral turnings (defines density), P3 - outer radius,
; P4 - Number of rotated unit spirals, P5 - speed, P6 - height

G1 X1 Y8       F[#FEEDF]
;go back to previous position
;G1 X8  Y8      F[#FEEDF] (not needed)
M30
```

SRFRLSv2

```
;"Fermat" spiral starting fron the side
; exponential function
; absolute coordinates
; rotated array
; approach in -X direction


;P1 - Inner radius, P2 - number of spiral turnings (defines density), P3 - outer radius,
;P4 - Number of rotated unit spirals, P5 - speed, P6 - height

1 RMIN=P1
2 NTURNS=P2
3 RMAX=P3
4 NUNITS=P4
```

```
5 FEEDR=P5
6 HEIGHT=P6

1 APWR=1
;smaller APWR values increase the density in the middle and vice versa, APWR=1 -> Archimedean
spiral

1 RSTEP=(RMAX-RMIN)/EXP(APWR, NTURNS)
1 DANGLE=5

1 WAIT

1 XSPCNT=MCS(1)-RMAX
1 YSPCNT=MCS(2)
POP([XSPCNT],[YSPCNT])
PLS(X[XSPCNT],Y[YSPCNT])
SplineDef(1213)
G90
1       FOR K%=1 TO HEIGHT
        1 FOR J%=1 TO  NUNITS
                1       ADDA=360/NUNITS
                        1       FOR I%=1 TO INT((NTURNS*360/DANGLE)+1)
                                        G6 (POL)        X[RMAX-RSTEP*EXP(APWR,DANGLE*(I%-1)/360)]
        A[-DANGLE*(I%-1)-ADDA*(J%-1)] F[FEEDR]
                        1       NEXT I%
                        1       FOR I%=INT((NTURNS*360/DANGLE)+1) STEP-1 TO 1
                                        G6 (POL)        X[RMAX-RSTEP*EXP(APWR,DANGLE*(I%-1)/360)]
        A[DANGLE*(I%-1)-ADDA*(J%-1)] F[FEEDR]
                        1       NEXT I%
                1       IF J%<NUNITS THEN
                        G2 (POL) X[RMAX] A[-ADDA*J%]  R[RMAX]  F[FEEDR]
                1       ELSE
                        G2 (POL) X[RMAX]       A0      R[RMAX] F[FEEDR]
                1 ENDIF
        1       NEXT J%
1       NEXT K%
G91

PEND
```

Appendix 2

ImageJ macro code listing

Chapter 4 ImageJ macro codes

Two-dimensional local thickness analysis macro

```
input=getDirectory("Choose a Directory");
list=getFileList(input);
output=getDirectory("Choose a Directory");

for(i=0;i<list.length;i++){
    open(input+list[i]);

        //Auto thresholding is enabled;
        run("Set Scale...", "distance=0.5869 known=1 pixel=1 unit=µm global");
        run("Threshold...");
        //Manually input values based on previous testing;
        setThreshold(0, 20);
        setOption("BlackBackground", false);
        run("Convert to Mask");
        run("Close");

        //Save a Tiff of the thresholded image;
        saveAs("Tiff", output+ "ThresholdImage" + list[i] + ".tiff");

        run("Local Thickness (complete process)", "threshold=60");

        //Save a Tiff and RGB Jpeg of the LocThk image;
        saveAs("Tiff", output+ "LocThickImage" + list[i] + ".tiff");
        //saveAs("Jpeg", output+ "LocThickImage" + list[i] + ".jpeg");

        //Trial to save output of histogram automatically. Doesn't work!;
        //saveAs("Tiff", output+ list[i] + ".tiff");

        run("Histogram", "bins=82 x_min=1 x_max=165 y_max=Auto");

        //Doesn't work (see Line 25);
        //selectWindow("Histogram of " + list[i]);
        saveAs("Results", output+ "Histogram of " + list[i] + ".csv");
}

print("Done");
```

Chapter 5 ImageJ macro codes

Two-dimensional local thickness analysis macro

```
input=getDirectory("Choose a Directory");
list=getFileList(input);
output=getDirectory("Choose a Directory");

for(i=0;i<list.length;i++){
    open(input+list[i]);

        //Auto thresholding is enabled;
        run("Set Scale...", "distance=0.5869 known=1 pixel=1 unit=µm global");
        run("Threshold...");
        //Manually input values based on previous testing;
        setThreshold(0, 20);
        setOption("BlackBackground", false);
        run("Convert to Mask");
        run("Close");

        //Save a Tiff of the thresholded image;
        saveAs("Tiff", output+ "ThresholdImage" + list[i] + ".tiff");

        run("Local Thickness (complete process)", "threshold=60");

        //Save a Tiff and RGB Jpeg of the LocThk image;
        saveAs("Tiff", output+ "LocThickImage" + list[i] + ".tiff");
        //saveAs("Jpeg", output+ "LocThickImage" + list[i] + ".jpeg");

        //Trial to save output of histogram automatically. Doesn't work!;
        //saveAs("Tiff", output+ list[i] + ".tiff");

        run("Histogram", "bins=82 x_min=1 x_max=165 y_max=Auto");

        //Doesn't work (see Line 25);
        //selectWindow("Histogram of " + list[i]);
        saveAs("Results", output+ "Histogram of " + list[i] + ".csv");
}

print("Done");
```

CD68 positively stained area analysis macro

```
input=getDirectory("Choose a Directory");
list=getFileList(input);
output=getDirectory("Choose a Directory");

for(i=0;i<list.length;i++){
    open(input+list[i]);

        imageTitle=getTitle();
        setBatchMode(false);

        run("RGB Color");
        selectWindow(imageTitle + " (RGB)");

        //selectWindow(imageTitle);

        makeRectangle(0,0, 1739.13, 1739.13);
        waitForUser("Draw ROI", "Draw ROI in original image");
        roiManager("Add");

        run("Colour Deconvolution", "vectors=[H DAB] hide");

        selectWindow(imageTitle + " (RGB)-(Colour_3)");
        //selectWindow(imageTitle + "-(Colour_3)");
        close();

        selectWindow(imageTitle + " (RGB)-(Colour_1)");
        //selectWindow(imageTitle + "-(Colour_1)");
        close();

        selectWindow(imageTitle + " (RGB)-(Colour_2)");
        //selectWindow(imageTitle + "-(Colour_2)");
        setAutoThreshold("Default");
        //run("Threshold...");
        //setThreshold(0, 174);
        setOption("BlackBackground", false);
        run("Convert to Mask");

        roiManager("Select", 0);
        roiManager("Update");
        saveAs("Tiff", output+ "Decon-Thr" + list[i] + ".tiff");
        run("Set Measurements...", "area perimeter area_fraction display redirect=None
decimal=3");
        run("Measure");

        roiManager("Deselect");
        roiManager("Delete");


}

print("Done");
```

Appendix 3

Staining protocols

Hematoxylin and eosin staining of formalin-fixed, paraffin-embedded sections

The following protocol is based on the literature (Riedelsheimer and Büchl-Zimmermann 2015) and protocols kindly provided by Ms. Purificación Ripalda Cemborain from the University of Navarra, Pamplona, Navarra, Spain.

Material:

- Glass cuvettes or jars
- Metal (or glass) slide mounting rack
- Stopwatch(es)
- Cellulose filter paper and glass funnel
- Water hose

Chemicals and reagents:

- Xylol (Carl Roth 9713.3) or Roti-Histol (Carl Roth 6640.1)
- Roti-Histokitt (Carl Roth 6638.2)
- Mayer's hematoxylin (Sigma MHS32-1L) (Filter before each use)
- Eosin G 0.5% water-soluble (Carl Roth X883.2)
- 100% Ethanol (EtOH) (and dilutions)
- Double distilled water (ddH_2O)
- Tap water (In Würzburg, degree of hardness: 3, more than 14 °dH or more than 2.5 mM $CaCO_3$, available from: https://www.wvv.de/de/privatkunden/trinkwasser/wissenswertes/wasserhaerte/)

Procedure:

1. After sectioning, the slides have to be left overnight in an oven at 37 °C to dry out.
2. Mount the slides on a metal rack.
3. Place slides in the oven at 60 °C for 30 minutes.
4. Immediately immerse the rack in:
    i. 15 minutes in xylol I
    ii. 5 minutes in xylol II
    iii. 2 minutes in 100% EtOH I
    iv. 2 minutes in 100% EtOH II
    v. 2 minutes in 96% EtOH
    vi. 2 minutes in 80% EtOH
    vii. 2 minutes in 60% EtOH
    viii. 5 minutes in ddH2O
5. 15 minutes in Mayer's hematoxylin

6. Remove and place the rack in the sink and wash it with a hose with tap water until no color is coming out.
7. For bluing wash in 10 minutes in running tap water using a hose, aimed at the side of the cuvette or alternatively use 0.1% $NaHCO_3$ (in ddH_2O) for 2 minutes.
8. 2 minutes in ddH_2O
9. 2 minutes in eosin 0.5%
10. Remove and place the rack in the sink and wash it with a hose with tap water until no color is coming out.
11. Dehydrate:
    i. 3-5 dips in 96% EtOH II
    ii. 3-5 dips in 96% EtOH III
    iii. 3-5 dips in 100% EtOH III
    iv. 3-5 dips in 100% EtOH IV
    v. 2 minutes in xylol III
    vi. Move to Xylol IV
12. To cover with a coverslip, take the slide out, plot out the extra xylol with tissue paper, add a drop of Roti-Histokitt on the section and place the coverslip on top. Press on the coverslip (gently) from one direction to the other to get out the air bubbles.
13. Leave to dry overnight under hood.

Picrosirius red staining of formalin-fixed, paraffin-embedded sections

The following protocol is based on the literature (Riedelsheimer and Büchl-Zimmermann 2015) and protocols kindly provided by Ms. Purificación Ripalda Cemborain from the University of Navarra, Pamplona, Navarra, Spain.

Material:

- Glass cuvettes or jars
- Metal (or glass) slide mounting rack
- Stopwatch(es)
- Cellulose filter paper and glass funnel
- Water hose

Chemicals and reagents:

- Xylol (Carl Roth 9713.3) or Roti-Histol (Carl Roth 6640.1)
- Roti-Histokitt (Carl Roth 6638.2)
- Direct Red 80 (Sigma-Aldrich 365548)
- 1.3% saturated picric acid solution (Sigma-Aldrich P6744-1GA)
- 100% Ethanol (EtOH) (and dilutions)
- Double distilled water (ddH_2O)
- Tap water (In Würzburg, degree of hardness: 3, more than 14 °dH or more than 2.5 mM $CaCO_3$, available from: https://www.wvv.de/de/privatkunden/trinkwasser/wissenswertes/wasserhaerte/)
- 0.5% acetic acid solution in ddH_2O

Picrosirius red staining solution preparation from an IHC World protocol (accessed 14.11.2020, https://www.ihcworld.com/_protocols/special_stains/sirius_red.htm): Dissolve 0.5 g of Direct Red 80 in 500 mL of 1.3% saturated picric acid solution. Mix well. Solution can be stored for at least 3 years and reused several times.

Procedure:

1. After sectioning, the slides have to be left overnight in an oven at 37 °C to dry out.
2. Mount the slides on a metal rack.
3. Place slides in the oven at 60 °C for 30 minutes.
4. Immediately immerse the rack in:
    i. 15 minutes in xylol I
    ii. 5 minutes in xylol II
    iii. 2 minutes in 100% EtOH I
    iv. 2 minutes in 100% EtOH II
    v. 2 minutes in 96% EtOH
    vi. 2 minutes in 80% EtOH
    vii. 2 minutes in 60% EtOH
    viii. 5 minutes in ddH2O
5. Stain for 1 hour in picrosirius red solution.
6. Wash by dipping 3 times in two changes of 0.5% acetic acid.

7. Dehydrate:
    i. 3-5 dips in 96% EtOH II
    ii. 3-5 dips in 96% EtOH III
    iii. 3-5 dips in 100% EtOH III
    iv. 3-5 dips in 100% EtOH IV
    v. 2 minutes in xylol III
    vi. Move to Xylol IV
8. To cover with a coverslip, take the slide out, plot out the extra xylol with tissue paper, add a drop of Roti-Histokitt on the section and place the coverslip on top. Press on the coverslip (gently) from one direction to the other to get out the air bubbles.
9. Leave to dry overnight under hood.

Immunohistochemical staining of formalin-fixed, paraffin-embedded sections

The following protocol is based on the recommendations of the manufacturers of the used reagents (Abcam, Vector Labs, and Dianova) and modified with protocols kindly provided by Ms. Purificación Ripalda Cemborain from the University of Navarra, Pamplona, Navarra, Spain.

Material:

- Glass cuvettes and plastic Hellendahl staining jars
- Metal (or glass) slide mounting racks
- Pressure cooker
- Cellulose filter paper and glass funnel
- Water hose

Chemicals and reagents:

- Xylol (Carl Roth 9713.3) or Roti-Histol (Carl Roth 6640.1)
- 100% Ethanol (EtOH) (and dilutions)
- Double distilled water (ddH_2O)
- Tap water (In Würzburg, degree of hardness: 3, more than 14 °dH or more than 2.5 mM $CaCO_3$, available from: https://www.wvv.de/de/privatkunden/trinkwasser/wissenswertes/wasserhaerte/)
- 1X Phosphate buffered saline (PBS)
- Roti-Histokitt (Carl Roth 6638.2)
- Harris hematoxylin (Sigma HHS32-1L) (Filter before each use)
- ImmPACT NovaRED (Vector Labs SK-4805) or Enhanced DAB (Sigma D3939-1SET)
- 5X BSA (Histological grade) or supplied normal serum in ImmPRESS kit.
- Primary antibodies:
    1. anti-CD68 polyclonal rabbit anti-mouse antibody (1:500, Abcam ab125212)
    2. anti-CD31 rat anti-mouse antibody (1:50, clone SZ31, Dianova DIA-310)
    3. Rabbit IgG control (same concentration as CD68 antibody, Vector Labs I-1000)
    4. Rat IgG control (same concentration as CD31 antibody, Vector Labs I-4000)
- ImmPRESS HRP kits, Vector Labs:
    1. Goat anti-rat MP-7444
    2. Goat anti-rabbit MP-7451-15
- 3% hydrogen peroxide (H_2O_2) in ddH_2O
- Citric acid (anhydrous) (Carl Roth X863.1)

Antigen retrieval solution recipe for heat-induced epitope retrieval from an IHC World protocol (accessed 14.11.2020, http://www.ihcworld.com/_protocols/epitope_retrieval/citrate_buffer.htm): Dissolve 1.92 g of anhydrous citric acid in 1 L of water. Adjust the pH to 6.0 using 1 N NaOH. Add 0.5 mL of Tween-20 and mix well. Store at room temperature for 3 months or at 4 °C for longer periods.

Procedure:

Day 1:

1. After sectioning, the slides have to be left overnight in an oven at 37 °C to dry.
2. Mount the slides on the metal rack.
3. Place slides in the oven at 60 °C for 30 minutes.
4. Immediately immerse the rack in:
    i. 15 minutes in xylol I
    ii. 5 minutes in xylol II
    iii. 2 minutes in 100% EtOH I
    iv. 2 minutes in 100% EtOH II
    v. 2 minutes in 96% EtOH I
    vi. 2 minutes in 80% EtOH
    vii. 2 minutes in 60% EtOH
    viii. 5 minutes in ddH_2O
5. 5 minutes in PBS
6. Antigen retrieval stage:
    i. Make sure that the cooker has at least 1 L of water inside.
    ii. Place the slides in the 10 mM citrate buffer solution (use once) at room temperature (RT) in a plastic Hallendahl jar and lower into the water in the cooker.
    iii. Heat in pressure cooking mode for 5 minutes at 50 kPa, then release the steam and carefully open the pressure cooker.
    iv. Take out the jar and leave at RT for 20 minutes.
7. 5 minutes in PBS at RT
8. Quenching of endogenous peroxidase activity by incubation in 3% of H_2O_2 (in ddH_2O)
9. 5 minutes in PBS at RT
10. Mark around the sample with hydrophobic pen. Move into humidified chamber.
11. Incubate in blocking solution for 45 minutes at RT in humidified chamber:
    i. Either 5% BSA in PBS (Mix well, do not shake and filter with 0.2 µm filter before usage. Solution can be aliquoted and frozen at -20 °C. Thaw just once).
    ii. Or from the ImmPRESS HRP Polymer Detection Kit, use the supplied 2.5% normal goat serum.
12. Do not wash afterwards, just remove excess fluid.
13. Prepare primary antibodies (dilute in PBS):
    i. CD68 1:500
    ii. CD31 1:50
    iii. Rat IgG control (same concentration as in CD31)
    iv. Rabbit IgG control (same concentration as in CD68)
14. Add primary antibody diluted in PBS. Incubate in humidified chamber for overnight at 4 °C.

Day 2:

1. Take out of 4 °C and wash for 10 minutes in PBS.
2. Add ImmPRESS secondary antibody for 30 minutes in humidified chamber.
3. Wash 3x10 minutes in PBS.

4. Incubate with HRP substrate after removing excess PBS. For NovaRED, 3 minutes or for Enhanced DAB, 5 minutes.
5. Stop further substrate reaction by immersion in ddH_2O.
6. Place slides back in a metal rack and counterstain with Harris' hematoxylin for 7 seconds.
7. Wash adequately with tap water using a hose.
8. Dehydrate:
    i. 3-5 dips in 96% EtOH II
    ii. 3-5 dips in 96% EtOH III
    iii. 3-5 dips in 100% EtOH III
    iv. 3-5 dips in 100% EtOH IV
    v. 2 minutes in xylol III
    vi. Move to Xylol IV
9. To cover with a coverslip, take the slide out, plot out the extra xylol with tissue paper, add a drop of Roti-Histokitt on the section and place the coverslip on top. Press on the coverslip (gently) from one direction to the other to get out the air bubbles.
10. Leave to dry overnight under hood.

Appendix 4

Immunohistochemical staining controls

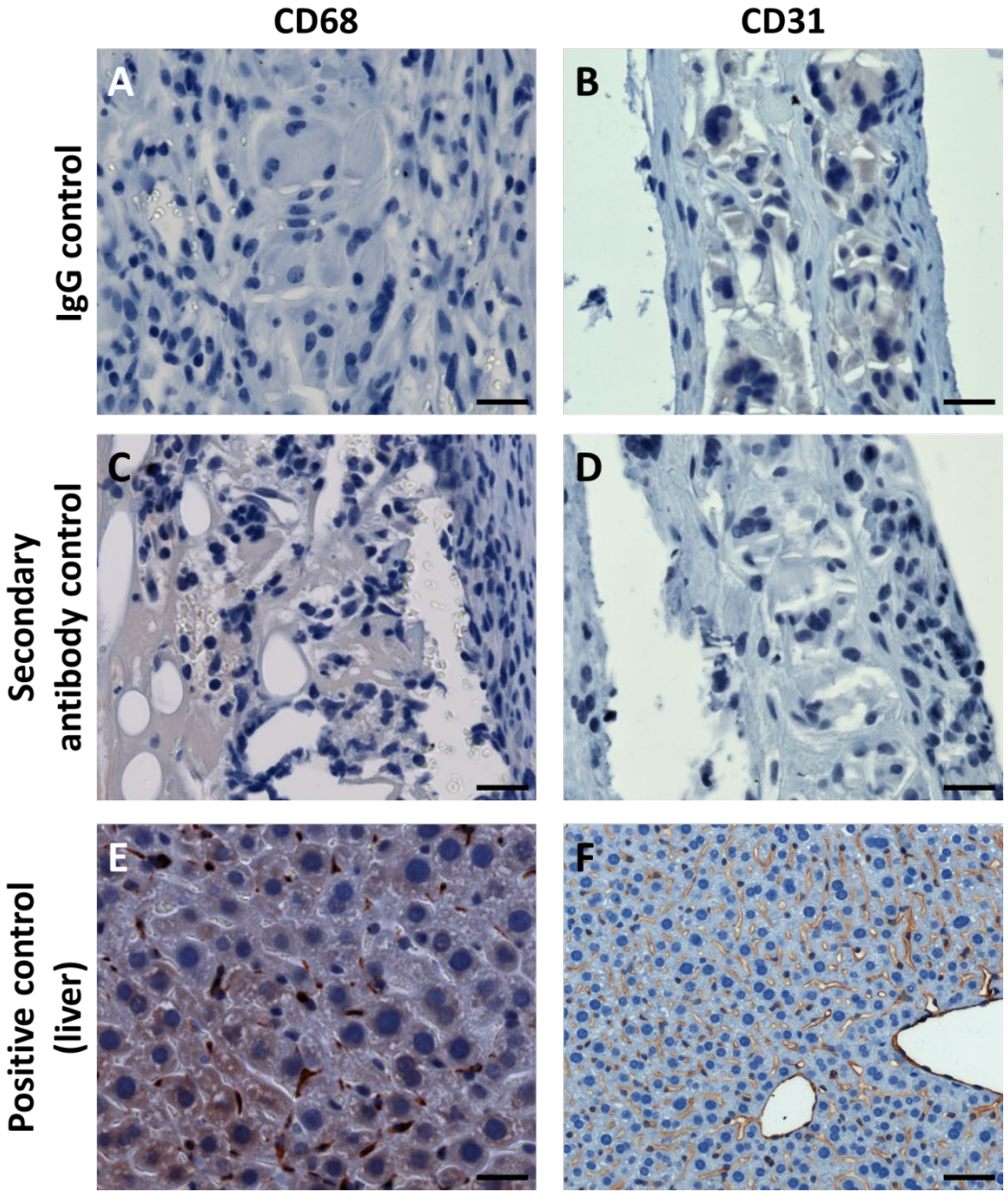

Supplementary Figure 1. Representative micrographs for the controls used in both CD68 and CD31 IHC staining. CD68 staining with a polyclonal rabbit anti-mouse primary antibody and a goat anti-rabbit secondary detection system. CD31 staining with a monoclonal rat anti-mouse primary antibody and a goat anti-rat secondary detection system. IgG controls were used from the same species as the primary antibody. Secondary controls were performed with omission of primary antibodies and incubation in PBS instead. Positive controls show Kupffer cells (CD68) and endothelial cells (CD31) in mouse liver tissue. Scale bars in (A-E) are 25 µm. Scale bar in (F) is 50 µm.

Appendix 5

Additional images for Chapter 5

The following micrographs are captured using sequential sections and show histochemical staining with HE and PSR, as well as IHC staining for CD68 and CD31. The same ROI was selected in each figure, representing frame area (**Supplementary Figure 2**), scaffold area immediately adjacent to the frame (**Supplementary Figure 3**) and an area in the middle of the scaffold (**Supplementary Figure 4**). All images were taken from the same, whole slide scans of a Day 14 box sample.

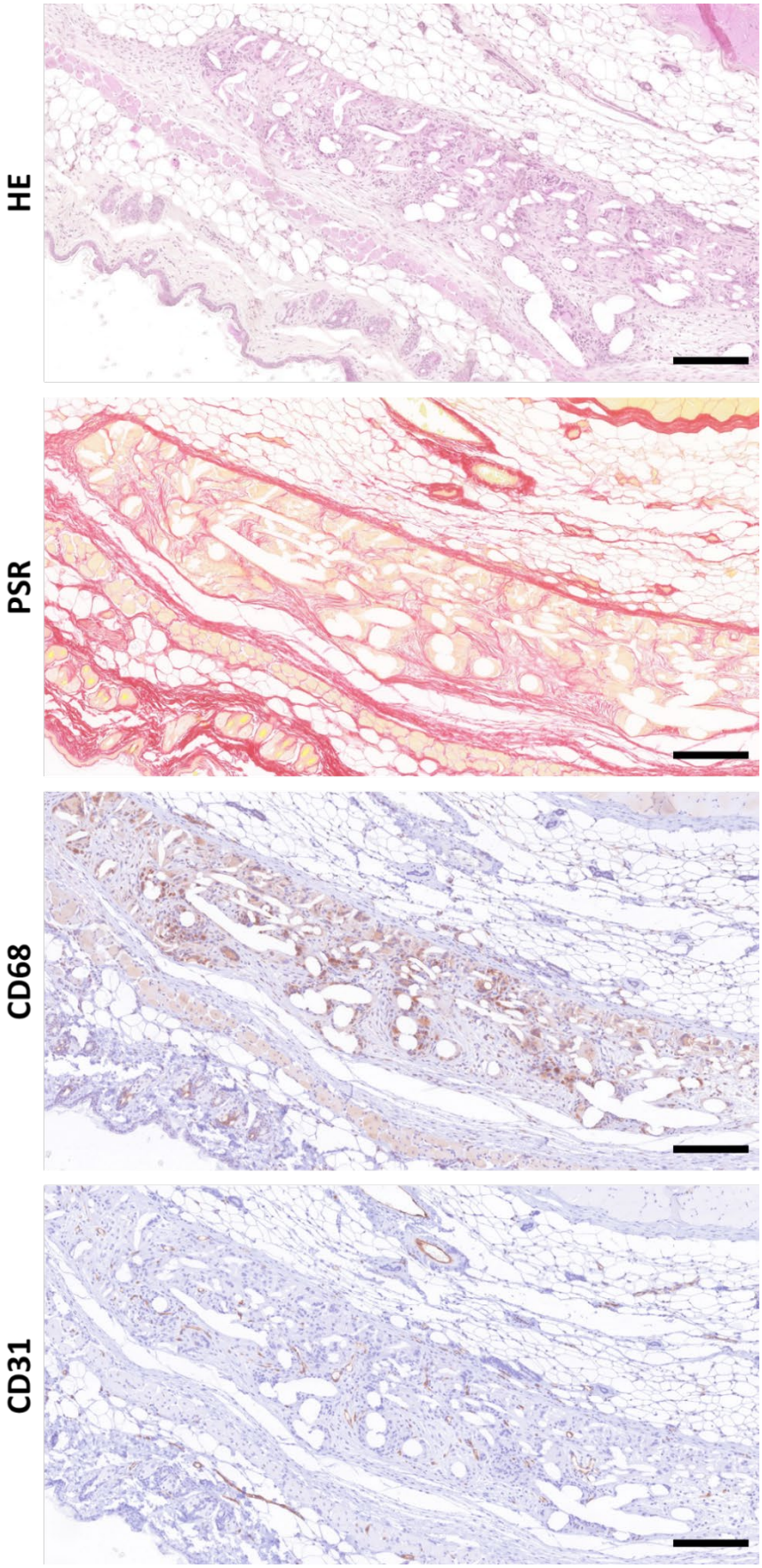

Supplementary Figure 2. Representative images from the frame region. Scale bars are 200 µm.

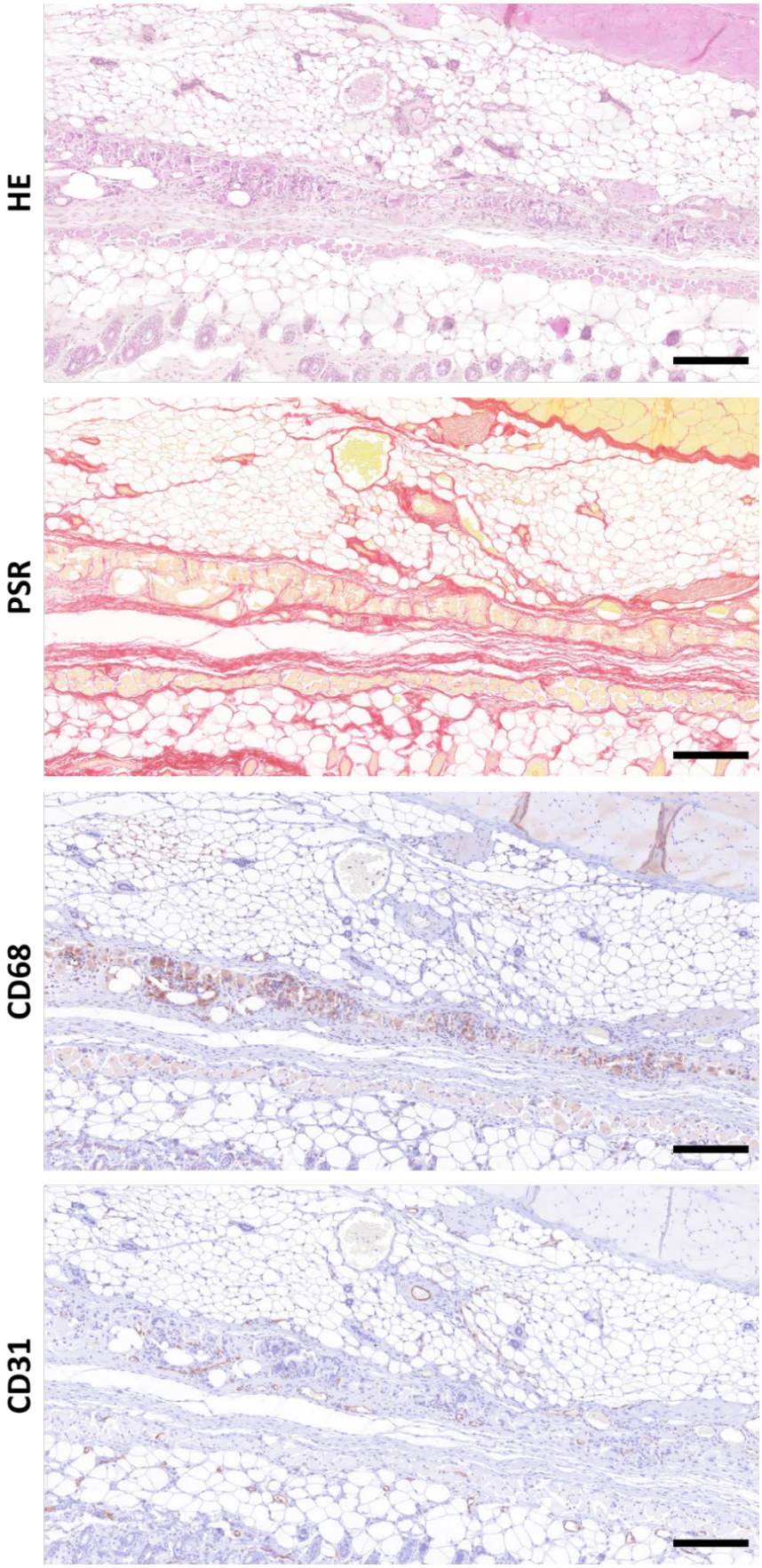

Supplementary Figure 3. Representative images from the area adjacent to the frame region. Scale bars are 200 µm.

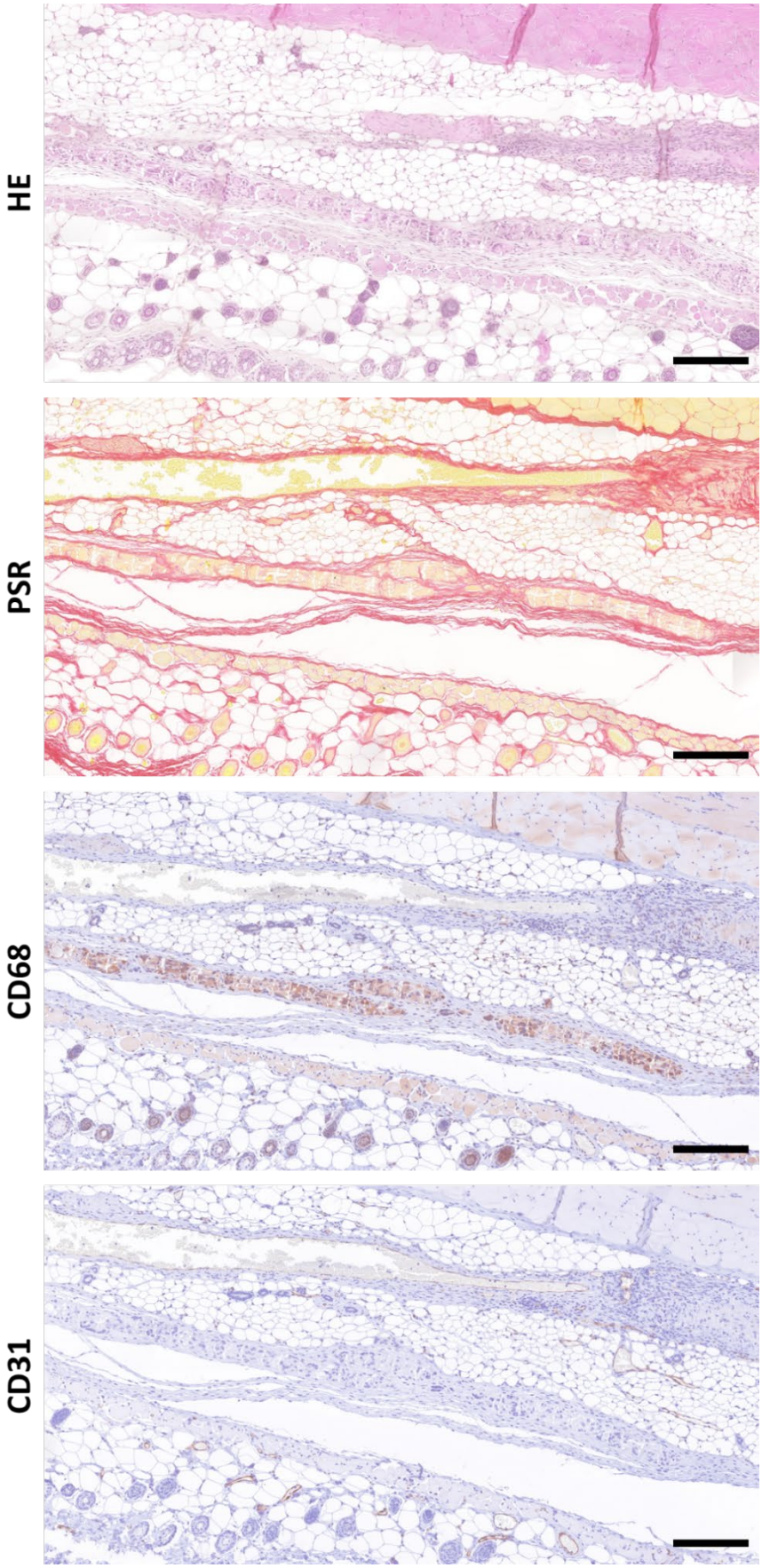

Supplementary Figure 4. Representative images from the middle of the scaffold. Scale bars are 200 µm

.

References

Abbah, S. A., Lam, C. X., Hutmacher, D. W., Goh, J. C. and Wong, H. K. (2009). "Biological performance of a polycaprolactone-based scaffold used as fusion cage device in a large animal model of spinal reconstructive surgery." Biomaterials **30**(28): 5086-5093.

Abbasi, N., Hamlet, S., Dau, V. T. and Nguyen, N.-T. (2020). "Calcium phosphate stability on melt electrowritten PCL scaffolds." Journal of Science: Advanced Materials and Devices **5**(1): 30-39.

Abdal-hay, A., Abbasi, N., Gwiazda, M., Hamlet, S. and Ivanovski, S. (2018). "Novel polycaprolactone/hydroxyapatite nanocomposite fibrous scaffolds by direct melt-electrospinning writing." European Polymer Journal **105**: 257-264.

Abhay, S. and Haines, S. J. (1997). "Repairing Holes in the Head: A History of Cranioplasty." Neurosurgery **40**(3): 588-603.

Abràmoff, M. D., Magalhães, P. J. and Ram, S. J. (2004). "Image processing with ImageJ." Biophotonics international **11**(7): 36-42.

Abruzzo, A., Fiorica, C., Palumbo, V. D., Altomare, R., Damiano, G., Gioviale, M. C., Tomasello, G., Licciardi, M., Palumbo, F. S., Giammona, G. and Lo Monte, A. I. (2014). "Using Polymeric Scaffolds for Vascular Tissue Engineering." International Journal of Polymer Science **2014**: 1-9.

Adamo, J. E., Grayson, W. L., Hatcher, H., Brown, J. S., Thomas, A., Hollister, S. and Steele, S. J. (2018). "Regulatory interfaces surrounding the growing field of additive manufacturing of medical devices and biologic products." Journal of clinical and translational science **2**(5): 301-304.

Adamovich, A., Park, S., Siskin, G. P., Englander, M. J., Mandato, K. D., Herr, A. and Keating, L. J. (2015). "The ABCs of the FDA: A Primer on the Role of the United States Food and Drug Administration in Medical Device Approvals and IR Research." J Vasc Interv Radiol **26**(9): 1324-1330.

Adamzyk, C., Kachel, P., Hoss, M., Gremse, F., Modabber, A., Holzle, F., Tolba, R., Neuss, S. and Lethaus, B. (2016). "Bone tissue engineering using polyetherketoneketone scaffolds combined with autologous mesenchymal stem cells in a sheep calvarial defect model." J Craniomaxillofac Surg **44**(8): 985-994.

Agarwal, S., Wendorff, J. H. and Greiner, A. (2009). "Progress in the field of electrospinning for tissue engineering applications." Adv Mater **21**(32-33): 3343-3351.

Agata, K., Saito, Y. and Nakajima, E. (2007). "Unifying principles of regeneration I: Epimorphosis versus morphallaxis." Dev Growth Differ **49**(2): 73-78.

Agrawal, A., Lee, B. H., Irvine, S. A., An, J., Bhuthalingam, R., Singh, V., Low, K. Y., Chua, C. K. and Venkatraman, S. S. (2015). "Smooth Muscle Cell Alignment and Phenotype Control by Melt Spun Polycaprolactone Fibers for Seeding of Tissue Engineered Blood Vessels." Int J Biomater **2015**: 434876.

Agrawal, C. M., Niederauer, G. G. and Athanasiou, K. A. (1995). "Fabrication and Characterization of PLA-PGA Orthopedic Implants." Tissue Eng **1**(3): 241-252.

Aicale, R. and Maffulli, N. (2019). "Lower limb joint repair and replacement: an overview." F1000Res **8**: F1000 Faculty Rev-2122.

Al-Maawi, S., Orlowska, A., Sader, R., James Kirkpatrick, C. and Ghanaati, S. (2017). "In vivo cellular reactions to different biomaterials-Physiological and pathological aspects and their consequences." Semin Immunol **29**: 49-61.

Ali, O. A., Huebsch, N., Cao, L., Dranoff, G. and Mooney, D. J. (2009). "Infection-mimicking materials to program dendritic cells in situ." Nat Mater **8**(2): 151-158.

Amato, G., Romano, G., Agrusa, A., Marasa, S., Cocorullo, G., Gulotta, G., Goetze, T. and Puleio, R. (2015). "Biologic response of inguinal hernia prosthetics: a comparative study of conventional static meshes versus 3D dynamic implants." Artif Organs **39**(1): E10-23.

Ambrose, C. G. and Clanton, T. O. (2004). "Bioabsorbable implants: review of clinical experience in orthopedic surgery." Ann Biomed Eng **32**(1): 171-177.

Amid, P. K. (1997). "Classification of biomaterials and their related complications in abdominal wall hernia surgery." Hernia **1**(1): 15-21.

Anderson, J. M. (1988). "Inflammatory response to implants." ASAIO Trans **34**(2): 101-107.

Anderson, J. M., Rodriguez, A. and Chang, D. T. (2008). "Foreign body reaction to biomaterials." Semin Immunol **20**(2): 86-100.

Anwar, R., Kini, S. G., Sait, S. and Bruce, W. J. (2016). "Early clinical and radiological results of total knee arthroplasty using patient-specific guides in obese patients." Arch Orthop Trauma Surg **136**(2): 265-270.

Arora, M., Chan, E. K., Gupta, S. and Diwan, A. D. (2013). "Polymethylmethacrylate bone cements and additives: A review of the literature." World J Orthop **4**(2): 67-74.

Baldwin, J. G., Wagner, F., Martine, L. C., Holzapfel, B. M., Theodoropoulos, C., Bas, O., Savi, F. M., Werner, C., De-Juan-Pardo, E. M. and Hutmacher, D. W. (2016). "Periosteum tissue engineering in an orthotopic in vivo platform." Biomaterials **121**: 193-204.

Banker, S. (2020, 13.04.2020). "COVID-19 And 3D Printing." Retrieved 15.06.2020, from https://www.forbes.com/sites/stevebanker/2020/04/13/covid-19-and-3d-printing/#4dd3a4433f7a.

Baranowski, T., Dobrovolskij, D., Dremel, K., Hölzing, A., Lohfink, G., Schladitz, K. and Zabler, S. (2019). "Local fiber orientation from X-ray region-of-interest computed tomography of large fiber reinforced composite components." Composites Science and Technology **183**: 107786.

Barber, F. A. and Dockery, W. D. (2006). "Long-term absorption of poly-L-lactic Acid interference screws." Arthroscopy **22**(8): 820-826.

Barbolt, T. A. (2006). "Biology of polypropylene/polyglactin 910 grafts." Int Urogynecol J Pelvic Floor Dysfunct **17 Suppl 1**(1): S26-30.

Barham, R. E., Butz, G. W. and Ansell, J. S. (1978). "Comparison of wound strength in normal, radiated and infected tissues closed with polyglycolic and chromic catgut sutures." Surg Gynecol Obstet **146**(6): 901-907.

Bartnikowski, M., Klein, T. J., Melchels, F. P. and Woodruff, M. A. (2014). "Effects of scaffold architecture on mechanical characteristics and osteoblast response to static and perfusion bioreactor cultures." Biotechnol Bioeng **111**(7): 1440-1451.

Bartnikowski, M., Vaquette, C. and Ivanovski, S. (2020). "Workflow for highly porous resorbable custom 3D printed scaffolds using medical grade polymer for large volume alveolar bone regeneration." Clin Oral Implants Res **31**(5): 431-441.

Bas, O., D'Angella, D., Baldwin, J. G., Castro, N. J., Wunner, F. M., Saidy, N. T., Kollmannsberger, S., Reali, A., Rank, E., De-Juan-Pardo, E. M. and Hutmacher, D. W. (2017). "An Integrated Design, Material, and Fabrication Platform for Engineering Biomechanically and Biologically Functional Soft Tissues." ACS Appl Mater Interfaces.

Bas, O., De-Juan-Pardo, E. M., Chhaya, M. P., Wunner, F. M., Jeon, J. E., Klein, T. J. and Hutmacher, D. W. (2015). "Enhancing structural integrity of hydrogels by using highly organised melt electrospun fibre constructs." European Polymer Journal **72**(Supplement C): 451-463.

Bas, O., De-Juan-Pardo, E. M., Meinert, C., D'Angella, D., Baldwin, J. G., Bray, L. J., Wellard, R. M., Kollmannsberger, S., Rank, E., Werner, C., Klein, T. J., Catelas, I. and Hutmacher, D. W. (2017). "Biofabricated soft network composites for cartilage tissue engineering." Biofabrication **9**(2): 025014.

Bas, O., Lucarotti, S., Angella, D. D., Castro, N. J., Meinert, C., Wunner, F. M., Rank, E., Vozzi, G., Klein, T. J., Catelas, I., De-Juan-Pardo, E. M. and Hutmacher, D. W. (2018). "Rational design and fabrication of multiphasic soft network composites for tissue engineering articular cartilage: A numerical model-based approach." Chemical Engineering Journal **340**: 15-23.

Baylon, K., Rodriguez-Camarillo, P., Elias-Zuniga, A., Diaz-Elizondo, J. A., Gilkerson, R. and Lozano, K. (2017). "Past, Present and Future of Surgical Meshes: A Review." Membranes (Basel) **7**(3).

Benicewicz, B. C. and Hopper, P. K. (1990). "Review : Polymers for Absorbable Surgical Sutures--Part I." Journal of Bioactive and Compatible Polymers **5**(4): 453-472.

Benicewicz, B. C. and Hopper, P. K. (1991). "Review : Polymers for Absorbable Surgical Sutures--Part II." Journal of Bioactive and Compatible Polymers **6**(1): 64-94.

Berger, D. (2016). "Evidence-Based Hernia Treatment in Adults." Dtsch Arztebl Int **113**(9): 150-157; quiz 158.

Berry, E., Brown, J. M., Connell, M., Craven, C. M., Efford, N. D., Radjenovic, A. and Smith, M. A. (1997). "Preliminary experience with medical applications of rapid prototyping by selective laser sintering." Med Eng Phys **19**(1): 90-96.

Berry, E., Marsden, A., Dalgarno, K. W., Kessel, D. and Scott, D. J. (2002). "Flexible tubular replicas of abdominal aortic aneurysms." Proc Inst Mech Eng H **216**(3): 211-214.

Bertlein, S., Hikimoto, D., Hochleitner, G., Hummer, J., Jungst, T., Matsusaki, M., Akashi, M. and Groll, J. (2018). "Development of Endothelial Cell Networks in 3D Tissues by Combination of Melt Electrospinning Writing with Cell-Accumulation Technology." Small **14**(2): 1701521.

Bezwada, R. S., Jamiolkowski, D. D., Lee, I. Y., Agarwal, V., Persivale, J., Trenkabenthin, S., Erneta, M., Suryadevara, J., Yang, A. and Liu, S. (1995). "Monocryl(R) Suture, a New Ultra-Pliable Absorbable Monofilament Suture." Biomaterials **16**(15): 1141-1148.

Bhrany, A. D., Irvin, C. A., Fujitani, K., Liu, Z. and Ratner, B. D. (2013). "Evaluation of a sphere-templated polymeric scaffold as a subcutaneous implant." JAMA Facial Plast Surg **15**(1): 29-33.

Bilsel, Y. and Abci, I. (2012). "The search for ideal hernia repair; mesh materials and types." Int J Surg **10**(6): 317-321.

Birnbaum, K. D. and Sanchez Alvarado, A. (2008). "Slicing across kingdoms: regeneration in plants and animals." Cell **132**(4): 697-710.

Blackman, L. D., Gunatillake, P. A., Cass, P. and Locock, K. E. S. (2019). "An introduction to zwitterionic polymer behavior and applications in solution and at surfaces." Chemical Society Reviews **48**(3): 757-770.

Blakeney, B. A., Tambralli, A., Anderson, J. M., Andukuri, A., Lim, D. J., Dean, D. R. and Jun, H. W. (2011). "Cell infiltration and growth in a low density, uncompressed three-dimensional electrospun nanofibrous scaffold." Biomaterials **32**(6): 1583-1590.

Blanca, M. J., Alarcón, R., Arnau, J., Bono, R. and Bendayan, R. (2017). "Non-normal data: Is ANOVA still a valid option?" Psicothema **29**(4): 552-557.

Blaudez, F., Ivanovski, S., Ipe, D. and Vaquette, C. (2020). "A comprehensive comparison of cell seeding methods using highly porous melt electrowriting scaffolds." Mater Sci Eng C Mater Biol Appl **117**: 111282.

Blum, C., Schlegelmilch, K., Schilling, T., Shridhar, A., Rudert, M., Jakob, F., Dalton, P. D., Blunk, T., Flynn, L. E. and Groll, J. (2019). "Extracellular Matrix-Modified Fiber Scaffolds as a Proadipogenic Mesenchymal Stromal Cell Delivery Platform." Acs Biomaterials Science & Engineering **5**(12): 6655-6666.

Bock, N., Shokoohmand, A., Kryza, T., Rohl, J., Meijer, J., Tran, P. A., Nelson, C. C., Clements, J. A. and Hutmacher, D. W. (2019). "Engineering osteoblastic metastases to delineate the adaptive response of androgen-deprived prostate cancer in the bone metastatic microenvironment." Bone Res **7**(1): 13.

Brach Del Prever, E. M., Bistolfi, A., Bracco, P. and Costa, L. (2009). "UHMWPE for arthroplasty: past or future?" J Orthop Traumatol **10**(1): 1-8.

Bradley, R. S., Robinson, I. K. and Yusuf, M. (2017). "3D X-Ray Nanotomography of Cells Grown on Electrospun Scaffolds." Macromol Biosci **17**(2): 1600236.

Bradley, R. S. and Withers, P. J. (2016). "Correlative multiscale tomography of biological materials." MRS Bulletin **41**(07): 549-556.

Bringman, S., Conze, J., Cuccurullo, D., Deprest, J., Junge, K., Klosterhalfen, B., Parra-Davila, E., Ramshaw, B. and Schumpelick, V. (2010). "Hernia repair: the search for ideal meshes." Hernia **14**(1): 81-87.

Brockes, J. P. and Kumar, A. (2008). "Comparative aspects of animal regeneration." Annu Rev Cell Dev Biol **24**: 525-549.

Broos, P. L. and Sermon, A. (2004). "From unstable internal fixation to biological osteosynthesis. A historical overview of operative fracture treatment." Acta Chir Belg **104**(4): 396-400.

Brown, T. D., Dalton, P. D. and Hutmacher, D. W. (2011). "Direct writing by way of melt electrospinning." Adv Mater **23**(47): 5651-5657.

Brown, T. D., Daltona, P. D. and Hutmacher, D. W. (2016). "Melt electrospinning today: An opportune time for an emerging polymer process." Progress in Polymer Science **56**: 116-166.

Brown, T. D., Slotosch, A., Thibaudeau, L., Taubenberger, A., Loessner, D., Vaquette, C., Dalton, P. D. and Hutmacher, D. W. (2012). "Design and fabrication of tubular scaffolds via direct writing in a melt electrospinning mode." Biointerphases **7**(1-4): 13.

Buffington, S., Browning, M. B. and Cosgriff-Hernández, E. (2014). Clinically Applied Biomaterials: Soft Tissue. BIOMEDICAL TECHNOLOGY AND DEVICES. J. E. Moore Jr. and D. J. Maitland. USA, CRC Press.

Bukharova, T. B., Antonov, E. N., Popov, V. K., Fatkhudinov, T., Popova, A. V., Volkov, A. V., Bochkova, S. A., Bagratashvili, V. N. and Gol'dshtein, D. V. (2010). "Biocompatibility of tissue engineering constructions from porous polylactide carriers obtained by the method of selective laser sintering and bone marrow-derived multipotent stromal cells." Bull Exp Biol Med **149**(1): 148-153.

Burmeister, F., Steenhusen, S., Houbertz, R., Asche, T. S., Nickel, J., Nolte, S., Tucher, N., Josten, P., Obel, K., Wolter, H., Fessel, S., Schneider, A. M., Gartner, K. H., Beck, C., Behrens, P., Tunnermann, A. and Walles, H. (2015). Two-photon polymerization of inorganic-organic polymers for biomedical and microoptical applications. Optically Induced Nanostructures: Biomedical and Technical Applications. K. Konig and A. Ostendorf. Berlin, De Gruyter.

Burn, M. B., Ta, A. and Gogola, G. R. (2016). "Three-Dimensional Printing of Prosthetic Hands for Children." J Hand Surg Am **41**(5): e103-109.

Camarda, L., D'Arienzo, A., Morello, S., Peri, G., Valentino, B. and D'Arienzo, M. (2015). "Patient-specific instrumentation for total knee arthroplasty: a literature review." Musculoskelet Surg **99**(1): 11-18.

Campbell, T. A. and Ivanova, O. S. (2013). "Additive Manufacturing as a Disruptive Technology: Implications of Three-Dimensional Printing." Technology & Innovation **15**(1): 67-79.

Canedo-Dorantes, L. and Canedo-Ayala, M. (2019). "Skin Acute Wound Healing: A Comprehensive Review." Int J Inflam **2019**: 3706315.

Cao, H., McHugh, K., Chew, S. Y. and Anderson, J. M. (2010). "The topographical effect of electrospun nanofibrous scaffolds on the in vivo and in vitro foreign body reaction." J Biomed Mater Res A **93**(3): 1151-1159.

Cao, Y., Vacanti, J. P., Paige, K. T., Upton, J. and Vacanti, C. A. (1997). "Transplantation of chondrocytes utilizing a polymer-cell construct to produce tissue-engineered cartilage in the shape of a human ear." Plast Reconstr Surg **100**(2): 297-302; discussion 303-294.

Carlota, V. (2020, 23.03.2020). "Medically approved emergency 3D printed ventilator goes into production." Retrieved 15.06.2020, from https://www.3dnatives.com/en/3d-printed-respirator-230320205/#!

Castilho, M., Feyen, D., Flandes-Iparraguirre, M., Hochleitner, G., Groll, J., Doevendans, P. A. F., Vermonden, T., Ito, K., Sluijter, J. P. G. and Malda, J. (2017). "Melt Electrospinning Writing of Poly-Hydroxymethylglycolide-co-epsilon-Caprolactone-Based Scaffolds for Cardiac Tissue Engineering." Adv Healthc Mater **6**(18).

Castilho, M., Hochleitner, G., Wilson, W., van Rietbergen, B., Dalton, P. D., Groll, J., Malda, J. and Ito, K. (2018). "Mechanical behavior of a soft hydrogel reinforced with three-dimensional printed microfibre scaffolds." Sci Rep **8**(1): 1245.

Castilho, M., van Mil, A., Maher, M., Metz, C. H. G., Hochleitner, G., Groll, J., Doevendans, P. A., Ito, K., Sluijter, J. P. G. and Malda, J. (2018). "Melt Electrowriting Allows Tailored Microstructural and Mechanical Design of Scaffolds to Advance Functional Human Myocardial Tissue Formation." Advanced Functional Materials **28**(40): 1803151.

Castro, N. J., Meinert, C., Levett, P. and Hutmacher, D. W. (2017). "Current developments in multifunctional smart materials for 3D/4D bioprinting." Current Opinion in Biomedical Engineering **2**: 67-75.

Chae, M. P., Rozen, W. M., McMenamin, P. G., Findlay, M. W., Spychal, R. T. and Hunter-Smith, D. J. (2015). "Emerging Applications of Bedside 3D Printing in Plastic Surgery." Front Surg **2**: 25.

Charo, R. A. and Sipp, D. (2018). "Rejuvenating Regenerative Medicine Regulation." N Engl J Med **378**(6): 504-505.

Chen, C. H., Lee, M. Y., Shyu, V. B., Chen, Y. C., Chen, C. T. and Chen, J. P. (2014). "Surface modification of polycaprolactone scaffolds fabricated via selective laser sintering for cartilage tissue engineering." Mater Sci Eng C Mater Biol Appl **40**: 389-397.

Chen, C. H., Shyu, V. B., Chen, J. P. and Lee, M. Y. (2014). "Selective laser sintered poly-epsilon-caprolactone scaffold hybridized with collagen hydrogel for cartilage tissue engineering." Biofabrication **6**(1): 015004.

Chen, F., Hochleitner, G., Woodfield, T., Groll, J., Dalton, P. D. and Amsden, B. G. (2016). "Additive Manufacturing of a Photo-Cross-Linkable Polymer via Direct Melt Electrospinning Writing for Producing High Strength Structures." Biomacromolecules **17**(1): 208-214.

Chen, R., Zhang, H., Yan, J. and Bryers, J. D. (2018). "Scaffold-mediated delivery for non-viral mRNA vaccines." Gene Ther **25**(8): 556-567.

Chen, S., Jones, J. A., Xu, Y., Low, H. Y., Anderson, J. M. and Leong, K. W. (2010). "Characterization of topographical effects on macrophage behavior in a foreign body response model." Biomaterials **31**(13): 3479-3491.

Cheng, B. C., Jaffee, S., Averick, S., Swink, I., Horvath, S. and Zhukauskas, R. (2019). "A Comparative Study of Three Biomaterials in an Ovine Bone Defect Model." Spine J.

Chhaya, M. P., Poh, P. S., Balmayor, E. R., van Griensven, M., Schantz, J. T. and Hutmacher, D. W. (2015). "Additive manufacturing in biomedical sciences and the need for definitions and norms." Expert Rev Med Devices **12**(5): 537-543.

Christen, M. O. and Vercesi, F. (2020). "Polycaprolactone: How a Well-Known and Futuristic Polymer Has Become an Innovative Collagen-Stimulator in Esthetics." Clin Cosmet Investig Dermatol **13**: 31-48.

Chua, C. K., Leong, K. F., Tan, K. H., Wiria, F. E. and Cheah, C. M. (2004). "Development of tissue scaffolds using selective laser sintering of polyvinyl alcohol/hydroxyapatite biocomposite for craniofacial and joint defects." J Mater Sci Mater Med **15**(10): 1113-1121.

Ciardelli, G., Chiono, V., Vozzi, G., Pracella, M., Ahluwalia, A., Barbani, N., Cristallini, C. and Giusti, P. (2005). "Blends of poly-(epsilon-caprolactone) and polysaccharides in tissue engineering applications." Biomacromolecules **6**(4): 1961-1976.

Cipitria, A., Wagermaier, W., Zaslansky, P., Schell, H., Reichert, J. C., Fratzl, P., Hutmacher, D. W. and Duda, G. N. (2015). "BMP delivery complements the guiding effect of scaffold architecture without altering bone microstructure in critical-sized long bone defects: A multiscale analysis." Acta Biomater **23**: 282-294.

Clinkenbeard, R. E., Johnson, D. L., Parthasarathy, R., Altan, M. C., Tan, K. H., Park, S. M. and Crawford, R. H. (2002). "Replication of human tracheobronchial hollow airway models using a selective laser sintering rapid prototyping technique." AIHA J (Fairfax, Va) **63**(2): 141-150.

Cobb, W. S., Kercher, K. W. and Heniford, B. T. (2005). "The Argument for Lightweight Polypropylene Mesh in Hernia Repair." Surgical Innovation **12**(1): 63-69.

Collee, J. G., Bradley, R. and Liberski, P. P. (2006). "Variant CJD (vCJD) and bovine spongiform encephalopathy (BSE): 10 and 20 years on: part 2." Folia Neuropathol **44**(2): 102-110.

Conn, J., Jr., Oyasu, R., Welsh, M. and Beal, J. M. (1974). "Vicryl (polyglactin 910) synthetic absorbable sutures." Am J Surg **128**(1): 19-23.

Cooke, S. L. and Whittington, A. R. (2016). "Influence of therapeutic radiation on polycaprolactone and polyurethane biomaterials." Mater Sci Eng C Mater Biol Appl **60**(Supplement C): 78-83.

Cortes, R. A., Miranda, E., Lee, H. and Gertner, M. E. (2008a). Biomaterials and the Evolution of Hernia Repair II: Composite Meshes. Surgery. J. Norton, P. Barie, R. R. Bollinger et al., Springer New York**:** 2305-2315.

Cortes, R. A., Miranda, E., Lee, H. and Gertner, M. E. (2008b). Biomaterials and the Evolution of Hernia Repair I: The History of Biomaterials and the Permanent Meshes. Surgery. J. Norton, P. Barie, R. R. Bollinger et al., Springer New York**:** 2291-2304.

Costa, P. F., Vaquette, C., Zhang, Q., Reis, R. L., Ivanovski, S. and Hutmacher, D. W. (2014). "Advanced tissue engineering scaffold design for regeneration of the complex hierarchical periodontal structure." J Clin Periodontol **41**(3): 283-294.

Creylman, V., Muraru, L., Pallari, J., Vertommen, H. and Peeraer, L. (2013). "Gait assessment during the initial fitting of customized selective laser sintering ankle foot orthoses in subjects with drop foot." Prosthet Orthot Int **37**(2): 132-138.

Crump, S. S. (1992). Apparatus and method for creating three-dimensional objects, Google Patents.

Dalton, P. D. (2017). "Melt electrowriting with additive manufacturing principles." Current Opinion in Biomedical Engineering **2**: 49-57.

Dalton, P. D., Klinkhammer, K., Salber, J., Klee, D. and Moller, M. (2006). "Direct in vitro electrospinning with polymer melts." Biomacromolecules **7**(3): 686-690.

Dalton, P. D., Vaquette, C., Farrugia, B. L., Dargaville, T. R., Brown, T. D. and Hutmacher, D. W. (2013). "Electrospinning and additive manufacturing: converging technologies." Biomaterials Science **1**(2): 171-185.

Dalton, P. D., Woodfield, T. B. F., Mironov, V. and Groll, J. (2020). "Advances in Hybrid Fabrication toward Hierarchical Tissue Constructs." Adv Sci (Weinh) **7**(11): 1902953.

Darney, P. D., Monroe, S. E., Klaisle, C. M. and Alvarado, A. (1989). "Clinical evaluation of the Capronor contraceptive implant: preliminary report." Am J Obstet Gynecol **160**(5 Pt 2): 1292-1295.

Dash, T. K. and Konkimalla, V. B. (2012). "Poly-small je, Ukrainian-caprolactone based formulations for drug delivery and tissue engineering: A review." J Control Release **158**(1): 15-33.

de Ruijter, M., Hrynevich, A., Haigh, J. N., Hochleitner, G., Castilho, M., Groll, J., Malda, J. and Dalton, P. D. (2018). "Out-of-Plane 3D-Printed Microfibers Improve the Shear Properties of Hydrogel Composites." Small **14**(8): 1702773.

de Ruijter, M., Ribeiro, A., Dokter, I., Castilho, M. and Malda, J. (2018). "Simultaneous Micropatterning of Fibrous Meshes and Bioinks for the Fabrication of Living Tissue Constructs." Adv Healthc Mater **0**(0): e1800418.

Deckard, C. R. (1989). Method and apparatus for producing parts by selective sintering, Google Patents.

Deerenberg, E. B., Timmermans, L., Hogerzeil, D. P., Slieker, J. C., Eilers, P. H., Jeekel, J. and Lange, J. F. (2015). "A systematic review of the surgical treatment of large incisional hernia." Hernia **19**(1): 89-101.

Delalat, B., Harding, F., Gundsambuu, B., De-Juan-Pardo, E. M., Wunner, F. M., Wille, M.-L., Jasieniak, M., Malatesta, K. A. L., Griesser, H. J., Simula, A., Hutmacher, D. W., Voelcker, N. H. and Barry, S. C. (2017a). "3D printed lattices as an activation and expansion platform for T cell therapy." Biomaterials **140**: 58-68.

Delalat, B., Harding, F., Gundsambuu, B., De-Juan-Pardo, E. M., Wunner, F. M., Wille, M. L., Jasieniak, M., Malatesta, K. A. L., Griesser, H. J., Simula, A., Hutmacher, D. W., Voelcker, N. H. and Barry, S. C. (2017b). "3D printed lattices as an activation and expansion platform for T cell therapy." Biomaterials **140**: 58-68.

Department of Mechanical Engineering. (2012, Dec 6, 2012). "Selective Laser Sintering, Birth of an Industry." Retrieved Feb 11, 2016, from http://www.me.utexas.edu/news/news/selective-laser-sintering-birth-of-an-industry.

Deutsch, H. (2010). "High-dose bone morphogenetic protein-induced ectopic abdomen bone growth." Spine J **10**(2): e1-4.

Dias, M. R., Guedes, J. M., Flanagan, C. L., Hollister, S. J. and Fernandes, P. R. (2014). "Optimization of scaffold design for bone tissue engineering: A computational and experimental study." Med Eng Phys **36**(4): 448-457.

Domingos, M., Dinucci, D., Cometa, S., Alderighi, M., Bartolo, P. J. and Chiellini, F. (2009). "Polycaprolactone Scaffolds Fabricated via Bioextrusion for Tissue Engineering Applications." Int J Biomater **2009**: 239643.

Dondossola, E., Alexander, S., Holzapfel, B. M., Filippini, S., Starbuck, M. W., Hoffman, R. M., Navone, N., De-Juan-Pardo, E. M., Logothetis, C. J., Hutmacher, D. W. and Friedl, P. (2018). "Intravital microscopy of osteolytic progression and therapy response of cancer lesions in the bone." Sci Transl Med **10**(452).

Dondossola, E., Holzapfel, B. M., Alexander, S., Filippini, S., Hutmacher, D. W. and Friedl, P. (2016). "Examination of the foreign body response to biomaterials by nonlinear intravital microscopy." Nat Biomed Eng **1**: 0007.

Dougherty, P. J., Carter, P. R., Seligson, D., Benson, D. R. and Purvis, J. M. (2004). "Orthopaedic Surgery Advances Resulting from World War II." The Journal of Bone & Joint Surgery **86**(1): 176-181.

Du, Y., Liu, H., Shuang, J., Wang, J., Ma, J. and Zhang, S. (2015). "Microsphere-based selective laser sintering for building macroporous bone scaffolds with controlled microstructure and excellent biocompatibility." Colloids Surf B Biointerfaces **135**: 81-89.

Dupont, K. M., Boerckel, J. D., Stevens, H. Y., Diab, T., Kolambkar, Y. M., Takahata, M., Schwarz, E. M. and Guldberg, R. E. (2012). "Synthetic scaffold coating with adeno-associated virus encoding BMP2 to promote endogenous bone repair." Cell Tissue Res **347**(3): 575-588.

Ergun, A., Yu, X., Valdevit, A., Ritter, A. and Kalyon, D. M. (2011). "In vitro analysis and mechanical properties of twin screw extruded single-layered and coextruded multilayered poly(caprolactone) scaffolds seeded with human fetal osteoblasts for bone tissue engineering." J Biomed Mater Res A **99**(3): 354-366.

Eshraghi, S. and Das, S. (2010). "Mechanical and microstructural properties of polycaprolactone scaffolds with one-dimensional, two-dimensional, and three-dimensional orthogonally oriented porous architectures produced by selective laser sintering." Acta Biomater **6**(7): 2467-2476.

Eshraghi, S. and Das, S. (2012). "Micromechanical finite-element modeling and experimental characterization of the compressive mechanical properties of polycaprolactone-hydroxyapatite composite scaffolds prepared by selective laser sintering for bone tissue engineering." Acta Biomater **8**(8): 3138-3143.

Estes, C. S., Schmidt, K. J., McLemore, R., Spangehl, M. J. and Clarke, H. D. (2013). "Effect of body mass index on limb alignment after total knee arthroplasty." J Arthroplasty **28**(8 Suppl): 101-105.

Evans, N. T., Torstrick, F. B., Lee, C. S., Dupont, K. M., Safranski, D. L., Chang, W. A., Macedo, A. E., Lin, A. S., Boothby, J. M., Whittingslow, D. C., Carson, R. A., Guldberg, R. E. and Gall, K. (2015). "High-strength, surface-porous polyether-ether-ketone for load-bearing orthopedic implants." Acta Biomater **13**: 159-167.

Falagas, M. E. and Kasiakou, S. K. (2005). "Mesh-related infections after hernia repair surgery." Clinical Microbiology and Infection **11**(1): 3-8.

Farag, A., Hashimi, S. M., Vaquette, C., Bartold, P. M., Hutmacher, D. W. and Ivanovski, S. (2018). "The effect of decellularized tissue engineered constructs on periodontal regeneration." J Clin Periodontol **45**(5): 586-596.

Farag, A., Hashimi, S. M., Vaquette, C., Volpato, F. Z., Hutmacher, D. W. and Ivanovski, S. (2018). "Assessment of static and perfusion methods for decellularization of PCL membrane-supported periodontal ligament cell sheet constructs." Arch Oral Biol **88**: 67-76.

Farrugia, B. L., Brown, T. D., Upton, Z., Hutmacher, D. W., Dalton, P. D. and Dargaville, T. R. (2013). "Dermal fibroblast infiltration of poly(epsilon-caprolactone) scaffolds fabricated by melt electrospinning in a direct writing mode." Biofabrication **5**(2): 025001.

FDA. (2008, 06.08.2015). "FDA Public Health Notification: Life-threatening Complications Associated with Recombinant Human Bone Morphogenetic Protein in Cervical Spine Fusion." Retrieved 21.02.2016, 2016, from http://www.fda.gov/MedicalDevices/Safety/AlertsandNotices/PublicHealthNotifications/ucm062000.htm.

FDA. (2018a, 31.01.2018). "Milestones in U.S. Food and Drug Law History." Retrieved 26.01.2020, from https://www.fda.gov/about-fda/fdas-evolving-regulatory-powers/milestones-us-food-and-drug-law-history.

FDA. (2018b, 27.09.2018). "Premarket Notification 510(k)." Retrieved 10.11.2019, from https://www.fda.gov/medical-devices/premarket-submissions/premarket-notification-510k.

FDA. (2019a, 30.09.2019). "Implants and Prosthetics." Retrieved 16.02.2020, from https://www.fda.gov/medical-devices/products-and-medical-procedures/implants-and-prosthetics.

FDA. (2019b, 24.06.2019). "A History of Medical Device Regulation & Oversight in the United States." Retrieved 26.01.2020, from https://www.fda.gov/medical-devices/overview-device-regulation/history-medical-device-regulation-oversight-united-states.

FDA. (2019c, 20.11.2019). "De Novo Classification Request." Retrieved 15.06.2020, from https://www.fda.gov/medical-devices/premarket-submissions/de-novo-classification-request.

FDA. (2019d, 26.03.2015). "IDE Early/Expanded Access." Retrieved 22.02.2016, 2016, from http://www.fda.gov/MedicalDevices/DeviceRegulationandGuidance/HowtoMarketYourDevice/InvestigationalDeviceExemptionIDE/ucm051345.htm#emergencyuse.

FDA (2019e). Humanitarian Use Device (HUD) Designations: Guidance for Industry and Food and Drug Administration Staff. FDA. fda.gov.

FDA. (2019f, 16.04.2019). "FDA takes action to protect women's health, orders manufacturers of surgical mesh intended for transvaginal repair of pelvic organ prolapse to stop selling all devices." Retrieved 24.06.2020, from https://www.fda.gov/news-events/press-announcements/fda-takes-action-protect-womens-health-orders-manufacturers-surgical-mesh-intended-transvaginal.

Fella, C., Balles, A., Hanke, R., Last, A. and Zabler, S. (2017). "Hybrid setup for micro- and nano-computed tomography in the hard X-ray range." Rev Sci Instrum **88**(12): 123702.

Feng, X. and McDonald, J. M. (2011). "Disorders of bone remodeling." Annu Rev Pathol **6**(1): 121-145.

Feng, Z., Dong, Y., Zhao, Y., Bai, S., Zhou, B., Bi, Y. and Wu, G. (2010). "Computer-assisted technique for the design and manufacture of realistic facial prostheses." Br J Oral Maxillofac Surg **48**(2): 105-109.

Fernandes, N., van den Heever, J., Hoogendijk, C., Botha, S., Booysen, G. and Els, J. (2016). "Reconstruction of an Extensive Midfacial Defect Using Additive Manufacturing Techniques." J Prosthodont **25**(7): 589-594.

Fitzgibbons, R. J., Jr. and Forse, R. A. (2015). "Clinical practice. Groin hernias in adults." N Engl J Med **372**(8): 756-763.

Flanigan, P., Kshettry, V. R. and Benzel, E. C. (2014). "World War II, tantalum, and the evolution of modern cranioplasty technique." Neurosurg Focus **36**(4): E22.

Florczak, S., Lorson, T., Zheng, T., Mrlik, M., Hutmacher, D. W., Higgins, M. J., Luxenhofer, R. and Dalton, P. D. (2019). "Melt electrowriting of electroactive poly(vinylidene difluoride) fibers." Polymer International **68**(4): 735-745.

Frazza, E. J. and Schmitt, E. E. (1971). "A new absorbable suture." J Biomed Mater Res **5**(2): 43-58.

Fuchs, A., Youssef, A., Seher, A., Hartmann, S., Brands, R. C., Muller-Richter, U. D. A., Kubler, A. C. and Linz, C. (2019). "A new multilayered membrane for tissue engineering of oral hard- and soft tissue by means of melt electrospinning writing and film casting - An in vitro study." J Craniomaxillofac Surg **47**(4): 695-703.

Fuchs, A., Youssef, A., Seher, A., Hochleitner, G., Dalton, P. D., Hartmann, S., Brands, R. C., Müller-Richter, U. D. A. and Linz, C. (2019). "Medical-grade polycaprolactone scaffolds made by melt electrospinning writing for oral bone regeneration – a pilot study in vitro." BMC Oral Health **19**(1): 28.

Fuhrich, D. G., Lessey, B. A. and Savaris, R. F. (2013). "Comparison of HSCORE assessment of endometrial beta3 integrin subunit expression with digital HSCORE using computerized image analysis (ImageJ)." Anal Quant Cytopathol Histpathol **35**(4): 210-216.

Fukano, Y., Usui, M. L., Underwood, R. A., Isenhath, S., Marshall, A. J., Hauch, K. D., Ratner, B. D., Olerud, J. E. and Fleckman, P. (2010). "Epidermal and dermal integration into sphere-templated porous poly(2-hydroxyethyl methacrylate) implants in mice." J Biomed Mater Res A **94**(4): 1172-1186.

Fuller, K. P., Gaspar, D., Delgado, L. M., Pandit, A. and Zeugolis, D. I. (2016). "Influence of porosity and pore shape on structural, mechanical and biological properties of poly -caprolactone electro-spun fibrous scaffolds." Nanomedicine (Lond) **11**(9): 1031-1040.

Fusser, M., Overbye, A., Pandya, A. D., Morch, Y., Borgos, S. E., Kildal, W., Snipstad, S., Sulheim, E., Fleten, K. G., Askautrud, H. A., Engebraaten, O., Flatmark, K., Iversen, T. G., Sandvig, K., Skotland, T. and Maelandsmo, G. M. (2019). "Cabazitaxel-loaded Poly(2-ethylbutyl cyanoacrylate) nanoparticles improve treatment efficacy in a patient derived breast cancer xenograft." J Control Release **293**: 183-192.

Gellman, B. N. (2011). Methods of manufacturing linearly expandable ureteral stents, Google Patents.

Giannini, S., Cadossi, M., Mazzotti, A., Ramponi, L., Belvedere, C. and Leardini, A. (2016). "Custom-Made Total Talonavicular Replacement in a Professional Rock Climber." The Journal of Foot and Ankle Surgery **55**(6): 1271-1275.

Gittard, S. D. and Narayan, R. J. (2010). "Laser direct writing of micro- and nano-scale medical devices." Expert Rev Med Devices **7**(3): 343-356.

Global Trade Review. (2020, 31.03.2020). "From just in time to just in case: Covid-19 brings supply chain resilience to the fore." Retrieved 15.06.2020, from https://www.gtreview.com/news/sponsored-statement/from-just-in-time-to-just-in-case-covid-19-brings-supply-chain-resilience-to-the-fore/.

Goh, B. T., Teh, L. Y., Tan, D. B., Zhang, Z. and Teoh, S. H. (2015). "Novel 3D polycaprolactone scaffold for ridge preservation--a pilot randomised controlled clinical trial." Clin Oral Implants Res **26**(3): 271-277.

Goldman, D. (2014). "Regeneration, morphogenesis and self-organization." Development **141**(14): 2745-2749.

Gonzalez-Gil, A. B., Lamo-Espinosa, J. M., Muinos-Lopez, E., Ripalda-Cemborain, P., Abizanda, G., Valdes-Fernandez, J., Lopez-Martinez, T., Flandes-Iparraguirre, M., Andreu, I., Elizalde, M. R., Stuckensen, K., Groll, J., De-Juan-Pardo, E. M., Prosper, F. and Granero-Molto, F. (2019). "Periosteum-derived mesenchymal progenitor cells in engineered implants promote fracture healing in a critical-size defect rat model." J Tissue Eng Regen Med **13**(5): 742-752.

Gottfried, E., Kunz-Schughart, L. A., Weber, A., Rehli, M., Peuker, A., Muller, A., Kastenberger, M., Brockhoff, G., Andreesen, R. and Kreutz, M. (2008). "Expression of CD68 in non-myeloid cell types." Scand J Immunol **67**(5): 453-463.

Greenberg, J. A. and Clark, R. M. (2009). "Advances in suture material for obstetric and gynecologic surgery." Rev Obstet Gynecol **2**(3): 146-158.

Gronet, P. M., Waskewicz, G. A. and Richardson, C. (2003). "Preformed acrylic cranial implants using fused deposition modeling: A clinical report." The Journal of Prosthetic Dentistry **90**(5): 429-433.

Grosshaus, C., Bakirci, E., Berthel, M., Hrynevich, A., Kade, J. C., Hochleitner, G., Groll, J. and Dalton, P. D. (2020). "Melt Electrospinning of Nanofibers from Medical-Grade Poly(epsilon-Caprolactone) with a Modified Nozzle." Small **16**(44): e2003471.

Gu, B. K., Choi, D. J., Park, S. J., Kim, M. S., Kang, C. M. and Kim, C. H. (2016). "3-dimensional bioprinting for tissue engineering applications." Biomater Res **20**(1): 12.

Guan, J., Fujimoto, K. L., Sacks, M. S. and Wagner, W. R. (2005). "Preparation and characterization of highly porous, biodegradable polyurethane scaffolds for soft tissue applications." Biomaterials **26**(18): 3961-3971.

Gupta, G., Athanikar, S. B., Pai, V. V. and Naveen, K. N. (2014). "Giant cells in dermatology." Indian J Dermatol **59**(5): 481-484.

Haigh, J. N., Chuang, Y. M., Farrugia, B., Hoogenboom, R., Dalton, P. D. and Dargaville, T. R. (2015). "Hierarchically Structured Porous Poly(2-oxazoline) Hydrogels." Macromol Rapid Commun **37**(1): 93–99.

Haigh, J. N., Dargaville, T. R. and Dalton, P. D. (2017). "Additive manufacturing with polypropylene microfibers." Mater Sci Eng C Mater Biol Appl **77**: 883-887.

Hanke, R., Fuchs, T., Salamon, M. and Zabler, S. (2016). "X-ray microtomography for materials characterization." Materials Characterization Using Nondestructive Evaluation (NDE) Methods. Duxford, UK: Woodhead: 45-79.

Hansske, F., Bas, O., Vaquette, C., Hochleitner, G., Groll, J., Kemnitz, E., Hutmacher, D. W. and Borner, H. G. (2017). "Via precise interface engineering towards bioinspired composites with improved 3D printing processability and mechanical properties." J Mater Chem B **5**(25): 5037-5047.

Hao, L., Savalani, M. M., Zhang, Y., Tanner, K. E. and Harris, R. A. (2006). "Selective laser sintering of hydroxyapatite reinforced polyethylene composites for bioactive implants and tissue scaffold development." Proc Inst Mech Eng H **220**(4): 521-531.

He, W. and Benson, R. (2014). Polymeric Biomaterials. Handbook of Polymer Applications in Medicine and Medical Devices. K. Modjarrad and S. Ebnesajjad. USA, Elsevier Inc.

Henderson, S., Ibe, I., Cahill, S., Chung, Y. H. and Lee, F. Y. (2019). "Bone Quality and Fracture-Healing in Type-1 and Type-2 Diabetes Mellitus." J Bone Joint Surg Am **101**(15): 1399-1410.

HerniaSurge Group (2018). "International guidelines for groin hernia management." Hernia **22**(1): 1-165.

Hewitt, S. M., Baskin, D. G., Frevert, C. W., Stahl, W. L. and Rosa-Molinar, E. (2014). "Controls for immunohistochemistry: the Histochemical Society's standards of practice for validation of immunohistochemical assays." J Histochem Cytochem **62**(10): 693-697.

Higgins, J. M. (2015). "Red blood cell population dynamics." Clin Lab Med **35**(1): 43-57.

Hildebrand, H. F. (2013). Biomaterials – a history of 7000 years. BioNanoMaterials. **14:** 119.

Ho, S. T. and Hutmacher, D. W. (2006). "A comparison of micro CT with other techniques used in the characterization of scaffolds." Biomaterials **27**(8): 1362-1376.

Hochleitner, G., Chen, F., Blum, C., Dalton, P. D., Amsden, B. and Groll, J. (2018). "Melt electrowriting below the critical translation speed to fabricate crimped elastomer scaffolds with non-linear extension behaviour mimicking that of ligaments and tendons." Acta Biomater **72**: 110-120.

Hochleitner, G., Fursattel, E., Giesa, R., Groll, J., Schmidt, H. W. and Dalton, P. D. (2018). "Melt Electrowriting of Thermoplastic Elastomers." Macromol Rapid Commun **0**(0): e1800055.

Hochleitner, G., Hummer, J. F., Luxenhofer, R. and Groll, J. (2014). "High definition fibrous poly(2-ethyl-2-oxazoline) scaffolds through melt electrospinning writing." Polymer **55**(20): 5017-5023.

Hochleitner, G., Jungst, T., Brown, T. D., Hahn, K., Moseke, C., Jakob, F., Dalton, P. D. and Groll, J. (2015). "Additive manufacturing of scaffolds with sub-micron filaments via melt electrospinning writing." Biofabrication **7**(3): 035002.

Hochleitner, G., Kessler, M., Schmitz, M., Boccaccini, A. R., Tessmar, J. and Groll, J. (2017). "Melt electrospinning writing of defined scaffolds using polylactide-poly (ethylene glycol) blends with 45S5 bioactive glass particles." Materials Letters **205**: 257-260.

Hochleitner, G., Youssef, A., Hrynevich, A., Haigh, J. N., Jungst, T., Groll, J. and Dalton, P. D. (2016). "Fibre pulsing during melt electrospinning writing." BioNanoMaterials **17**(3-4): 159–171.

Hoffman, T., Khademhosseini, A. and Langer, R. (2019). "Chasing the Paradigm: Clinical Translation of 25 Years of Tissue Engineering." Tissue Eng Part A **25**(9-10): 679-687.

Hollister, S. J. (2009a). "Scaffold design and manufacturing: from concept to clinic." Adv Mater **21**(32-33): 3330-3342.

Hollister, S. J. (2009b). "Scaffold engineering: a bridge to where?" Biofabrication **1**(1): 012001.

Hollister, S. J. (2017). "Paediatric devices that grow up." Nat Biomed Eng **1**(10): 777-778.

Hollister, S. J., Flanagan, C. L., Zopf, D. A., Morrison, R. J., Nasser, H., Patel, J. J., Ebramzadeh, E., Sangiorgio, S. N., Wheeler, M. B. and Green, G. E. (2015). "Design control for clinical translation of 3D printed modular scaffolds." Ann Biomed Eng **43**(3): 774-786.

Holtzman, Y. and WTP Advisors. (2012, 17.07.2012). "The U.S. Medical Device Industry in 2012: Challenges at Home and Abroad." Retrieved 15.06.2020, from https://www.mddionline.com/stub/us-medical-device-industry-2012-challenges-home-and-abroad.

Holzapfel, B. M., Hutmacher, D. W., Nowlan, B., Barbier, V., Thibaudeau, L., Theodoropoulos, C., Hooper, J. D., Loessner, D., Clements, J. A., Russell, P. J., Pettit, A. R., Winkler, I. G. and Levesque, J. P. (2015). "Tissue engineered humanized bone supports human hematopoiesis in vivo." Biomaterials **61**: 103-114.

Holzapfel, B. M., Wagner, F., Loessner, D., Holzapfel, N. P., Thibaudeau, L., Crawford, R., Ling, M. T., Clements, J. A., Russell, P. J. and Hutmacher, D. W. (2014). "Species-specific homing mechanisms of human prostate cancer metastasis in tissue engineered bone." Biomaterials **35**(13): 4108-4115.

Hott, M. E., Megerian, C. A., Beane, R. and Bonassar, L. J. (2004). "Fabrication of tissue engineered tympanic membrane patches using computer-aided design and injection molding." Laryngoscope **114**(7): 1290-1295.

Hou, Q., Grijpma, D. W. and Feijen, J. (2003). "Porous polymeric structures for tissue engineering prepared by a coagulation, compression moulding and salt leaching technique." Biomaterials **24**(11): 1937-1947.

Hrynevich, A., Elci, B. S., Haigh, J. N., McMaster, R., Youssef, A., Blum, C., Blunk, T., Hochleitner, G., Groll, J. and Dalton, P. D. (2018). "Dimension-Based Design of Melt Electrowritten Scaffolds." Small **14**(22): e1800232.

Hsiao, W. K., Lorber, B. and Paudel, A. (2020). "Can 3D printing of oral drugs help fight the current COVID-19 pandemic (and similar crisis in the future)?" Expert Opin Drug Deliv: 1-4.

Huber-Lang, M., Lambris, J. D. and Ward, P. A. (2018). "Innate immune responses to trauma." Nature Immunology **19**(4): 327-341.

Hunter, D. J. and Bierma-Zeinstra, S. (2019). "Osteoarthritis." Lancet **393**(10182): 1745-1759.

Huotilainen, E., Paloheimo, M., Salmi, M., Paloheimo, K. S., Bjorkstrand, R., Tuomi, J., Markkola, A. and Makitie, A. (2014). "Imaging requirements for medical applications of additive manufacturing." Acta Radiol **55**(1): 78-85.

Hurson, C., Tansey, A., O'Donnchadha, B., Nicholson, P., Rice, J. and McElwain, J. (2007). "Rapid prototyping in the assessment, classification and preoperative planning of acetabular fractures." Injury **38**(10): 1158-1162.

Hutmacher, D. W. (2000). "Scaffolds in tissue engineering bone and cartilage." Biomaterials **21**(24): 2529-2543.

Hutmacher, D. W., Schantz, T., Zein, I., Ng, K. W., Teoh, S. H. and Tan, K. C. (2001). "Mechanical properties and cell cultural response of polycaprolactone scaffolds designed and fabricated via fused deposition modeling." J Biomed Mater Res **55**(2): 203-216.

Hynes, R. O. (2009). "The extracellular matrix: not just pretty fibrils." Science **326**(5957): 1216-1219.

Iismaa, S. E., Kaidonis, X., Nicks, A. M., Bogush, N., Kikuchi, K., Naqvi, N., Harvey, R. P., Husain, A. and Graham, R. M. (2018). "Comparative regenerative mechanisms across different mammalian tissues." NPJ Regen Med **3**(1): 6.

Jannasch, M., Gaetzner, S., Groeber, F., Weigel, T., Walles, H., Schmitz, T. and Hansmann, J. (2019). "An in vitro model mimics the contact of biomaterials to blood components and the reaction of surrounding soft tissue." Acta Biomater **89**: 227-241.

Janzen, D., Bakirci, E., Wieland, A., Martin, C., Dalton, P. D. and Villmann, C. (2020). "Cortical Neurons form a Functional Neuronal Network in a 3D Printed Reinforced Matrix." Adv Healthc Mater **9**(9): e1901630.

Jarow, J. P. and Baxley, J. H. (2015). "Medical devices: US medical device regulation." Urol Oncol **33**(3): 128-132.

Jeon, J. E., Vaquette, C., Theodoropoulos, C., Klein, T. J. and Hutmacher, D. W. (2014). "Multiphasic construct studied in an ectopic osteochondral defect model." J R Soc Interface **11**(95): 20140184.

Jin, Y., He, Y. and Shih, A. (2016). "Process Planning for the Fuse Deposition Modeling of Ankle-Foot-Othoses." Procedia CIRP **42**: 760-765.

Jordan, S. W., Fligor, J. E., Janes, L. E. and Dumanian, G. A. (2018). "Implant Porosity and the Foreign Body Response." Plast Reconstr Surg **141**(1): 103e-112e.

Junge, K., Binnebosel, M., von Trotha, K. T., Rosch, R., Klinge, U., Neumann, U. P. and Lynen Jansen, P. (2012). "Mesh biocompatibility: effects of cellular inflammation and tissue remodelling." Langenbecks Arch Surg **397**(2): 255-270.

Jungst, T., Muerza-Cascante, M. L., Brown, T. D., Standfest, M., Hutmacher, D. W., Groll, J. and Dalton, P. D. (2015). "Melt electrospinning onto cylinders: effects of rotational velocity and collector diameter on morphology of tubular structures." Polymer International **64**(9): 1086-1095.

Jungst, T., Pennings, I., Schmitz, M., Rosenberg, A. J. W. P., Groll, J. and Gawlitta, D. (2019). "Heterotypic Scaffold Design Orchestrates Primary Cell Organization and Phenotypes in Cocultured Small Diameter Vascular Grafts." Advanced Functional Materials **29**(43): 1905987.

Kade, J. C. and Dalton, P. D. (2020). "Polymers for Melt Electrowriting." Adv Healthc Mater: e2001232.

Kannan, R. Y., Salacinski, H. J., Butler, P. E., Hamilton, G. and Seifalian, A. M. (2005). "Current status of prosthetic bypass grafts: a review." J Biomed Mater Res B Appl Biomater **74**(1): 570-581.

Karchin, A., Simonovsky, F. I., Ratner, B. D. and Sanders, J. E. (2011). "Melt electrospinning of biodegradable polyurethane scaffolds." Acta Biomater **7**(9): 3277-3284.

Kasper, F. K., Ghivizzani, M. M. and Chiquet, B. T. (2019). "Emerging applications of 3D printing in nasoalveolar molding therapy: a narrative review." Journal of 3D Printing in Medicine **3**(4): 195-208.

Kastellorizios, M., Tipnis, N. and Burgess, D. J. (2015). "Foreign Body Reaction to Subcutaneous Implants." Adv Exp Med Biol **865**: 93-108.

Kelly, S. (2019, 13.09.2019). "FDA finalizes 4 guidances to clarify 510(k) pathways." Retrieved 15.06.2020, from https://www.medtechdive.com/news/fda-finalizes-four-guidances-to-clarify-510k-pathways/562877/.

Kettle, C., Dowswell, T. and Ismail, K. M. (2010). "Absorbable suture materials for primary repair of episiotomy and second degree tears." Cochrane Database Syst Rev(6): CD000006.

Kim, Y. S., Smoak, M. M., Melchiorri, A. J. and Mikos, A. G. (2019). "An Overview of the Tissue Engineering Market in the United States from 2011 to 2018." Tissue Eng Part A **25**(1-2): 1-8.

Kirby, G. T. S., White, L. J., Steck, R., Berner, A., Bogoevski, K., Qutachi, O., Jones, B., Saifzadeh, S., Hutmacher, D., Shakesheff, K. M. and Woodruff, M. A. (2016). "Microparticles for Sustained Growth Factor Delivery in the Regeneration of Critically-Sized Segmental Tibial Bone Defects." Materials **9**(4): 259.

Klimczak, A., Mirosławska-Kempińska, B., Biegańska-Płonka, M., Mik, M. and Dziki, A. (2011). Manual Stitching - the Past and the Present. Polish Journal of Surgery. **83:** 527.

Klinge, U., Dietz, U., Fet, N. and Klosterhalfen, B. (2014). "Characterisation of the cellular infiltrate in the foreign body granuloma of textile meshes with its impact on collagen deposition." Hernia **18**(4): 571-578.

Klinge, U. and Klosterhalfen, B. (2012). "Modified classification of surgical meshes for hernia repair based on the analyses of 1,000 explanted meshes." Hernia **16**(3): 251-258.

Klinge, U., Klosterhalfen, B., Ottinger, A. P., Junge, K. and Schumpelick, V. (2002). "PVDF as a new polymer for the construction of surgical meshes." Biomaterials **23**(16): 3487-3493.

Klopfleisch, R. and Jung, F. (2017). "The pathology of the foreign body reaction against biomaterials." J Biomed Mater Res A **105**(3): 927-940.

Klosterhalfen, B. and Klinge, U. (2013). "Retrieval study at 623 human mesh explants made of polypropylene – impact of mesh class and indication for mesh removal on tissue reaction." Journal of Biomedical Materials Research Part B: Applied Biomaterials **101**(8): 1393-1399.

Kondo, K., Harada, N., Masuda, H., Sugo, N., Terazono, S., Okonogi, S., Sakaeyama, Y., Fuchinoue, Y., Ando, S., Fukushima, D., Nomoto, J. and Nemoto, M. (2016). "A neurosurgical simulation of skull base tumors using a 3D printed rapid prototyping model containing mesh structures." Acta Neurochir (Wien) **158**(6): 1213-1219.

Kontakis, G. M., Pagkalos, J. E., Tosounidis, T. I., Melissas, J. and Katonis, P. (2007). "Bioabsorbable materials in orthopaedics." Acta Orthop Belg **73**(2): 159-169.

Kurtz, S. M. and Devine, J. N. (2007). "PEEK biomaterials in trauma, orthopedic, and spinal implants." Biomaterials **28**(32): 4845-4869.

Kurtz, S. M., Muratoglu, O. K., Evans, M. and Edidin, A. A. (1999). "Advances in the processing, sterilization, and crosslinking of ultra-high molecular weight polyethylene for total joint arthroplasty." Biomaterials **20**(18): 1659-1688.

Landgraf, M., Lahr, C. A., Kaur, I., Shafiee, A., Sanchez-Herrero, A., Janowicz, P. W., Ravichandran, A., Howard, C. B., Cifuentes-Rius, A., McGovern, J. A., Voelcker, N. H. and Hutmacher, D. W. (2020). "Targeted camptothecin delivery via silicon nanoparticles reduces breast cancer metastasis." Biomaterials **240**: 119791.

Landgraf, M., Lahr, C. A., Sanchez-Herrero, A., Meinert, C., Shokoohmand, A., Pollock, P. M., Hutmacher, D. W., Shafiee, A. and McGovern, J. A. (2019). "Humanized bone facilitates prostate cancer metastasis and recapitulates therapeutic effects of zoledronic acid in vivo." Bone Res **7**(1): 31.

Langer, R., Cima, L. G., Tamada, J. A. and Wintermantel, E. (1990). "Future directions in biomaterials." Biomaterials **11**(9): 738-745.

Langer, R. and Vacanti, J. P. (1993). "Tissue engineering." Science **260**(5110): 920-926.

Les, A. S., Ohye, R. G., Filbrun, A. G., Ghadimi Mahani, M., Flanagan, C. L., Daniels, R. C., Kidwell, K. M., Zopf, D. A., Hollister, S. J. and Green, G. E. (2019). "3D-printed, externally-implanted, bioresorbable airway splints for severe tracheobronchomalacia." Laryngoscope **129**(8): 1763-1771.

Liao, H. T., Lee, M. Y., Tsai, W. W., Wang, H. C. and Lu, W. C. (2016). "Osteogenesis of adipose-derived stem cells on polycaprolactone-beta-tricalcium phosphate scaffold fabricated via selective laser sintering and surface coating with collagen type I." J Tissue Eng Regen Med **10**(10): E337-E353.

Liashenko, I., Hrynevich, A. and Dalton, P. D. (2020). "Designing Outside the Box: Unlocking the Geometric Freedom of Melt Electrowriting using Microscale Layer Shifting." Adv Mater **32**(28): e2001874.

Lin, A. S. P., Barrows, T. H., Cartmell, S. H. and Guldberg, R. E. (2003). "Microarchitectural and mechanical characterization of oriented porous polymer scaffolds." Biomaterials **24**(3): 481-489.

Liu, A., Xue, G. H., Sun, M., Shao, H. F., Ma, C. Y., Gao, Q., Gou, Z. R., Yan, S. G., Liu, Y. M. and He, Y. (2016). "3D Printing Surgical Implants at the clinic: A Experimental Study on Anterior Cruciate Ligament Reconstruction." Sci Rep **6**: 21704.

Loessner, D., Rockstroh, A., Shokoohmand, A., Holzapfel, B. M., Wagner, F., Baldwin, J., Boxberg, M., Schmalfeldt, B., Lengyel, E., Clements, J. A. and Hutmacher, D. W. (2019). "A 3D tumor microenvironment regulates cell proliferation, peritoneal growth and expression patterns." Biomaterials **190-191**: 63-75.

Loh, Q. L. and Choong, C. (2013). "Three-Dimensional Scaffolds for Tissue Engineering Applications: Role of Porosity and Pore Size." Tissue Engineering Part B-Reviews **19**(6): 485-502.

Lohfeld, S., Cahill, S., Barron, V., McHugh, P., Durselen, L., Kreja, L., Bausewein, C. and Ignatius, A. (2012). "Fabrication, mechanical and in vivo performance of polycaprolactone/tricalcium phosphate composite scaffolds." Acta Biomater **8**(9): 3446-3456.

Long, J. P., Hollister, S. J. and Goldstein, S. A. (2012). "A paradigm for the development and evaluation of novel implant topologies for bone fixation: in vivo evaluation." J Biomech **45**(15): 2651-2657.

Lorenz, H. P., Longaker, M. T., Perkocha, L. A., Jennings, R. W., Harrison, M. R. and Adzick, N. S. (1992). "Scarless wound repair: a human fetal skin model." Development **114**(1): 253-259.

Lovett, M., Lee, K., Edwards, A. and Kaplan, D. L. (2009). "Vascularization strategies for tissue engineering." Tissue Eng Part B Rev **15**(3): 353-370.

Low, S. W., Ng, Y. J., Yeo, T. T. and Chou, N. (2009). "Use of Osteoplug (TM) polycaprolactone implants as novel burr-hole covers." Singapore Medical Journal **50**(8): 777-780.

Luijendijk, R. W., Hop, W. C., van den Tol, M. P., de Lange, D. C., Braaksma, M. M., JN, I. J., Boelhouwer, R. U., de Vries, B. C., Salu, M. K., Wereldsma, J. C., Bruijninckx, C. M. and Jeekel, J. (2000). "A comparison of suture repair with mesh repair for incisional hernia." N Engl J Med **343**(6): 392-398.

Lyons, J., Li, C. and Ko, F. (2004). "Melt-electrospinning part I: processing parameters and geometric properties." Polymer **45**(22): 7597-7603.

Mangano, F., Chambrone, L., van Noort, R., Miller, C., Hatton, P. and Mangano, C. (2014). "Direct metal laser sintering titanium dental implants: a review of the current literature." Int J Biomater **2014**: 461534.

Maradit Kremers, H., Larson, D. R., Crowson, C. S., Kremers, W. K., Washington, R. E., Steiner, C. A., Jiranek, W. A. and Berry, D. J. (2015). "Prevalence of Total Hip and Knee Replacement in the United States." J Bone Joint Surg Am **97**(17): 1386-1397.

Marshall, A. J. and Ratner, B. D. (2005). "Quantitative characterization of sphere-templated porous biomaterials." Aiche Journal **51**(4): 1221-1232.

Martelli, N., Serrano, C., van den Brink, H., Pineau, J., Prognon, P., Borget, I. and El Batti, S. (2016). "Advantages and disadvantages of 3-dimensional printing in surgery: A systematic review." Surgery **159**(6): 1485-1500.

Martine, L. C., Holzapfel, B. M., McGovern, J. A., Wagner, F., Quent, V. M., Hesami, P., Wunner, F. M., Vaquette, C., De-Juan-Pardo, E. M., Brown, T. D., Nowlan, B., Wu, D. J., Hutmacher, C. O., Moi, D., Oussenko, T., Piccinini, E., Zandstra, P. W., Mazzieri, R., Levesque, J. P., Dalton, P. D., Taubenberger, A. V. and Hutmacher, D. W. (2017). "Engineering a humanized bone organ model in mice to study bone metastases." Nat Protoc **12**(4): 639-663.

Mattei, L., Pellegrino, P., Calo, M., Bistolfi, A. and Castoldi, F. (2016). "Patient specific instrumentation in total knee arthroplasty: a state of the art." Ann Transl Med **4**(7): 126.

Mazzoli, A. (2013). "Selective laser sintering in biomedical engineering." Med Biol Eng Comput **51**(3): 245-256.

McGovern, J. A., Shafiee, A., Wagner, F., Lahr, C. A., Landgraf, M., Meinert, C., Williams, E. D., Russell, P. J., Clements, J. A., Loessner, D., Holzapfel, B. M., Risbridger, G. P. and Hutmacher, D. W. (2018). "Humanization of the Prostate Microenvironment Reduces Homing of PC3 Prostate Cancer Cells to Human Tissue-Engineered Bone." Cancers (Basel) **10**(11): 438.

McKeen, L. W. (2014). 3 - Plastics Used in Medical Devices A2 - Modjarrad, Kayvon. Handbook of Polymer Applications in Medicine and Medical Devices. S. Ebnesajjad. Oxford, William Andrew Publishing**:** 21-53.

McMaster, R., Hoefner, C., Hrynevich, A., Blum, C., Wiesner, M., Wittmann, K., Dargaville, T. R., Bauer-Kreisel, P., Groll, J., Dalton, P. D. and Blunk, T. (2019). "Tailored Melt Electrowritten Scaffolds for the Generation of Sheet-Like Tissue Constructs from Multicellular Spheroids." Adv Healthc Mater: e1801326.

Melchels, F. P., Barradas, A. M., van Blitterswijk, C. A., de Boer, J., Feijen, J. and Grijpma, D. W. (2010). "Effects of the architecture of tissue engineering scaffolds on cell seeding and culturing." Acta Biomater **6**(11): 4208-4217.

Melchels, F. P., Bertoldi, K., Gabbrielli, R., Velders, A. H., Feijen, J. and Grijpma, D. W. (2010). "Mathematically defined tissue engineering scaffold architectures prepared by stereolithography." Biomaterials **31**(27): 6909-6916.

Meng, Z. J., He, J. K., Cai, Z. H., Wang, F. P., Zhang, J. L., Wang, L., Ling, R. and Li, D. C. (2020). "Design and additive manufacturing of flexible polycaprolactone scaffolds with highly-tunable mechanical properties for soft tissue engineering." Materials & Design **189**: 108508.

Michalopoulos, G. K. and DeFrances, M. C. (1997). "Liver regeneration." Science **276**(5309): 60-66.

Middleton, J. C. and Tipton, A. J. (2000). "Synthetic biodegradable polymers as orthopedic devices." Biomaterials **21**(23): 2335-2346.

Migonney, V. (2014). History of Biomaterials. Biomaterials, John Wiley & Sons, Inc.**:** 1-10.

Miron, R. J., Zohdi, H., Fujioka-Kobayashi, M. and Bosshardt, D. D. (2016). "Giant cells around bone biomaterials: Osteoclasts or multi-nucleated giant cells?" Acta Biomater **46**(Supplement C): 15-28.

Mori, K., Yamamoto, T., Oyama, K., Ueno, H., Nakao, Y. and Honma, K. (2008). "Modified three-dimensional skull base model with artificial dura mater, cranial nerves, and venous sinuses for training in skull base surgery: technical note." Neurol Med Chir (Tokyo) **48**(12): 582-587; discussion 587-588.

Moroni, L., Burdick, J. A., Highley, C., Lee, S. J., Morimoto, Y., Takeuchi, S. and Yoo, J. J. (2018). "Biofabrication strategies for 3D in vitro models and regenerative medicine." Nat Rev Mater **3**(5): 21-37.

Morrison, R. J., Hollister, S. J., Niedner, M. F., Mahani, M. G., Park, A. H., Mehta, D. K., Ohye, R. G. and Green, G. E. (2015). "Mitigation of tracheobronchomalacia with 3D-printed personalized medical devices in pediatric patients." Sci Transl Med **7**(285): 285ra264.

Morrison, R. J., Sengupta, S., Flanangan, C. L., Ohye, R. G., Hollister, S. J. and Green, G. E. (2017). "Treatment of Severe Acquired Tracheomalacia With a Patient-Specific, 3D-Printed, Permanent Tracheal Splint." JAMA Otolaryngol Head Neck Surg **143**(5): 523-525.

Mota, C., Puppi, D., Gazzarri, M., Bartolo, P. and Chiellini, F. (2013). "Melt electrospinning writing of three-dimensional star poly(E-caprolactone) scaffolds." Polymer International **62**(6): 893-900.

Moulic, S. G., Singh, S., Hussain, R., Murthy, G., Khawade, Y. and Bettaiah, N. (2019). "Digital transformation and 3D printing of transtibial load-bearing prosthesis in India: recent advances, challenges and future perspectives." Journal of 3D Printing in Medicine **3**(4): 185-193.

Mueller, A. A., Paysan, P., Schumacher, R., Zeilhofer, H. F., Berg-Boerner, B. I., Maurer, J., Vetter, T., Schkommodau, E., Juergens, P. and Schwenzer-Zimmerer, K. (2011). "Missing facial parts computed by a morphable model and transferred directly to a polyamide laser-sintered prosthesis: an innovation study." Br J Oral Maxillofac Surg **49**(8): e67-71.

Muerza-Cascante, M. L., Haylock, D., Hutmacher, D. W. and Dalton, P. D. (2015). "Melt electrospinning and its technologization in tissue engineering." Tissue Eng Part B Rev **21**(2): 187-202.

Muerza-Cascante, M. L., Shokoohmand, A., Khosrotehrani, K., Haylock, D., Dalton, P. D., Hutmacher, D. W. and Loessner, D. (2016). "Endosteal-like extracellular matrix expression on melt electrospun written scaffolds." Acta Biomater.

Muratoglu, O. K., O'Connor, D. O., Bragdon, C. R., Delaney, J., Jasty, M., Harris, W. H., Merrill, E. and Venugopalan, P. (2002). "Gradient crosslinking of UHMWPE using irradiation in molten state for total joint arthroplasty." Biomaterials **23**(3): 717-724.

Muto, J., Carrau, R. L., Oyama, K., Otto, B. A. and Prevedello, D. M. (2017). "Training model for control of an internal carotid artery injury during transsphenoidal surgery." Laryngoscope **127**(1): 38-43.

Nahm, D., Weigl, F., Schafer, N., Sancho, A., Frank, A., Groll, J., Villmann, C., Schmidt, H. W., Dalton, P. D. and Luxenhofer, R. (2020). "A versatile biomaterial ink platform for the melt electrowriting of chemically-crosslinked hydrogels." Materials Horizons **7**(3): 928-933.

Nakayama, M. (2018). "Macrophage Recognition of Crystals and Nanoparticles." Front Immunol **9**: 103.

Narayanan, G., Vernekar, V. N., Kuyinu, E. L. and Laurencin, C. T. (2016). "Poly (lactic acid)-based biomaterials for orthopaedic regenerative engineering." Adv Drug Deliv Rev **107**: 247-276.

No, Y. J., Castilho, M., Ramaswamy, Y. and Zreiqat, H. (2020). "Role of Biomaterials and Controlled Architecture on Tendon/Ligament Repair and Regeneration." Adv Mater **32**(18): e1904511.

Norman, J., Madurawe, R. D., Moore, C. M., Khan, M. A. and Khairuzzaman, A. (2016). "A new chapter in pharmaceutical manufacturing: 3D-printed drug products." Adv Drug Deliv Rev.

Ntagiopoulos, P. G., Demey, G., Tavernier, T. and Dejour, D. (2015). "Comparison of resorption and remodeling of bioabsorbable interference screws in anterior cruciate ligament reconstruction." Int Orthop **39**(4): 697-706.

Obregon, F., Vaquette, C., Ivanovski, S., Hutmacher, D. W. and Bertassoni, L. E. (2015). "Three-Dimensional Bioprinting for Regenerative Dentistry and Craniofacial Tissue Engineering." J Dent Res **94**(9 Suppl): 143S-152S.

Ong, K. L., Villarraga, M. L., Lau, E., Carreon, L. Y., Kurtz, S. M. and Glassman, S. D. (2010). "Off-label use of bone morphogenetic proteins in the United States using administrative data." Spine (Phila Pa 1976) **35**(19): 1794-1800.

Oxford Performance Materials. (2011, 09.12.2011). "OPM Announces Patient-Specific Implants." Retrieved 20.11.2016, 2016, from http://www.oxfordpm.com/opm-announces-patient-specific-implants.

Ozkanli, S., Soylemez, M. S., Sahin, A., Senol, S., Bilsel, K. and Ceylan, H. H. (2014). "Unusual implant-related soft tissue reaction presenting as a swollen leg: a case report." J Med Case Rep **8**: 187.

Paindelli, C., Navone, N., Logothetis, C. J., Friedl, P. and Dondossola, E. (2019). "Engineered bone for probing organotypic growth and therapy response of prostate cancer tumoroids in vitro." Biomaterials **197**: 296-304.

Park, H., Temenoff, J. S. and Mikos, A. G. (2007). Biodegradable Orthopedic Implants. Engineering of Functional Skeletal Tissues. F. Bronner, M. C. Farach-Carson and A. G. Mikos. London, Springer London**:** 55-68.

Partee, B., Hollister, S. J. and Das, S. (2006). "Selective Laser Sintering Process Optimization for Layered Manufacturing of CAPA[sup ®] 6501 Polycaprolactone Bone Tissue Engineering Scaffolds." Journal of Manufacturing Science and Engineering **128**(2): 531.

Pashuck, E. T. and Stevens, M. M. (2012). "Designing regenerative biomaterial therapies for the clinic." Sci Transl Med **4**(160): 160sr164.

Patel, H., Ostergard, D. R. and Sternschuss, G. (2012). "Polypropylene mesh and the host response." Int Urogynecol J **23**(6): 669-679.

Pavia-Jimenez, A., Tcheuyap, V. T. and Brugarolas, J. (2014). "Establishing a human renal cell carcinoma tumorgraft platform for preclinical drug testing." Nat Protoc **9**(8): 1848-1859.

Pennings, I., van Haaften, E. E., Jungst, T., Bulsink, J. A., Rosenberg, A., Groll, J., Bouten, C. V. C., Kurniawan, N. A., Smits, A. and Gawlitta, D. (2019). "Layer-specific cell differentiation in bi-layered vascular grafts under flow perfusion." Biofabrication **12**(1): 015009.

Pereira, B. A., Lister, N. L., Hashimoto, K., Teng, L., Flandes-Iparraguirre, M., Eder, A., Sanchez-Herrero, A., Niranjan, B. and Melbourne Urological Research, A. (2019). "Tissue engineered human prostate microtissues reveal key role of mast cell-derived tryptase in potentiating cancer-associated fibroblast (CAF)-induced morphometric transition in vitro." Biomaterials **197**: 72-85.

Pfaff, M. J. and Steinbacher, D. M. (2016). "Plastic Surgery Applications Using Three-Dimensional Planning and Computer-Assisted Design and Manufacturing." Plast Reconstr Surg **137**(3): 603e-616e.

Pike, J. M. and Gelberman, R. H. (2010). "Zone II combined flexor digitorum superficialis and flexor digitorum profundus repair distal to the A2 pulley." J Hand Surg Am **35**(9): 1523-1527.

Pillai, C. K. and Sharma, C. P. (2010). "Review paper: absorbable polymeric surgical sutures: chemistry, production, properties, biodegradability, and performance." J Biomater Appl **25**(4): 291-366.

Piskin, E., Bolgen, N., Egri, S. and Isoglu, I. A. (2007). "Electrospun matrices made of poly(alpha-hydroxy acids) for medical use." Nanomedicine (Lond) **2**(4): 441-457.

Pitt, C. G., Chasalow, F. I., Hibionada, Y. M., Klimas, D. M. and Schindler, A. (1981). "Aliphatic polyesters. I. The degradation of poly(ϵ-caprolactone) in vivo." Journal of Applied Polymer Science **26**(11): 3779-3787.

Pitt, C. G., Gratzl, M. M., Kimmel, G. L., Surles, J. and Schindler, A. (1981). "Aliphatic polyesters II. The degradation of poly (DL-lactide), poly (epsilon-caprolactone), and their copolymers in vivo." Biomaterials **2**(4): 215-220.

Pitt, C. G. and Schindler, A. (1981). "Aliphatic polyesters I." Biomaterials **2**(4): 215-220.

Powell, S. K., Ristovski, N., Liao, S., Blackwood, K. A., Woodruff, M. A. and Momot, K. I. (2014). "Characterization of the Microarchitecture of Direct Writing Melt Electrospun Tissue Engineering Scaffolds Using Diffusion Tensor and Computed Tomography Microimaging." 3D Printing and Additive Manufacturing **1**(2): 95-103.

Prantl, L. (2009). Serologic and Histologic Findings in Capsule Contracture Patients with Silicone Gel Implants. Breast Augmentation. M. A. Shiffman. Berlin, Heidelberg, Springer Berlin Heidelberg**:** 649-654.

Prater, T., Bean, Q., Werkheiser, N., Grguel, R., Beshears, R., Rolin, T., Huff, T., Ryan, R., Ledbetter, F. and Ordonez, E. (2017). "Analysis of specimens from phase I of the 3D printing in Zero G technology demonstration mission." Rapid Prototyping Journal **23**(6): 1212-1225.

Prater, T., Edmunson, J., Ledbetter, F., Fiske, M., Hill, C., Meyyappan, M., Roberts, C., Huebner, L., Hall, P. and Werkheiser, N. (2019). "NASA's In-Space Manufacturing Project: Update on Manufacturing Technologies and Materials to Enable More Sustainable and Safer Exploration."

Prater, T., Werkheiser, N., Ledbetter, F., Timucin, D., Wheeler, K. and Snyder, M. (2019). "3D Printing in Zero G Technology Demonstration Mission: complete experimental results and summary of related material modeling efforts." International Journal of Advanced Manufacturing Technology **101**(1-4): 391-417.

Prater, T. J., Werkheiser, M. J., Jehle, A., Ledbetter, F., Bean, Q., Wilkerson, M., Soohoo, H. and Hipp, B. (2017). NASA's In-Space Manufacturing Project: Development of a Multimaterial Fabrication Laboratory for the International Space Station. AIAA SPACE and Astronautics Forum and Exposition.

Pritchard, J., Foley, P. and Wong, H. (2003). "Langerhans and Langhans: what's misleading in a name?" Lancet **362**(9387): 922.

Probst, F. A., Hutmacher, D. W., Muller, D. F., Machens, H. G. and Schantz, J. T. (2010). "[Calvarial reconstruction by customized bioactive implant]." Handchir Mikrochir Plast Chir **42**(6): 369-373.

Probst, F. A., Metzger, M., Ehrenfeld, M. and Cornelius, C. P. (2016). "Computer-Assisted Designed and Manufactured Procedures Facilitate the Lingual Application of Mandible Reconstruction Plates." J Oral Maxillofac Surg **74**(9): 1879-1895.

Quent, V., Taubenberger, A. V., Reichert, J. C., Martine, L. C., Clements, J. A., Hutmacher, D. W. and Loessner, D. (2018). "A humanised tissue-engineered bone model allows species-specific breast cancer-related bone metastasis in vivo." J Tissue Eng Regen Med **12**(2): 494-504.

Rados, C. (2006). Medical Device & Radiological Health Regulations Come of Age. FDA Consumer Magazine.

Rai, B., Oest, M. E., Dupont, K. M., Ho, K. H., Teoh, S. H. and Guldberg, R. E. (2007). "Combination of platelet-rich plasma with polycaprolactone-tricalcium phosphate scaffolds for segmental bone defect repair." J Biomed Mater Res A **81**(4): 888-899.

Ramot, Y., Haim-Zada, M., Domb, A. J. and Nyska, A. (2016). "Biocompatibility and safety of PLA and its copolymers." Adv Drug Deliv Rev **107**: 153-162.

Rankin, T. M., Giovinco, N. A., Cucher, D. J., Watts, G., Hurwitz, B. and Armstrong, D. G. (2014). "Three-dimensional printing surgical instruments: are we there yet?" J Surg Res **189**(2): 193-197.

Rathi, V. K. and Ross, J. S. (2019). "Modernizing the FDA's 510(k) Pathway." N Engl J Med **381**(20): 1891-1893.

Ratner, B. D. (2013). A History of Biomaterials Biomaterials Science (Third Edition), Academic Press**:** xli-liii.

Ratner, B. D. (2019). "Biomaterials: Been There, Done That, and Evolving into the Future." Annu Rev Biomed Eng **21**(1): 171-191.

Ratner, B. D., Hoffman, A. S., Schoen, F. J. and Lemons, J. E. (2013). Introduction - Biomaterials Science: An Evolving, Multidisciplinary Endeavor. Biomaterials Science (Third Edition). USA, Academic Press**:** xxv-xxxix.

Ravi, S. and Chaikof, E. L. (2010). "Biomaterials for vascular tissue engineering." Regen Med **5**(1): 107-120.

Reilkoff, R. A., Bucala, R. and Herzog, E. L. (2011). "Fibrocytes: emerging effector cells in chronic inflammation." Nat Rev Immunol **11**(6): 427-435.

Ren, J. Y., Blackwood, K. A., Doustgani, A., Poh, P. P., Steck, R., Stevens, M. M. and Woodruff, M. A. (2014). "Melt-electrospun polycaprolactone strontium-substituted bioactive glass scaffolds for bone regeneration." Journal of Biomedical Materials Research Part A **102**(9): 3140-3153.

Reneker, D. H. and Yarin, A. L. (2008). "Electrospinning jets and polymer nanofibers." Polymer **49**(10): 2387-2425.

Research and Markets. (2019, 19.09.2019). "Global Medical Devices Market Report 2019-2022." Retrieved 15.06.2020, from https://www.globenewswire.com/news-release/2019/09/19/1918062/0/en/Global-Medical-Devices-Market-Report-2019-2022-A-521-Billion-Opportunity-Analysis.html.

Riedelsheimer, B. and Büchl-Zimmermann, S. (2015). Färbungen. Romeis - Mikroskopische Technik. M. Mulisch and U. Welsch. Berlin, Heidelberg, Springer Berlin Heidelberg**:** 171-282.

Rimell, J. T. and Marquis, P. M. (2000). "Selective laser sintering of ultra high molecular weight polyethylene for clinical applications." J Biomed Mater Res **53**(4): 414-420.

Roberts, S. F., Fischhoff, M. A., Sakowski, S. A. and Feldman, E. L. (2012). "Perspective: Transforming science into medicine: how clinician-scientists can build bridges across research's "valley of death"." Acad Med **87**(3): 266-270.

Robinson, T. M., Hutmacher, D. W. and Dalton, P. D. (2019). "The Next Frontier in Melt Electrospinning: Taming the Jet." Advanced Functional Materials **29**(44).

Roder, A., Garcia-Gareta, E., Theodoropoulos, C., Ristovski, N., Blackwood, K. A. and Woodruff, M. A. (2015). "An Assessment of Cell Culture Plate Surface Chemistry for in Vitro Studies of Tissue Engineering Scaffolds." J Funct Biomater **6**(4): 1054-1063.

Roll, S., Muller-Nordhorn, J., Keil, T., Scholz, H., Eidt, D., Greiner, W. and Willich, S. N. (2008). "Dacron vs. PTFE as bypass materials in peripheral vascular surgery--systematic review and meta-analysis." BMC Surg **8**(1): 22.

Roman Regueros, S., Albersen, M., Manodoro, S., Zia, S., Osman, N. I., Bullock, A. J., Chapple, C. R., Deprest, J. and MacNeil, S. (2014). "Acute in vivo response to an alternative implant for urogynecology." Biomed Res Int **2014**: 853610.

Ronfard, V., Vertes, A. A., May, M. H., Dupraz, A., van Dyke, M. E. and Bayon, Y. (2017). "Evaluating the Past, Present, and Future of Regenerative Medicine: A Global View." Tissue Eng Part B Rev **23**(2): 199-210.

Roosa, S. M., Kemppainen, J. M., Moffitt, E. N., Krebsbach, P. H. and Hollister, S. J. (2010). "The pore size of polycaprolactone scaffolds has limited influence on bone regeneration in an in vivo model." J Biomed Mater Res A **92**(1): 359-368.

Roskies, M. G., Fang, D., Abdallah, M. N., Charbonneau, A. M., Cohen, N., Jordan, J. O., Hier, M. P., Mlynarek, A., Tamimi, F. and Tran, S. D. (2017). "Three-dimensionally printed polyetherketoneketone scaffolds with mesenchymal stem cells for the reconstruction of critical-sized mandibular defects." Laryngoscope **127**(11): E392-e398.

rti surgical. (2019). "TETRAfuse 3D Technology." from http://www.rtix.com/en_us/healthcare-professionals/tetrafuse-3d-technology.

Rubalcaba, S. (2018). "Understanding the De Novo Medical Device Classification Process." Retrieved 15.06.2020, 2018, from https://www.rcri-inc.com/understanding-de-novo-medical-device-classification-process/.

Ryan, J. R., Almefty, K. K., Nakaji, P. and Frakes, D. H. (2016). "Cerebral Aneurysm Clipping Surgery Simulation Using Patient-Specific 3D Printing and Silicone Casting." World Neurosurg **88**: 175-181.

Saidy, N. T., Wolf, F., Bas, O., Keijdener, H., Hutmacher, D. W., Mela, P. and De-Juan-Pardo, E. M. (2019). "Biologically Inspired Scaffolds for Heart Valve Tissue Engineering via Melt Electrowriting." Small **15**(24): e1900873.

Salerno, A., Oliviero, M., Di Maio, E., Iannace, S. and Netti, P. A. (2009). "Design of porous polymeric scaffolds by gas foaming of heterogeneous blends." J Mater Sci Mater Med **20**(10): 2043-2051.

Salmi, M., Paloheimo, K. S., Tuomi, J., Wolff, J. and Makitie, A. (2013). "Accuracy of medical models made by additive manufacturing (rapid manufacturing)." J Craniomaxillofac Surg **41**(7): 603-609.

Sanchez Alvarado, A., Newmark, P. A., Robb, S. M. and Juste, R. (2002). "The Schmidtea mediterranea database as a molecular resource for studying platyhelminthes, stem cells and regeneration." Development **129**(24): 5659-5665.

Sanders, J. E., Bale, S. D. and Neumann, T. (2002). "Tissue response to microfibers of different polymers: polyester, polyethylene, polylactic acid, and polyurethane." J Biomed Mater Res **62**(2): 222-227.

Sastry, A. (2014). "Overview of the US FDA medical device approval process." Curr Cardiol Rep **16**(6): 494.

Savalani, M. M., Hao, L., Zhang, Y., Tanner, K. E. and Harris, R. A. (2007). "Fabrication of porous bioactive structures using the selective laser sintering technique." Proc Inst Mech Eng H **221**(8): 873-886.

Schaefer, N., Janzen, D., Bakirci, E., Hrynevich, A., Dalton, P. D. and Villmann, C. (2019). "3D Electrophysiological Measurements on Cells Embedded within Fiber-Reinforced Matrigel." Adv Healthc Mater **0**(0): e1801226.

Schantz, J. T., Lim, T. C., Ning, C., Teoh, S. H., Tan, K. C., Wang, S. C. and Hutmacher, D. W. (2006). "Cranioplasty after trephination using a novel biodegradable burr hole cover: technical case report." Neurosurgery **58**(1 Suppl): ONS-E176; discussion ONS-E176.

Schantz, J. T., Ng, M. M. L., Netto, P., Ming, J. C. L., Wong, K. M., Hutmacher, D. W. and Teoh, S. H. (2002). "Application of an X-ray microscopy technique to evaluate tissue-engineered bone-scaffold constructs." Materials Science & Engineering C-Biomimetic and Supramolecular Systems **20**(1-2): 9-17.

Schemitsch, E. H. (2017). "Size Matters: Defining Critical in Bone Defect Size!" J Orthop Trauma **31 Suppl 5**: S20-S22.

Schindelin, J., Arganda-Carreras, I., Frise, E., Kaynig, V., Longair, M., Pietzsch, T., Preibisch, S., Rueden, C., Saalfeld, S., Schmid, B., Tinevez, J. Y., White, D. J., Hartenstein, V., Eliceiri, K., Tomancak, P. and Cardona, A. (2012). "Fiji: an open-source platform for biological-image analysis." Nat Methods **9**(7): 676-682.

Schmidt-Bleek, K., Petersen, A., Dienelt, A., Schwarz, C. and Duda, G. N. (2014). "Initiation and early control of tissue regeneration - bone healing as a model system for tissue regeneration." Expert Opin Biol Ther **14**(2): 247-259.

Schumpelick, V., Klinge, U., Rosch, R. and Junge, K. (2006). "Light weight meshes in incisional hernia repair." J Minim Access Surg **2**(3): 117-123.

Scotland, T. (2014). "The First World War and its influence on the development of orthopaedic surgery." J R Coll Physicians Edinb **44**(2): 163-169.

Serafini, M. R., Medeiros Savi, F., Ren, J., Bas, O., O'Rourke, N., Maher, C. and Hutmacher, D. W. (2020). "The Patenting and Technological Trends in Hernia Implants (2008-2018)." Tissue Eng Part B Rev **0**(ja): null.

Sertoglu, K. (2020, 09.04.2020). "Volunteers develop 3D printable ventilator based on 1965 U.S. Army design." Retrieved 15.06.2020, from https://3dprintingindustry.com/news/volunteers-develop-3d-printable-ventilator-based-on-1965-u-s-army-design-170653/.

Shafiee, A., Baldwin, J. G., Patel, J., Holzapfel, B. M., Fisk, N. M., Khosrotehrani, K. and Hutmacher, D. W. (2017). "Fetal Bone Marrow-Derived Mesenchymal Stem/Stromal Cells Enhance Humanization and Bone Formation of BMP7 Loaded Scaffolds." Biotechnol J **12**(12): 1700414.

Shafiee, A., McGovern, J. A., Lahr, C. A., Meinert, C., Moi, D., Wagner, F., Landgraf, M., De-Juan-Pardo, E., Mazzieri, R. and Hutmacher, D. W. (2018). "Immune System Augmentation via Humanization Using Stem/Progenitor Cells and Bioengineering in a Breast Cancer Model Study." Int J Cancer.

Shah, S. M., Crawshaw, J. P. and Boek, E. S. (2017). "Three-dimensional imaging of porous media using confocal laser scanning microscopy." J Microsc **265**(2): 261-271.

Sharma, U., Concagh, D., Core, L., Kuang, Y., You, C., Pham, Q., Zugates, G., Busold, R., Webber, S., Merlo, J., Langer, R., Whitesides, G. M. and Palasis, M. (2018). "The development of bioresorbable composite polymeric implants with high mechanical strength." Nat Mater **17**(1): 96-103.

Sheikh, Z., Brooks, P. J., Barzilay, O., Fine, N. and Glogauer, M. (2015). "Macrophages, Foreign Body Giant Cells and Their Response to Implantable Biomaterials." Materials (Basel) **8**(9): 5671-5701.

Shi, S. R., Shi, Y. and Taylor, C. R. (2011). "Antigen retrieval immunohistochemistry: review and future prospects in research and diagnosis over two decades." J Histochem Cytochem **59**(1): 13-32.

Shirazi, S. F. S., Gharehkhani, S., Mehrali, M., Yarmand, H., Metselaar, H. S. C., Adib Kadri, N. and Osman, N. A. A. (2016). "A review on powder-based additive manufacturing for tissue engineering: selective laser sintering and inkjet 3D printing." Science and Technology of Advanced Materials **16**(3): 033502.

Shokoohmand, A., Ren, J., Baldwin, J., Atack, A., Shafiee, A., Theodoropoulos, C., Wille, M. L., Tran, P. A., Bray, L. J., Smith, D., Chetty, N., Pollock, P. M., Hutmacher, D. W., Clements, J. A., Williams, E. D. and Bock, N. (2019). "Microenvironment engineering of osteoblastic bone metastases reveals osteomimicry of patient-derived prostate cancer xenografts." Biomaterials **220**: 119402.

Shor, L., Guceri, S., Wen, X., Gandhi, M. and Sun, W. (2007). "Fabrication of three-dimensional polycaprolactone/hydroxyapatite tissue scaffolds and osteoblast-scaffold interactions in vitro." Biomaterials **28**(35): 5291-5297.

Simoncelli, T. (2013). Paving the Way for Personalized Medicine: FDA's role in a New Era of Medical Product Development, FDA.

Simpson, R. L., Wiria, F. E., Amis, A. A., Chua, C. K., Leong, K. F., Hansen, U. N., Chandrasekaran, M. and Lee, M. W. (2008). "Development of a 95/5 poly(L-lactide-co-glycolide)/hydroxylapatite and beta-tricalcium phosphate scaffold as bone replacement material via selective laser sintering." J Biomed Mater Res B Appl Biomater **84**(1): 17-25.

Sims, N. A. and Martin, T. J. (2014). "Coupling the activities of bone formation and resorption: a multitude of signals within the basic multicellular unit." Bonekey Rep **3**: 481.

Sing, S. L., An, J., Yeong, W. Y. and Wiria, F. E. (2016). "Laser and electron-beam powder-bed additive manufacturing of metallic implants: A review on processes, materials and designs." J Orthop Res **34**(3): 369-385.

Slezak, P., Slezak, C., Hartinger, J., Teuschl, A. H., Nurnberger, S., Redl, H. and Mittermayr, R. (2018). "A Low Cost Implantation Model in the Rat That Allows a Spatial Assessment of Angiogenesis." Front Bioeng Biotechnol **6**(3): 3.

Smith, M. H., Flanagan, C. L., Kemppainen, J. M., Sack, J. A., Chung, H., Das, S., Hollister, S. J. and Feinberg, S. E. (2007). "Computed tomography-based tissue-engineered scaffolds in craniomaxillofacial surgery." Int J Med Robot **3**(3): 207-216.

Sparks, D. S., Saifzadeh, S., Savi, F. M., Dlaska, C. E., Berner, A., Henkel, J., Reichert, J. C., Wullschleger, M., Ren, J., Cipitria, A., McGovern, J. A., Steck, R., Wagels, M., Woodruff, M. A., Schuetz, M. A. and Hutmacher, D. W. (2020). "A preclinical large-animal model for the assessment of critical-size load-bearing bone defect reconstruction." Nat Protoc **15**(3): 877-924.

Sridharan, R., Cameron, A. R., Kelly, D. J., Kearney, C. J. and O'Brien, F. J. (2015). "Biomaterial based modulation of macrophage polarization: a review and suggested design principles." Materials Today **18**(6): 313-325.

Study Group 1 of the Global Harmonization Task Force WHO (2012). Definition of the Terms 'Medical Device' and 'In Vitro Diagnostic (IVD) Medical Device', World Health Organization.

Sudheesh Kumar, P. T., Hashimi, S., Saifzadeh, S., Ivanovski, S. and Vaquette, C. (2018). "Additively manufactured biphasic construct loaded with BMP-2 for vertical bone regeneration: A pilot study in rabbit." Mater Sci Eng C Mater Biol Appl **92**: 554-564.

Sun, H., Mei, L., Song, C., Cui, X. and Wang, P. (2006). "The in vivo degradation, absorption and excretion of PCL-based implant." Biomaterials **27**(9): 1735-1740.

Sussman, E. M., Halpin, M. C., Muster, J., Moon, R. T. and Ratner, B. D. (2014). "Porous implants modulate healing and induce shifts in local macrophage polarization in the foreign body reaction." Ann Biomed Eng **42**(7): 1508-1516.

Suzuki, M., Yakushiji, N., Nakada, Y., Satoh, A., Ide, H. and Tamura, K. (2006). "Limb regeneration in Xenopus laevis froglet." ScientificWorldJournal **6 Suppl 1**: 26-37.

Takeo, M., Lee, W. and Ito, M. (2015). "Wound healing and skin regeneration." Cold Spring Harb Perspect Med **5**(1): a023267.

Tan, J. Z., Ditchfield, M. and Freezer, N. (2012). "Tracheobronchomalacia in children: review of diagnosis and definition." Pediatr Radiol **42**(8): 906-915; quiz 1027-1028.

Tan, K. H., Chua, C. K., Leong, K. F., Cheah, C. M., Cheang, P., Abu Bakar, M. S. and Cha, S. W. (2003). "Scaffold development using selective laser sintering of polyetheretherketone-hydroxyapatite biocomposite blends." Biomaterials **24**(18): 3115-3123.

Tarsitano, A., Ciocca, L., Scotti, R. and Marchetti, C. (2016). "Morphological results of customized microvascular mandibular reconstruction: A comparative study." J Craniomaxillofac Surg **44**(6): 697-702.

Tartal, J. (2014). Quality System Regulation Overview. FDA Small Business Regulatory Education for Industry (REdl). Burlingame, CA, USA, FDA.

Tatara, A. M. (2020). "Role of Tissue Engineering in COVID-19 and Future Viral Outbreaks." Tissue Eng Part A **26**(9-10): 468-474.

ten Harkel, B., Schoenmaker, T., Picavet, D. I., Davison, N. L., de Vries, T. J. and Everts, V. (2015). "The Foreign Body Giant Cell Cannot Resorb Bone, But Dissolves Hydroxyapatite Like Osteoclasts." PLoS One **10**(10): e0139564.

Teo, A. J. T., Mishra, A., Park, I., Kim, Y. J., Park, W. T. and Yoon, Y. J. (2016). "Polymeric Biomaterials for Medical Implants and Devices." Acs Biomaterials-Science & Engineering **2**(4): 454-472.

Teo, L., Teoh, S. H., Liu, Y., Lim, L., Tan, B., Schantz, J. T. and Seah, L. L. (2015). "A Novel Bioresorbable Implant for Repair of Orbital Floor Fractures." Orbit **34**(4): 192-200.

Thibaudeau, L., Taubenberger, A. V., Holzapfel, B. M., Quent, V. M., Fuehrmann, T., Hesami, P., Brown, T. D., Dalton, P. D., Power, C. A., Hollier, B. G. and Hutmacher, D. W. (2014). "A tissue-engineered humanized xenograft model of human breast cancer metastasis to bone." Dis Model Mech **7**(2): 299-309.

Thibaudeau, L., Taubenberger, A. V., Theodoropoulos, C., Holzapfel, B. M., Ramuz, O., Straub, M. and Hutmacher, D. W. (2015). "New mechanistic insights of integrin beta1 in breast cancer bone colonization." Oncotarget **6**(1): 332-344.

Tian, L., Prabhakaran, M. P. and Ramakrishna, S. (2015). "Strategies for regeneration of components of nervous system: scaffolds, cells and biomolecules." Regen Biomater **2**(1): 31-45.

Touri, M., Kabirian, F., Saadati, M., Ramakrishna, S. and Mozafari, M. (2019). "Additive Manufacturing of Biomaterials − The Evolution of Rapid Prototyping." Advanced Engineering Materials **21**(2): 1800511.

Tourlomousis, F., Ding, H., Kalyon, D. M. and Chang, R. C. (2017). "Melt Electrospinning Writing Process Guided by a "Printability Number"." Journal of Manufacturing Science and Engineering-Transactions of the Asme **139**(8).

Tran, P. A., Nguyen, H. T., Hubbard, P. J., Dang, H. P. and Hutmacher, D. W. (2018). "Mineralization of plasma treated polymer surfaces from super-saturated simulated body fluids." Materials Letters **230**: 12-15.

Tumbleston, J. R., Shirvanyants, D., Ermoshkin, N., Janusziewicz, R., Johnson, A. R., Kelly, D., Chen, K., Pinschmidt, R., Rolland, J. P., Ermoshkin, A., Samulski, E. T. and DeSimone, J. M. (2015). "Additive manufacturing. Continuous liquid interface production of 3D objects." Science **347**(6228): 1349-1352.

Tylek, T., Blum, C., Hrynevich, A., Schlegelmilch, K., Schilling, T., Dalton, P. D. and Groll, J. (2020). "Precisely defined fiber scaffolds with 40 mum porosity induce elongation driven M2-like polarization of human macrophages." Biofabrication **12**(2): 025007.

Uhthoff, H. K., Poitras, P. and Backman, D. S. (2006). "Internal plate fixation of fractures: short history and recent developments." Journal of Orthopaedic Science **11**(2): 118-126.

Ulery, B. D., Nair, L. S. and Laurencin, C. T. (2011). "Biomedical Applications of Biodegradable Polymers." J Polym Sci B Polym Phys **49**(12): 832-864.

Ullherr, M. and Zabler, S. (2015). "Correcting multi material artifacts from single material phase retrieved holo-tomograms with a simple 3D Fourier method." Opt Express **23**(25): 32718-32727.

van Noort, R. (2012). "The future of dental devices is digital." Dent Mater **28**(1): 3-12.

Vaquette, C., Ivanovski, S., Hamlet, S. M. and Hutmacher, D. W. (2013). "Effect of culture conditions and calcium phosphate coating on ectopic bone formation." Biomaterials **34**(22): 5538-5551.

Vaquette, C., Saifzadeh, S., Farag, A., Hutmacher, D. W. and Ivanovski, S. (2019). "Periodontal Tissue Engineering with a Multiphasic Construct and Cell Sheets." J Dent Res **98**(6): 673-681.

Varol, C., Mildner, A. and Jung, S. (2015). "Macrophages: development and tissue specialization." Annu Rev Immunol **33**: 643-675.

Veiseh, O., Doloff, J. C., Ma, M., Vegas, A. J., Tam, H. H., Bader, A. R., Li, J., Langan, E., Wyckoff, J., Loo, W. S., Jhunjhunwala, S., Chiu, A., Siebert, S., Tang, K., Hollister-Lock, J., Aresta-Dasilva, S., Bochenek, M., Mendoza-Elias, J., Wang, Y., Qi, M., Lavin, D. M., Chen, M., Dholakia, N., Thakrar, R., Lacik, I., Weir, G. C., Oberholzer, J., Greiner, D. L., Langer, R. and Anderson, D. G. (2015). "Size- and shape-dependent foreign body immune response to materials implanted in rodents and non-human primates." Nat Mater **14**(6): 643-651.

Vert, M., Doi, Y., Hellwich, K.-H., Hess, M., Hodge, P., Kubisa, P., Rinaudo, M. and Schué, F. (2012). Terminology for biorelated polymers and applications (IUPAC Recommendations 2012). Pure and Applied Chemistry. **84:** 377.

Visser, J., Melchels, F. P. W., Jeon, J. E., van Bussel, E. M., Kimpton, L. S., Byrne, H. M., Dhert, W. J. A., Dalton, P. D., Hutmacher, D. W. and Malda, J. (2015). "Reinforcement of hydrogels using three-dimensionally printed microfibres." Nature Communications **6**: 10.

Vogt, B., Desgrippes, A. and Desfemmes, F. N. (2015). "Changing the double-pigtail stent by a new suture stent to improve patient's quality of life: a prospective study." World J Urol **33**(8): 1061-1068.

Wake, N., Chandarana, H., Huang, W. C., Taneja, S. S. and Rosenkrantz, A. B. (2016). "Application of anatomically accurate, patient-specific 3D printed models from MRI data in urological oncology." Clin Radiol **71**(6): 610-614.

Wang, F., Shor, L., Darling, A., Khalil, S., Sun, W., Güçeri, S. and Lau, A. (2004). "Precision extruding deposition and characterization of cellular poly-ε-caprolactone tissue scaffolds." Rapid Prototyping Journal **10**(1): 42-49.

Wang, Z., Cui, Y., Wang, J., Yang, X., Wu, Y., Wang, K., Gao, X., Li, D., Li, Y., Zheng, X. L., Zhu, Y., Kong, D. and Zhao, Q. (2014). "The effect of thick fibers and large pores of electrospun poly(epsilon-caprolactone) vascular grafts on macrophage polarization and arterial regeneration." Biomaterials **35**(22): 5700-5710.

Wanibuchi, M., Noshiro, S., Sugino, T., Akiyama, Y., Mikami, T., Iihoshi, S., Miyata, K., Komatsu, K. and Mikuni, N. (2016). "Training for Skull Base Surgery with a Colored Temporal Bone Model Created by Three-Dimensional Printing Technology." World Neurosurgery **91**: 66-72.

Wanibuchi, M., Ohtaki, M., Fukushima, T., Friedman, A. H. and Houkin, K. (2010). "Skull base training and education using an artificial skull model created by selective laser sintering." Acta Neurochir (Wien) **152**(6): 1055-1059; discussion 1059-1060.

Webb, J. C. and Spencer, R. F. (2007). "The role of polymethylmethacrylate bone cement in modern orthopaedic surgery." J Bone Joint Surg Br **89**(7): 851-857.

Weber, J. S. and Mule, J. J. (2015). "Cancer immunotherapy meets biomaterials." Nat Biotechnol **33**(1): 44-45.

Webster, J. D., Miller, M. A., DuSold, D. and Ramos-Vara, J. (2009). "Effects of Prolonged Formalin Fixation on Diagnostic Immunohistochemistry in Domestic Animals." Journal of Histochemistry and Cytochemistry **57**(8): 753-761.

Weigand, A., Boos, A. M., Tasbihi, K., Beier, J. P., Dalton, P. D., Schrauder, M., Horch, R. E., Beckmann, M. W., Strissel, P. L. and Strick, R. (2016). "Selective isolation and characterization of primary cells from normal breast and tumors reveal plasticity of adipose derived stem cells." Breast Cancer Res **18**(1): 32.

Wesemann, C., Pieralli, S., Fretwurst, T., Nold, J., Nelson, K., Schmelzeisen, R., Hellwig, E. and Spies, B. C. (2020). "3-D Printed Protective Equipment during COVID-19 Pandemic." Materials (Basel) **13**(8).

Williams, J. M., Adewunmi, A., Schek, R. M., Flanagan, C. L., Krebsbach, P. H., Feinberg, S. E., Hollister, S. J. and Das, S. (2005). "Bone tissue engineering using polycaprolactone scaffolds fabricated via selective laser sintering." Biomaterials **26**(23): 4817-4827.

Wiria, F. E., Leong, K. F., Chua, C. K. and Liu, Y. (2007). "Poly-epsilon-caprolactone/hydroxyapatite for tissue engineering scaffold fabrication via selective laser sintering." Acta Biomater **3**(1): 1-12.

Wong, J. Y. and Pfahnl, A. C. (2014). "3D printing of surgical instruments for long-duration space missions." Aviat Space Environ Med **85**(7): 758-763.

Woodruff, M. A. and Hutmacher, D. W. (2010). "The return of a forgotten polymer-Polycaprolactone in the 21st century." Progress in Polymer Science **35**(10): 1217-1256.

Woodward, S. C., Brewer, P. S., Moatamed, F., Schindler, A. and Pitt, C. G. (1985). "The intracellular degradation of poly(epsilon-caprolactone)." J Biomed Mater Res **19**(4): 437-444.

Wu, G., Bi, Y., Zhou, B., Zemnick, C., Han, Y., Kong, L. and Zhao, Y. (2009). "Computer-aided design and rapid manufacture of an orbital prosthesis." Int J Prosthodont **22**(3): 293-295.

Wunner, F. M., Eggert, S., Maartens, J., Bas, O., Dalton, P. D., De-Juan-Pardo, E. M. and Hutmacher, D. W. (2019). "Design and Development of a Three-Dimensional Printing High-Throughput Melt Electrowriting Technology Platform." 3D Printing and Additive Manufacturing **6**(2): 82-90.

Wunner, F. M., Maartens, J., Bas, O., Gottschalk, K., De-Juan-Pardo, E. M. and Hutmacher, D. W. (2018). "Electrospinning writing with molten poly (ε-caprolactone) from different directions – Examining the effects of gravity." Materials Letters **216**: 114-118.

Wunner, F. M., Mieszczanek, P., Bas, O., Eggert, S., Maartens, J., Dalton, P. D., De-Juan-Pardo, E. M. and Hutmacher, D. W. (2019). "Printomics: the high-throughput analysis of printing parameters applied to melt electrowriting." Biofabrication **11**(2): 025004.

Wunner, F. M., Wille, M. L., Noonan, T. G., Bas, O., Dalton, P. D., De-Juan-Pardo, E. M. and Hutmacher, D. W. (2018). "Melt Electrospinning Writing of Highly Ordered Large Volume Scaffold Architectures." Adv Mater **30**(20): e1706570.

Xia, H., Li, X., Gao, W., Fu, X., Fang, R. H., Zhang, L. and Zhang, K. (2018). "Tissue repair and regeneration with endogenous stem cells." Nature Reviews Materials **3**(7): 174-193.

Xia, Y., Zhou, P., Cheng, X., Xie, Y., Liang, C., Li, C. and Xu, S. (2013). "Selective laser sintering fabrication of nano-hydroxyapatite/poly-epsilon-caprolactone scaffolds for bone tissue engineering applications." Int J Nanomedicine **8**: 4197-4213.

Yamanaka, N., Okamoto, E., Kawamura, E., Kato, T., Oriyama, T., Fujimoto, J., Furukawa, K., Tanaka, T., Tomoda, F. and Tanaka, W. (1993). "Dynamics of normal and injured human liver regeneration after hepatectomy as assessed on the basis of computed tomography and liver function." Hepatology **18**(1): 79-85.

Yen, H. J., Tseng, C. S., Hsu, S. H. and Tsai, C. L. (2009). "Evaluation of chondrocyte growth in the highly porous scaffolds made by fused deposition manufacturing (FDM) filled with type II collagen." Biomed Microdevices **11**(3): 615-624.

Yoko, S., Kobayashi, Y., Iiri, T., Kitazawa, H., Okabe, M., Kobayashi, H., Okazaki, E. and Aizawa, Y. (2013). "Pacing lead-induced granuloma in the atrium: a foreign body reaction to polyurethane." Case Rep Cardiol **2013**: 396595.

Yoon, Y. I., Park, K. E., Lee, S. J. and Park, W. H. (2013). "Fabrication of microfibrous and nano-/microfibrous scaffolds: melt and hybrid electrospinning and surface modification of poly(L-lactic acid) with plasticizer." Biomed Res Int **2013**: 309048.

Youssef, A., Hollister, S. J. and Dalton, P. D. (2017). "Additive manufacturing of polymer melts for implantable medical devices and scaffolds." Biofabrication **9**(1): 012002.

Youssef, A., Hrynevich, A., Fladeland, L., Balles, A., Groll, J., Dalton, P. D. and Zabler, S. (2019). "The Impact of Melt Electrowritten Scaffold Design on Porosity Determined by X-Ray Microtomography." Tissue Eng Part C Methods **25**(6): 367-379.

Zaiss, S., Brown, T. D., Reichert, J. C. and Berner, A. (2016). "Poly(epsilon-caprolactone) Scaffolds Fabricated by Melt Electrospinning for Bone Tissue Engineering." Materials **9**(4): 232.

Zargar, N. and Carr, A. (2018). "The regulatory ancestral network of surgical meshes." PLoS One **13**(6): e0197883.

Zein, I., Hutmacher, D. W., Tan, K. C. and Teoh, S. H. (2002). "Fused deposition modeling of novel scaffold architectures for tissue engineering applications." Biomaterials **23**(4): 1169-1185.

Zeng, C., Xiao, J., Wu, Z. and Huang, W. (2015). "Evaluation of three-dimensional printing for internal fixation of unstable pelvic fracture from minimal invasive para-rectus abdominis approach: a preliminary report." Int J Clin Exp Med **8**(8): 13039-13044.

Zhang, Q., Hwang, J. W., Oh, J. H., Park, C. H., Chung, S. H., Lee, Y. S., Baek, J. H., Ryoo, H. M. and Woo, K. M. (2017). "Effects of the fibrous topography-mediated macrophage phenotype transition on the recruitment of mesenchymal stem cells: An in vivo study." Biomaterials **149**: 77-87.

Zhang, R., Billingsley, M. M. and Mitchell, M. J. (2018). "Biomaterials for vaccine-based cancer immunotherapy." J Control Release **292**: 256-276.

Zhang, Y., Al-Maawi, S., Wang, X., Sader, R., James Kirkpatrick, C. and Ghanaati, S. (2019). "Biomaterial-induced multinucleated giant cells express proinflammatory signaling molecules: A histological study in humans." J Biomed Mater Res A **107**(4): 780-790.

Zhou, G., Jiang, H., Yin, Z., Liu, Y., Zhang, Q., Zhang, C., Pan, B., Zhou, J., Zhou, X., Sun, H., Li, D., He, A., Zhang, Z., Zhang, W., Liu, W. and Cao, Y. (2018). "In Vitro Regeneration of Patient-specific Ear-shaped Cartilage and Its First Clinical Application for Auricular Reconstruction." EBioMedicine **28**: 287-302.

Zhou, W. Y., Lee, S. H., Wang, M., Cheung, W. L. and Ip, W. Y. (2008). "Selective laser sintering of porous tissue engineering scaffolds from poly(L: -lactide)/carbonated hydroxyapatite nanocomposite microspheres." J Mater Sci Mater Med **19**(7): 2535-2540.

Zopf, D. A., Flanagan, C. L., Wheeler, M., Hollister, S. J. and Green, G. E. (2014). "Treatment of severe porcine tracheomalacia with a 3-dimensionally printed, bioresorbable, external airway splint." JAMA Otolaryngol Head Neck Surg **140**(1): 66-71.

Zopf, D. A., Hollister, S. J., Nelson, M. E., Ohye, R. G. and Green, G. E. (2013). "Bioresorbable airway splint created with a three-dimensional printer." N Engl J Med **368**(21): 2043-2045.

Zyczkowski, M., Nowakowski, K., Kuczmik, W., Urbanek, T., Kaletka, Z., Bryniarski, P., Muskala, B. and Paradysz, A. (2014). "Tension-free vaginal tape, transobturator tape, and own modification of transobturator tape in the treatment of female stress urinary incontinence: comparative analysis." Biomed Res Int **2014**: 347856.

Acknowledgments

This journey was years and years in the making and did not just start in 2015. Throughout, I have received an enormous amount of help and support from lots of people, whom I will try and give my best effort to acknowledge here.

Prof. Dalton: Thank you Paul for all the help and support throughout the years. Thank you for putting your trust in me and in my decisions. You always believed in me, even when I, myself, did not. Ever since we have met in November 2014, you have been a source of support, enthusiasm, inspiration and immense knowledge. Working with you was a great pleasure. I learned many things from you in our long discussions: working with people, presenting my work, writing, “choosing my battles”, seeing opportunities in every ~~problem~~ challenge and, of course, science!

Prof. Groll: Thank you for giving me the opportunity to do my doctorate in your wonderful department and for funding me. I always found a listening ear with you when I needed. You always had solutions to my problems, and you trusted and supported my decisions and work.

Prof. Jakob and Prof. Blunk: Thank you for being members of my committee and for your many helpful ideas and comments during our meetings. Prof. Jakob supervised my Master’s thesis and taught me many things and guided me when I was clueless and still fresh out of my clinical background.

FMZ has been my second home for years, and to my friends and colleagues there, you have my sincerest gratitude. FMZ was a great place to work at and I had a great time there doing science, but also getting to know a lot of different people and spending great time with them. The interdisciplinarity of FMZ improved my knowledge in areas I would not have thought possible: chemistry, physics and percolation theory! The list of people to thank includes current and former FMZ members, and I hope I do not forget anyone.

Andrei Hrynevich, much of this would have been possible without your help, thank you for everything my dear friend. The Biofabrication Team: Dr. Tomasz Jüngst, Dr. Gernot Hochleitner, Dr. Carina Blum, Ezgi Bakirci, Christoph Bohm, Daniel Nahm and Juliane Kade, working with all of you was a great pleasure. Thank you all. I must single out Tomasz and Gernot, you both really have left a great impact on me. I wish you all the best in all your future endeavors. The *alternate* Biofabrication Team: Jodie Haigh, Dr. Mylene de Ruijter, Daimon Hall and Thomas Robinson: you are the best! Dr. Jörg Teßmar, Dr. Andrea Ewald, Tanja Dambach, Birgit Langner-Bischof and Prof. Uwe Gbureck: Thank you for making my life a lot easier with administrative tasks, for always having my back and for the tremendous guidance support from Andrea in the animal experiments. Alevtina Rosenthal, Isabell Biermann, Franziska Viet, Van Am Doan, Lina Kötzner, Simone Werner and Judith Friedlein for their technical support. Harald Hümpfer and Anton Hofmann for always making miracles happen. Big thanks go to Willi Smolan, Dr. Ana Sancho, Dr. Julia Liebsher, Dr. Michaela Rödel, Junwen Shan, Dr. Susanne and Markus Meininger, Dr. Claus Moseke, Dr. Michael Schmidt, Dr. Kai Stuckensen, Sonja Horvat, Enrico Webelhorst, Constantin Berger, Esteban Ceballos, Florian Pinzner, Ib Holzmeister, Leonard Forster, Manuel Roesener, Dr. Martha Schamel, Dr. Mehmet Berat Taskin, Philipp Stahlhut, Jan Weichhold, Dr. Thomas Bock, Dr. Tatjana Schilling and Dr. Katrin Schlegelmilch.

Science is always about working together, therefore I would like to extend my thanks and appreciation to the collaboration partners in Department of Cellular Therapies, University of Navarra, Pamplona (Purificación Ripalda Cemborain, Tania Lopez Martinez, José Valdés-Fernández and Prof. Froilán Granero-Moltó), Department of X-ray Microscopy, University of Würzburg (PD Dr. Simon Zabler, Dr. Christian Fella, Andreas Balles, Daniel Althoff and Logan Fladeland), Department of Oral and Maxillofacial Plastic Surgery, University Hospital Würzburg (Prof. Dr. Dr. Christian Linz, Dr. Dr. Andreas Fuchs, Irina Kucerov and Margit Schleyer) and Department of Experimental Trauma Surgery, Regensburg University Hospital (Prof. Denitsa Docheva and Heyong Yin).

Dr. Stephan Schröder-Köhne, Dr. Franz-Xaver Kober and Dr. Gabriele Blum-Oehler: thank you for everything you have done from 2013 onwards. My FOKUS family: Ana, Andrea, Ashley, Cheek, Diyaa, Gayathri, Manju, Manli and Prathibha, we have been through a lot together and I always had your support and encouragement. To my mentors in Egypt who taught me research and showed me there were more possibilities than I could imagine: Prof. Mohamed Elshinawi, Prof. Mona Mohamed and Dr. Youssef Farag, thank you all.

This journey would not have even started if it was not for my parents. They encouraged, supported and completely financed me during my Master's studies. Thank you and God bless you. I also want to thank my dear siblings, Noha and Adham for supporting me. My parents helped starting the journey, but it was you, Passant, who kept it going. Thank you for always being by my side, for putting up with my stressful days (which were a lot), my constant absence (even when I am by your side), for pushing me forward, for being you. There is only you and this is for you. And then came the little guy who placed everything on hold, but to his credit, he was more than happy to play with the keyboard during the writing of this thesis, as a way of encouragement for me to write. Mourad, you bring light and happiness to this world.